UNIVERSIDADE DE SANTIAGO DE COMPOSTELA

Departamento de Física de Partículas

PHENOMENOLOGY OF THE DETECTION OF ULTRA-HIGH ENERGY COSMIC RAYS AND NEUTRINOS USING THE RADIO TECHNIQUE

Ph.D. Thesis

Daniel García Fernández

Santiago de Compostela, xaneiro 2016.

USC
UNIVERSIDADE
DE SANTIAGO
DE COMPOSTELA

UNIVERSIDADE DE SANTIAGO DE COMPOSTELA

Departamento de Física de Partículas

PHENOMENOLOGY OF THE DETECTION OF ULTRA-HIGH ENERGY COSMIC RAYS AND NEUTRINOS USING THE RADIO TECHNIQUE

Tese presentada para optar ao Grao de Doutor en Física por:

Daniel García Fernández

Santiago de Compostela, xaneiro 2016

Asdo: Daniel García Fernández

USC
UNIVERSIDADE
DE SANTIAGO
DE COMPOSTELA

Jaime Álvarez Muñiz,
Profesor Titular Doutor da Universidade de Santiago de Compostela

CERTIFICA:

que a memoria titulada: "Phenomenology of the detection of ultra-high energy cosmic rays and neutrinos using the radio technique" foi realizada, baixo a miña dirección, por Daniel García Fernández no Departamento de Física de Partículas da Universidade de Santiago de Compostela, e constitúe o traballo de Tese que presenta para optar ó grao de Doutor en Física.

En Santiago de Compostela, a xaneiro de 2016

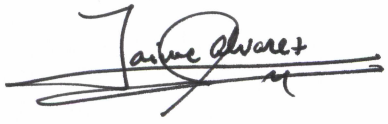

Asdo: Jaime Álvarez Muñiz

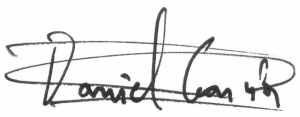

Asdo: Daniel García Fernández

USC
UNIVERSIDADE
DE SANTIAGO
DE COMPOSTELA

A Cri.

Senza te questa tesi non esisterebbe.

E neanch'io.

USC
UNIVERSIDADE
DE SANTIAGO
DE COMPOSTELA

Acknowledgements

Four years have passed since I started this thesis. The first years were marked by excitement about the beginning of a new era in my life, with new paradigms, new acquantainces and a peace of mind unlike I had ever felt up to that point. Stagnation came after a while, although I have to admit it had to do more with my mental processes than with the circumstances surrounding me. I did consider quitting physics. At some point, I even thought about not finishing this work.

But some things compelled me to stay. I discovered I really loved teaching physics and talking to my students. I learned to love my work, its successes, its nuances, its defects... The superficial infatuation from the beginning had turn into a more mature appreciation and understanding. The habits you can acquire when you work in physics the right way — curiosity, discipline, creativity, facing the problems with a calmed mind, among many others, are traits that have been useful for every other aspect of my life.

At this stage of uncertainty and changes to come, one thing is certain — I am not the same person that started this work. I have to thank (and sometimes curse) the following people, the ones that kept me on my feet and changed my life in ways I could never imagine.

A Cris, por ser a mellor persoa que xamáis atopei e atoparei. E por todo o demáis que só ela sabe.

A meus pais, Pili e Plácido, pola súa comprensión e apoio incondicional. A toda a miña familia por tantos momentos: a avoa Josefa; ós tíos Roberto e Auri, José Luis e Mari, Manolo e Conchi, Antonio e María José; ós primos Álex, Andrea, Nerea... A Eduardo, Pilar e Eric por tratarme como un da familia desde o primeiro momento.

A Jaime por ser un director de tese sempre atento e involucrado e por deixarme aprender física e non só física no proceso. A Enrique por demostrarme que a intuición en física importa. A Washington, de quen aprendín a como escrutar todo problema ata o mínimo detalle, e que sempre é posible mudar e reinventarse radicalmente se un o precisa, ademáis de por ser un amigo. A Andrés e Matías, por seren brillantes colaboradores. Harm, for believing in Santiago's group and for having many insightful discussions with us. A Gonzalo e Valerio, per permettermi di scoprire la fisica sperimentale. A Carlos Merino, por deixarme descubrir o gratificante que pode ser dar clase.

A meus amigos de onte e de sempre. A Adrián Delgado por ter sido e seguir sendo a miña vangarda (sempre anos tras de ti, paseniño...). A Alfonso "Lujas" por demostrar que, pase o que pase, sempre será un amigo fiel. A Álvaro Fernández polos momentos bos,

e tamén polos malos dos que aprendín tanto da vida. A Raúl (BR) por ser sincero pase o que pase. A Fátima por aquel quince de setembro. A Ger e Ángela, por estar sempre cun sorriso na cara, irradiando ledicia e facendo felices a todos. A Brân pola súa integridade e polas conversas que me axudaron ano tras ano. A Sara, por contaxiarme sempre o seu entusiasmo e ganas de vivir. A Lydia e Rober, porque velos sempre me alegra o día. A Martín, por anos, vivencias e aficións compartidas. A Mau por saber que, incluso a traverso da distancia e o tempo, seguimos tendo un vínculo. A Raúl Mella, por axudarme a medrar por dentro e presentarme a tanta xente excepcional (el incluído). A Jojhy porque aínda que pase o tempo nunca deixa de ser unha persoa bondadosa. A Brais, porque por algún motivo desde parvulitos nos levamos ben. A Carlos Ramallal, porque desde aquelas partidas de rol na súa casa sabe que me ten gañado para sempre. A Jano, por facerme descubrir tanto e por deixarme disfrutar do seu humor. A Cris, Ceci e Luisa por facelos felices. A Rubén e Xián porque me devolven o optimismo no mundo. Á xente da miña promoción, os meus primeiros amigos: Adrián, Saínza, Yelco, Leticia, Pedro Iglesias, Pedro Montes, Fran, Dani Abruñedo, Olalla, Silvia, Alba, Laura, David Riobóo, Lucas, Mante, Eva, Andrea, Pablo Calvo...

Durante os meus anos universitarios coñecín a moitas persoas que se convertiron en parte irreemplazable da miña vida. A Josu, polas improvisacións, os concertos, os festivais, as aventuras. Por facerme ver que nunha mente colle todo o que ti queiras e porque ser caótico bo é unha boa opción nun mundo caótico. A Alexey, por ser un artista da física, da fotografía e da vida. A Álvaro Magaña por inaugurar a nova xeración de físicos[1] e por intentar sempre pensar un pouco máis alá có resto. A Jorge, por ter unha brúxula moral e unha claridade mental imbatibles. A Ana, porque parece que a fixeron de encarga para el. A Antón, porque sempre poderemos cantar Alabama song. A Carlos, porque tanto estudio, café, cañas e parranda, une. A Carlota, pola compaña e anécdotas, e por servir de apoio moral a medio departamento. A Eva, por ser sempre tan amable e por erguerse vez tras vez, incluso aquela vez co nitróxeno. A Guille (Indalecio), por amosarme de que é capaz unha mente humana. A Isa, por ser a primeira en acollerme cando cheguei a Compostela. A Iñigo, por conservar a ilusión en todo e en todos a pesar do tempo, que se che ve nos ollos. A Inés por acollerme en astropartículas e por aturar os meus ruidiños. A Guille (Torralba) por non facer ruidiños pero botar bombas de poucos decibelios cando se pon a falar. A Karen, por ser tan boa xente. A Julio, porque en contra da opinión popular[2], nunca me pareceu que dera noxo, senón todo o contrario. A Carro, o noso inimitable

[1] Si, vai ser pai.

[2] Pablo.

camarada. A Mateo, porque aínda que non o crea lle teño moito aprecio e porque sempre me arrepentirei da patada aquela. A Manoel (Calvo), porque unha relación da que se aprendeu pode pagar a pena recuperala. A Manoel (Moldes), por amosarme que facer o que che peta é posible e ata necesario. A Nacho, por ser capaz de sorprenderme cada vez que quedo con el. A Pablo, porque a súa capacidade de facer mil cousas sempre me fascinou e intento imitala. A Rodri, por ser o meu moucho bipolar preferido. A Julio René por ser ese eterno personaxe compostelán. A Patricia por descubrirme a arte do mate. A Xabi, polos cursos acelerados de retranca. A Rosalía, porque ti e máis eu sabemos que merecías ser a raíña da biblioteca. A Vicente, por ser un gran compañeiro de habita e mellor amigo e confidente. A Jacobo por axudarme a expandir horizontes musicais e filosóficos e por ter razón en tanto. A Marta, por axudarme a ser mellor persoa e porque aínda teño remordementos. A Aida, Fran, Damián e Penín, quen me lembraron por que empezara o doutorado e ós que desexo que sexa unha boa etapa nas súas vidas.

Houbo xente que se atreveu a estudiar xaponés, coma min. E unha das mellores recompensas de atreverme a estudialo foi que os puiden coñecer. A Jose, por ese humor punzante e envelenado, pero quen no fondo é un mochi kawaii. A Fernando, porque os productos da súa mente me producen risa e terror a partes iguais. A Manuel, porque nunca me cansarei das súas conversas densas e frenéticas.

A Raúl, Álvaro, Abi, Javi, Inés, Pablo Montero, Paco e compañía por grandes noites con eventos fóra do alcance desta tese.

A música tamén me axudou moito estes anos. Débolle moito a todos os músicos que quixeron tocar conmigo. A Aitor, Alexis, Pablo, Yasia e Difet por permitirme ter a actuación máis divertida da miña vida en Capitol. A Álvaro, Guillermo, Nico, Iria, Samuel e Fernando por acollerme no seu combo e darme a oportunidade de comprobar que son máis versátil do que cría (aínda que hai moito que mellorar). A Josu porque non paro de aprender del e a tamén a Paul, porque tres persoas son máis que suficientes para reventar unha sala. A Rodri, Ian e Akeno por aquel concerto marciano con traxes de sumo e puchos soviéticos. A meu tío Manolo por introducirme no mundo do rock. Ós meus mestres, que levaron (e levarán) as miñas habilidades a niveis que se me antollaban imposibles: Quique Alvarado, Suso Atanes, Leo Pimentel e Javier Constenla.

Unha aperta a todos.

Time may change me
But I can't trace time
Changes, David Bowie

USC
UNIVERSIDADE
DE SANTIAGO
DE COMPOSTELA

Publications

Some of the original work of this thesis has produced published papers, conference talks and contributions.

The study of the electric field of a particle track and the validity of the ZHS formula, from Chapter 3, has produced a Physical Review D paper [1].

The application of the ZHS code to the AMY experiment treated in Chapter 5 has been present in conference talks such as [2].

The study of the reflection of the electric field on a surface and the updating of the ZHAireS code into ZHAireS-Reflex (Chapter 6) has produced an Astroparticle Physics paper [3] and conference talks such as [4]. Besides, it has been the basis for a spectrum measurement using only radio measurements as explained in [5, 6].

Bibliografia

[1] D. García-Fernández, J. Alvarez-Muñiz, W. R. Carvalho Jr., A. Romero-Wolf, and E. Zas. Calculations of electric fields for radio detection of ultrahigh energy particles. *Physical Review D*, **87**(023003), 2013.

[2] V. Verzi. The AMY (Air Microwave Yield) experiment to measure the ghz emission from air shower plasma. In *Proceedings of Acoustic and Radio EeV Neutrino Detection Activities (ARENA) 2014*.

[3] J. Alvarez-Muñiz, W.R. Carvalho Jr., D. García-Fernández, H. Schoorlemmer, and E. Zas. Simulations of reflected radio signals from cosmic ray induced air showers. *Astroparticle Physics*, **66**:31, 2015.

[4] D. García-Fernández *et al.* Radio emission from ultra-high energy cosmic-ray showers after reflecting on the Earth. In *Proceedings of the 34th International Cosmic Ray Conference (ICRC 2015)*, number 266.

[5] H. Schoorlemmer *et al.* Energy and flux measurements of ultra-high energy cosmic rays observed during the first ANITA flight. In *Proceedings of the 34th International Cosmic Ray Conference (ICRC 2015)*, number 272.

[6] H. Schoorlemmer *et al.* Energy and flux measurements of ultra-high energy cosmic rays observed during the first ANITA flight. arxiv:1506.05396. Accepted in Astroparticle Physics in press.

Contents

Chapter 1

Introduction

Cosmic rays were discovered in 1912 by Victor Hess [1] when, after a series of balloon flights, saw that the ionisation of air at 5000 m was more than twice the ionisation present at sea level, indicating that there was a source of ionising radiation from outside the Earth. Millikan then coined the term *cosmic rays* for this radiation, for he believed it was composed by gamma rays coming from outer space. It was later discovered that there were more cosmic rays coming from the west than from the east [2], and that therefore most cosmic rays were positively charged [3]. Besides, because of the presence of the atmosphere, many of the detected cosmic rays must be *secondary particles* produced after a *primary particle* from outer space interacts with the atmosphere or the interstellar medium between the source and the Earth. It took thirty years to elucidate that the primary cosmic rays were mainly protons [4], at least at low energies.

Pierre Auger and his colleagues [5] found that at ground level, some particles arrived at the same time with a milisecond level of precision, even for distances as large as 100 m, suggesting that these secondary particles were part of an extensive air shower created by the interaction of a primary with the atmosphere. They estimated the largest showers to be produced by a primary of 10^{15} eV, which was an energy beyond the reach of any known physical process at the time.

Cosmic rays proved themselves useful for particle physics in the early days, as demonstrated by the discovery of the positron [6] or the muon [7], along with many other particles. However, since the 1950s particle physics has been done mainly in accelerator experiments and the study of cosmic rays was used to research interactions at energies higher than what was possible at accelerators and to investigate their properties (spectrum, composition...) in order to find their possible sources and acceleration mechanisms.

The spectrum of the cosmic rays extends to 10^{18} eV and beyond, which is the region of what we usually call *ultra high energy cosmic rays*. The highest primary ever measured was seen by the Fly's Eye fluorescence detector and had an energy of $3 \cdot 10^{20}$ eV. Between the PeV and the EeV region[1], the particles are usually labeled *very high energy cosmic*

[1] 1 PeV= 10^{15} eV, 1 EeV= 10^{18} eV.

rays. Since ultra high energy particles exist, it is expected that some of them produce ultra high energy neutrinos on their propagation through the universe, which propagate in straight lines (gravitational effects neglected) and could help us to trace the sources of the cosmic rays.

The main subject of this thesis is the study of the ultra high energy cosmic rays and neutrinos, and their detection by means of the radio technique.

1.1 Ultra High Energy Cosmic Rays

Ultra High Energy Cosmic Rays (UHECRs) with energies in the EeV range and above, have energies $\gtrsim 10^6$ times larger than those that can be obtained at man-made accelerators, and therefore pose several questions that have been unanswered so far. Some of the most important ones are

- How many particles arrive at a certain energy, *i.e.*, which is the spectrum of the UHECRs?
- What kind of particles are the ones who arrive at ultra high energies? Or, equivalently, what is the composition of the UHECRs?
- Are there excesses of cosmic rays from certain regions of the sky? That is, can we identify their sources?
- What is the acceleration mechanism present in these sources to accelerate particles to energies as large as 10^{20} eV?
- How do they interact with the cosmic background radiation?
- What kind of particles do cosmic rays create on their propagation towards the Earth?
- How strong are the magnetic fields they traverse before reaching the Earth?

In the following we give a brief summary of what we know so far about the answers to these questions.

1.1.1 Brief summary of experimental evidence

In Fig. 1.1 we show the cosmic-ray spectrum (from [8]), from 10^9 eV to 10^{20} eV. It spans 11 decades of energy, along which the flux $\mathrm{d}N/\mathrm{d}E$ falls by 25 orders of magnitude, and yet

the spectrum is mainly featureless. It can be described by a broken power law, $E^{-\gamma}$, with γ the *spectral index*. $\gamma \sim 2.7$ below the *knee* at ~ 1 PeV and $\gamma \sim 3$ between the knee and the *ankle* around 3 EeV. While the reason for the features of the knee and the ankle is not known, it is suspected that they are related to the nature of the sources and perhaps the transition from galactic to extragalactic sources [9].

In Fig. 1.2 we show the latest results [10] of the Pierre Auger Observatory (Auger) [11] for the UHECR region. The ankle can be seen around 4 EeV, along with a change of the spectral index. Above $10^{19.5}$ eV, the flux decreases dramatically, a feature that is usually called *suppression*.

The knee is likely to indicate the maximum energy to which protons can be accelerated and confined in our galaxy [12]. The ankle can have various interpretations. If the primaries are mainly iron or a mixture, it can be an indication that Galactic cosmic rays are created up to that energy. Else, if the composition is dominated by protons, the ankle can be explained by the propagation of the protons interacting with the Cosmic Microwave Background (CMB) and producing e^+e^- pairs [13]. Likewise, the suppression of the spectrum at large energies offers a range of explanations. The suppression can be due to the GZK effect (*i.e.* to the interaction of UHECR with the CMB - see below [14, 15]). The composition of the cosmic rays can alter the interpretation as well, since the GZK effect depends on the nucleus that is propagating. Another possibility is that the suppression of the spectrum is a consequence of the maximum energy that cosmic rays can be accelerated to by the sources.

Knowing the composition of the UHECRs is vital for understanding their origin. The best indicator for determining the composition is the depth $X_{\max}$ in the atmosphere of the maximum of the shower induced by the primary particle, usually given in g/cm^2. The depth of the shower maximum scales approximately as $\ln(E/A)$, being E the energy of the primary and A the mass number of the primary. Therefore, on average, protons penetrate more into the atmosphere (have a larger $X_{\max}$) than iron nuclei.

Determining the composition of the UHECRs is one of the challenges in Astroparticle Physics, evidenced by the latest results by Auger [16] and Telescope Array (TA) [17]. In Fig. 1.3. Auger data hint towards a mixture of nuclei around 10^{17} eV, then towards a lighter component near the ankle and then towards a heavy component again at higher energies. TA, on the other hand, suggests that the primaries are mostly protons. There is work in progress to treat both data sets with the same reconstruction algorithms, and so far both data sets produce compatible results when treated in the same way [18].

In order to know the arrival directions of the cosmic rays and therefore try to determine

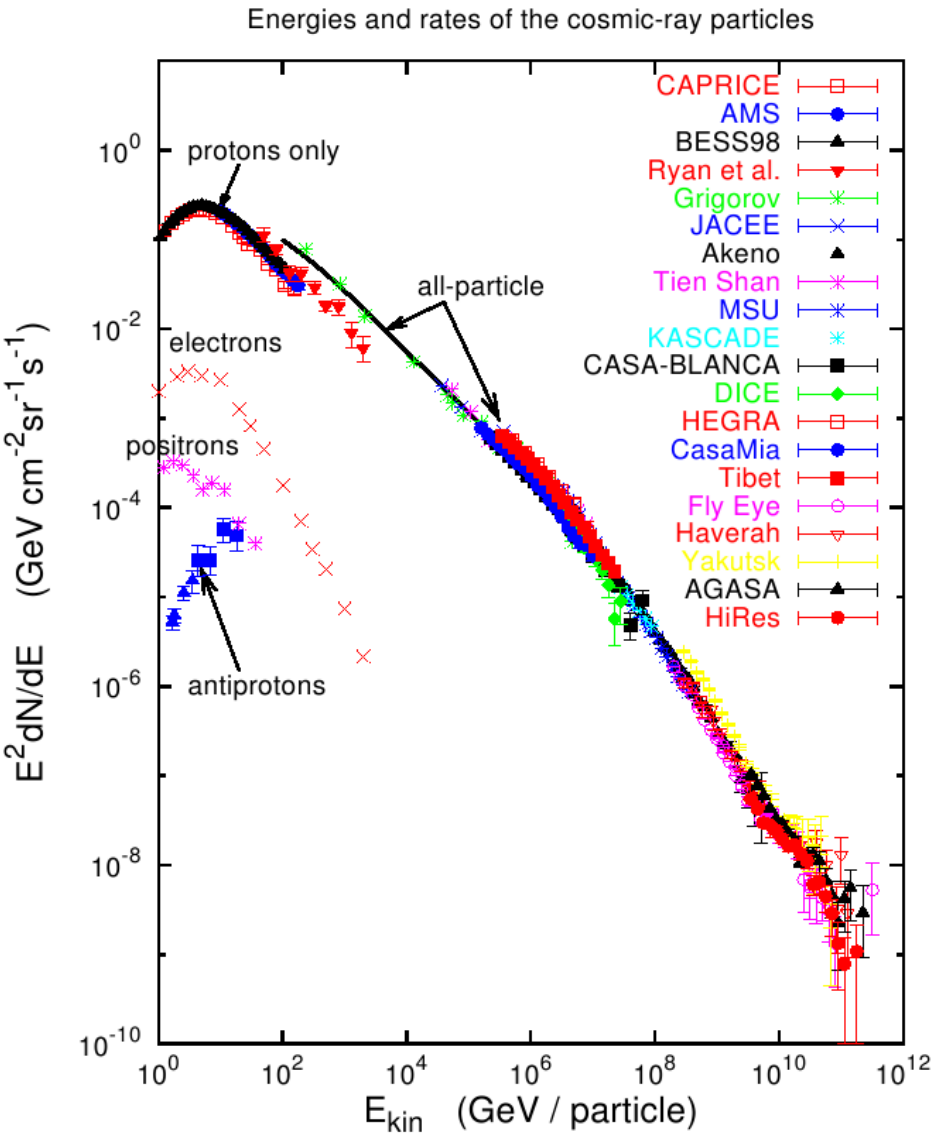

Figure 1.1: Cosmic Ray flux multiplied by E^2 as a function of primary energy for several primary species as observed by the listed experiments that had taken place until 2005. Taken from [8].

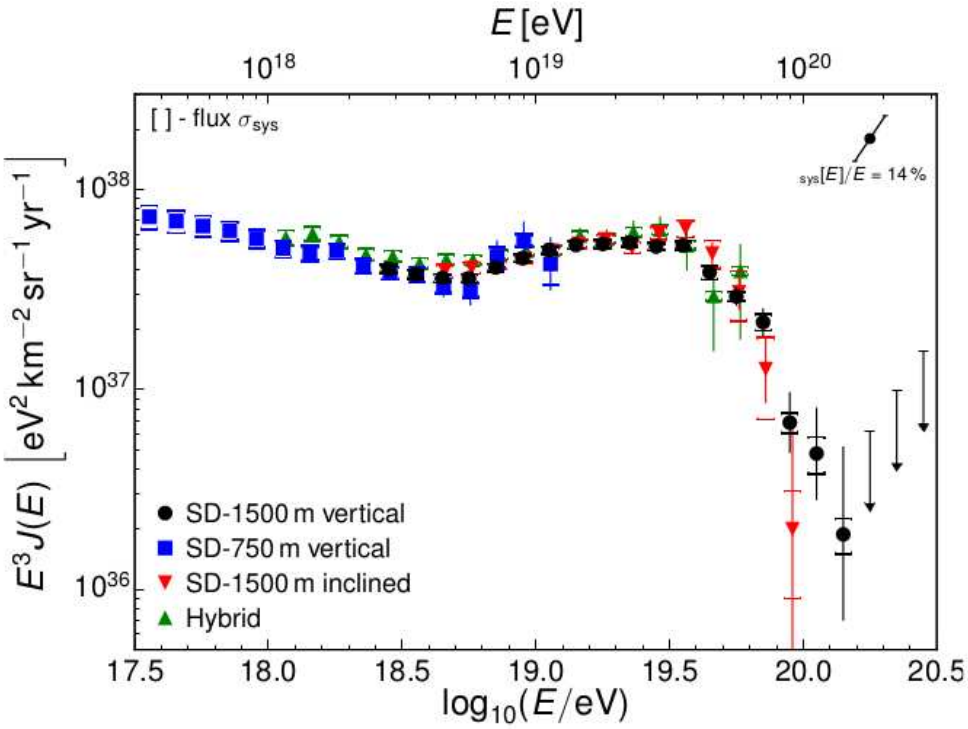

Figure 1.2: Cosmic Ray flux multiplied by E^3 as a function of primary energy for several primary species as observed at the Pierre Auger Observatory. The ankle and the suppresion at high energies can be clearly seen. Taken from [10].

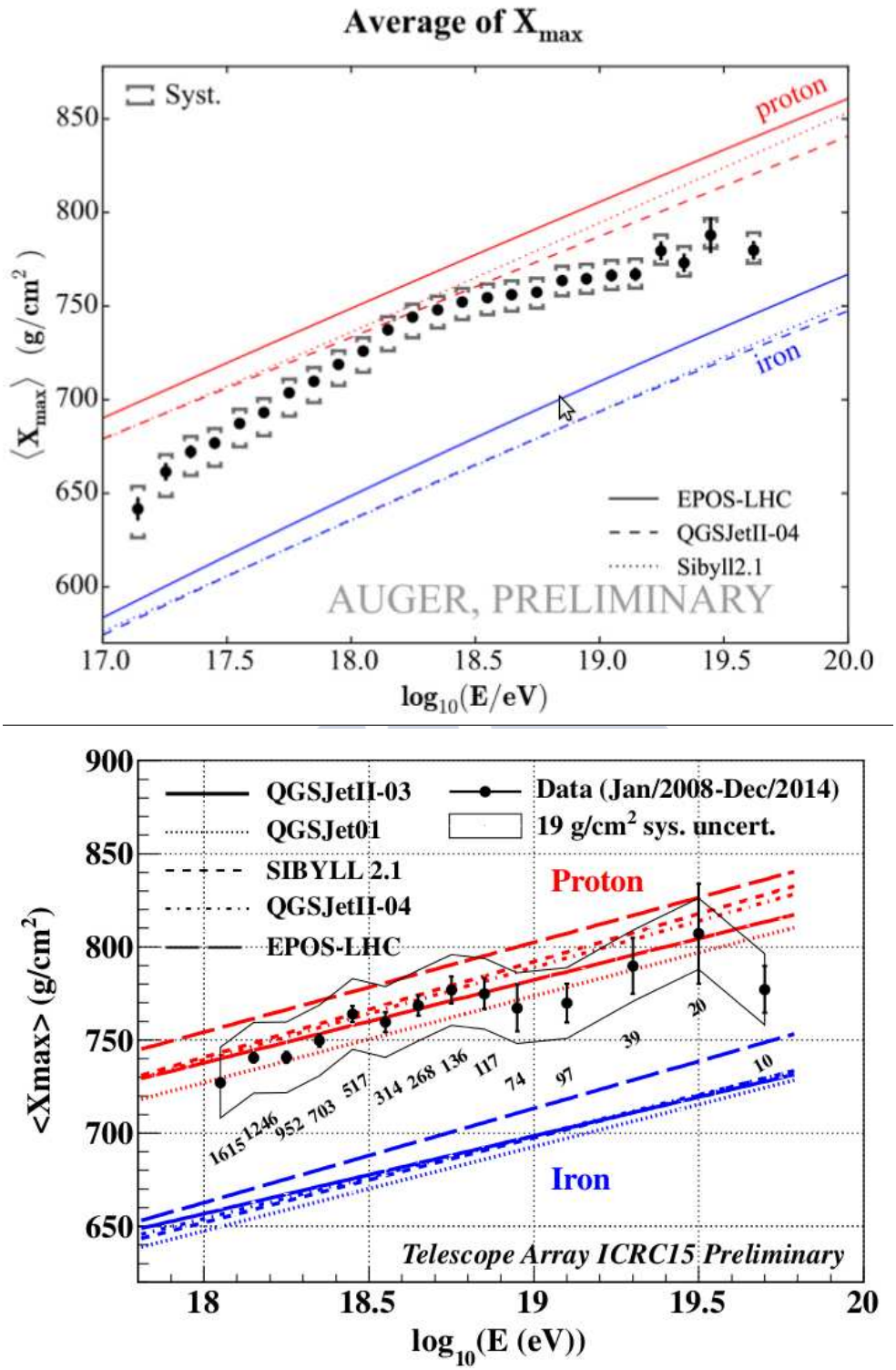

Figure 1.3: Mean measured $X_{\max}$ as a function of the primary energy. Expected curves for proton (red lines) and iron (blue lines) are shown for several hadronic interaction models. Top: Results from Auger [16]. Bottom: Results from Telescope Array [17]

.

the sources, anisotropies studies that look for excesses in the sky have been carried out. At UHE, TA in the Northern Hemisphere and Auger in the Southern Hemisphere have reported anisotropies with a small statistical significance (all below 3.5σ). Auger observed in 2007 a correlation with a population of Active Galactic Nuclei (AGN) [19], but with more statistics and comparisons with several astrophysical catalogs no significant correlation with known sources has been found [20, 21], implying that if the cosmic rays come from known sources they have been significantly deflected on their way to us. Another possibility is that the sources are transient and are no longer seen in radio or the optical when the cosmic rays arrive at the Earth. However, some degree of anisotropy is still present at energies larger than a few tens of EeV. TA has located an excess in a region they call the Hot Spot near the Ursa Major cluster [22] for energies > 57 EeV with a 3.4σ level of significance [23]. Auger has found an excess of events near Centaurus A above 54 EeV with a 4.3σ significance [21]. For lower energies, results are compatible with isotropy. No meaningful correlation with sources has been found, either. Interestingly, Auger has found a dipole in the arrival direction distribution of cosmic rays with $E > 8$ EeV [21]. Its origin is not yet explained.

1.1.2 Propagation effects: the GZK cut-off

On their way from the source to the Earth, cosmic rays can interact either with cosmic magnetic fields that deflect them but do not affect their energy or composition or with cosmic backgrounds that do affect their energy or composition.

Cosmic magnetic fields are not well known. Depending on their intensity and the rigidity of the particles, the effect of these fields can range from a small deflection of the order of a few degrees at high energies or for light nuclei, to a diffusive regime at low energies or for heavy nuclei. Recent observations of the Galactic magnetic fields suggest that the deflection should not exceed $\sim 10^{\circ}Z$ (40 EeV/E). Galactic magnetic fields are not uniform, so the deflection depends on the direction of observation, and their effect could be either a dispersion of the cosmic rays around the source or a deflection with a small dispersion. The magnitude of extragalactic magnetic fields is not well known, but measurements of Faraday rotation indicate fiels of $\sim$ 1 - 40 μG in the core of clusters of galaxies. Simulations of the effects of these magnetic fields are highly complex, and their results are very discrepant (see Fig. 9 in [9]).

While propagating, cosmic rays interact with the Cosmic Microwave Background (CMB) at the highest energies (above ~ 50 EeV), and with infrared, optical and ultraviolet backgrounds at lower energies.

For UHECR protons, photopion production in the CMB, also called GZK effect [14, 15] is the most important process. The dominant reactions are the following:

$$p + \gamma_{\text{CMB}} \rightarrow \pi^+ + n \tag{1.1}$$

$$p + \gamma_{\text{CMB}} \rightarrow \pi^0 + p \tag{1.2}$$

p is a proton, n a neutron and π represents the pions. The threshold energy, assuming a head-on collision is

$$E_{\text{threshold}} \simeq \frac{6.8 \cdot 10^{16}\ \text{eV}^2}{E_\gamma/\text{eV}}. \tag{1.3}$$

Assuming a mean photon of the CMB (T $\approx$ 2.725 K), its energy will be $E_\gamma \approx 6.4 \cdot 10^{-4}$ eV. The threshold energy for the process will be $\sim 10^{20}$ eV. The actual threshold energy is lower ($\sim$ 50 EeV) because of the CMB photons with energies above average. At this center-of-mass energy of $\sim$ 500 MeV, the cross section will be large because of the excitation of the Δ^+ resonance ($m_{\Delta^+} \approx 1232\ \text{MeV}/c^2$):

$$p + \gamma_{\text{CMB}} \rightarrow \Delta^+ \rightarrow p + \pi^0, \text{ or } n + \pi^+. \tag{1.4}$$

Another important process at these energies is the Bethe-Heitler process, also called electron-positron pair production:

$$p + \gamma_{\text{CMB}} \rightarrow p + e^+ + e^-. \tag{1.5}$$

The threshold energy of the proton for this process assuming a mean CMB photon is $\sim$ 0.8 EeV.

For nuclei with $A > 1$ with ultrahigh energies, the important reaction is photodisintegration with CMB and photons from infrared to ultraviolet [24]. The excitation of the Δ^+ resonance can also happen, in a similar way to Eq. (1.4). Nuclei can also undergo photo-pair production, that does not affect their mass number, and spallation with interstellar matter and other cosmic rays, which does affect their mass number.

A consequence of the GZK effect for protons and photodisintegration for nuclei is the reduction of the distance the cosmic rays are able to travel at energies beyond $\sim$ 50 EeV (or trans-GZK energies), implying that the sources must lie within a few hundreds of megaparsecs from Earth. In Fig. 1.4 we show the attenuation length for protons (left) and iron nuclei (right). Around 10^{20} eV, which corresponds to $\log_{10}\gamma \sim 11$ for protons and $\log_{10}\gamma \sim 9.3$ for iron nuclei, the mean free path decreases radically.

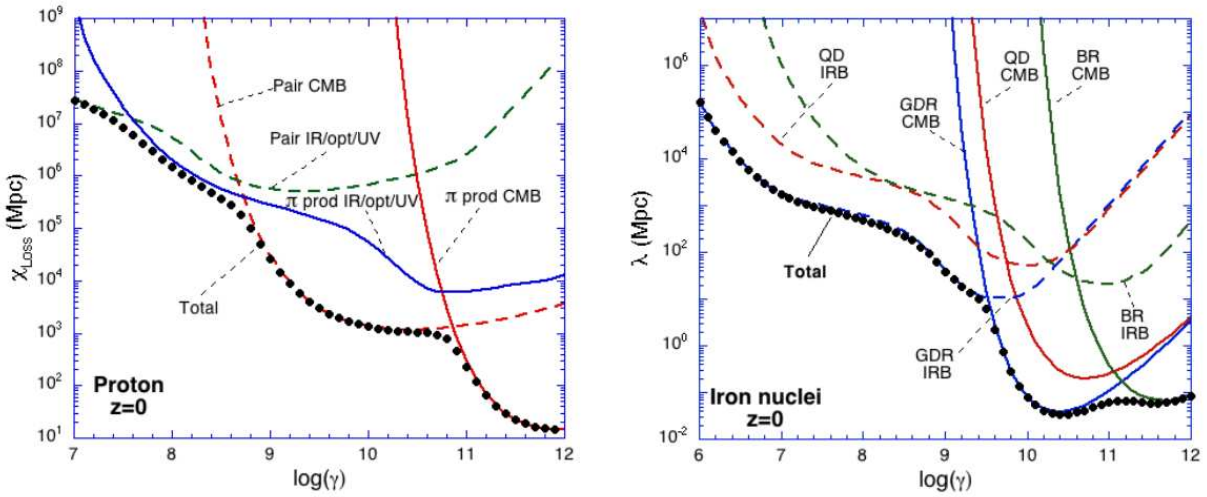

Figure 1.4: Attenuation length as a function of the decimal logarithm of the Lorentz factor γ. Left: attenuation length for protons due to pair and pion production with CMB and infrared, optical and ultraviolet (IR/opt/UV) photons. Right: attenuation length for iron nuclei due to the quasi deuteron (QD), giant dipole resonance (GDR) and baryonic resonance (BR) processes with infrared background (IRB) and CMB photons. Taken from [25].

Another feature of the interactions at high energy is that, at trans-GZK energies, nuclei with mass number $1 < A < 20$ possess a short attenuation length and cannot travel farther than few tens of megaparsecs. Protons and iron nuclei, on the contrary, survive more than 100 Mpc, as seen in Fig. 1.5.

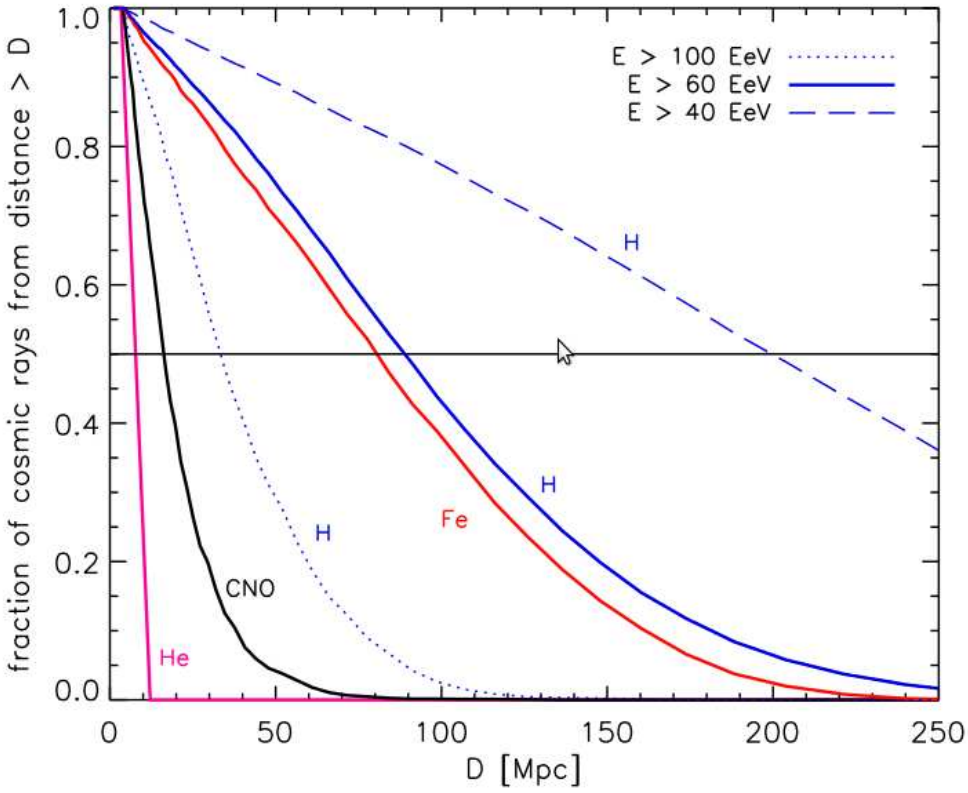

Figure 1.5: Fraction of cosmic rays that survive propagation over a distance $> D$, for protons above 40, 60 and 100 EeV and for He, CNO and Fe above 60 EeV. At trans-GZK energies ($E \gtrsim 60$ EeV) only protons and irons survive propagation beyond $D \gtrsim 50$ Mpc. Taken from [9].

Although propagation effects can be calculated analytically for protons, this is not the case for nuclei. Monte Carlo codes are best suited for this task, and also for including the effects of the inhomogeneity of the sources and the magnetic fields. Examples are CRPropa [26], SimProp [27] or the code in [25]. The calculated CR spectra agree well with the data for a variety of physical models, see [9].

1.1.3 Acceleration and potential sources

Charged particles can be accelerated through electric fields. However, large scale electric fields are not abundant in the universe. Magnetic fields are, however, very common. The variation of these magnetic fields in time and in space induce electric fields that can accelerate particles. In order to explain the spectrum of cosmic rays, we need acceleration mechanisms that can infuse particles with energies of the scale of EeV and that provide a power-law spectrum.

Fermi [28] elaborated an acceleration model in which particles gained energy when travelling through the inhomogeneities of the magnetic field in a cloud. If a particle with relative speed β enters a magnetic cloud and then exits after scattering randomly, without participating in collisions that drain energy from it, the mean increase in its energy E is proportional to $\Delta E/E \propto \beta^2$. This is called *second order Fermi process*, and the resulting spectrum follows a power-law spectrum as required. However, magnetic clouds are not well known, and the resulting spectrum is quite dependent on their properties.

If the macroscopic motion that gives energy to a microscopic particle is coherent, such as in a shock wave, we obtain the *first order Fermi process* [29]. In a shock wave, we have the up-stream region, where the shock has not arrived yet, and the down-stream region, the region the shock wave leaves behind. A particle travelling back and forth between both regions of the stream can increase its energy. The energy gain is, in this case, proportional to β. After n iterations, a particle that enters with energy E_0 has an average energy of

$$E_n = E_0 \left(1 + \frac{4}{3}\beta\right)^n . \tag{1.6}$$

The cosmic ray spectrum derived from this model also follows a power law as required. Acceleration through shocks could take place in supernova remnants (SNR), gamma ray burst (GRB) shocks, jets and hot spots of AGN and gravitational accretion shocks in general, all of them candidate sources for cosmic rays [9]. On the downside, there are details concerning the conditions for the rebound of particles back and forth the shock or the kind of shock that is most efficient that are not completely understood.

Another possible way of accelerating cosmic rays is with unipolar inductors [30], for instance, neutron stars or magnetised black holes. Neutron stars, through the rotation of their magnetic fields, create relativistic outflows of particles where a huge electric field is present. This electric field can accelerate particles at energies $> 10^{20}$ eV if it is created by young neutron stars [9]. This model also predicts a power law spectrum.

The general characteristics that a source must possess in order to accelerate cosmic rays up to hundreds of EeV and confine them until they reach these energies leave us with

a few known candidate structures in the universe.

The Larmor radius of a particle with total energy E and charge $Z|e|$ in a magnetic field B for the ultrarelativistic regime can be written as

$$r_{\mathrm{L}} = \frac{E}{Z|e|cB}. \tag{1.7}$$

If a source has a magnetic field B and extension R, the Larmor radius of a particle of energy E has to be less than the extension of the source, $r_{\mathrm{L}} \leq R$. This means that the maximum energy a particle can achieve is

$$E_{\mathrm{max}} = Z|e|cBR \sim 1 \text{ EeV } Z \left(\frac{B}{1\ \mu\mathrm{G}}\right) \left(\frac{R}{1 \text{ kpc}}\right). \tag{1.8}$$

One way of representing which astrophysical regions can accelerate cosmic rays up to a given energy is to present candidate sources in a B-R phase space with the uncertainties of these parameters. This is called the Hillas plot [31], and we show it in Fig. 1.6. For a fixed maximum energy E_{max}, we have a line of (R, B) pairs in the phase space as given by Eq. (1.8). When the extension of the sources or their magnetic field is large enough so that they lie above the line, they can in principle accelerate cosmic rays to the energy indicated by the line. Heavier nuclei are easier to confine due to their larger electric charge. Sources above the proton line in Fig. 1.6 are thought to present shockwaves and relativistic outflows capable of accelerating particles. In Fig. 1.6 we see that neutron stars, active galactic nuclei (AGN), gamma ray bursts (GRBs) and shocks in the intergalactic medium (IGM shocks) meet the general requirements for particle acceleration up to 10^{20} eV.

We must note that the Hillas criterion is a necessary condition, but it is not sufficient. More conditions are needed for a source to be able to accelerate particles up to a definite energy. For instance, the acceleration time must be smaller than the escape time of the cosmic rays, smaller than the time the particles lose most of their energy and smaller than the life time of the source. In addition, sources must possess a luminosity sufficiently high so that they account for the observed fluxes of cosmic rays.

The largest structures of the Universe, such as clusters of galaxies, have dark matter and gas accretion regions where shock acceleration can happen. AGN also present accretion disks around a central super-massive black hole, and therefore they should be able to accelerate particles via shock acceleration. AGN can be associated with jets that terminate in lobes (also called *hot spots*). GRBs lead to several shock regions with large magnetic fields as well, and the fact that they are transient objects could explain the absence of clear correlations of cosmic rays with astrophysical catalogs. Neutron stars are also good

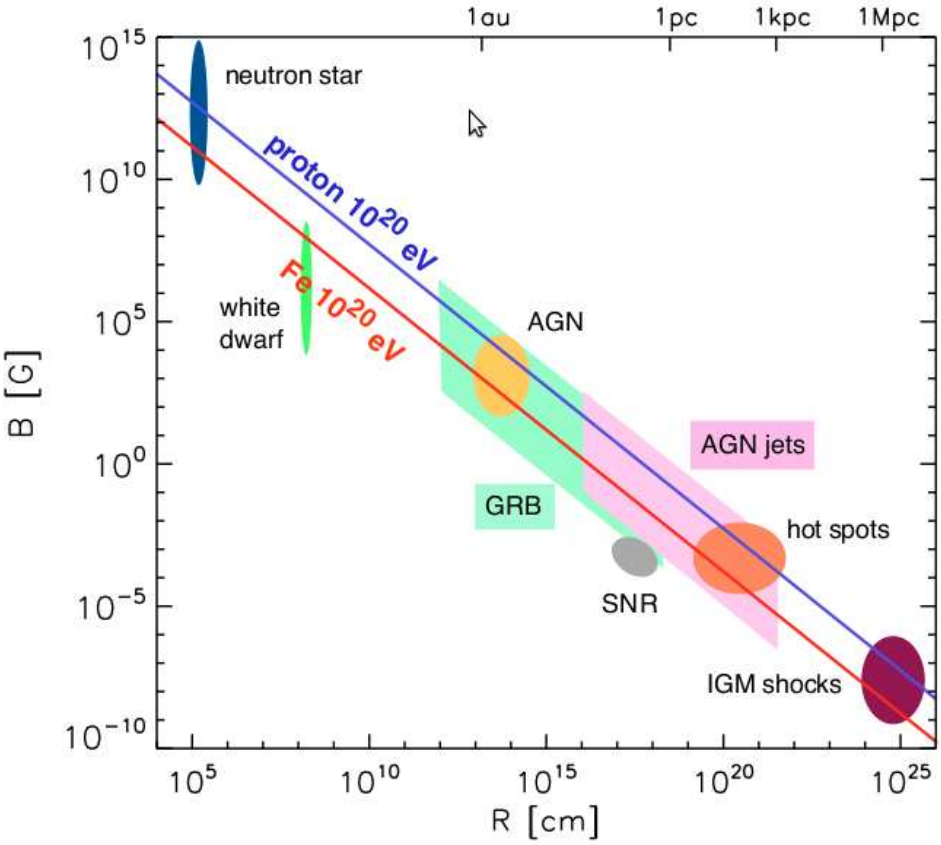

Figure 1.6: Hillas diagram, depicting the magnetic field (B) and source extension (R) phase space. The expected regions of the phase space for several astrophysical objects are shown: active galactic nuclei (AGN), active galactic nuclei jets (AGN jets), hot spots, supernova remnants (SNR), gamma ray bursts (GRBs), neutron stars, white dwarfs and intergalactic matter shocks (IGM shocks). Lines indicate the regions above which an object can contain protons (blue line) or iron nuclei (red line) with an energy of 10^{20} eV. Taken from [9].

candidate sources due to their very large magnetic fields and the possibility of acceleration due to unipolar induction. So far, these candidates are the best ones for explaining the origin of cosmic rays [32].

1.1.4 Detection techniques

Below 10^{15} eV, primary cosmic rays can be detected directly through ballon-borne or space-based experiments flown at high-altitude to intercept the primary cosmic rays before they interact in the atmosphere. However, the flux decreases dramatically with energy and it is not feasible to fly a volume large enough so that a sizeable number of primary cosmic rays can be detected. If we want to study cosmic rays above $\sim$ 1 PeV we have to resort, then, to measure the secondary particles that are created in an air shower when the primary cosmic ray interacts with the atmosphere. Since the atmosphere is a large volume with $\sim$ 1000 g/cm^2 of vertical depth and there are lots of surface on the ground, this can compensate for the low cosmic ray fluxes at ultra-high energies.

The generic method for detection of air showers is the *air shower array* or *surface detector array*. It consists in spreading particle detectors in an array on the ground. The detectors are usually plastic scintillators and water Cherenkov detectors. The spacing between the components of the array depends on the properties of the shower to be detected. The larger the energies and zenithal angles, the more separation, since the shower generates a larger footprint on the ground. Above 10^{19} eV the separation can be larger than 1 km, as in the Pierre Auger Observatory [11].

Most of the particles of the shower that arrive at the ground are muons, electrons/positrons and photons. Plastic scintillators are a few cm thick and are equally sensitive to muons and electrons. However, water Cherenkov tanks typically absorb the electrons while they are completely traversed by muons. The particles emit Cherenkov light inside the tank that is converted into an electrical current by photomultipliers.

Shower arrays have the problem that since they measure the shower at a single stage of its development, there is some uncertainty on the energy of the primary initiating the shower mainly due to shower-to-shower fluctuations. It was found using MC calculations and empirical models for air showers that the signal from the showers of a certain energy at an optimum distance from the shower core presents a minimal deviation from shower to shower [33]. This approach is the one that is being used right now in experiments such as the Telescope Array and the Pierre Auger Observatory, and has been used in past experiments such as AGASA.

Ultimately, the problem of the detection with ground arrays is that shower fluctuations

are very large. Also, showers need to be modelled with Monte Carlo which are subject to large uncertainties that stem mainly from the lack of data on the hadronic interactions at UHECR energies, which is vital to understand the interaction of the primary cosmic ray with the matter in the atmosphere.

Another technique for UHECR detection is the *fluorescence* method. When a charged particle travels through the atmosphere, it excites the 1N and 2P band of the nitrogen. After the excitation, fluorescence photons in the 300-450 nm range are emitted isotropically. Since the emission from a region in the sky is proportional to the number of charged particles in that region, using photomultipliers to detect the fluorescence light radiated by the air shower, we can trace the longitudinal development of the shower, or, equivalently, the number of charged particles as a function of the atmospheric depth.

With the number of photons that arrive at the multipliers and knowing the fluorescence yield, a quantity that links the number of photons received with the energy deposit of the shower (that can be measured in accelerators [34, 35]), we can estimate the number of charged particles at a given stage of shower development. The calorimetric energy of a shower [36] is estimated by fitting a Gaisser-Hillas function to the reconstructed energy deposit profile and integrating it. The total energy of the shower is obtained by correcting for the "invisible energy" carried away by neutrinos and high energy muons, obtained from Monte Carlo shower simulations.

The disadvantages of the fluorescence technique are its low duty cycle, since it must be used only in moonless nights in order to minimise the optical noise, and the Cherenkov radiation of the shower, that constitutes an important background. Besides, the atmospheric properties have to be monitored accurately because the fluorescence yield varies as a function of temperature, pressure and humidity.

A clear advantage of the fluorescence technique is the capability of measuring directly the shower profile, and therefore measuring the depth of shower maximum $X_{\max}$, which is the most important estimator for the composition of the primary particle.

The present thesis deals mainly with the radio technique, consisting in detecting with antennas the electric field emitted by the particles of a cosmic ray shower, either in dense media (ice, salt...) or in the atmosphere. The basics of this technique are covered in Chapter 2.

1.2 Ultra-high energy neutrinos (UHEνs)

Neutrinos are very light particles, several orders of magnitude lighter than the rest of the fermions. They are electrically neutral so they do not interact electromagnetically. They do not feel strong interactions, either. Neutrinos interact via the weak interaction only. Their interaction cross sections are very low, typically $\sim 10^{-7}$ times smaller than the proton cross sections at EeV, which makes them *elusive* particles.

These properties are precisely what makes them good cosmic messengers if we can detect them, because they can travel through the universe without interacting or being deflected by magnetic fields. They can reach Earth from the edge of the Universe practically without attenuation.

In the following we will review the production mechanism for UHEνs, their potential sources, give a brief introduction to the detection techniques and discuss the events detected by the IceCube experiment.

1.2.1 Production

At low energies $\sim 10^{-4}$ eV, a cosmogenic neutrino flux akin to the cosmic microwave background is expected, but detection is currently unfeasible. At $\sim$ MeV energies, the neutrinos measured on Earth come from the fusion reactions in the Sun, supernovae, natural radiactivity and nuclear reactors. At $\sim$ GeV energies and above, we find the flux of the so-called *atmospheric neutrinos*, produced in air showers induced by cosmic rays. These are routinely measured in current neutrino detectors [37]. At tens of TeV up to PeV neutrinos produced at astrophysical sources have recently been found (see Section 1.2.3) although their sources have not been identified.

In this work we are interested in neutrinos of astrophysical and cosmogenic origin with energies in the EeV range and above. We know that very high and ultra-high energy neutrinos must exist because of the detection of cosmic rays at these energies. The astrophysical production of neutrinos can take place via the decay of charged pions in the *beam dump* of protons in dense matter, in/at/around the potential sources of UHECRs, or through photopion production in a similar way to the GZK effect (see Section 1.1.2):

$$\begin{aligned} p + \gamma \;\; &\rightarrow \;\; \pi^+ + n \\ &\quad\;\; \pi^+ \rightarrow \mu^+ + \nu_\mu \\ &\quad\;\; \mu^+ \rightarrow e^+ + \nu_e + \bar{\nu}_\mu \end{aligned} \tag{1.9}$$

where the target photons can be ambient photons at the source or those of the CMB or UV, optical and IR backgrounds. On average the energy of each neutrino is

$$\langle E_\nu \rangle = \frac{1}{4} E_{\pi^+} = \frac{1}{4} \times \frac{1}{5} E_p = \frac{1}{20} E_p, \tag{1.10}$$

where E_p is the energy of the incident proton, and the total energy in the neutrino channel is three times the energy of a single neutrino,

$$\langle E_{\nu,\text{total}} \rangle \approx \frac{3}{4} \times \frac{1}{5} E_p = \frac{3}{20} E_p = 0.15 E_p. \tag{1.11}$$

Photopion production can also occur if the photon interacts with a nucleus, although the process is much more complex this way and not as efficient. The energy threshold for a proton is

$$E_{\text{threshold}} \simeq \frac{6.8 \cdot 10^{16}\ \text{eV}^2}{E_\gamma/\text{eV}}, \tag{1.12}$$

but the threshold for a nucleus of mass number A is approximately $AE_{\text{threshold}}$. Therefore, if cosmic rays are predominantly heavy nuclei, the neutrino flux will be drastically reduced. Also, photodisintegration of nuclei leads to small fluxes since proton fragments have to be produced first in order to increase the efficiency, and then reinteract with the CMB to produce neutrinos, a second order process leading to small neutrino intensities [38].

The reaction in Eq. (1.9) can also occur for lower proton (or nucleus) energy provided the photon has a larger energy. Depending on the energy of the cosmic ray, neutrinos can be produced in collisions with infrared, optical, ultraviolet or gamma photons.

If we restrict the production of neutrinos to protons interacting with the CMB or UV/Opt/IR backgrounds, a typical predicted neutrino flux is shown in Fig. 1.7 where the different processes contributing are indicated. These are neutrinos produced by the GZK process, also called *cosmogenic neutrinos*. The right peak of the total flux in Fig. 1.7, in the EeV range, is produced by the decay of the charged pions when a UHECR proton interacts with a CMB photon. An average neutrino carries an energy $\langle E_\nu \rangle \sim E_p/20$, and therefore this peak is sensitive (among other things) to the maximum energy of the UHECRs. The position and height of the peak depends also on the composition and the source evolution (see Fig. 1.8). The left peak of the total flux is produced by the decay of the charged pions when a proton interacts with the UV/IR background, and lies at ~ 10 PeV. The flux marked with a dashed line represents the flux due to the disintegration of the neutrons in Eq. (1.9). A neutrino coming from neutron decay has an average energy $\langle E_\nu \rangle \sim 3\ 10^{-4} E_p$, hence the displacement of the neutron decay curve. The curve has the

same two-peak structure as the total flux, with the right peak, at PeV energies, produced by the interactions with the CMB and the left one, at sub-PeV energies, produced by the interactions with the UV/IR background.

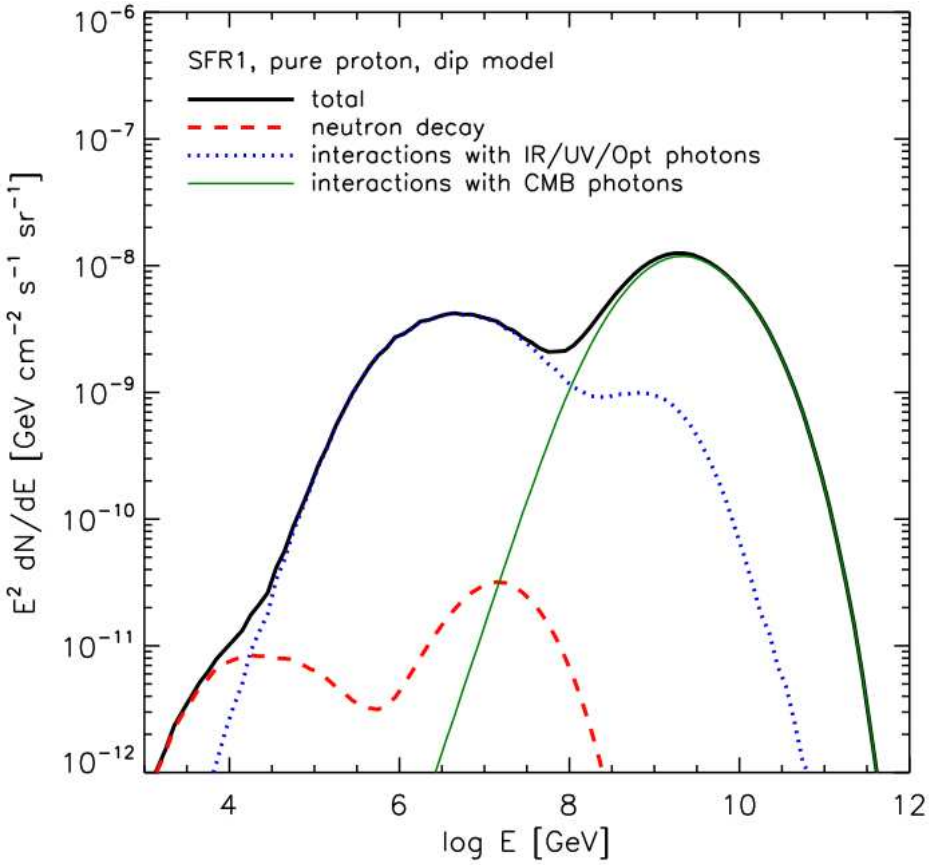

Figure 1.7: Contribution of the different processes to the neutrino flux, considering all flavours. The case of a pure proton composition, assuming a star formation rate type evolution for the source emissivity and a dip transition model is presented. The black solid line indicates the total flux. The green solid line represents the neutrino emission due to the interaction of cosmic rays with CMB photons and the blue dotted line with UV, optical and IR photons. The red dashed line is the contribution of the neutron decay. Taken from [38].

Cosmogenic neutrinos can give us very valuable information on the nature of the sources of UHECRs, since neutrino abundance is largely dependent on their evolution with redshift. Their abundance is an indicator of the composition of the cosmic rays, for we expect larger fluxes if the primaries are protons, and lower fluxes were the primaries heavier nuclei.

These dependences on the source evolution and UHECR composition are illustrated in Fig. (1.8).

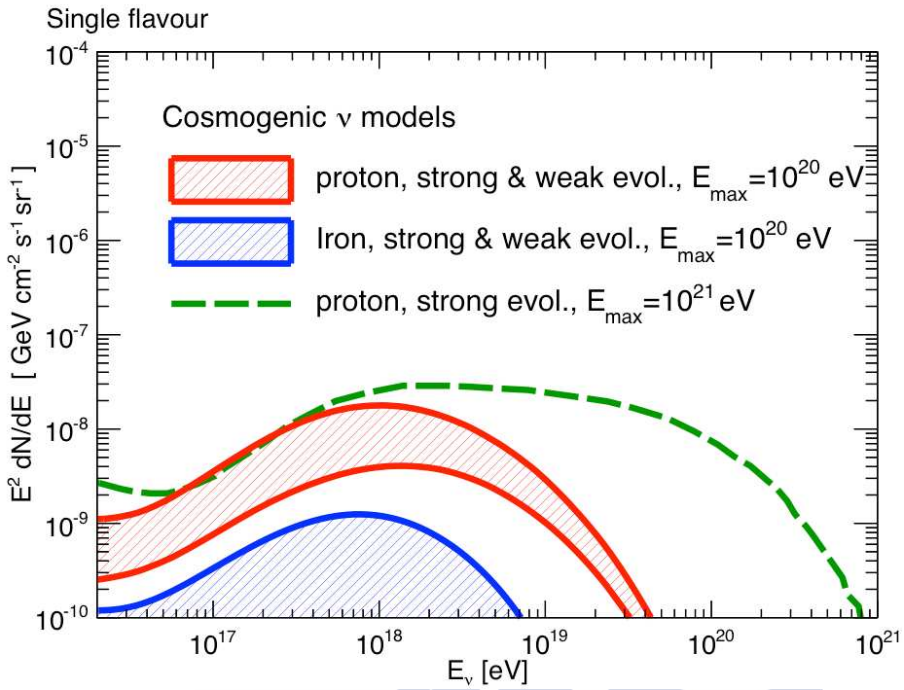

Figure 1.8: Expected cosmogenic neutrino flux for several models. The dashed green line represents a pure proton composition at the source with a maximum energy of 10^{21} eV. The red (blue) line indicates a pure proton (iron) composition with a maximum energy of 10^{20} eV. The upper curve is calculated for a strong dependence on source evolution and the lower one for a weak dependence on source evolution.

UHE neutrinos can also be produced in interactions of UHECRs with matter and radiation in/at/around the potential sources of UHECRs. Charged pions are produced in the interactions of UHECR decaying into neutrinos. In this regard, one would expect that the sources the neutrinos could point at are the same sources that accelerate cosmic rays.

As for the origin of UHECRs, the principal candidates for the UHE neutrino sources are those explained in Section 1.1.3 and shown in Fig. 1.6, like AGN, GRBs or even neutron stars. The detection of neutrinos from an expected CR source would be a sign (a *smoking gun*) that hadrons are being accelerated in the source.

In the case of GRBs, for instance [39], it would provide evidence that the GRBs have a hadronic component, as the leptonic *vs* hadronic mechanism has been a long-standing

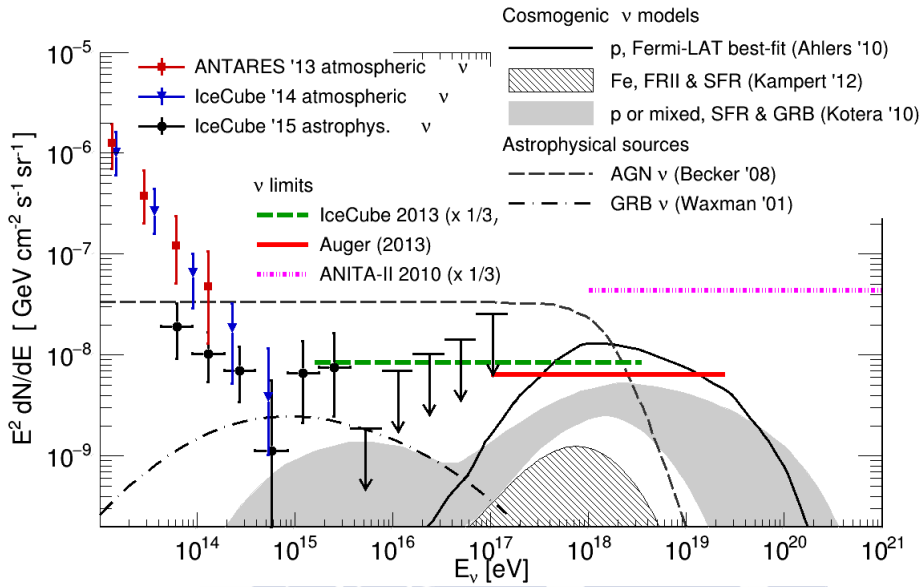

Figure 1.9: Expected diffuse neutrino fluxes from different diffuse astrophysical/cosmic models. The coloured points represent the measurements of atmospheric muon neutrinos and antineutrinos by ANTARES and IceCube. The black points represent the astrophysical flux measured by the IceCube experiment. We also show upper limits to the diffuse neutrino flux from the IceCube, Auger and ANITA experiments, assuming an energy spectrum $\propto E^{-2}$. Some models of neutrino production in the plot are already excluded at more than 90% CL by these limits.

debate. GRBs are transient sources and if they happen to be a source of cosmic rays there is the possibility that we cannot correlate the arrival directions of cosmic rays with GRBs if the cosmic rays arrive much later than the gamma rays. However, neutrinos can arrive slightly later than the gamma rays, as it occurred with the supernova 1987A. The arrival of ultra-high energy neutrinos in coincidence with a GRB would constitute unambiguous proof of the acceleration of hadrons within the burst.

In Fig. 1.9 we show different predictions for neutrino fluxes from astrophysical sources as well as the measured atmospheric neutrino flux and the astrophysical flux measured by the IceCube experiment (see Section 1.2.3).

1.2.2 Detection techniques

The most popular method for the detection of neutrinos consists in using a matrix of light detectors embedded in a transparent medium. In current experiments, the medium is either ice or water at great depths. The medium provides a large volume for the neutrinos to interact and shielding against secondary particles produced by cosmic rays. The medium has to be transparent so that the Cherenkov photons produced by the neutrino interaction can propagate with little attenuation. Ice and water are transparent at optical frequencies.

A high energy neutrino can interact with a nucleus N of the medium either via charged current (CC) or neutral current (NC) weak interactions. Although only electronic neutrinos (ν_e) and muon neutrinos (ν_μ) and their antineutrinos are produced in a first approximation in interactions of UHECRs and matter or radiation, neutrino oscillations over the cosmological distances at which the potential sources are located render a flux with approximately equal numbers of ν_e, ν_μ and ν_τ (tau neutrinos) [40]. Letting $l = e, \mu, \tau$ denote the three flavours, we can write the CC reaction as

$$\nu_l + N \rightarrow l + X, \tag{1.13}$$

and the NC reaction as

$$\nu_l + N \rightarrow \nu_l + X. \tag{1.14}$$

Depending on the reaction (CC or NC) and on the type of incoming neutrino (or antineutrino, since they are not distinguishable), several event clases are available. Let us consider the CC case (Eq. (1.13)).

- If the incident neutrino is an electron neutrino ν_e, an electron is created. This electron produces an electromagnetic shower after a few tens of cm, and almost at the same

time the fragmentation of the nucleus in the deep inelastic scattering reaction creates a hadronic shower.

- If the incident neutrino is a muon neutrino ν_μ, a muon exits the reaction and produces a long track, while near the interaction vertex a hadronic shower is created.
- If the incident neutrino is a ν_τ, the τ lepton travels some distance before decaying and producing a shower. Near the vertex the hadronic shower produced by the nucleon is present, then we find the τ track, and on its end there is the second hadronic shower produced by its decay. The signature of this event is a *double bang*.

In the NC case (Eq. (1.14)), a hadronic cascade is created, while the neutrino continues its travel through the medium. Flavours are not distinguishable. A summary of the possible reactions is shown in Fig. 1.10.

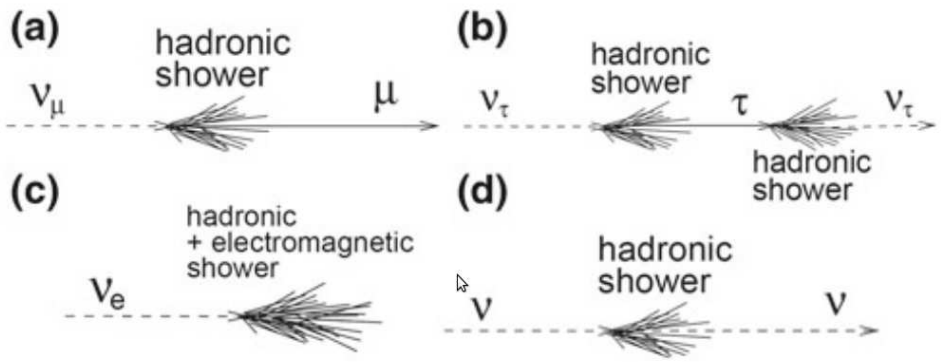

Figure 1.10: Event signatures for different neutrino flavours and interactions. a) CC interaction of a ν_μ producing a hadronic shower and a long μ track. b) CC interaction of a τ produces two hadronic showers and a τ track (double bang). c) CC interaction of ν_e produces an electromagnetic and a hadronic shower. d) NC interaction for all flavours produces a hadronic shower. Taken from [41].

Current experiments for the detection of neutrinos are the experiment in Lake Baikal, the AMANDA experiment at the South Pole, the ANTARES detector in the Mediterranean Sea and the IceCube experiment in the South Pole. ANTARES is the largest neutrino detector in the Northern hemisphere, while IceCube is the only detector that has a km^3 scale. KM3NeT is a projected experiment hosting a neutrino telescope with a volume of several cubic kilometers scheduled to be built in the Mediterranean Sea [41].

We have seen that neutrinos produce particle showers when interacting in dense media. The showers can produce electric field at radio frequencies in the MHz to GHz frequency range that can be detected if the medium is transparent. At radio frequencies, ice is transparent, so detection of neutrinos with a radio array in Antarctica could be possible. This is the philosophy behind experiments such as the Askaryan Radio Array (ARA) [42], ARIANNA [43] and ANITA [44]. Radio detection of UHE showers in dense media will be further discussed in Chapter 2.

Detection in the atmosphere is also possible, in principle. While protons, heavier nuclei and even photons interact shortly after entering the atmosphere, neutrinos can initiate showers quite deep in the atmosphere. Showers induced by neutrinos close to a ground detector have a considerable amount of electromagnetic component at the ground, that can be detectable with a surface array or a radio array.

1.2.3 Brief summary of experimental data

Auger [45] has attempted the detection of Earth-skimming showers induced by tau neutrinos that travel in a slightly upward direction and showers initiated by any neutrino flavour moving down at large angles with respect to the vertical and interact close to the detector. No neutrinos were found, and an upper band to the diffuse neutrino flux with 90% confidence level was calculated, $k_{90} < 6.4\ 10^{-9}$ GeV cm^{-2} s^{-1} sr^{-1}, shown in Fig. 1.9.

IceCube is a detector that monitors a cubic kilometer of highly transparent Antarctic ice using 5,160 Digital Optical Modules deployed on 86 strings at a depth of 1.5-2.5 km below the surface. In the core of the detector lies a sub-array of high quantum efficiency PMTs called DeepCore. To study the downgoing neutrinos, IceCube also possesses a surface cosmic ray detector, the IceTop, to remove the atmospheric neutrino and muon background.

The most interesting finding of IceCube is that of an excess of high-energy astrophysical neutrinos over the atmospheric neutrino background at TeV-PeV energies [46]. Since at PeV energies the flux of neutrinos is appreciably reduced by the Earth, events were looked for in the downgoing sample in addition to the upgoing sample. For the course of 3 years, 37 events interacting within the instrumental volume and passing the cuts have been observed. 28 were shower-like and 9 had a muon track associated.

In Fig. 1.11 we show a histogram of the number of events as a function of energy together with the expectation for several backgrounds. The data deviate from the hypothesis that the signal is due only to the background by about 5.7σ. A fit to a E^{-2} spectrum is also shown in the figure, which is compatible with the data and with what is expected from

cosmic ray accelerators, although the data also suggests that the spectrum can be softer. There are 3 events with energy > 1 PeV in the 3-year IceCube data set - the highest energy neutrinos ever detected.

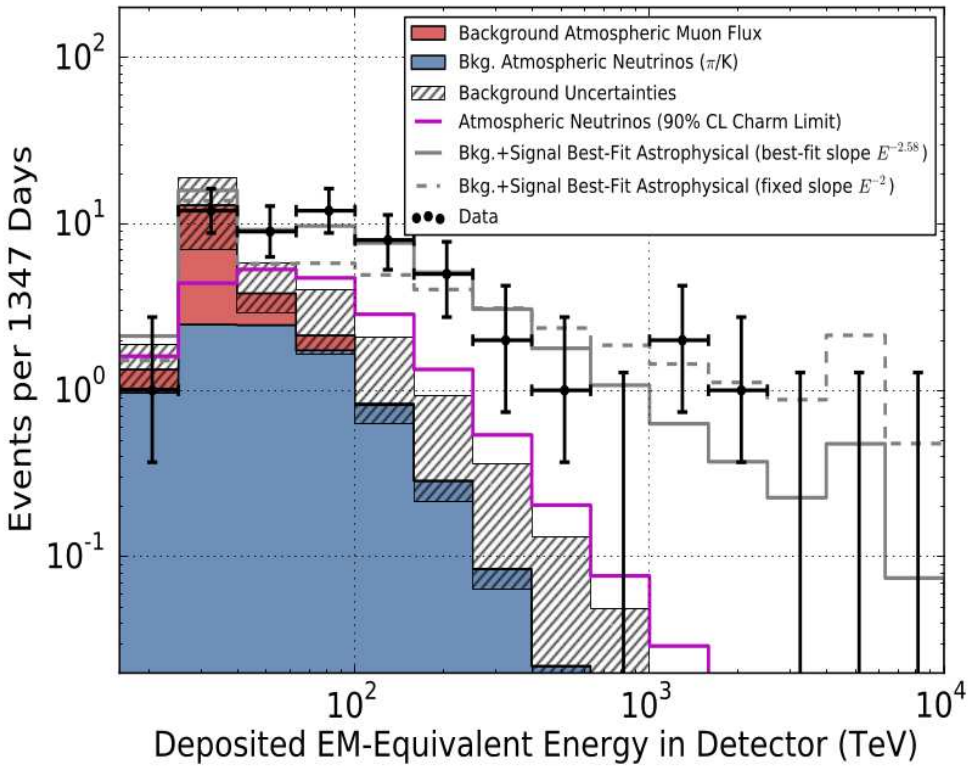

Figure 1.11: Distribution of the deposited energies E_{dep} of observed IceCube events (crosses) compared with predictions. Atmospheric muons and neutrino backgrounds are shown along with their sum, while the hashed regions signals their uncertainties. A E^{-2} fit to the IceCube data (sum of background and signal) is also shown. Taken from [47].

At the present moment, no hypothesis test has yielded a statistically significant evidence of clustering or correlations of these neutrinos, meaning that point sources, of existing, have not been identified. Searches for a diffuse flux of astrophysical neutrinos performed by other neutrino detectors such as BAIKAL and ANTARES have yielded negative results. The planned KM3NeT in the Mediterranean Sea is being built with the goal of answering the questions about the nature and origin of this astrophysical flux.

Bibliography

[1] V. F. Hess. Über Beobachtungen der durchdringenden Strahlung bei sieben Freiballonfahrten. *Physikalische Zeitschrift*, **XIII**:1084, 1912.

[2] T. H. Johnson. The azimuthal asymmetry of the cosmic radiation. *Physical Review*, **43**:834, 1933.

[3] L. Alvarez and A. H. Compton. A positively charged component of cosmic rays. *Physical Review*, **43**:835, 1933.

[4] M. Schein, W. P. Jesse, and E. O. Wollan. The nature of the primary cosmic radiation and the origin of the mesotron. *Physical Review*, **59**:615, 1941.

[5] P. Auger *et al.* Extensive cosmic-ray showers. *Reviews of Modern Physics*, **11**:288, 1939.

[6] C. D. Anderson. The positive electron. *Physical Review*, **43**:491, 1933.

[7] J. C. Street and E. C. Stevenson. New evidence for the existence of a particle of mass intermediate between the proton and electron. *Physical Review*, **52**:1003, 1937.

[8] A. M. Hillas. Cosmic rays: recent progress and some current questions, 2006. arXiv:astro-ph/0607109.

[9] K. Kotera and A. V. Olinto. The astrophysics of ultrahigh energy cosmic rays. *Annual Reviews of Astronomy and Astrophysics*, **49**:119, 2011.

[10] I. Valiño for The Pierre Auger Collaboration. The flux of ultra-high energy cosmic rays after ten years of operation of the Pierre Auger Observatory. In *Proceedings of the 34th International Cosmic Ray Conference (ICRC 2015)*, number 271. Available in arxiv:1509.03732 [astro-ph].

[11] The Pierre Auger Collaboration. The Pierre Auger Observatory. *Nuclear Instruments and Methods in Physics Research A*, **798**:172, 2015.

[12] J. Blümer, R. Engel, and J. R. Hörandel. Cosmic rays from the knee to the highest energies. *Progress in Particle and Nuclear Physics*, **63**:293, 2009.

[13] V. Berezinsky, A. Gazizov, and S. Grigorieva. On astrophysical solution to ultrahigh energy cosmic rays. *Physical Review D*, **74**(043005), 2006.

[14] K. Greisen. End to the cosmic ray spectrum? *Physical Review Letters*, **16**:748, 1966.

[15] G. T. Zatsepin and V. A. Kuzmin. Upper limit of the spectrum of cosmic rays. *Journal of Experimental and Theoretical Physics Letters*, **4**:78, 1966.

[16] A. Porcelli for The Pierre Auger Collaboration. Measurements of $X_{\max}$ above 10^{17} ev with the fluorescence detector of the Pierre Auger Observatory. In *Proceedings of the 34th International Cosmic Ray Conference (ICRC 2015)*, number 420. Available in arxiv:1509.03732 [astro-ph].

[17] T. Fujii for the Telescope Array Collaboration. Energy spectrum and mass composition of ultra-high energy cosmic rays measured with the Telescope Array fluorescence detector using a monocular analysis. In *Proceedings of the 34th International Cosmic Ray Conference (ICRC 2015)*, number 320.

[18] M. Unger for The Pierre Auger Collaboration and the Telescope Array Collaboration. Report of the Working Group on the composition of ultra-high energy cosmic rays. In *Proceedings of the 34th International Cosmic Ray Conference (ICRC 2015)*, number 307. Available in arxiv:1310.0647 [astro-ph].

[19] A. Aab *et al.* Correlation of the highest-energy cosmic rays with nearby extragalactic objects. *Science*, **318**:938, 2007.

[20] A. Aab *et al.* Searches for anisotropies in the arrival directions of the highest energy cosmic rays detected by the Pierre Auger Observatory. *The Astrophysical Journal*, **804**:15, 2015.

[21] The Pierre Auger Collaboration. Pierre Auger Observatory: Contributions to the 34th International Cosmic Ray Conference (ICRC 2015), 2015. arXiv:1509.03732 [astro-ph].

[22] R. U. Abbasi *et al.* Indications of intermediate-scale anisotropy of cosmic rays with energy greater than 57 EeV in the northern sky measured with the surface detector of the Telescope Array experiment. *The Astrophysical Journal*, **790**:L21, 2014.

[23] P. Tinyakov for the Telescope Array Collaboration. TA anisotropy summary. In *Proceedings of the 34th International Cosmic Ray Conference (ICRC 2015)*, number 326.

[24] E. Khan *et al.* Photodisintegration of ultra-high-energy cosmic rays revisited. *Astroparticle Physics*, **23**:191, 2005.

[25] D. Allard *et al.* Cosmogenic neutrinos from the propagation of ultrahigh energy nuclei. *Journal of Cosmology and Astroparticle Physics*, **9**:005, 2006.

[26] E. Armengaud, G. Sigl, T. Beau, and F. Minati. CRPropa: A numerical tool for the propagation of UHE cosmic rays, γ-rays and neutrinos. *Astroparticle Physics*, **28**:463, 2007.

[27] R. Aloisio, D. Boncioli, A. F. Grillo, S. Petrera, and F. Salamida. Simprop: a simulation code for ultra high energy ray propagation. *Journal of Cosmology and Astroparticle Physics*, **10**:007, 2012.

[28] E. Fermi. On the origin of the cosmic radiation. *Physical Review*, **75**:1169, 1949.

[29] A. R. Bell. Particle acceleration by astrophysical shocks. *Astrophysical Journal Letters*, **221**:L29, 1978.

[30] V. S. Berezinsky *et al. Astrophysics of cosmic rays.* North Holland, 1990.

[31] A. M. Hillas. The origin of ultra-high-energy cosmic rays. *Annual Review of Astronomy and Astrophysics*, **22**:425, 1984.

[32] P. Blasi. The origin of galactic cosmic rays. *Astronomy and Astrophysics Review*, **21**:70, 2013.

[33] D. Newton, J. Knapp, and A. A. Watson. The optimum distance at which to determine the size of a giant air shower. *Astroparticle Physics*, **26**:414, 2007.

[34] F. Arqueros, J. R. Hörandерl, and B. Keilhauer. Air fluorescence relevant for cosmic ray detection - Review of pioneering measurements. *Nuclear Instruments and Methods in Physics Research A*, **597**:23, 2008.

[35] J. Rosado, F. Blanco, and F. Arqueros. Comparison of available measurements of the absolute fluorescence yield. *Astroparticle Physics*, **34**:164, 2010.

[36] J. Abraham *et al.* The fluorescence detector of the Pierre Auger Observatory. *Nuclear Instruments and Methods in Physics A*, **620**:227, 2010.

[37] P. Desiati for the IceCube Collaboration. Recent observations of atmospheric neutrinos with the IceCube observatory. In *Proceedings of the 34th International Cosmic Ray Conference (ICRC 2015)*, number 028.

[38] K. Kotera, D. Allard, and A. Olinto. Cosmogenic neutrinos: parameter space and detectabilty from PeV to ZeV. *Journal of Cosmology and Astroparticle Physics*, **1010**:013, 2010.

[39] P. Mészáros. Gamma ray bursts as neutrino sources. To appear in "Neutrino Astronomy. Current status, future prospects". Eds. T. K. Gaisser and A. Karle (World Scientific Review Volume). arxiv:1511.01396v1 [astro-ph].

[40] H. Athar, M. Jezabek, and O. Yasuda. Effects of neutrino mixing on high-energy cosmic neutrino flux. *Physical Review D*, **62**(103007), 2000.

[41] M. Spurio. *Particles and Astrophysics. A Multi-Messenger Approach*. Springer International Publishing Switzerland, 2015, and references therein.

[42] T. Meures. *Development of a Sub-glacial Radio Telescope for the Detection of GZK neutrinos*. Springer Thesis, 2015.

[43] S. R. Klein for the ARIANNA collaboration. ARIANNA: A radio detector array for cosmic neutrinos on the Ross Ice Shelf, 2012. arXiv:1207.3846.

[44] P. W. Gorham *et al.* The Antarctic Impulsive Transient Antenna ultra-high energy neutrino detector: Design, performance, and sensitivity for the 2006–2007 balloon flight. *Astroparticle Physics*, **32**:10, 2009.

[45] A. Aab *et al.* Improved limit to the diffuse flux of ultrahigh energy neutrinos from the Pierre Auger Observatory. *Astroparticle Physics*, **91**(092008), 2015.

[46] M. G. Aartsen *et al.* Evidence for high-energy extraterrestrial neutrinos at the IceCube detector. *Science*, **342**(1242856-1), 2013.

[47] C. Pérez de los Heros. The quest for dark matter with neutrino telescopes, 2015. arXiv:1511.03500v1.

Chapter 2

Radio detection of UHECRs and UHEνs

A detailed understanding of the electric field emitted by the secondary particles created by primary UHE cosmic rays or neutrinos is key to the successful exploitation of the radio technique, and in particular to extract information on the properties of the primary particles. The low flux at ultra-high energies forces us to use huge detection volumes transparent at radio frequencies, such as ice or air. Moreover, as will be shown in this chapter, we expect coherence of the electric fields in the MHz-GHz frequency range, making the radio emission most efficient at those frequencies. For this reason we focus on understanding the spatial and spectral features of the electric field at those frequencies, both in dense media and air.

In this chapter we will review the properties of the radiation from particle showers at MHz-GHz frequencies and briefly describe several experiments that are currently operating or are planned for the future. First, we will cover the basics of radio emission from particle showers. Then, we will discuss radiation in dense media (ice) and after that radiation in air.

2.1 Basics of radio emission

2.1.1 The source of the radiation

We can think about the radio emission from a particle shower as an interplay between three key elements:

1. The existence of a net or unbalanced charge moving in the shower. This is a sufficient condition for the appearance of coherence at wavelengths smaller than the typical dimensions of the shower, although not necessary, since the geomagnetic effect can also create coherent electric fields (see Section 2.3.2). In a shower, many particles are travelling together at speed $v \sim c$, *i.e.*, near the speed of light. If the shower is

electrically neutral and positive and negative charges have similar trajectories, their fields will cancel out on average.

2. The movement of the charged particles. Radiation from the shower is produced when:
   - The charged particles are accelerated or decelerated in the medium.
   - The charged particles move faster than the speed of light in the medium, $v > c/n$, with n the refractive index. A shockwave is created, and Cherenkov radiation is emitted.
   - The net charge of the shower varies with time. This can be regarded as an acceleration/deceleration, since variation of the charge implies that charged particles are being dragged into the shower or created (acceleration) or stopped in the medium (deceleration).
3. The dimensions of the source and the observation wavelength. These determine if the emitted radiation is fully coherent, incoherent, or a mixture of both. If the wavelength of observation λ is much larger than the shower dimensions then the fields interfere coherently. The total field in this case is proportional to the excess number of charged particles N in the shower that contribute coherently, which is known to be proportional to the shower energy E_{shower}. As a consequence, the electric field power scales with $N^2 \propto E^2_{\text{shower}}$, favouring the detection of ultra-high energy particles.

In particle showers initiated by cosmic rays and neutrinos, electrons and positrons outnumber the other charged particles. Two effects dominate the emission from the shower. Due to the Askaryan effect (see Section 2.2.1), electrons from the medium are entrained into the shower flow by shower photons of a few MeV energy, and by shower electrons and positrons interacting with the atomic electrons of the medium. This creates a net charge imbalance in the shower particles, with more electrons than positrons, which is key to the emission of coherent radiation, especially in dense media (ice, for instance). In lighter media (air, for instance), the geomagnetic field deflects the charged particles very significantly. Particles with opposite charge are deflected into opposite directions, and contribute to a net current. These two mechanisms enhance the emission and the dominance of one or the other is dependent on the medium.

2.1.2 Modelling radio emission in particle showers

A shower is a collection of particles. Among those, charged ones radiate photons because of their movement and their interactions with the medium. If the photons have sufficiently

low energy and they are emitted in large numbers, as it is the case at radio wavelengths, we can use classical electrodynamics (Maxwell's equations) for computing the electric field of a particle shower. Two complementary approaches are available, namely, the *macroscopic* approach and the *microscopic* approach.

The *macroscopic* approach consists in modelling the shower as a macroscopic current (without the *graininess* of the particles) and then calculate its associated radiation electric field. Examples of this are the Macroscopic GeoMagnetic Radiation Model (MGMR) [1] and the EVA model [2]. The advantages of these models is that they provide analytical formulas and give physical insight about the dominant mechanisms involved in radio emission. Among the disadvantages, the macroscopic modelling of the current eliminates the effect of the graininess of the shower on the electric field simplifying the properties of the shower, and requires an *a priori* knowledge of the emission mechanisms.

Microscopic models make extensive use of Monte Carlo codes for simulating a shower and track the particles in it. The field of each particle track is calculated and added to obtain the total emission from the shower. No prior assumptions are made on the emission mechanisms — the field of a single track is derived from first principles. Codes like ZHS [3], ZHAireS [4, 5] and CoREAS [6] are examples of the microscopic approach. Current microscopic models are more accurate than macroscopic ones and are able to reproduce the features of the radio emission. Among the disadvantages of the microscopic models, we find that the calculation of the fields is done sacrificing the clarity of an analytical formula for the total field of the shower. Also, Monte Carlo calculations are usually more time-consuming than macroscopic approaches.

In the middle ground of both approaches we find models that try to mix the microscopic and macroscopic models. An example is SELFAS [7], a code that samples the shower from universal distributions and follows the sampled particles with a Monte Carlo code. The field for each particle is then calculated and added. Another example is the model in [8], where a macroscopic current is parametrised from simulations and its electric field is readily calculated, reaching a good agreement with the calculations from first principles.

Throughout this work we will focus on the *microscopic* approach. However, for the sake of gaining insight into radio emission, we will also discuss several simple models.

2.1.3 The "box model" for shower development

We will describe here the so-called *box model* for shower development that can explain many of the spectral features of the emitted radiation simply by relating them to the spatial dimensions of the shower.

The box model has been introduced in [3, 9] and discussed in detail in [10, 11]. In this simplified model, the particle cascade is characterised by three scales: the scale of longitudinal development L, the scale of lateral spread transverse to the shower axis R, and the thickness of the shower front D. These quantities are drawn in Fig. 2.1. We consider the observer in the far-field so that every point in the cascade radiates towards the observer forming an angle θ with respect to the shower axis, as shown in Fig. 2.1. Under this assumption, we can calculate the delays in the arrival times of the emission from each point of the shower simply by dividing the distance from the emitting point to the observer by the speed of light in the medium. We assume the shower to advance at a speed very close to the speed of light c, and since the speed of light in the medium c/n is smaller than c, relativistic effects will play a crucial role inducing purely relativistic "Cherenkov-like" phenomena as we will show below.

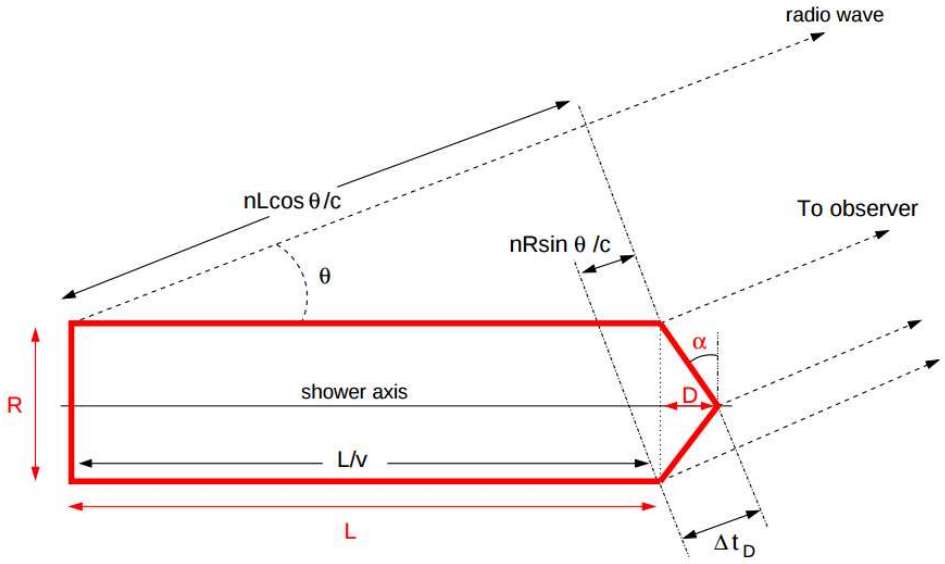

Figure 2.1: The "box model" of shower development over the lifetime of the shower. The shower dimensions are indicated in red colour. The travel time of the shower ($L/v \simeq L/c$) as well as the travel time of the signal from different emitting points are also indicated in black (see text for details).

If the wavelength of observation λ is much larger than the shower dimensions, all parts of the shower contribute with approximately the same phases to the total field and the emission is coherent. If λ is smaller than the shower dimensions, the fields contribute with different and varying phases and destructive interference sets in, which induces a cut-off

in the frequency (ω) spectrum. Depending on the shower and the observer position, the shower scale (L, R or D) responsible for the cut-off will be different.

Let us firstly assume the shower to be a one-dimensional line of current with constant net charge Q, spreading over a length L. For the moment we assume $R = 0$ and $D = 0$, neglecting the lateral shower spread and the shower front width. If the shower starts at $t = 0$, the arrival time of the radiation from the beginning of the shower to the observer in the far-field in Fig. 2.1 is

$$t_{\text{begin}} = \frac{nL}{c}\cos\theta, \tag{2.1}$$

while the arrival time for the radiation of the end of the shower is just given by the propagation time of the shower

$$t_{\text{end}} = \frac{L}{c}, \tag{2.2}$$

which gives us the delay between the radiation from the beginning and the end of the shower induced by the shower longitudinal scale:

$$\Delta t_L(L,\theta) = t_{\text{end}} - t_{\text{begin}} = \frac{L}{c}(1 - n\cos\theta). \tag{2.3}$$

We can infer some interesting relativistic effects from Eq. (2.3). If the angle $\cos\theta = (n\beta)^{-1}$, which is the definition of the Cherenkov angle θ_C, a far-field observer sees all the wavefronts emitted at different stages in the longitudinal development of the shower at the same time, *i.e.*, $\Delta t_L(L,\theta_C) = 0$. If $\theta < \theta_C$, $\Delta t_L < 0$ and the observer sees first the end of the shower and then the beginning, in an apparent violation of causality. On the contrary, if $\theta > \theta_C$ the observer sees first the beginning of the shower, and then its end. Since the observer sees the radiation in a finite interval of time $|\Delta t_L|$, this translates into a cutoff in the spectrum at $\omega_{\text{cut}}(L,\theta) \sim |\Delta t_L|^{-1}$.

We can refine the model introducing the lateral scale R of shower development. We assume that the shower can be modelled as a two-dimensional current extending longitudinally over L and laterally over R with cylindrical symmetry, still assuming a negligible width of the shower front $D = 0$. This scale induces a new delay, as seen in Fig. (2.1),

$$\Delta t_R(L,\theta) = \frac{nR}{c}\sin\theta, \tag{2.4}$$

which is the arrival time difference of the radiation that comes from each side of the shower. In this case, even for an observer at θ_C the wavefronts are no longer in phase. This in turn

induces a cut-off frequency in the spectrum $\omega_{\rm cut} \sim \Delta t_R^{-1}$. If $\theta \neq \theta_C$ the wavefronts are not in phase at the observer due to both the longitudinal and lateral shower dimensions, and the radiation typically lasts a time interval Δt given by the maximum of the time intervals induced by the lateral and longitudinal scales:

$$\Delta t \approx \max[\Delta t_L, \Delta t_R] = \max[nR\sin\theta/c, |L(1-n\cos\theta)/c|]. \tag{2.5}$$

This in turn induces a cut-off frequency at $\omega_{\rm cut} \sim \Delta t^{-1}$.

The only scale left is the width of the shower front D at a certain distance to the shower axis. Assuming a conical model for the front with an opening angle α with $\tan\alpha = 2D/R$ as shown in Fig. 2.1, the time delay between the "tip" and the "edge" of the conical front can be written as

$$\Delta t_D = \frac{n}{c}\sqrt{D^2 + \left(\frac{R}{2}\right)^2}\,\sin(\theta+\alpha), \tag{2.6}$$

and in this case the time duration of the pulse is given by the maximum of Δt_L, Δt_R and Δt_D. Eq. (2.6) is true for $\theta < \alpha$ or $\theta > \alpha$, but in the latter case the delay due to the lateral scale Δt_R in Eq. (2.4) dominates over Δt_D.

Let us now put numbers to the shower dimensions and time intervals in the case of a dielectric radio-transparent medium such as ice and air. The typical values of the shower dimensions in both media are given in Table 2.1 obtained from Monte Carlo simulations of shower development [3, 4, 5, 12], along with the values of the refractive index and the Cherenkov angle.

In ice, the Cherenkov angle is rather large $\theta_C \sim 56^\circ$ and for an observer placed at $\theta \sim \theta_C$ the value of $\Delta t_R \sim 1$ ns is larger than both Δt_D few ps and $\Delta t_L \sim 0$ at θ_C. It is then the lateral shower spread the one responsible for the onset of destructive interference inducing a cut-off frequency $\omega_{\rm cut} \sim 1$ GHz (see Fig. 2.4). Just a few degrees away from the Cherenkov angle, Δt_L is larger than Δt_R and Δt_D, and it is the spread along the shower axis the important scale determining the cut-off frequency in the spectrum that depends on the observation angle and is $\omega_{\rm cut} \sim$ tens or hundreds of MHz.

The picture changes significantly in air. Since the refractive index n is close to 1, at $\theta = \theta_C \sim 1^\circ$ the shower front is "head-on", *i.e.* perpendicular to the observer direction and Δt_R is small ~ 10 ns. It is then the width of the shower front that determines the coherence of the emission $\Delta t_D \sim 20$ ns, inducing a cut-off frequency $\omega_{\rm cut} \sim 50$ MHz where the spectrum starts to flatten (see Fig. 2.12). As in the case of ice, just a few degrees away from the Cherenkov direction, the longitudinal spread of the shower becomes responsible for the interference.

Medium	L	$R \sim 2r_{\text{Moliere}}$	D at $R/2$	n	θ_C	$\Delta t_L(\theta_C)$	$\Delta t_R(\theta_C)$	$\Delta t_D(\theta_C)$
Ice	$\sim$ 5 - 10 m	$\sim$ 0.2 m	0.015 m	1.78	$\sim 56°$	~ 0	$\sim$ 1 ns	$\sim$ 0.5 ns
Air	$\sim$ 5 - 10 km	$\sim$ 200 m	6 m	1.0003	$\sim 1°$	~ 0	$\sim$ 10 ns	$\sim$ 23 ns

Table 2.1: Typical values of the shower longitudinal and lateral dimensions (L and R) as well as width of the shower front D (see Fig. 2.1) in ice and air [5], along with the values of the refractive index n and the Cherenkov angle θ_C. Also given are the typical duration in time of the radiation emitted at θ_C induced by the different shower scales (see text for details). Observers in the Fraunhofer regime are assumed.

This picture is very much simplified, especially for showers in the atmosphere, due to several reasons. First, the observers are not in the far-field region in realistic situations. Second, in the atmosphere, the refractive index is not constant but varies altitude. Third, in extensive showers, a small region of the shower compared to the total longitudinal development L that contains an important fraction of the charged particles in the shower can contribute coherently up to GHz frequencies dominating the emission [12]. A more accurate discussion based on these ideas and the box model of the interplay between λ and shower scales for showers in the atmosphere can be found in [5].

2.1.4 Electric field in the microscopic approach. ZHS formula in frequency and time domains

The idea behind the microscopic approach is to model the charges and currents of the shower that are the input to Maxwell's equations as a collection of individual charged particle tracks using detailed Monte Carlo simulations of shower development. Knowing the electric field from a single particle track, the superposition principle of electromagnetism can be applied, adding up the fields from individual tracks to obtain the total electric field. This procedure automatically takes into account interference (coherence effects). This approach is the one implemented in the ZHS, ZHAireS and CoREAS Monte Carlo codes. For that purpose, the trajectory of the particles is divided in small straight steps assumed to be travelled at constant speed β. The direction and speed of the particle changes from one step to the next one to effectively model the actual movement of the particle.

Let us assume a current induced by a charged particle with the charge of the positron $e > 0$ that instantaneously accelerates at time t_1, moves at constant velocity $\mathbf{v}$ along a straight track and halts again instantaneously at time t_2, *i.e* a "boxcar" function of the

form

$$\mathbf{J}(\mathbf{x},t) = e\mathbf{v}\delta^{(3)}(\mathbf{x}-\mathbf{v}t)\Theta(t-t_1)\Theta(t_2-t), \tag{2.7}$$

with $\delta^{(3)}$ the three-dimensional Dirac distribution and Θ the step or Heaviside function. In [3] the radiation electric field of this current is calculated using the Coulomb gauge. In the Coulomb gauge and in the far-field of a radiation source, the radiation electric field can be calculated using only the current projected onto the direction transverse to the direction of observation, which we call the transverse current[1]. Making (1) the far-field approximation ($kr = k|\mathbf{x}' - \mathbf{x}| \gg 1$), where k is the wavenumber and r is the distance from the observer at position $\mathbf{x}$ to a point in the source located at $\mathbf{x}'$, (2) the Fraunhofer approximation in the phase of the electric field defined as $kr \approx k(R - vt\cos\theta)$ with $R = |\mathbf{x}|$, we arrive at the following expression for the electric field of a single track in the frequency domain:

$$\boxed{\mathbf{E}_{\text{ZHS}}(\mathbf{x},\omega) = \frac{e\mu_r i\omega}{4\pi\epsilon_0 c^2}\frac{e^{ikR}}{R}\mathbf{v}_\perp \frac{e^{i\mathbf{k}\cdot\mathbf{v}t_1}}{i(\omega - \mathbf{k}\cdot\mathbf{v})}\left[e^{i(\omega-\mathbf{k}\cdot\mathbf{v})t_2} - e^{i(\omega-\mathbf{k}\cdot\mathbf{v})t_1}\right]}, \tag{2.8}$$

where μ_r is the relative permeability of the medium, ϵ_0 is the permittivity of the vacuum and $\mathbf{v}_\perp$ is the projection of the velocity perpendicular to the direction of observation. This result is a factor 1/2 of that in [3] due to a different Fourier transform definition. In Chapter 3 we derive Eq. (2.8) in the Lorenz gauge.

The non-cancellation of the end of one step (left term inside the brackets) and the beginning of the next adjacent step (right term in its corresponding expression) leads to the appearance of a radiated electric field. This can happen because the velocity vector $\mathbf{v}$ changes direction and/or modulus (after an interaction or energy loss of the charged particle) or the distance to the observer changes. Eq. (2.8) has a finite limit at the Cherenkov angle, where the Cherenkov angle is $\theta_C = \cos^{-1}(1/n\beta)$ and therefore $\omega - kv\cos\theta = \omega(1 - n\beta\cos\theta) = 0$:

$$\mathbf{E}_{\text{ZHS}}(\theta_C,\omega) = \mathbf{E}_{\text{ZHS}}(\mathbf{x},\omega) = \frac{q\mu_r i\omega}{4\pi\epsilon_0 c^2}\frac{e^{ikR}}{R}e^{i\omega n\beta\cos\theta_C t_1}\mathbf{v}_\perp(t_2 - t_1) \tag{2.9}$$

This finite limit is crucial for the calculation of the electric field in a shower where the observer at the Cherenkov angle typically sees the largest field amplitude. Eq. (2.9) implies that the electric field is proportional to the projected tracklength of the particles $l_\perp = |\mathbf{v}_\perp|(t_2 - t_1)$. The finite limit at the Cherenkov angle gives, in the far-field and

[1]The actual transverse current of the Coulomb gauge is more complex, but it reduces to the projection onto the perpendicular to the line of observation at long distances from the source [13].

Fraunhofer regimes, the same result as an exact calculation of the field with no approximations whatsoever (see Chapter 3 and [14]). Also the ZHS formula in Eq. (2.8) reproduces Cherenkov radiation and is valid for most situations of interest concerning detectors searching for ultra-high energy particles in dense media and in air (see Chapter 3 and [14]).

The ZHS formula in Eq. (2.8) is valid only if $kR \gg 1$ or equivalently $\lambda \ll 2\pi nR$, *i.e.* for small wavelengths compared to the observation distance. In this frequency range (typically $\nu \gtrsim 10$ MHz for $R \gtrsim 10$ m), we can transform Eq. (2.8) back to the time domain. This yields the same result as if we had calculated the radiation field in the time domain using the Coulomb gauge and under the far-field and Fraunhofer approximations, as shown in [15]. The time domain version of the ZHS formula can be written as

$$\boxed{\mathbf{E}_{\mathrm{ZHS}}(\mathbf{x},t) = \frac{e\mu_r}{4\pi\epsilon_0 c^2 R}\mathbf{v}_\perp \frac{\delta(t-\frac{nR}{c}-(1-n\beta\cos\theta)t_1)-\delta(t-\frac{nR}{c}-(1-n\beta\cos\theta)t_2)}{1-n\beta\cos\theta}}, \tag{2.10}$$

which corresponds to the contributions due to two impulses, one when the particle accelerates and another one when the particle decelerates.

The time domain picture helps in understanding the radiation as a signal produced by accelerations and decelerations of the particles that takes a different amount of time to reach the observer depending on the track position and geometry. Eq. (2.10) has also a very important practical application. If we want to calculate the total electric field of a particle shower at several frequencies with Eq. (2.8), we have to apply it to every particle track, add the contributions, and repeat *for each* frequency. With Eq. (2.10), we can calculate the field in time domain for each particle track, add every contribution to get the total field and then numerically transform the total field to frequency instead of transforming the field of each track. This is computationally less expensive than calculating in the frequency domain, and it is accurate as long as we are transforming to a range in frequency in which the ZHS formula is valid, the time bin is small enough for the frequency in consideration and the numerical Fourier transform is set to the desired precision.

2.2 Radio detection in dense media

Dense media ($\rho \sim 1$ g/cm^2) are appropriate for conducting a radio experiment that intends to detect neutrinos. Neutrinos could interact inside large and dense natural volumes, and if the medium is transparent to radio waves the radiation field coming from the resulting showers can be detected from large distances allowing a cost-effective distribution of the

radio antennas. Huge natural transparent volumes are available in Nature, such as ice at the poles. The Moon can also be used for neutrino detection (see Section 2.2.3).

We will discuss the properties of the electric field from electromagnetic and hadronic showers in ice as an example of radiation in dense media, where the shower longitunidal dimension is ~ 10 m, the effect of the geomagnetic field on separating the e^- and the e^+ in the shower is negligible and the dominant emission mechanism is the Askaryan effect described below. We will also review some current and projected experiments operating in Antarctica.

2.2.1 The Askaryan effect

The interaction of neutrinos with a nucleus in dense media can produce an electromagnetic shower and/or a hadronic shower (see Section 1.2.2). The development of an electromagnetic shower of ultra-high energy is dominated by pair production,

$$\gamma + \gamma \rightarrow e^+ + e^-, \tag{2.11}$$

and bremsstrahlung,

$$e^{+/-} + N \rightarrow e^{+/-} + N + \gamma, \tag{2.12}$$

where N is a nucleus. Bremsstrahlung and pair production are electrically neutral processes, but the fact that the medium where the shower develops is made of matter induces an asymmetry in the charge distribution of the shower. As the shower particles propagate, they ionise matter and drag new electrons from the medium into the cascade. At $\sim$ MeV energies and above, we can think of the electrons in the medium as free electrons at rest, with the processes that cause the ionisation at these energies being the Compton effect,

$$\gamma + e^-_{\text{atomic}} \rightarrow \gamma + e^-, \tag{2.13}$$

where a shower photon frees an electron from an atom, the Bhabha process,

$$e^+ + e^-_{\text{atomic}} \rightarrow e^+ + e^-, \tag{2.14}$$

where the particle that drags the atomic electron into the shower is a positron, and finally, the Møller process,

$$e^- + e^-_{\text{atomic}} \rightarrow e^- + e^-, \tag{2.15}$$

which is basically an electron-electron scattering. Positron annihilation also plays a role removing positive charge from the shower:

$$e^+ + e^-_{\text{atomic}} \rightarrow \gamma + \gamma \tag{2.16}$$

This "entrainment" of electrons of the medium as the shower evolves is the so-called *Askaryan effect* [16]. This effect appears in any medium with bound electrons, and since the cross sections of the above processes are largest at energies of tens of MeV for the incident particle, the electrons, positrons and photons in the shower around those energies are responsible for the bulk of the effect. Since hadronic showers have an important electromagnetic component, they will present this effect as well. As a consequence of the Askaryan effect an excess charge develops in the shower. Although Askaryan's initial guess was that the excess charge was about 10% [16], this was because of the simplifications he made in his analytical calculation. A Monte Carlo calculation with the ZHS code [3] reveals that the excess charge Δq, defined as the difference of the electron and positron abundances divided by the sum of electrons and positrons is

$$\Delta q = \frac{N(e^-) - N(e^+)}{N(e^-) + N(e^+)} \sim 25\%, \tag{2.17}$$

and it exhibits a light dependence with the shower development and the primary energy. The Askaryan effect was experimentally confirmed in 2001 in a beam experiment at SLAC [17].

2.2.2 Properties of radio emission in ice

As stated before, in dense media the deflection of particles in the geomagnetic field is small due to the relatively large density of the medium, or equivalently, the relatively small shower dimensions. For instance, a 10 MeV electron travelling in ice along $L \sim 1$ m (~ 3 radiation lengths in ice) deviates laterally only ~ 0.5 mm due to the magnetic field of the Earth. As a consequence the Askaryan mechanism is responsible for the bulk of net charge and radio emission in the shower. The net negative charge varies in time as the shower penetrates in the medium in the same way as the number of particles in the shower. This variation is in fact what induces most of the radiation electric field, also called *Askaryan radiation* in this case [8].

We will focus on understanding the radio signal in ice, taking $n = 1.78$ as the refractive index, assumed constant. The Cherenkov angle in ice is, therefore, $\theta_C = \cos^{-1}(1/(n\beta)) \approx 56°$.

In Fig. 2.2 we show the electric field as a function of time calculated with the ZHS [3] Monte Carlo, a code that simulates the development of an electromagnetic shower in a dense medium and then calculates the resulting electric field with the eponymous ZHS formula, either in the frequency (Eq. (2.8)) or in the time (Eq. (2.10)) domain (see also Chapter 3). In Fig. 2.2 we see that the electric field for a 10^{15} eV electron-induced shower at the Cherenkov angle (left) is a very narrow bipolar pulse of nanosecond duration. In Fig. 2.2 (right) we also show the electric field of the same shower for observers at $\theta_c - 5°$ and $\theta_c + 5°$. The time duration of these pulses increases as the observer moves away from the Cherenkov angle θ_c, in agreement with the simple box model described in Section 2.1.3. The field is also linearly polarised in the direction of the transverse velocity as expected from Eqs. (2.8) and (2.10).

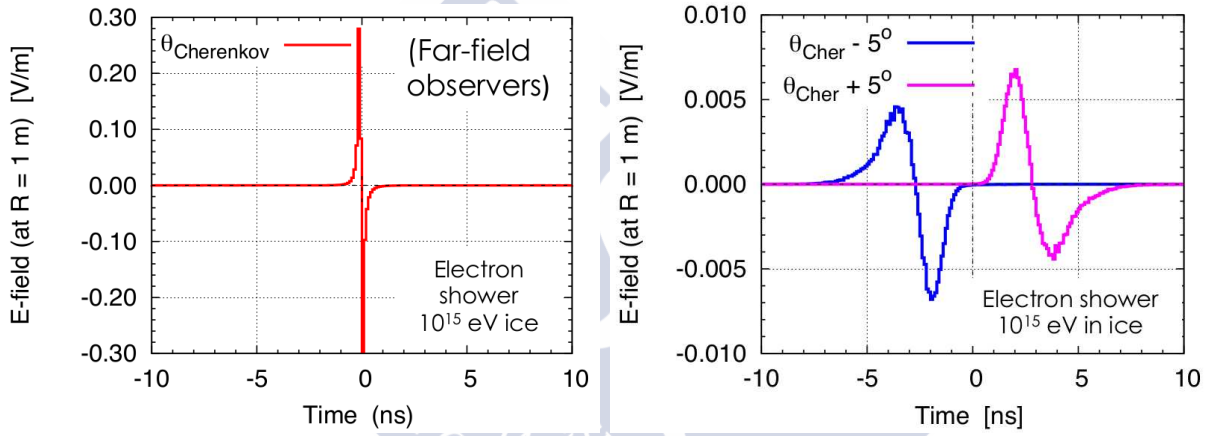

Figure 2.2: Magnitude of the electric field as a function of time as obtained in ZHS simulations of a single 1 PeV electron-induced shower in ice for different observation angles. Left panel: observation at the Cherenkov angle. Right panel: observation at $\theta_C - 5°$ (blue line) and at $\theta_C + 5°$ (pink line). Taken from [15, 18].

The relativistic effects predicted by the box model are also apparent in Fig. 2.2, namely the compression of the pulse near the Cherenkov angle and the reversal of the sign of the pulse inside ($\theta < \theta_C$) and outside ($\theta > \theta_C$) the Cherenkov cone.

In Fig. 2.3 we show the dependence of the electric field as a function of the observation angle for three frequencies. The angular pattern is analogous to the pattern of the Fraunhofer diffraction in optics, with a width inversely proportional to frequency $\Delta\theta \sim 1/\omega$. This coincidence arises because the total field of a shower can be cast into an integral that is very similar to the Fraunhofer diffraction integral [19]. The peak of the angular pattern

lies at the Cherenkov angle, where the emission was expected to be the largest due to the enhanced coherence already predicted by the box model.

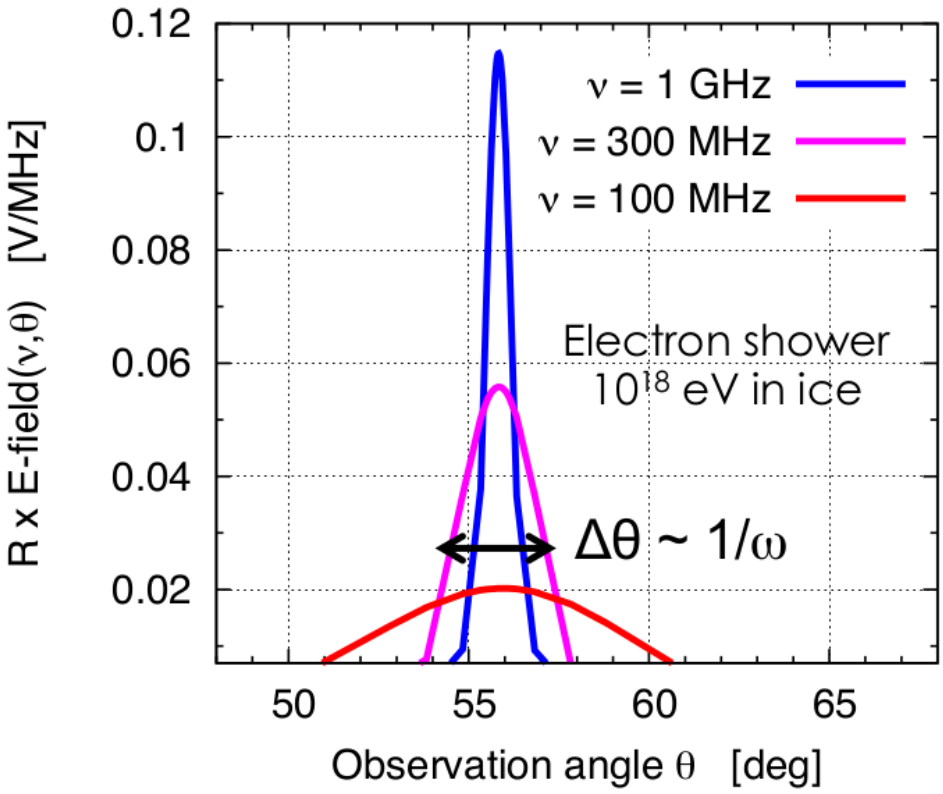

Figure 2.3: Magnitude of the electric field in frequency domain times the observation distance as a function of the observation angle. Frequencies are 1 GHz (blue), 300 MHz (pink) and 100 MHz (red). The electric field is created by a 10^{18} eV electron-induced shower in ice and has been calculated with the ZHS code. Taken from [18].

In Fig. 2.4 we show the frequency spectrum for a 10^{18} eV electron shower in ice for three angles: the Cherenkov angle θ_C, $\theta_C - 1°$ and $\theta_C - 5°$. The spectrum is broad-band, and widest at the Cherenkov angle. The field increases with frequency up to a cut-off that depends on the angle, being the cut-off largest at the Cherenkov angle and diminishing when the observer deviates from it. The magnitude of the cut-off is in qualitative agreement with what is predicted by the box model (see Table 2.1).

For ultra-high energy showers (EeV range) the Landau-Pomeranchuk-Migdal (LPM) effect is relevant [3]. The LPM effect is a suppression of the pair production and bremsstrahlung cross sections at large energies or high densities due to the fact that the incident particles

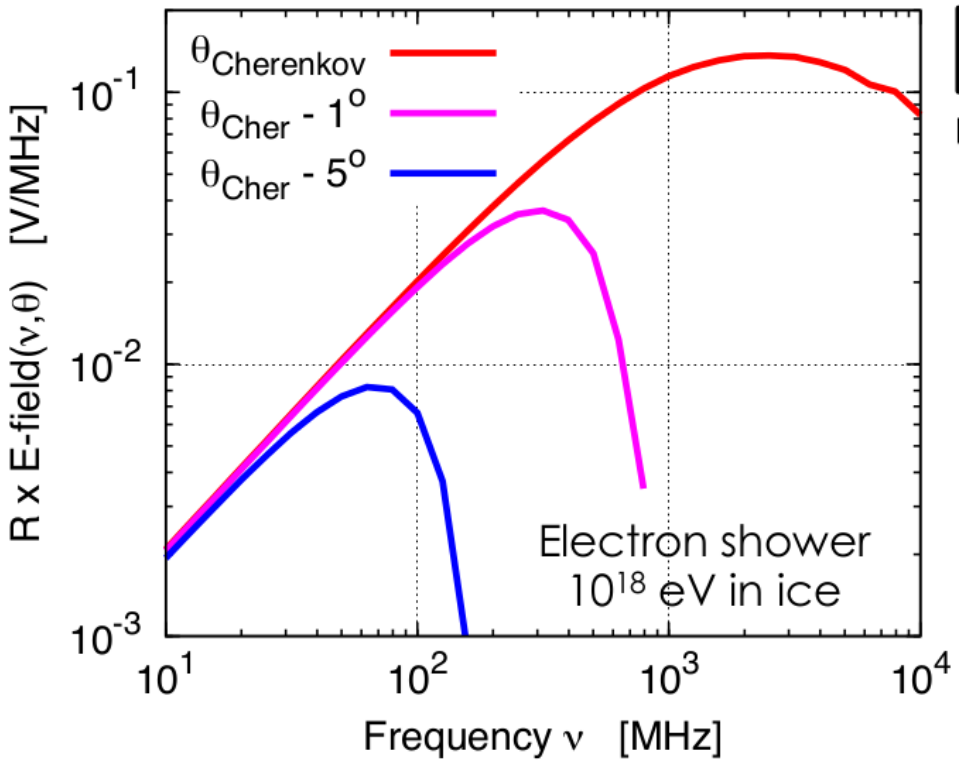

Figure 2.4: Magnitude of the electric field in frequency domain times the observation distance as a function of the frequency. Observation angles are the Cherenkov angle θ_C (red), $\theta_C - 1°$ (pink) and $\theta_C - 5°$ (blue). The electric field is created by a 10^{18} eV electron-induced shower in ice and has been calculated with the ZHS code. Taken from [18].

are influenced by the medium as a collection of particles rather than by the particles in the medium separately. This effect is included in the ZHS code.

The predictions of the ZHS code are limited to purely electromagnetic showers and electromagnetic interactions. However, neutrinos can induce hadronic showers. In order to simulate them, the well-known AIRES code [20] for the simulation of extensive air showers was modified to allow the simulation of showers in dense media through the use of a package called TIERRAS [21]. The implementation of the ZHS formula (Eqs. (2.8) and (2.10)) in this program marked the creation of ZHAireS [4], a code with the capabilities of simulating electromagnetic and hadronic showers in air and dense media and calculating the associated electric field. For electromagnetic showers below the pion photoproduction threshold, the results of ZHS are very similar to the results of ZHAireS [4].

The dominant radiation mechanism in hadronic showers is the same as in electron-induced ones, namely, emission of coherent Askaryan radiation from the excess of electrons over positrons. Although the hadronic component of a hadronic shower takes an important fraction of the energy of primary hadron, and the charged hadrons also emit radiation, the total tracklength of the charged hadrons is much smaller than the total tracklength of the electrons and positrons, and the electric field is proportional to the tracklength of charged particles [3], as can be seen in Eq. (2.9).

In Fig. 2.5 we show the frequency spectrum of the field emitted by hadronic and purely electromagnetic showers of the same primary energy. There are small differences in the spectra of both types of showers, namely the normalisation of the spectrum is smaller in hadronic showers than in electron-induced ones, and also the cut-off frequencies are typically larger in hadronic showers except at the Cherenkov angle. These differences stem mainly from the different fraction of shower energy going into the electron component in both showers and from their different spatial distributions. The emission is proportional to the energy of the electromagnetic part of the shower, and hadronic showers are known to have a smaller electromagnetic energy. As a consequence they emit less electric field, as shown in Fig. 2.5. Another important effect is the shift in the cut-off frequency at angles away from the Cherenkov angle, which is determined by the longitudinal development of the shower according to the box model. Electron-induced showers develop more slowly than hadronic ones and hence penetrate more in the medium. As a result, for a fixed energy, hadronic showers are shorter on average and we expect their cut-off frequencies for observation angles away from the Cherenkov angle (where the longitudinal development is important) to be larger than in electron-induced cascades.

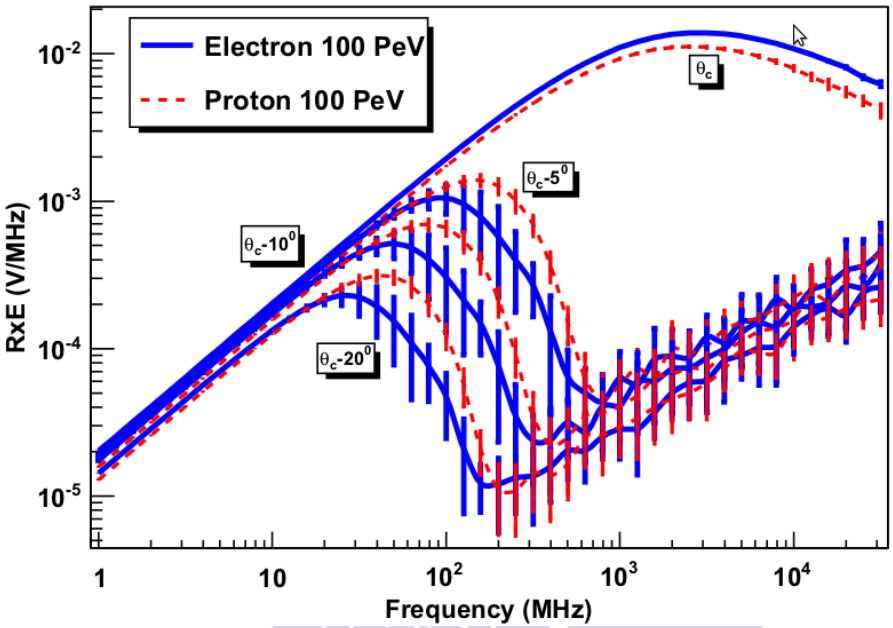

Figure 2.5: Average frequency spectrum of the Cherenkov radiation obtained in ZHAireS simulations of electron (solid blue line) and proton (dashed red line) showers with primary energy $E_0 = 100$ PeV. The spectrum is shown at four observation angles with respect to the shower axis. The RMS of 20 simulated showers is also shown. Taken from [4].

2.2.3 Experiments exploiting the radio technique in dense media

As mentioned before, a huge volume is required to detect neutrinos, ~ 100 km^3 of water or the equivalent volume in other material. Furthermore, the medium has to be radio-transparent. Ice is a good alternative, due to the fact that there is lots of it in Antarctica and Greenland and the one in Antarctica has an attenuation length at $\nu = 380$ MHz of ~ 1450 m [22].

There are three main radio experiments exploiting the radio technique at Antarctica: ANITA (Antarctic Neutrino Impulsive Terrestrial Antenna), ARIANNA (Antarctic Ross Ice shelf Antenna Neutrino Array) and ARA (Askaryan Radio Array).

ANITA [23] is a balloon with antennas that flies over Antarctica at an altitude of 37 km. The measuring band covers from 200 MHz to 1200 MHz. The goal is to to detect up-going neutrinos that interact in the ice by observing the electric field that crosses the ice and travels through the air towards the antenna payload. We show a sketch of the concept in Fig. 2.6 (left). ANITA has a relatively high energy threshold of $\sim 10^{18}$ eV. Three series of flights (ANITA I, ANITA II and ANITA III) have taken place. ANITA I and ANITA II have found no evidence of neutrinos, however, direct and reflected emission from cosmic rays was found in the data of ANITA I [24] (see Chapter 6). Using these data, a first measurement of the cosmic ray spectrum using only the radio technique was possible [25, 26]. The data from the third flight (ANITA III), designed to have a factor 5 of improvement in neutrino sensitivity compared to ANITA II and also to look for cosmic rays explicitely, is being analysed at the moment [27]. A related concept is the Exa Volt Antenna (EVA) project [28], a parabolic balloon that will also be used to search for UHE neutrinos and detect UHE cosmic rays.

ARIANNA is a ground-based array of antennas buried just below the surface of the Ross Ice Shelf. It has been designed to have a total area of 10^3 km^2 when completed, covered by 900 antennas pointing downwards measuring from 80 MHz to 1 GHz. We show a sketch of the concept in Fig. 2.6 (right). One of its promising features is a relatively low energy threshold of $\sim 10^{17}$ eV, since the neutrino showers are expected to develop in the ice, close to the detectors. It will monitor a large volume of ice for a long livetime of the order of several years.

ARA [29, 30] is a projected 37 stations array (~ 100 km^2 of surface) buried 200 m below the surface of the South Pole, next to the IceCube experiment. So far, only three stations have been deployed. Each station is designed to have 8 horizontally-polarised, 8 vertically polarised and 4 surface antennas collecting data in the 200-850 MHz and 30-300 MHz bands. It has the lowest thresholds of the Antarctica experiments, $\sim 10^{16}$ eV, and,

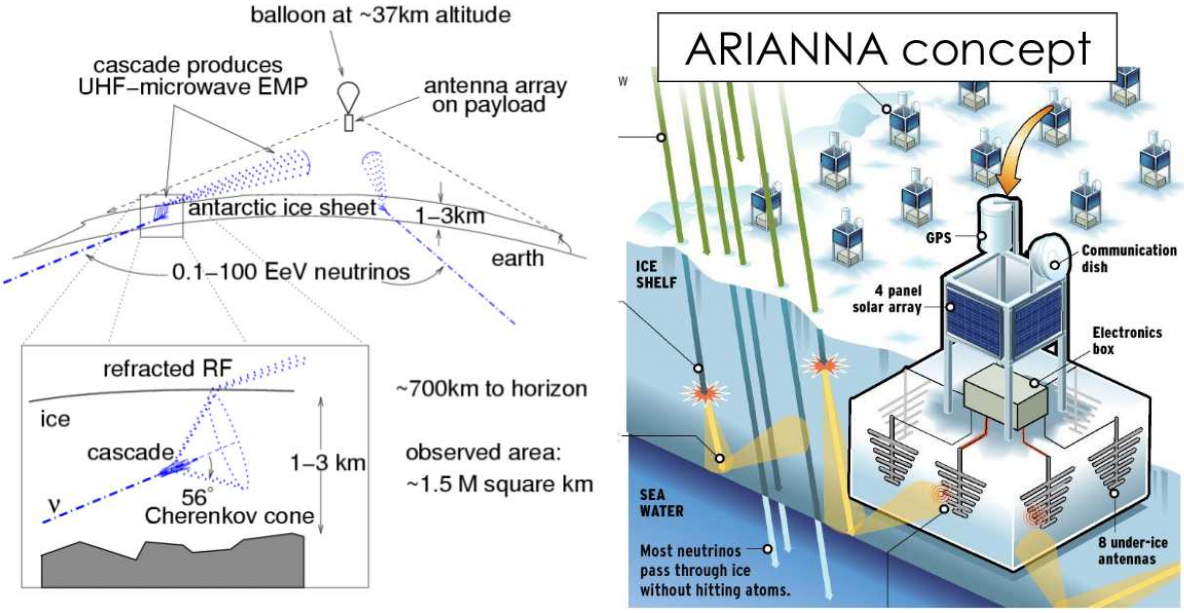

Figure 2.6: Left: Sketch of the ANITA experiment. Right: Sketch of the ARIANNA experiment. See text for details.

similarly to ARIANNA, covers a large volume and will offer a long livetime of several years.

The Greenland Neutrino Observatory (GNO) [31] is a new experiment still in prototype phase. Its conception is very similar to that of ARA, using horizontally and vertically polarised antennas buried in ice to detect neutrinos. The GNO collaboration have chosen Summit Station in Greenland to build their observatory.

An exotic and interesting concept is the use of the Moon as a target for neutrino interactions. The electric field created by the neutrino-induced showers near the surface of the Moon propagates towards Earth and could be detected above a certain threshold with existing radiotelescopes. This is the idea behind the LUNASKA experiment [32]. The advantage of this method would be the possibility of monitoring a huge surface - the Moon's surface. However, it presents a high energy threshold, since the showers develop in the Moon, roughly at 1 light-second from the detectors. Another complication is the limited time for observation using radiotelescopes that are usually carrying different research lines. LUNASKA found no neutrinos in its 2008 run. There are also plans to use the Square Kilometer Array (SKA) for this purpose [33].

As mentioned earlier, beam experiments were also carried out at SLAC. Their objective consisted on inducing an electromagnetic shower in a dense medium to detect the Askaryan

radiation and measure its properties using antennas. Bunches of bremsstrahlung photons of GeV energies were injected into a dense medium, with a total energy of $\sim 10^{17}$ - 10^{19} eV. Several media were tried: sand [17], ice [34] and salt [35]. The conclusions of these experiments were quite remarkable. The Askaryan radiation was seen, and the power of the radio wave increased quadratically with the shower energy (the sum of all the energies of the incident photons), as expected. The polarisation of the electric field was linear, also as expected. In the time domain, the shape of the pulses was bipolar and its duration was in the nano-second scale [36], agreeing with the ZHS simulations. The spectrum presented also a good agreement with the theoretical expectations of the ZHS Monte Carlo.

2.3 Radio detection in the atmosphere (air)

The electric field of cosmic-ray induced showers propagating in the atmosphere was detected in the MHz frequency range as early as the 1960s [37]. However, the radio technique in the atmosphere was soon abandoned because of the limitations in electronics at the time to deal with noise levels. Nowadays, nanosecond scale electronics is widely available, making the radio detection of particle showers in the atmosphere viable again.

Although dense media seem to be more appropriate for detecting neutrinos and in air measurements of extensive air showers initiated by cosmic rays (protons are nuclei) seem to be favoured, in principle it is possible to also detect neutrinos in the atmosphere. Their low interaction rate is compensated by the fact that neutrinos are the only primary particles that can develop showers close to the ground and thus leave a characteristic radio signal different from the cosmic ray induced signals.

The dominant mechanism of radio emission in the atmosphere in the MHz-GHz frequency range is the so-called geomagnetic mechanism. The Askaryan effect plays a subdominant role except for certain shower geometries. In the following we will discuss the geomagnetic mechanism of radio emission and its interplay with Askaryan radiation. After that, we will review current experiments using the atmosphere as detection medium.

2.3.1 Geomagnetic and Askaryan mechanisms in the atmosphere

In air the dominant mechanism for net charge production is the separation of electrons and positrons in the magnetic field of the Earth. This separation induces a drift electric current approximately perpendicular to the direction of the shower axis (which we call $\mathbf{V}$ and points towards the ground, see Fig. 2.7) and the magnetic field $\mathbf{B}$, that is, the current

is approximately parallel to $\mathbf{V} \times \mathbf{B}$. This corresponds to the direction of the Lorentz force experienced by a charged particle with instantaneous velocity along the shower axis.

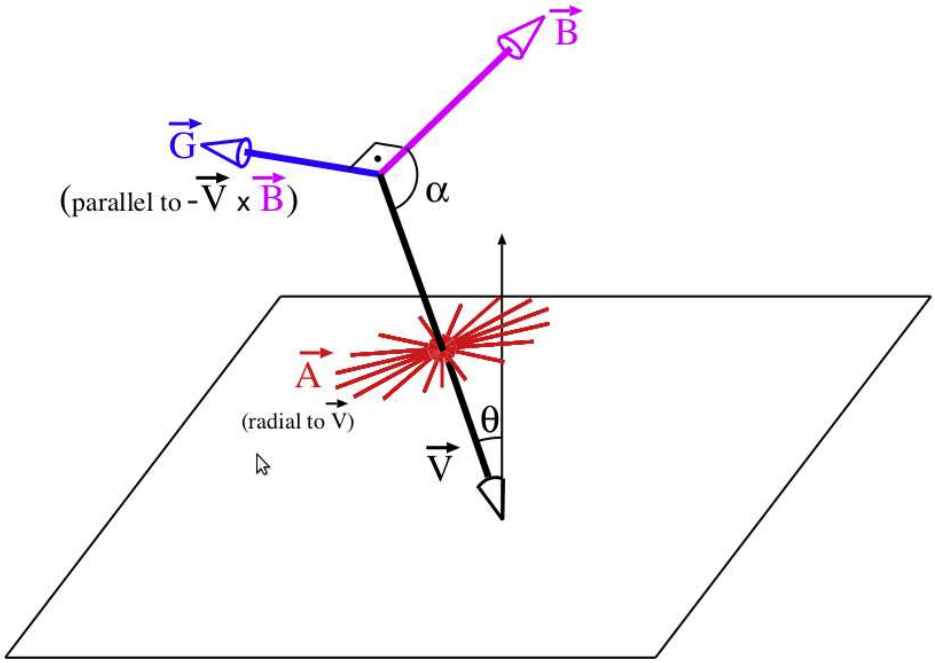

Figure 2.7: Scheme of the axis of a shower along with the polarisation of the emission due to the geomagnetic field **G** and Askaryan **A** mechanisms. **B** is the geomagnetic field pointing North and **V** marks the direction of the shower axis. The amplitudes of the geomagnetic and Askaryan fields drawn in the sketch are for illustrative purposes and not to scale. Taken from [38].

The drift current induced by the magnetic field $\mathbf{J}_{\text{geo}}$ travels with the shower front and varies in time as the number of particles producing the bulk of the radiation. The magnitude of the resulting electric field **G** is proportional to $|\mathbf{J}_{\text{geo}}|$ given by

$$|\mathbf{J}_{\text{geo}}| \propto |\mathbf{V} \times \mathbf{B}| = |\mathbf{V}||\mathbf{B}| \sin \alpha, \tag{2.18}$$

with α the angle between **V** and **B**, hence the electric field scales with $|\mathbf{B}| \sin \alpha$. In the shower plane, defined as the plane perpendicular to the shower axis, the approximate polarisation direction is a constant vector along the East-West line (assuming the magnetic field has no declination, that is, lies on the North-South plane), as shown in Fig. 2.8 (left).

The geomagnetic emission creates a bipolar pulse (as can be deduced after inspecting Eq. (2.10)). The polarisation of the field then changes direction with time. We choose the polarisation of the signal as the opposite of the direction of the field that arrives at the observer first. Let us assume the observer lies at $\theta > \theta_C$. The magnetic field causes the positrons to accelerate along the $\mathbf{V} \times \mathbf{B}$, direction, and therefore the product of their charge and their transverse velocity is the vector $e\mathbf{v}_{\perp,+}$ pointing in approximately the $\mathbf{V} \times \mathbf{B}$ direction near the shower axis[2]. Electrons are deflected in the opposite direction but due to their negative charge the induced current is $-e\mathbf{v}_{\perp,-} = e\mathbf{v}_{\perp,+}$ and has the same direction as for positrons. The denominator $(1 - n\beta\cos\theta)$ of Eq. (2.10) is positive and the rising pulse (*i.e.* that caused by the shower when it starts developing and that is given by the first term in Eq. (2.10)) has a polarisation towards $\mathbf{V} \times \mathbf{B}$. We choose the polarisation of the geomagnetic emission $\mathbf{G}$ as the opposite to this direction:

$$\mathbf{G} \parallel -\mathbf{V} \times \mathbf{B}, \tag{2.19}$$

as sketched in Fig. 2.7. In Fig. 2.8, as a particular case, the geomagnetic emission points west in the shower plane.

Had we chosen the observer at $\theta < \theta_C$ the polarisation would have been the same. Inside the Cherenkov cone, the first signal that arrives is the radiation from the end of the cascade. In this case, the second term in Eq. (2.10) corresponding to the deceleration of particles is the relevant one, which has a negative sign. However, the denominator $(1 - n\beta\cos\theta)$ is negative when $\theta < \theta_c$, which cancels out the negative signs, and therefore the polarisation inside the Cherenkov cone has the same direction as outside the Cherenkov cone, as sketched in Fig. 2.8.

As a consequence, the polarisation of the geomagnetic emission when the pulse first arrives at the observer lies along $-\mathbf{V} \times \mathbf{B}$.

Besides the geomagnetic current, there is a component of the current that is parallel to the shower axis, associated to the Askaryan mechanism. As in dense media, the magnitude of the electric field from this contribution is directly related to the variation of the (negative) excess charge as the shower develops in the atmosphere. The arrival direction of the shower $\mathbf{V}$ has little effect on the magnitude of this excess. As we have discussed before in Section 2.1.4, the polarisation of the radiation is oriented in the direction perpendicular to the observer's direction, but since in air the Cherenkov angle is $\theta_C \sim 1°$, the direction where the bulk of the emission is concentrated is very close to the shower axis, and the approximate polarisation of the Askaryan radiation is then approximately perpendicular to

[2]The bulk of the emission is produced around the Cherenkov angle which in air is small, $\theta_C \sim 1°$.

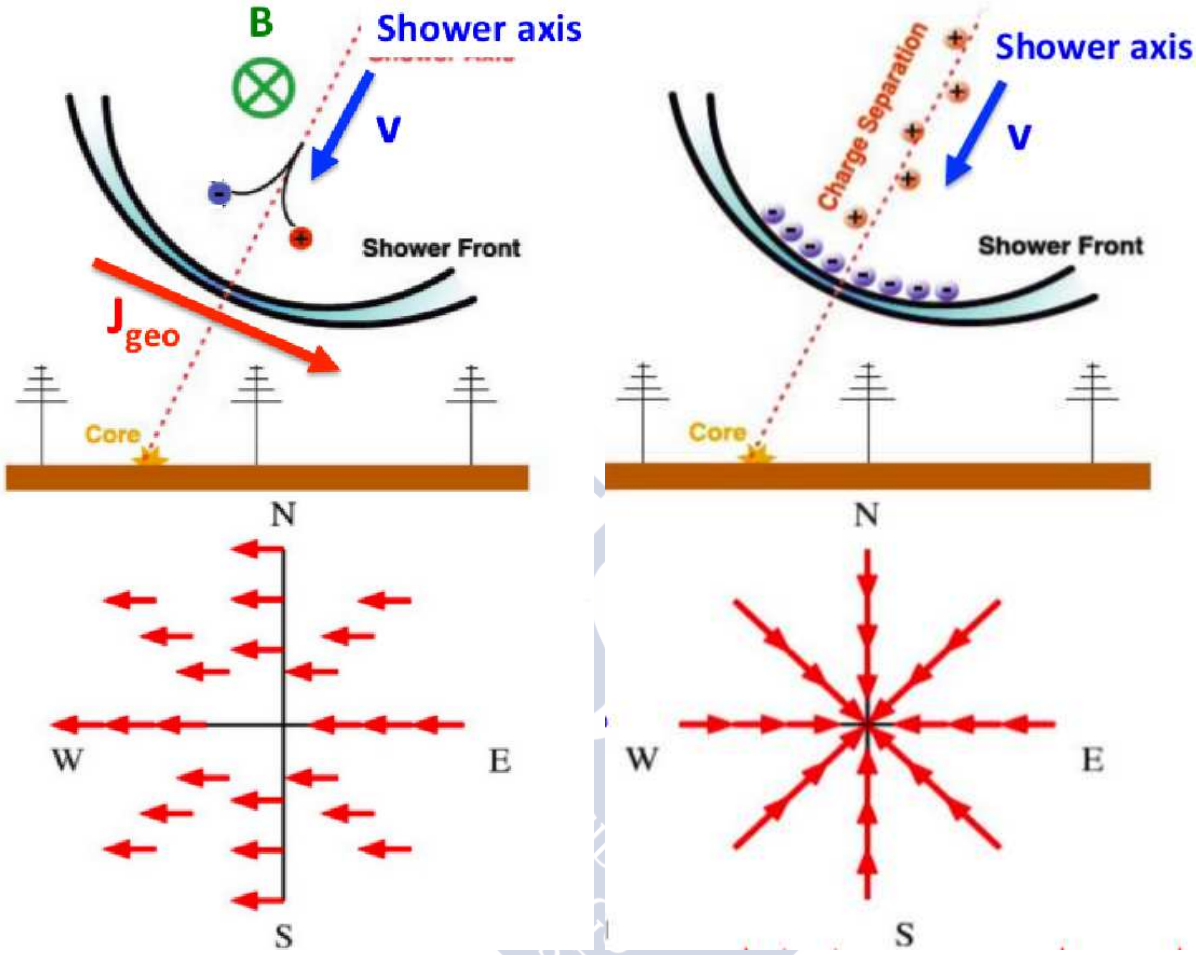

Figure 2.8: Top left: Sketch of the geomagnetic mechanism. The magnetic field **B** induces a current $\mathbf{J}_{\text{geo}}$. Bottom left: Approximate polarisation of the field induced by the geomagnetic current on a plane perpendicular to the shower axis. Top right: Sketch of the Askaryan mechanism. An excess of negative particles induces a radiation field. Bottom right: Approximate polarisation induced by the Askaryan mechanism in air and in a plane perpendicular to the shower axis. See text for details. Taken from the presentation of the proceeding [11]. Diagrams by H. Schoorlemmer and K. de Vries.

the shower axis, as sketched in Fig. 2.8. If we choose the direction of polarisation to be the opposite to the one that the electric field presents when the pulse first arrives (remember that the excess charge is negative) and apply the same reasoning as with the geomagnetic emission vector, then the polarisation is parallel to $e\mathbf{v}_\perp$ (see Eq (2.10)), where $\mathbf{v}_\perp$ points towards the shower axis, since it is the projection of the particle velocity onto the line perpendicular to the observer's direction. Therefore, the polarisation for the Askaryan mechanism is defined to be radial and pointing towards the shower axis. If we call the radial vector with respect to the shower axis $\mathbf{r}$, the Askaryan component $\mathbf{A}$ fulfils that

$$\mathbf{A} \parallel -\mathbf{r}, \tag{2.20}$$

as sketched in Figs. 2.7 and 2.8.

The interplay of the geomagnetic and Askaryan mechanisms with their differnt polarisations is the responsible for the azimuthally asymmetric patterns of the radiation field in the ground, as we will see below.

2.3.2 Properties of the radiation in air showers

We briefly summarize here some of the properties of the radiation emitted at radio frequencies in air showers concentrating on the spatial distribution of the signals at ground and on the frequency spectrum.

Let us first consider a vertical shower with the magnetic field horizontal (parallel to ground) and pointing towards the north, for the sake of simplicity. In that case, the shower plane coincides with the ground plane and the polarisations of the Askaryan and geomagnetic components on the ground are the ones sketched in Fig. 2.9. The North-South (NS) component of the field is due to the Askaryan radiation mainly, being more sizeable North and South of the shower core and almost null along the East-West (EW) line. The EW component of the field is dominated by the geomagnetic effect, with a constant polarisation vector. West of the shower core, the geomagnetic and Askaryan polarisations point in opposite directions and therefore the total field is reduced with respect to the field east of the shower core, where both mechanisms interfere constructively. These features are shown in the two-dimensional plots in Fig. 2.9. The ground pattern of the radiation of an air shower cannot be accurately described by a one-dimensional function.

The situation gets more complicated with inclined showers because the shower plane no longer coincides with the ground plane, where the antenna array is typically located. In the case of a $\theta = 45°$ shower coming from the West, the geomagnetic current points westwards and is perpendicular to the shower axis, while the Askaryan polarisation is

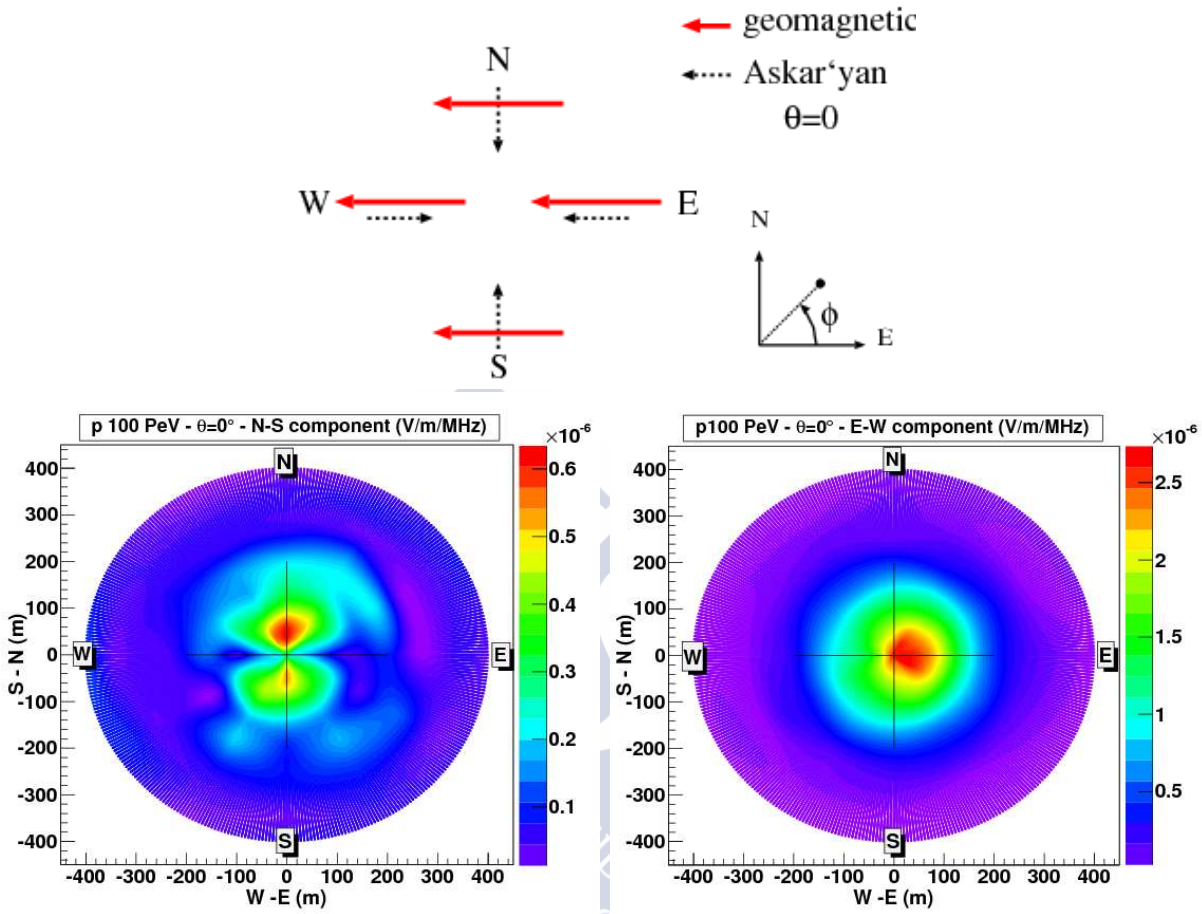

Figure 2.9: Top: Sketch of the projection on the ground of the electric field induced by the Askaryan and geomagnetic emission mechanisms in a vertical shower $\theta = 0°$. Bottom: Amplitude of different components of the electric field at 60 MHz. Left panel: North-South component of the electric field as a function of the position around the shower core as obtained in ZHAireS simulations of vertical showers induced by protons of evergy 10^{17} eV. Right panel: East-West component of the electric field obtained in the same simulations. The colour scale indicates the magnitude of the components of the field in V/m/MHz. Note the different scale in the left and right panels. Taken from [5].

directed towards the shower axis, only this time is tilted (see Fig. 2.10, top left). An important vertical component of the electric field appears, created both by the Askaryan and geomagnetic effects. In fact, the Lorentz force, and hence the geomagnetic polarisation, will only be horizontal if the plane defined by **B** and the shower axis is perpendicular to the ground (e.g., shower coming from the North-South line). In most geometries there will be a vertical component to the Lorentz force, which will cause a dependence of the polarisation and will induce signal asymmetries on the azimuthal angle of the shower, as can be seen in Fig. 2.10, where we show the results of ZHAireS simulations of the NS (top right), EW (bottom left) and vertical Z (bottom right) components of the electric field at 60 MHz for a 100 PeV proton shower with $\theta = 45^\circ$ coming from the west. There is a large asymmetry to the East in the EW and Z components, since in this particular geometry the dominant geomagnetic contribution makes an angle of $\sim 45^\circ$ with the horizontal, and thus the field has very similar EW and Z components.

Varying the incoming direction of the shower (the azimutal angle) will change the geomagnetic contribution and therefore the polarisation pattern on the ground [5]. However, the discussion is still valid, and the polarisation can be thought for all kind of geometries as the sum of the geomagnetic and Askaryan polarisations inducing asymmetries in the radio footprint at ground level.

Relativistic effects play a crucial role in the emission from air showers, similar to those in dense homogeneous media. In air showers the situation is more complicated because the refractive index of the atmosphere varies with altitude, which makes the arrival time dependant on the path and not only on the distance between emission and observation points. This is accounted for in the ZHAireS code, and it is of extreme relevance, for the arrival times of the radiation set the time duration of the pulse and by extension the coherence properties of the radiation. In a similar way to what happened for a constant refractive index, there is a cone (the *Cherenkov cone*), whose surface carries the largest electric field [12] and where the arrival times of the radiating parts of the cascade are very close temporally creating a narrow pulse (nanosecond scale). In this case, the apex of the cone responsible for the bulk of the radiation can be located at the shower maximum $X_{\max}$ and the aperture of the cone is approximately given by the Cherenkov angle at the altitude of $X_{\max}$. When the cone is projected on the ground, antennas placed near the elliptical ring shown in Fig. 2.11 will see the maximum electric field.

As the observation point moves away from the ring to the inner or outer regions of the Cherenkov cone, there is a significant broadening in time of the pulse, which is equivalent to a "reddening" of the spectrum. In Fig. 2.12 we show the frequency spectra for antennas

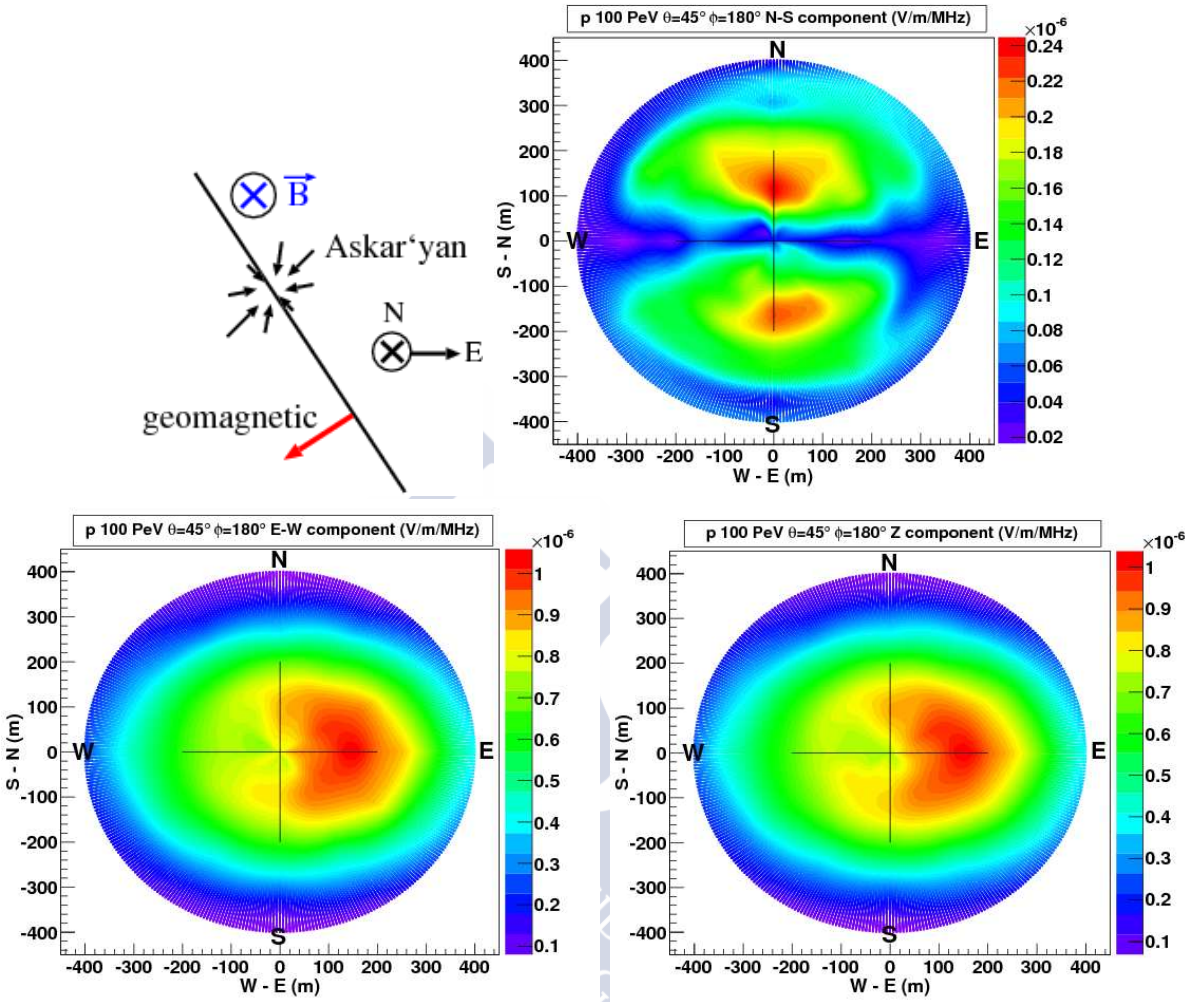

Figure 2.10: Top: Sketch of the projection on the ground of the electric field induced by the Askaryan and geomagnetic emission mechanisms in a vertical shower $\theta = 0°$ of 100 PeV of primary energy coming from the West. Bottom: Amplitude of different components of the electric field at 60 MHz. Left panel: North-South component of the electric field as a function of the position around the shower core as obtained in ZHAireS simulations of vertical showers induced by protons of energy 10^{17} eV. Right panel: East-West component of the electric field obtained in the same simulations. The colour scale indicates the magnitude of the components of the field in V/m/MHz. Note the different scale in the left and right panels. Taken from [5].

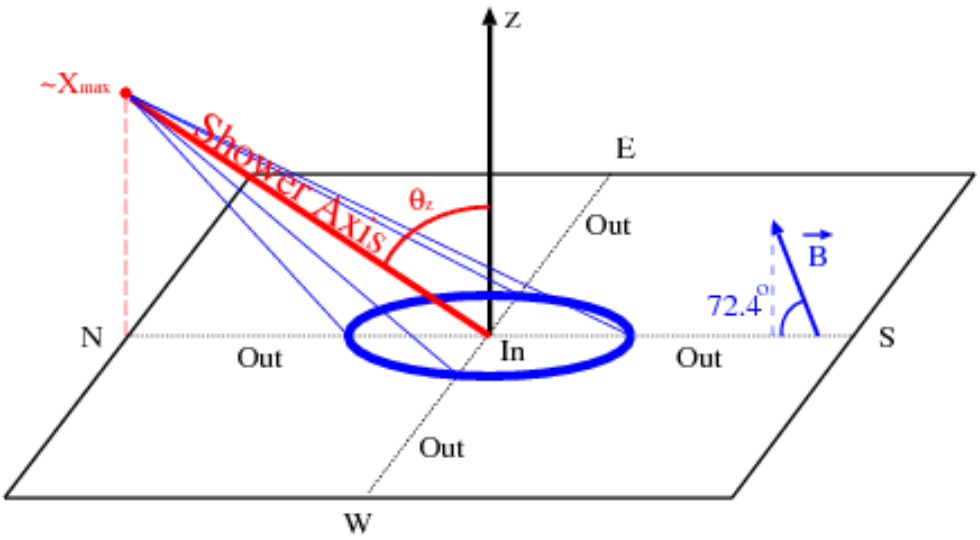

Figure 2.11: Geometry of shower whose radio emission is shown in Figs. 2.12, 2.13 and 2.14. θ_z is the zenithal angle of the shower, coming from the north in this case. Antennas are placed along the EW and NS lines (dotted lines). The magnetic field **B** used in the simulations for subsequent figures points towards the north and has an inclination of $-72.42°$. Also drawn is the Cherenkov cone centered at the depth of maximum shower development $X_{\max}$ and the ellipse of its intersection with the ground, where the radio signal is close to its maximum value. Taken from [12].

lying on the ground along the EW line in Fig. 2.11 that intercepts the shower axis. The spectrum becomes steeper (less coherence) as the observation points get further away from the Cherenkov ring. Antennas located very close to the ring contain a significant signal in the GHz region [12]. The distance to the shower axis can be related to the slope of the spectrum, with profound experimental implications for the energy determination of air showers (see Chapter 6 and [25]).

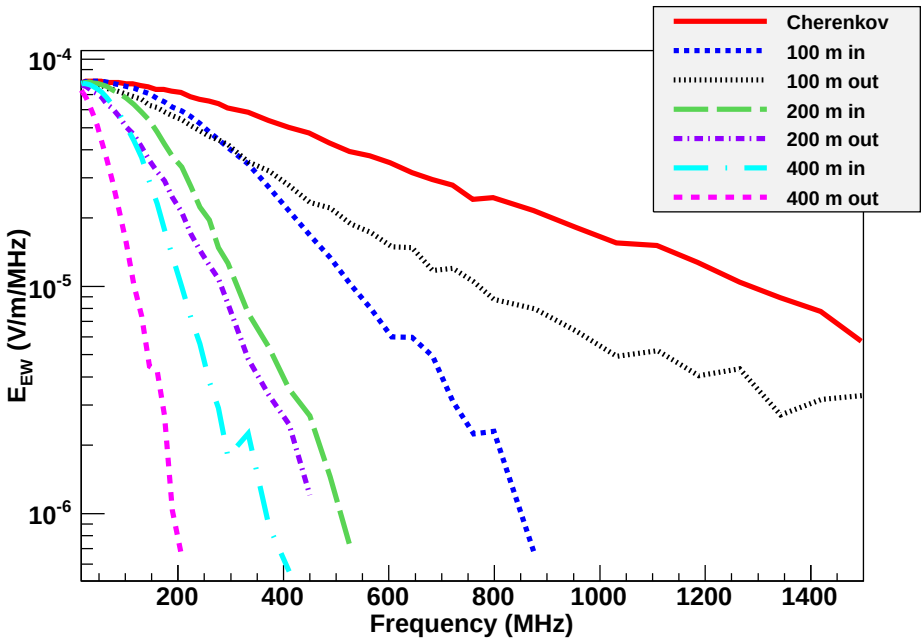

Figure 2.12: Frequency spectra on the ground for antennas at several distances along the EW line that intercepts the shower axis, inside and outside the Cherenkov cone for a 10^{19} eV proton shower with a zenith angle of $\theta_z = 80°$ coming from the north (see sketch in Fig. 2.11). The label "Cherenkov" refers to antennas that lie on the elliptical ring of Fig. 2.11, while numerical labels refer to the distance in meters from the ring to the antenna, either towards shower axis (in) or away from it (out). The antenna that sees $X_{\max}$ at the Cherenkov angle (solid red line) has a spectrum that extends well into the GHz frequency range.

In Fig. 2.13 we show the radio lateral distribution function (LDF), *i.e.* the amplitude of the Fourier transform of the electric field at a given frequency as a function of the distance to the shower core along the EW and NS lines on the ground. The projection of the Cherenkov cone on the ground makes and approximate ellipse with its major axis along

the NS direction and its minor axis along the EW direction. That is why the maxima of the LDF are further away along the NS line than along the EW line. In Fig. 2.13 we can also see that the field is slightly larger west of the core, since in that region the $-\mathbf{V} \times \mathbf{B}$ vector points eastwards (see Fig. 2.11) and so does the Askaryan component. Along the NS line the field is slightly larger north of the core than south of it, an effect related to the closer distance to shower maximum of observers north of the core (see Fig. 2.11)

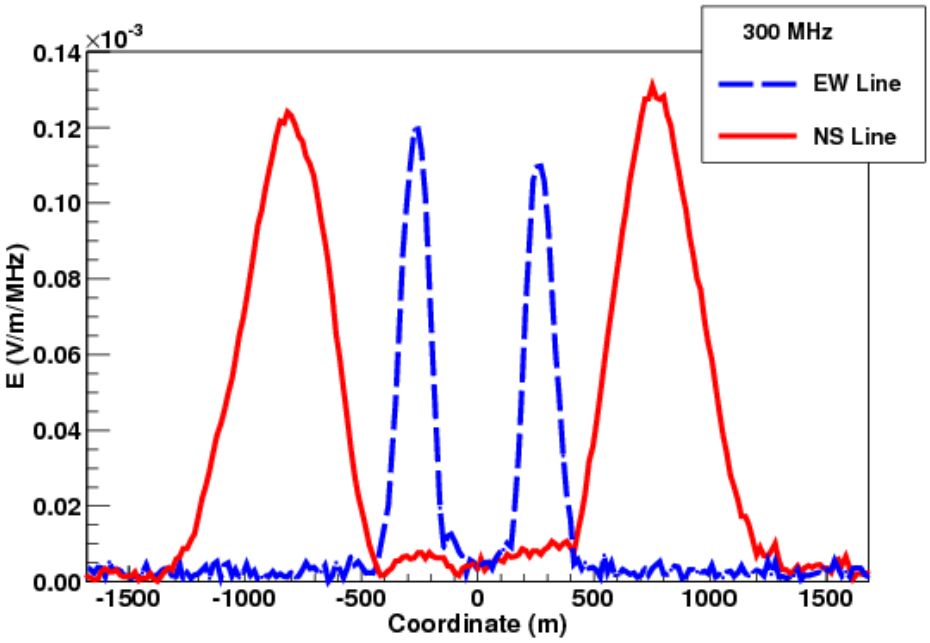

Figure 2.13: Fourier component (EW polarisation only) at 300 MHz as a function of distance to the shower core for a 10^{19} eV proton shower coming from the north with $\theta_z = 70°$. The antennas were placed along the NS and EW lines that intersect at the shower core. Negative coordinates are south (west) of the core for antennas along the NS (EW) line.

The LDF exhibits a variety of shapes, depending on the observation frequency. In Fig. 2.14 the Fourier components of the field as a function of distance to the core are plotted for fixed zenith angle. As the frequency drops the angular width of the Cherenkov ring broadens and eventually it becomes broader than the Cherenkov angle itself making a "plateau" in the radial coordinate on ground.

The simulations shown in this section were performed with the ZHAireS code and are consistent with data taken at LOPES [39], LOFAR [40] and ANITA [24] experiments among

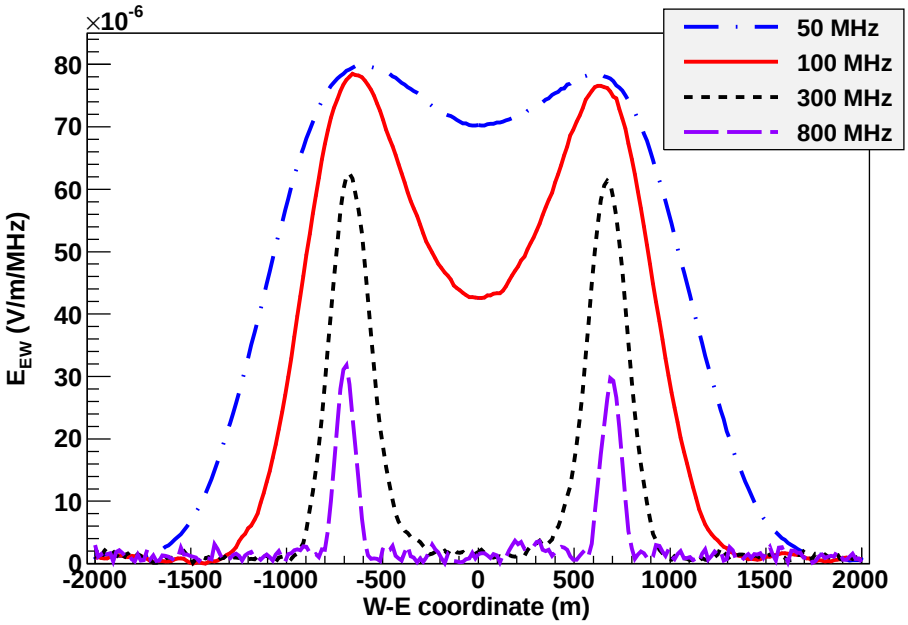

Figure 2.14: Fourier components (EW polarisation) of the electric field at 50, 100, 300 and 800 MHz as a function of the distance to the shower core for a 10^{19} eV proton shower coming from the north with zenith angle 80°. The antennas were placed along the EW line passing through the impact point of the shower (see Fig. 2.11).

others. The exponential fall of the spectrum is consistent with the measurements of the electric field reflected on the ground of Antarctica carried out by ANITA [24], but although it was thought that a mere extrapolation from the signals on the ground to the payload could suffice to describe the properties of the detected field, in reality the propagation from the ground to the ANITA payload after reflection changes some properties of the radiation [41]. This is the topic of Chapter 6 in this thesis.

Simulations of the electric field of air showers similar to those shown in this section are being used to develop methods of elucidating the $X_{\max}$ of the cosmic ray showers and with it, the nature of the primary particles [42]. The possibility of measuring composition using radio alone with high precision would help to consolidate the radio technique as a mature technique for measuring cosmic rays. This topic will be further discussed in Chapter 4.

2.3.3 Experiments exploiting radio emission in air showers

In the last years, we have been witnessing a revival of the radio observatories for detecting air showers. Among the most important ones we can find LOFAR [43], LOPES [44], AERA [45], CODALEMA [46] and Tunka-Rex [47]. In addition to them, we find SKA, which is an ambitious new project for building a huge radio observatory in Australia which can also be used for air shower detection [48].

The low-frequency array (LOFAR) is the first radio telescope designed with the capability to measure radio emission from cosmic-ray induced air showers in parallel with interferometric observations. Air showers are identified with the aid of a scintillator array named LORA. The electronic signals from the antennas are digitised, transported to a central digital processor, and combined in software to emulate a conventional antenna. LOFAR is distributed over northern Europe with the densest concentration in the north of the Netherlands, in the Province of Drenthe (see Fig. 2.15). The data is taken with low-band antennas (10-90 MHz) and high-band antennas (110-240 MHz). LOFAR has been measuring cosmic ray events between 10^{16} eV and 10^{18} eV since 2011. LOFAR has been able to reconstruct the shower maximum of air showers with an uncertainty of 17 g/cm^2, evidencing that radio is capable of measuring cosmic-ray composition [42].

The concept of LOFAR had its precursor in LOPES (LOFAR Prototype Station). LOPES had dipole antennas (in the 43-74 MHz band) triggered by KASCADE (Karlsruhe Shower Core and Array Detector), which is a particle detector array. KASCADE provided LOPES with shower parameters like muon number, electron number, direction of origin and position of the shower core, and these parameters were used as a guide for the radio detection. LOPES measured the LDF of the radio emission [39] and paved the way for

Figure 2.15: Superterp, the central part of the core of the LOFAR array located in the Netherlands. The Superterp is composed of six radio stations located on a 320 diameter island. The six stations can be combined to form a single, large station.

LOFAR.

The Auger Engineering Radio Array (AERA) is the radio extension of the Pierre Auger Observatory. AERA is being used to study the emission of radio waves from extensive air showers measuring the electric field from 30 to 80 MHz, with new prototypes that can measure lower frequencies and the vertical polarisation of the field recently installed. Currently, AERA has more than 200 radio stations over a surface of 6 km^2. AERA is constantly detecting cosmic ray events in coincidence with the rest of detectors of the Pierre Auger observatory, and their analysis is underway. AERA has been able to measure the contribution of the Askaryan mechanism to the emission [49], and the correlation between energy emitted in radio waves calibrated with the energy estimation of the primary cosmic rays by the FD detector of Auger [50].

CODALEMA [46] is a radio observatory located in Nançay, France, dedicated to the radio detection of extensive air showers. It currently consists of 57 self-triggering radio detection stations working in the 20-200 MHz band, over 1 km^2, an array of 13 scintillators acting as a particle detector and a compact array of 10 cabled antennas triggered by the particle detector to test the capabilities of a phased antenna cluster to select air shower events. CODALEMA will also host the EXTASIS project, designed to study the low-frequency (< 5 MHz) components of the electric field and the *sudden death* signal when the shower particles reach the ground [51].

Tunka-Rex [47] is the radio extension of the air-Cherenkov detector Tunka-133. It has recorded three years of air shower measurements. The detector consists of 44 antennas connected to air-Cherenkov and scintillator detectors placed in the Tunka valley, Siberia. They have shown that a reconstruction of the shower maximum with an uncertainty of 40 g/cm^2 is possible with this experiment [52].

The Square Kilometer Array (SKA) [48] is a project that intends to constitute the world's largest radio telescope in 2023, planned to be built in Australia. With a very dense and uniform antenna spacing in a fiducial area of 1 km^2, and a bandwidth of 50-350 MHz, SKA could provide very accurate measurements of air showers in coincidence with a particle array. The low-frequency part of the array will go into operation in 2020.

Bibliography

[1] O. Scholten, K. Werner, and F. Rusdyi. A macroscopic description of coherent geomagnetic radiation from cosmic-ray air shower. *Astroparticle Physics*, **29**:94, 2008.

[2] K. Werner, K. D. de Vries, and O. Scholten. A realistic treatment of geomagnetic Cherenkov radiation from cosmic ray air showers. *Astroparticle Physics*, **37**:5, 2012.

[3] E. Zas, F. Halzen, and T. Stanev. Electromagnetic pulses from high-energy showers: Implications for neutrino detection. *Physical Review D*, **45**:365, 1992.

[4] J. Alvarez-Muñiz, W. R. Carvalho Jr., M. Tueros, and E. Zas. Coherent Cherenkov radio pulses from hadronic showers up to EeV energies. *Astroparticle Physics*, **35**:287, 2012.

[5] J. Alvarez-Muñiz, W. R. Carvalho Jr., and E. Zas. Monte Carlo simulations of radio pulses in atmospheric showers using ZHAireS. *Astroparticle Physics*, **35**:325, 2012.

[6] T. Huege, M. Ludwig, and C. W. James. Simulating radio emission from air showers with CoREAS. *AIP Conference Proceedings*, **1535**:128, 2012.

[7] V. Marin and B. Revenu. Simulation of radio emission from cosmic ray air shower with SELFAS2. *Astroparticle Physics*, **35**:733, 2012.

[8] J. Alvarez-Muñiz, A. Romero-Wolf, and E. Zas. Practical and accurate calculations of the Askaryan effect. *Physical Review D*, **84**(103003), 2011.

[9] J. Alvarez-Muñiz, E. Marqués, R. A. Vázquez, and E. Zas. Coherent radio pulses from showers in different media: A unified parameterization. *Physical Review D*, **74**(023007), 2006.

[10] J. Alvarez-Muñiz, C. W. James, R. J. Protheroe, and E. Zas. Thinned simulations of extremely energetic showers in dense media for radio applications. *Astroparticle Physics*, **32**:100, 2009.

[11] J. Alvarez-Muñiz. Modeling radio emission from particle showers in dense media and air: a pedagogical overview. In *Press of Acoustic and Radio EeV Neutrino Detection Activities (ARENA) 2014*.

[12] J. Alvarez-Muñiz, A. Romero-Wolf W. R. Carvalho Jr., M. Tueros, and E. Zas. Coherent radiation from extensive air showers in the ultrahigh frequency band. *Physical Review D*, **86**(123007), 2012.

[13] J. D. Jackson. From Lorenz to Coulomb and other explicit gauge transformations. *American Journal of Physics*, **70**:917, 2002.

[14] D. García-Fernández, J. Alvarez-Muñiz, W. R. Carvalho Jr., A. Romero-Wolf, and E. Zas. Calculations of electric fields for radio detection of ultrahigh energy particles. *Physical Review D*, **87**(023003), 2013.

[15] J. Alvarez-Muñiz, A. Romero-Wolf, and E. Zas. Cerenkov radio pulses from electromagnetic showers in the time domain. *Physical Review D*, **81**(123009), 2010.

[16] G. A. Askar'yan. Excess negative charge of an electron-photon shower and its coherent radio emission. *Journal of Experimental and Theoretical Physics*, **41**:616, 1961.

[17] D. Saltzberg *et al.* Observation of the Askaryan effect: Coherent microwave Cherenkov emission from charge asymmetry in high-energy particle cascades. *Physical Review Letters*, **86**:2802, 2001.

[18] J. Alvarez-Muñiz. Detection of astrophysical ultra-high energy neutrinos with radio waves. Talk given at VI CPAN Days, Sevilla, Spain, 2014.

[19] J. Alvarez-Muñiz, R. A. Vázquez, and E. Zas. Characterization of neutrino signals with radiopulses in dense media through the Landau-Pomeranchuk-Migdal effect. *Physical Review D*, **61**(023001), 1999.

[20] S. Sciutto. <http://www.fisica.unlp.edu.ar/auger/aires/>.

[21] M. Tueros and S. Sciutto. TIERRAS: A package to simulate high energy cosmic ray showers underground, underwater and under-ice. *Computer Physics Communications*, **181**:380, 2010.

[22] S. Barwick *et al.* South Polar in situ radio-frequency ice attenuation. *Journal of Glaciology*, **51**:173, 2005.

[23] P. W. Gorham *et al.* The Antarctic Impulsive Transient Antenna ultra-high energy neutrino detector: Design, performance, and sensitivity for the 2006–2007 balloon flight. *Astroparticle Physics*, **32**:10, 2009.

[24] S. Hoover *et al.* Observation of ultrahigh-energy cosmic rays with the ANITA balloon-borne radio interferometer. *Physical Review Letters*, **105**(151101), 2010.

[25] H. Schoorlemmer *et al.* Energy and flux measurements of ultra-high energy cosmic rays observed during the first ANITA flight. In *Proceedings of the 34th International Cosmic Ray Conference (ICRC 2015)*, number 272.

[26] H. Schoorlemmer *et al.* Energy and flux measurements of ultra-high energy cosmic rays observed during the first ANITA flight. arxiv:1506.05396. Accepted in Astroparticle Physics in press.

[27] P. Gorham. Overview of the third flight of the ANITA long-duration balloon payload. In *Proceedings of the 34th International Cosmic Ray Conference (ICRC 2015)*, number 1111.

[28] P.W. Gorham *et al.* The ExaVolt Antenna: A large-aperture, balloon-embedded antenna for ultra-high energy particle detection. *Astroparticle Physics*, **35**:242, 2011.

[29] P. Allison *et al.* Design and initial performance of the Askaryan Radio Array prototype EeV neutrino detector at the South Pole. *Astroparticle Physics*, **35**:457, 2012.

[30] T. Meures. *Development of a Sub-glacial Radio Telescope for the Detection of GZK neutrinos*. Springer Thesis, 2015.

[31] S. A. Wissel *et al.* Site characterization and detector development for the Greenland Neutrino Observatory. In *Proceedings of the 34th International Cosmic Ray Conference (ICRC 2015)*, number 1150.

[32] C. W. James *et al.* LUNASKA experiments using the Australia Telescope Compact Array to search for ultrahigh energy neutrinos and develop technology for the lunar Cherenkov technique. *Physical Review D*, **81**:042003, 2010.

[33] J. Bray *et al.* The lunar Askaryan technique with the Square Kilometre Array. In *Proceedings of the 34th International Cosmic Ray Conference (ICRC 2015)*, number 291.

[34] P. W. Gorham *et al.* Observations of the Askaryan effect in ice. *Physical Review Letters*, **99**(171101), 2007.

[35] P. W. Gorham *et al.* Accelerator measurements of the Askaryan effect in rock salt: A roadmap toward teraton underground neutrino detectors. *Physical Review D*, **72**(023002), 2005.

[36] P. Miočinović *et al.* Time-domain measurement of broadband coherent Cherenkov radiation. *Physical Review D*, **74**(043002), 2006.

[37] H. R. Allan. *Progress in Elementary Particle and Cosmic Ray Physics*, **10**:169, 1971. and references therein.

[38] J. Alvarez-Muñiz, W. R. Carvalho Jr., H. Schoorlemmer, and E. Zas. Radio pulses from ultra-high energy atmospheric showers as the superposition of Askaryan and geomagnetic mechanisms. *Astroparticle Physics*, **59**:29, 2014.

[39] W. D. Apel *et al.* Lateral distribution of the radio signal in extensive air showers measured with LOPES. *Astroparticle Physics*, **32**:294, 2010.

[40] A. Corstanje *et al.* LOFAR: detecting cosmic rays with a radio telescope. In *Proceedings of the 32nd International Cosmic Ray Conference (ICRC 2011)*, page 192.

[41] J. Alvarez-Muñiz, W.R. Carvalho Jr., D. García-Fernández, H. Schoorlemmer, and E. Zas. Simulations of reflected radio signals from cosmic ray induced air showers. *Astroparticle Physics*, **66**:31, 2015.

[42] S. Buitink *et al.* Method for high precision reconstruction of air shower $X_{\max}$ using two-dimensional radio intensity profiles. *Physical Review D*, **90**(082003), 2014.

[43] P. Schellart *et al.* Detecting cosmic rays with the LOFAR radio telescope. *Astronomy and Astrophysics*, **A98**:560, 2013.

[44] H. Falcke *et al.* Detection and imaging of atmospheric radio flashes from cosmic ray air showers. *Nature*, **435**:313, 2005.

[45] F. G. Schröder *et al.* Radio detection of air showers with Auger Engineering Radio Array. In *Proceedings of the 33rd International Cosmic Ray Conference (ICRC 2013)*, number 0899.

[46] R. Dallier *et al.* Multi-scale and multi-frequency studies of cosmic ray air shower radio signals at the CODALEMA site. In *Proceedings of the 34th International Cosmic Ray Conference (ICRC 2015)*, number 293.

[47] D. Kostunin. The Tunka Radio Extension: reconstruction of energy and shower maximum of the first year data. In *Proceedings of the 34th International Cosmic Ray Conference (ICRC 2015)*, number 285.

[48] *et al.* T. Huege. High-precision measurements of extensive air showers with the SKA. In *Proceedings of the 34th International Cosmic Ray Conference (ICRC 2015)*, number 309.

[49] A. Aab *et al.* Probing the radio emission from air showers with polarization measurements. *Physical Review D*, **89**(052002), 2014.

[50] A. Aab *et al.* Energy estimation of cosmic rays with the Engineering Radio Array of the Pierre Auger Observatory, 2015. arxiv:1508.04267.

[51] B. Revenu *et al.* Reconstruction of the parameters of cosmic ray induced extensive air showers using radio detection and simulation. In *Proceedings of the 34th International Cosmic Ray Conference (ICRC 2015)*, number 397.

[52] P. A. Bezyazeekov *et al.* Probing the radio emission from air showers with polarization measurements. *Nuclear Instruments and Methods in Physics Research A*, **802**:89, 2015.

Chapter 3

Calculations of radio emission

In order for the radio technique to succeed, we need accurate predictions of the electric field created by a UHE cosmic ray shower. We will consider in this work the so-called *microscopic* approach, that consists in calculating the electric field adding up the fields created by the individual shower particles. The trajectories of the shower particles are calculated using Monte Carlo codes, and they are composed of *tracks*, defined as segments in which the particle is assumed to travel at a constant speed. We are particularly interested in an analytical formula for the field of a single track that can be embedded in most Monte Carlo codes. Since the number of particles in a shower at EeV energies is greater than 10^9, the calculation must be carried out in an efficient way.

3.1 Electric field of a single charged particle track

3.1.1 Exact calculation

Current of a track

Let us assume, without loss of generality, an electron that is ejected from an atom at time $t = t_1$ and travels at constant velocity $\mathbf{v}$ through a medium along a finite track until it is absorbed in another atom at $t = t_2$. If we neglect the movement of the atoms and think of the emission and absorption as instantaneous, we can write the electron current as

$$\mathbf{J}(\mathbf{x}, t) = -e\ \mathbf{v}\ \delta^{(3)}(\mathbf{x} - \mathbf{x_0} - \mathbf{v}t)\ \Theta(t - t_1)\ \Theta(t_2 - t), \tag{3.1}$$

where $e = |e|$ is the charge of a positron, $\mathbf{x}(t)$ is its position and $\mathbf{x}_0$ is an arbitrary reference position. The step Θ functions account for the fact that the electron only moves in the time interval (t_1, t_2). We are considering the loss and gain of speed as instantaneous. However, physically, they must have an associated typical time defined by quantum mechanics. If we call this time Δt_q, we expect the Fourier components of the field created by the current in Eq. (3.1) to be valid until the observation frequency is comparable to $1/\Delta t_q$. The low-frequency region is precisely the appropiate region for applying classical electrodynamics to

radiation processes (see chapter 6 in [1]). If we take as Δt_q a time related to the Compton wavelength λ_C of the electron,

$$\Delta t_q \sim \frac{h}{m_e c^2} = \frac{\lambda_C}{c} = \frac{2.426 \cdot 10^{-12} \text{ m}}{0.3 \text{ m ns}^{-1}} = 8.09 \cdot 10^{-12} \text{ ns}, \tag{3.2}$$

the order of magnitude of the maximum frequency up to which we expect the classical field to be valid is

$$\nu_{\text{classical}} \ll \frac{1}{\Delta t_q} \sim \frac{m_e c^2}{h} = \frac{c}{\lambda_C} \sim 1.24 \cdot 10^{11} \text{ GHz}. \tag{3.3}$$

We are interested in radio emission well below the THz, so modelling the current as in Eq. (3.1) is more than satisfactory for our purposes. If we had used the Compton wavelength of a proton (smaller than the electron's) we would have obtained an even larger upper frequency.

If we paste several tracks together in a way that the ending point of one is the starting point of the next one, we can model the trajectory as a collection of straight tracks. This trajectory can be interpreted as a particle that is travelling through a medium and at several points it interacts with the atoms in it, and that causes a change in its direction and speed as sketched in Fig. 3.1.

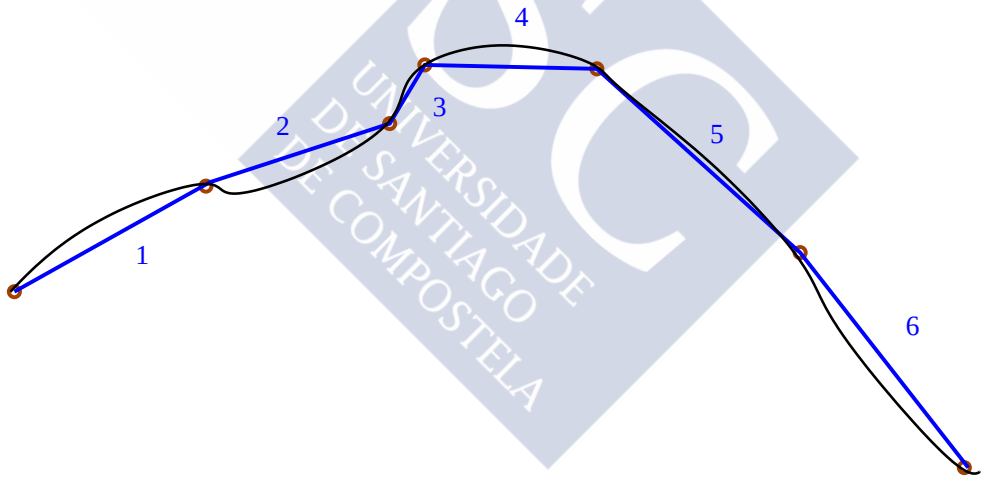

Figure 3.1: Sketch of the curved trajectory of a particle (black line) and its approximation using six straight tracks (blue lines, numbered). Initial and ending points for each track are marked with brown circles.

Charge must be conserved, so we invoke the continuity equation,

$$\nabla \cdot \mathbf{J} + \partial_t \rho = 0, \tag{3.4}$$

where ρ is the charge density and $\partial_t = \partial/\partial t$. Let us transform Eq. (3.4) to the frequency domain using the following definition of the Fourier Transform:

$$\mathrm{FT}[f(t)] \equiv f(\omega) \equiv \int_{-\infty}^{\infty} \mathrm{d}t \; e^{i\omega t} f(t). \tag{3.5}$$

The continuity equation in the frequency domain then reads:

$$\nabla \cdot \mathbf{J}(\mathbf{x}, \omega) - i\omega\rho(\mathbf{x}, \omega) = 0. \tag{3.6}$$

Charge conservation implies that

$$\rho = \frac{\nabla \cdot \mathbf{J}(\mathbf{x}, \omega)}{i\omega}, \tag{3.7}$$

that relates the charge density and the current, valid for all frequencies except for $\omega = 0$ (the static term), that has no effect on radiation fields. In other words, it is enough for our purposes to use the current of the track, ignoring the charge density of the surrounding medium and the track itself[1].

Maxwell's equations for the vector potential of a track

Let us assume a non-conductive medium that is linearly dielectric and magnetic with frequency-dependent permittivity $\epsilon(\omega)$ and permeability $\mu(\omega)$. We can write the curl of the magnetic field in the frequency domain (one of Maxwell's equations) using the track current in Eq. (3.1) (remember the transform definition in Eq. (3.5)),

$$\nabla \times \mathbf{B}(\mathbf{x}, \omega) = \mu\mathbf{J} - i\omega\mu\epsilon\mathbf{E}(\mathbf{x}, \omega). \tag{3.8}$$

Let us define the fields in terms of the scalar and vector potentials ϕ and $\mathbf{A}$,

$$\mathbf{E}(\mathbf{x}, \omega) = -\nabla\phi(\mathbf{x}, \omega) + i\omega\mathbf{A}(\mathbf{x}, \omega), \tag{3.9}$$

$$\mathbf{B}(\mathbf{x}, \omega) = \nabla \times \mathbf{A}(\mathbf{x}, \omega). \tag{3.10}$$

Inserting the definitions (3.9) and (3.10) into Eq. (3.8), we obtain:

$$\nabla^2\mathbf{A} + \mu\epsilon\omega^2\mathbf{A} - \nabla(\nabla \cdot \mathbf{A} - \mu\epsilon i\omega\phi) = -\mu\mathbf{J}. \tag{3.11}$$

[1]One has to be careful to avoid the temptation of writing a charge density in a similar way to the current density in Eq. (3.1). Charge cannot be created or destroyed and therefore cannot be represented by a Heaviside function, unless some other charge density is present.

The Lorenz gauge condition, expressed in the frequency domain, allows us to express the potential ϕ in terms of the vector potential $\mathbf{A}$,

$$i\epsilon\mu\omega\phi = \nabla \cdot \mathbf{A}. \tag{3.12}$$

As a consequence, $\mathbf{A}$ is enough to determine the fields at non-zero frequency. Inserting Eq. (3.12) in (3.11), we obtain

$$\nabla^2\mathbf{A} + \mu\epsilon\omega^2\mathbf{A} = -\mu\mathbf{J}, \tag{3.13}$$

which is the Helmholtz equation for the vector potential. Solving Eq. (3.13) and using Eqs. (3.12) and (3.9) we can obtain the electric field.

Although we could use Eq. (3.1) to solve Eq. (3.13), a more general solution can be given if we write the current as

$$\mathbf{J}(\mathbf{x}, t) = \hat{\mathbf{z}}\ qv\ Z(t)\ P(\mathbf{x}, t), \tag{3.14}$$

where $Z(t)$ substitutes the step function and $P(\mathbf{x}, t)$ is the distribution of charge, that can now be arbitrary. Since we are working in the frequency domain, the current in Eq. (3.14) must be transformed,

$$\mathbf{J}(\mathbf{x}, \omega) = \hat{\mathbf{z}} \int_{-\infty}^{\infty} \mathrm{d}t\ e^{i\omega t} qv\ Z(t)\ P(\mathbf{x}, t). \tag{3.15}$$

Solving for the potentials

Let us write once again Helmholtz's equation for the potential.

$$(\nabla^2 + k^2)\mathbf{A}(\mathbf{x}, \omega) = -\mu\mathbf{J}(\mathbf{x}, \omega), \tag{3.16}$$

where $k = \omega n/c$ and $c/n = (\sqrt{\mu\epsilon})^{-1}$. We can solve this equation using Green's method. From [2], we take the Green function of the Helmholtz equation for outgoing radiation,

$$G(\mathbf{x}, \mathbf{x}') = -\frac{e^{ik|\mathbf{x}-\mathbf{x}'|}}{4\pi|\mathbf{x} - \mathbf{x}'|}, \tag{3.17}$$

where $\mathbf{x}$ is the position of the observer and $\mathbf{x}'$ the position of the charge distribution (see Fig. 3.2). A solution for the vector potential can be written as follows,

$$\mathbf{A}(\mathbf{x}, \omega) = \frac{\mu}{4\pi} \int \mathrm{d}^3\mathbf{x}' \frac{e^{ik|\mathbf{x}-\mathbf{x}'|}}{|\mathbf{x} - \mathbf{x}'|} \mathbf{J}(\mathbf{x}', \omega). \tag{3.18}$$

Putting the transformed current in Eq. (3.15) into the potential,

$$\mathbf{A}(\mathbf{x},\omega) = \frac{\mu q v}{4\pi}\hat{z}\int \mathrm{d}^3\mathbf{x}'\mathrm{d}t' e^{i\omega t'}\frac{e^{ik|\mathbf{x}-\mathbf{x}'|}}{|\mathbf{x}-\mathbf{x}'|}\; Z(t')\; P(\mathbf{x}',t'). \tag{3.19}$$

The vector potential only has z component, as expected in the Lorenz gauge for a charge moving along that axis. Through Eq. (3.12), the scalar potential can be obtained by means of the divergence of $\mathbf{A}$.

$$\nabla\cdot\mathbf{A} = \partial_z A_z = \frac{\mu q v}{4\pi}\int \mathrm{d}^3\mathbf{x}'\mathrm{d}t'\; Z(t')\; P(\mathbf{x}',t')e^{i\omega t'}\frac{e^{ik|\mathbf{x}-\mathbf{x}'|}}{|\mathbf{x}-\mathbf{x}'|}\left[ik - \frac{1}{|\mathbf{x}-\mathbf{x}'|}\right]\frac{z-z'}{|\mathbf{x}-\mathbf{x}'|}, \tag{3.20}$$

where $\partial_z = \partial/\partial z$.

Exact solution for the electric field

The divergence of the vector potential can be written in a more convenient way to keep track of the derivatives needed to obtain $\mathbf{E}(\mathbf{x},\omega)$ using Eqs. (3.9) and (3.12).

$$\nabla\cdot\mathbf{A} = \partial_z A_z = \frac{\mu q v}{4\pi}\int \mathrm{d}^3\mathbf{x}'\;\mathrm{d}t'\; Z(t')\; P(\mathbf{x}',t')e^{i\omega t'} f_1 f_2 f_3 \quad \text{with} \tag{3.21}$$

$$f_1 = \frac{e^{ik|\mathbf{x}-\mathbf{x}'|}}{|\mathbf{x}-\mathbf{x}'|}; \qquad f_2 = \left[ik - \frac{1}{|\mathbf{x}-\mathbf{x}'|}\right]; \qquad f_3 = \frac{z-z'}{|\mathbf{x}-\mathbf{x}'|}. \tag{3.22}$$

The derivatives of f_1, f_2 and f_3 are necessary to calculate the fields. Performing first the derivative with respect to x,

$$\partial_x f_1 = \frac{e^{ik|\mathbf{x}-\mathbf{x}'|}}{|\mathbf{x}-\mathbf{x}'|}\left[ik - \frac{1}{|\mathbf{x}-\mathbf{x}'|}\right]\frac{x-x'}{|\mathbf{x}-\mathbf{x}'|} \tag{3.23}$$

$$\partial_x f_2 = \frac{x-x'}{|\mathbf{x}-\mathbf{x}'|^3}; \qquad \partial_x f_3 = -\frac{(z-z')(x-x')}{|\mathbf{x}-\mathbf{x}'|^3}. \tag{3.24}$$

Eqs. (3.23) and (3.24) allow us to write the derivative of Eq. (3.21) with respect to x:

$$\partial_x(\nabla\cdot\mathbf{A}) = \partial_x\partial_z A_z = \frac{\mu q v}{4\pi}\int \mathrm{d}^3\mathbf{x}'\;\mathrm{d}t'\; Z(t')\; P(\mathbf{x}',t')e^{i\omega t'}\frac{e^{ik|\mathbf{x}'-\mathbf{x}|}}{|\mathbf{x}-\mathbf{x}'|^3}(z-z')\times$$
$$\left[\left(ik - \frac{1}{|\mathbf{x}-\mathbf{x}'|}\right)^2(x-x') + \frac{x-x'}{|\mathbf{x}-\mathbf{x}'|^2} - \left(ik - \frac{1}{|\mathbf{x}-\mathbf{x}'|}\right)\frac{x-x'}{|\mathbf{x}-\mathbf{x}'|}\right]. \tag{3.25}$$

Because of the cylindrical symmetry of the problem, it is not necessary to calculate the y component. We must, however, calculate the z derivative in a similar way,

$$\partial_z f_1 = \frac{e^{ik|\mathbf{x}-\mathbf{x}'|}}{|\mathbf{x}-\mathbf{x}'|}\left[ik - \frac{1}{|\mathbf{x}-\mathbf{x}'|}\right]\frac{z-z'}{|\mathbf{x}-\mathbf{x}'|}, \tag{3.26}$$

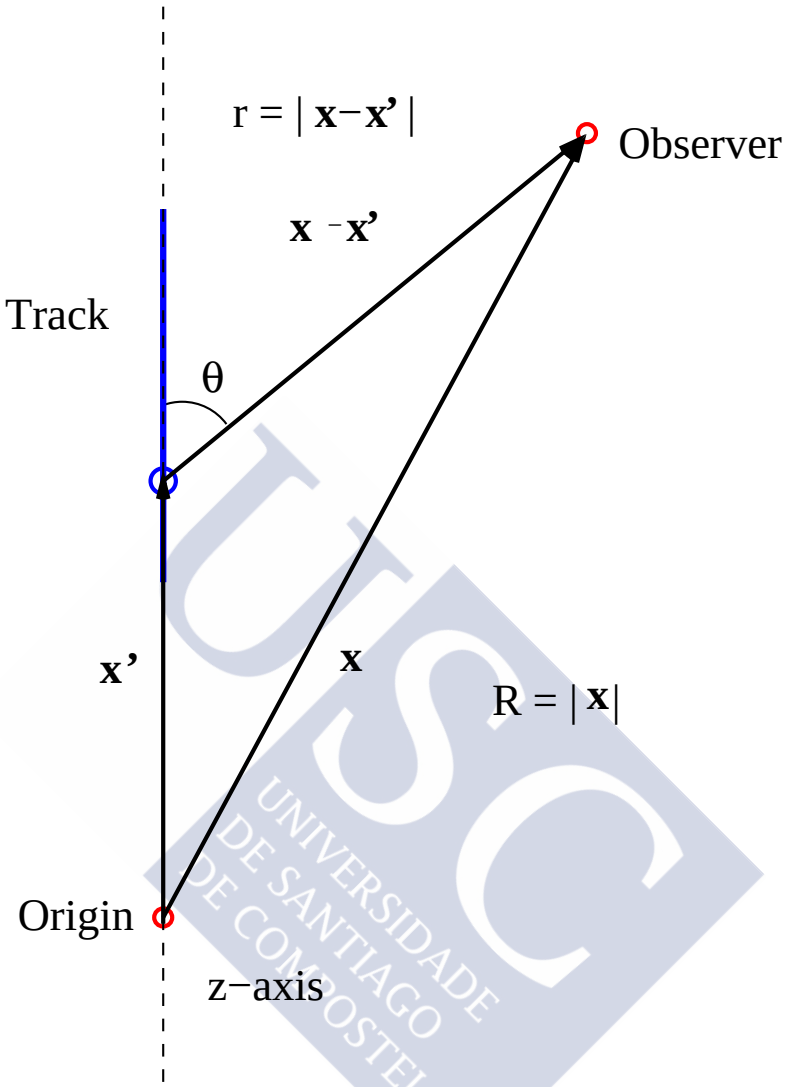

Figure 3.2: Sketch of the position $\mathbf{x}$ and charge distribution $\mathbf{x}'$ vectors. A track (blue line) is shown, along with the origin of the reference frame and the observer's position (red dots). $\mathbf{x}$ is the position vector of the observer and $\mathbf{x}'$ is the vector that marks the position of a point of the track. R is the distance from the origin of coordinates to the observation point and r is the distance from the observation point to the point of the track denoted by $\mathbf{x}'$. θ is the angle between the direction of the track and the $\mathbf{x} - \mathbf{x}'$ vector. The dashed vertical line represents the z axis of the reference frame.

$$\partial_z f_2 = \frac{z-z'}{|\mathbf{x}-\mathbf{x}'|^3}; \qquad \partial_z f_3 = -\frac{(z-z')^2}{|\mathbf{x}-\mathbf{x}'|^3} + \frac{1}{|\mathbf{x}-\mathbf{x}'|}, \tag{3.27}$$

and then,

$$\partial_z(\nabla\cdot\mathbf{A}) = \partial_z\partial_z A_z = \frac{\mu q v}{4\pi}\int \mathrm{d}^3\mathbf{x}'\ \mathrm{d}t'\ Z(t')P(\mathbf{x}',t')e^{i\omega t'}\frac{e^{ik|\mathbf{x}'-\mathbf{x}|}}{|\mathbf{x}-\mathbf{x}'|^2}\times$$
$$\left[\left(ik-\frac{1}{|\mathbf{x}-\mathbf{x}'|}\right)^2\frac{(z-z')^2}{|\mathbf{x}-\mathbf{x}'|}+\frac{(z-z')^2}{|\mathbf{x}-\mathbf{x}'|^3}-\left(ik-\frac{1}{|\mathbf{x}-\mathbf{x}'|}\right)\left(\frac{(z-z')^2}{|\mathbf{x}-\mathbf{x}'|^2}-1\right)\right]. \tag{3.28}$$

Eqs. (3.12), (3.19), (3.25) and (3.28), together with the expression for the electric field in Eq. (3.9) and various derivatives are all we need to obtain the electric field. The symmetry of the problem allows the substitution of x for the cylindrical radial coordinate ρ. The radial component of the electric field is then, according to Eq. (3.9),

$$E_\rho(\mathbf{x},\omega) = -\partial_\rho\phi = -\partial_\rho\frac{\nabla\cdot\mathbf{A}}{i\omega\mu\epsilon}. \tag{3.29}$$

Now, we take Eq. (3.14) and identify

$$Z(t) = \Theta(t-t_1)\ \Theta(t_2-t), \tag{3.30}$$

$$P(\mathbf{x},t) = \delta^{(3)}(\mathbf{x}-\mathbf{x_0}-\mathbf{v}t), \tag{3.31}$$

so that we are using the current of a track (Eq. (3.1)). Several definitions are convenient in order to make the equations more manageable,

$$r(t) \equiv \sqrt{\rho^2+(z-z_0-vt)^2} = |\mathbf{x}-\mathbf{x}'|, \tag{3.32}$$

$$b(t) \equiv ik - \frac{1}{r(t)}. \tag{3.33}$$

We change the name of the integration variable t' to t as well for convenience. Eqs. (3.25) and (3.29) bring us to an expression for the radial component (perpendicular to the track) of the electric field:

$$\boxed{E_\rho(\mathbf{x},\omega) = -\frac{qv}{4\pi i\epsilon\omega}\int_{t_1}^{t_2}\mathrm{d}t\ e^{i\omega t}\frac{e^{ikr(t)}}{r(t)^3}(z-z_0-vt)\rho\left[b(t)\left(b(t)-\frac{1}{r(t)}\right)+\frac{1}{r(t)^2}\right]} \tag{3.34}$$

We now proceed similarly for E_z. From Eq. (3.9),

$$E_z(\mathbf{x},\omega) = -\partial_z\phi + i\omega A_z = -\partial_z\frac{\nabla\cdot\mathbf{A}}{i\omega\mu\epsilon} + i\omega A_z. \tag{3.35}$$

We can write Eq. (3.35) as the sum of two integrals.

$$\boxed{\begin{aligned} E_z(\mathbf{x},\omega) = {} & \frac{i\omega\mu v q}{4\pi}\int_{t_1}^{t_2} \mathrm{d}t\; e^{i\omega t}\frac{e^{ikr(t)}}{r(t)} \\ & - \frac{qv}{4\pi i\omega\epsilon}\int_{t_1}^{t_2} \mathrm{d}t\; e^{i\omega t}\frac{e^{ikr(t)}}{r(t)^2}\left[b^2(t)\frac{(z-z_0-vt)^2}{r(t)} + \right. \\ & \left. + \frac{(z-z_0-vt)^2}{r(t)^3} - b(t)\left(\frac{(z-z_0-vt)^2}{r(t)^2} - 1\right)\right] \end{aligned}} \tag{3.36}$$

Eqs. (3.34) and (3.36) provide the electric field for a track [3]. In general, they possess no analytical solution and the integrals have to be performed numerically[2].

However, under certain conditions, these integrals can be simplified to obtain equations for relevant physical cases, such as the ZHS formula described below.

3.1.2 The ZHS formula

A practical, simple expression for the field of a single charged particle track moving at constant velocity is given in [4]. We will now rederive it and show the conditions that have to be met to use it. Eqs. (3.34) and (3.36) lead to the ZHS (Zas-Halzen-Stanev) expression under the following assumptions:

1. The observer is in the "far-field" zone, *i.e.*,

$$kr \gg 1. \tag{3.37}$$

2. The Fraunhofer approximation holds. This can be stated as a condition for the phase factor to be approximated as its first order Taylor series.

$$kr = k|\mathbf{x} - \mathbf{x}'| \approx k[R - v(t - t_0)\cos\theta], \tag{3.38}$$

where $R = |\mathbf{x}|$ is the distance from the observation point to a reference point where the track was located at t_0. θ is the angle that forms the track segment with the

[2]Throughout this chapter, the method of integration chosen was to subdivide the integration intervals and apply Simpson's rule until convergence. Although slow, it is a simple way to perform the calculations and compare the exact approach with the approximations and alternative expressions described in the next subsections.

line that connects the reference point and the observer (see sketch in Fig. 3.2). This approximation holds provided the parameter $\eta \ll 1$, defined as

$$\eta(t) = \frac{k[v(t-t_0)]^2}{R}\sin^2\theta \ll 1. \tag{3.39}$$

$\eta(t)$ represents the second order in the Taylor series of Eq. (3.38), and it must be small at any time from t_1 to t_2 (the existing time of the track). A more commonly used and nearly equivalent form of this condition [5] is

$$\eta' = \frac{kL^2}{R}\sin^2\theta \ll 1, \tag{3.40}$$

where $L = v(t_2 - t_1)$ is the length of the track. The condition on η is necessary to ensure that the second and higher order terms for the phases $i(\omega t + kr)$ in Eqs. (3.34) and (3.36) can be ignored even when the first order approximation in Eq. (3.38) is zero, as it occurs for the observation at the Cherenkov angle defined as $\cos\theta_c = 1/\beta n$ with $\beta = v/c$.

3. The distance to the observer in the denominators of Eqs. (3.34) and (3.36) can be approximated as

$$\frac{1}{r(t)} \approx \frac{1}{R} \tag{3.41}$$

over the length L of the track, where R is the distance to a reference point along the track (we will use the midpoint of the track for our algorithm). The error when making this approximation is of the order of L/R.

The far-field condition in Eq. (3.37) allows a simplification of the expressions involving $b(t)$,

$$b \approx ik, \qquad b - \frac{1}{r} \approx b, \qquad b^2 + \frac{1}{r^2} \approx b^2, \tag{3.42}$$

while Eq. (3.41) can be used to approximate some fractions,

$$\frac{\rho}{r(t)} \approx \frac{\rho}{R} = \sin\theta, \tag{3.43}$$

$$\frac{z - z_0 - vt}{r(t)} \approx \frac{z - z_0 - vt_0}{R} = \cos\theta. \tag{3.44}$$

With these approximations the radial component of the field in Eq. (3.34) becomes

$$E_\rho \approx i\frac{qv}{\omega}\frac{1}{4\pi\epsilon}\frac{e^{ikR}}{R}(ik)^2\sin\theta\cos\theta\ e^{i\mathbf{k}\cdot\mathbf{v}t_0}\int_{t_1}^{t_2}\mathrm{d}t\ e^{i(\omega-\mathbf{k}\cdot\mathbf{v})t}. \tag{3.45}$$

Eq. (3.45) can be easily integrated yielding

$$E_\rho = -iq\omega\frac{\mu}{4\pi}v\sin\theta\cos\theta\ \frac{e^{ikR}}{R}\ e^{i\mathbf{k}\cdot\mathbf{v}t_0}\left[\frac{e^{i(\omega-\mathbf{k}\cdot\mathbf{v})t_2}-e^{i(\omega-\mathbf{k}\cdot\mathbf{v})t_1}}{i(\omega-\mathbf{k}\cdot\mathbf{v})}\right]. \tag{3.46}$$

Making $t_0 = t_1$ this becomes the expression for the radial field of the ZHS formula [4], aside from a 2 factor due to a different Fourier transform convention. We can obtain the z component of the field in a similar way from Eq. (3.36) with the following approximation

$$kR \gg 1 \Rightarrow k^2 \gg \frac{k}{R}, \tag{3.47}$$

and then,

$$\begin{aligned} E_z &\approx -i\omega^2\frac{qv}{\omega}\frac{\mu}{4\pi}\frac{e^{ikR}}{R}\ e^{i\mathbf{k}\cdot\mathbf{v}t_0}\cos^2\theta\int_{t_1}^{t_2}\mathrm{d}t\ e^{i(\omega-\mathbf{k}\cdot\mathbf{v})t} \\ &+ iqv\omega\frac{\mu}{4\pi}\frac{e^{ikR}}{R}\ e^{i\mathbf{k}\cdot\mathbf{v}t_0}\int_{t_1}^{t_2}\mathrm{d}t\ e^{i(\omega-\mathbf{k}\cdot\mathbf{v})t}. \end{aligned} \tag{3.48}$$

This can be cast into

$$E_z = iq\omega\frac{\mu}{4\pi}v\sin^2\theta\frac{e^{ikR}}{R}e^{i\mathbf{k}\cdot\mathbf{v}t_0}\int_{t_1}^{t_2}\mathrm{d}t\ e^{i(\omega-\mathbf{k}\cdot\mathbf{v})t}. \tag{3.49}$$

Upon integration, and making $t_0 = t_1$ for simplicity, the ZHS formula for the z component is recovered,

$$E_z = iq\omega\frac{\mu}{4\pi}v\sin^2\theta\frac{e^{ikR}}{R}e^{i\mathbf{k}\cdot\mathbf{v}t_1}\left[\frac{e^{i(\omega-\mathbf{k}\cdot\mathbf{v})t_2}-e^{i(\omega-\mathbf{k}\cdot\mathbf{v})t_1}}{i(\omega-\mathbf{k}\cdot\mathbf{v})}\right]. \tag{3.50}$$

In order to highlight the similarity with the original ZHS formula, we define:

$$\mathbf{v}_\perp = \sin\theta(-\cos\theta\hat{\rho}+\sin\theta\hat{z}). \tag{3.51}$$

Also, we make $\mu = \mu_r\mu_0 = \mu_r/(\epsilon_0 c^2)$. With that,

$$\boxed{\mathbf{E}_{\mathrm{ZHS}}(\mathbf{x},\omega) = \frac{q\mu_r i\omega}{4\pi\epsilon_0 c^2}\frac{e^{ikR}}{R}\mathbf{v}_\perp e^{i\mathbf{k}\cdot\mathbf{v}t_1}\frac{e^{i(\omega-\mathbf{k}\cdot\mathbf{v})t_2}-e^{i(\omega-\mathbf{k}\cdot\mathbf{v})t_1}}{i(\omega-\mathbf{k}\cdot\mathbf{v})}.}, \tag{3.52}$$

Eq. (3.52) is the original ZHS equation[3] but with a different Fourier transform normalization (a factor of 2).

[3]The original ZHS formula made the assumption that $t_0 = 0$, which explains the lack of a phase in [4]. t_0 is relevant when adding the field from different tracks in case they are far away from each other or noticeably separated in time, so we choose to make $t_0 = t_1$ without loss of generality and include it in the formula.

3.1.3 The ZHS algorithm

To calculate the electric field emitted by a distribution of current, such as the one produced in a high energy shower, the ZHS algorithm models the current as a collection of charged particle tracks and then uses the ZHS expression in Eq. (3.52) to obtain the emission from all the tracks. The resulting field is the (vectorial complex) sum of all the contributions.

The ZHS algorithm can be applied to any distribution of current as long as the conditions in Eqs. (3.37), (3.38), (3.39) and (3.41) apply. What happens if the far-field condition (Eq. (3.37)) is fulfilled for a particular track, but not the other ones? Since Maxwell's equations are linear, we can divide the track into several smaller ones so that they are sufficiently small to fulfil Eqs. (3.38), (3.39) and (3.41), and add the contribution to the field of the track of each subtrack. Following this simple procedure, the resulting electric field is a good approximation to the exact formula (Eqs. (3.34) and (3.36)).

Another way of looking at this is realising that the expression for the exact field of Eqs. (3.34) and (3.36) is the electric field expressed as an integral, which can be written as,

$$\mathbf{E}(\mathbf{x},\omega) = \int_{t_0}^{t_n} \mathrm{d}t\ \frac{\mathrm{d}\mathbf{E}}{\mathrm{d}t} = \sum_{i=0}^{n-1} \int_{t_i}^{t_{i+1}} \mathrm{d}t\ \frac{\mathrm{d}\mathbf{E}}{\mathrm{d}t}, \tag{3.53}$$

where we have divided the integral in several fragments, but the actual result remains unchanged (we have made no approximations). If the number of divisions is large enough so that the length of each subtrack is small enough to guarantee the conditions in Eqs. (3.38), (3.39) and (3.41) and if (and only if) the far-field condition is fulfilled, we can write the total field as:

$$\mathbf{E}(\mathbf{x},\omega) \approx \sum_{i=0}^{n-1} \frac{q\mu_r i\omega}{4\pi\epsilon_0 c^2} \frac{e^{ikR_i}}{R_i} \mathbf{v}_{\perp,i} \frac{e^{i\omega t_{i+1} - \mathbf{k}\cdot\mathbf{v}(t_{i+1}-t_i)} - e^{i\omega t_i}}{i(\omega - \mathbf{k}\cdot\mathbf{v}_i)}. \tag{3.54}$$

In short, as long as the far-field condition is fulfilled ($kr \gg 1$), the other two conditions, necessary for the ZHS expression to be valid, can always be fulfilled by dividing the track in small enough subtracks. Then the ZHS formula can be applied to each division and the fields added in order to obtain the total electric field.

The ZHS algorithm has been shown to describe the radiation emitted in several circumstances such as synchrotron [6] and transition radiation [7]. In the following we will compare the results of the ZHS algorithm with those of the exact formulation. We will also show that the ZHS algorithm can reproduce the classical Cherenkov radiation field.

3.1.4 ZHS formula *vs* exact formula: single tracks

In this section we evaluate numerically the exact expressions for the ρ and z components of the electric field in Eqs. (3.34) and (3.36) and compare it to the results from the ZHS formula (Eq. (3.52)) with proper subdivisions of the track (*i.e.* applying the ZHS algorithm).

In Fig. 3.3 we show the results for a single track of 1.2×10^{-3} m of length in ice as a function of the observation frequency. Both calculations are shown, as well as their relative difference. The spectra have been obtained for several observers at different distances (R) measured with respect to the centre of the track and placed at the Cherenkov angle.

The condition $kR \gg 1$ in ice with refractive index $n = 1.78$ can be cast as

$$kR \sim 3.7 \left(\frac{\nu}{100 \text{ MHz}}\right) \left(\frac{R}{1 \text{ m}}\right) \gg 1. \tag{3.55}$$

For observers at distances $R = 100$, 10, 1 and 0.1 m from the particle track, the condition expressed by Eq. (3.55) is fulfilled as long as $\nu \gtrsim 1$, 10, 100 MHz and 1 GHz, respectively. In Fig. 3.3 we show that when this criterion is met there is a relative difference of less than $\sim 2\%$ between the ZHS and exact calculations. The accuracy can be orders of magnitude better. For instance, if $kR > 37$ is enforced, the corresponding relative difference is below $\sim 0.01\%$. This condition is satisfied for $R > 10$ m and $\nu \gtrsim 100$ MHz, which corresponds to a range of frequencies and distances tipically encountered in experiments that search for neutrino-induced radio transients.

We must remark that these conclusions apply as long as $kR \gg 1$, regardless of the length L of the track and provided it is divided in sufficient small subtracks. This can be seen in Fig. 3.4 for a track of length $L = 1.2$ m. The same range of validity as in Fig. 3.3 is obtained.

If we fix the frequency, the condition in Eq. (3.55) indicates that the ZHS algorithm will be a good approximation only at sufficiently large distances R to the track. This is illustrated in Fig. 3.5 for a track of length $L = 1.2$ m. The Fourier components at frequencies of $\nu = 10$, 100 MHz and 1 GHz are in agreement (relative difference $\lesssim 6\%$) with the exact calculation, respectively, at $R \gtrsim 10$, 1, and 0.1 m, as expected. A typical distance between antennas in experiments such as the Askaryan Radio Array (ARA) [8] is $\sim$ 10-100 m and the length of a shower in ice is $\sim$ few m, so we expect the ZHS algorithm to be accurate enough in most experimental situations.

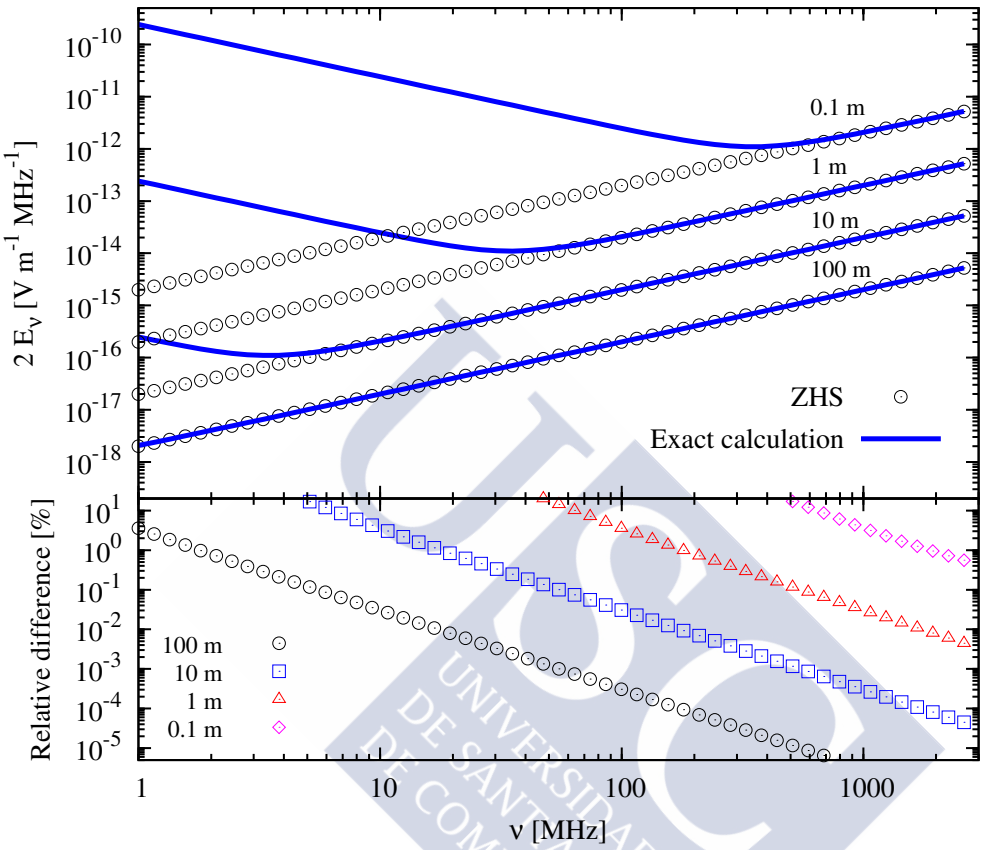

Figure 3.3: Top: Fourier components of the electric field modulus for a single particle track as obtained with the exact calculation of Eqs. (3.34) and (3.36) (solid lines) and with the ZHS algorithm of Eq. (3.52) (open symbols). The length of the track is $L = 1.2\ 10^{-3}$ m, the speed is $v \approx c$ and the field is shown for observers at distances (from top to bottom lines) $R = 0.1$ m, 1 m, 10 m and 100 m, with respect to the center of the track, and placed at the Cherenkov angle in ice ($n = 1.78$). Bottom: Relative difference (in percentage) between the exact solution and that obtained with the ZHS algorithm for the same distances.

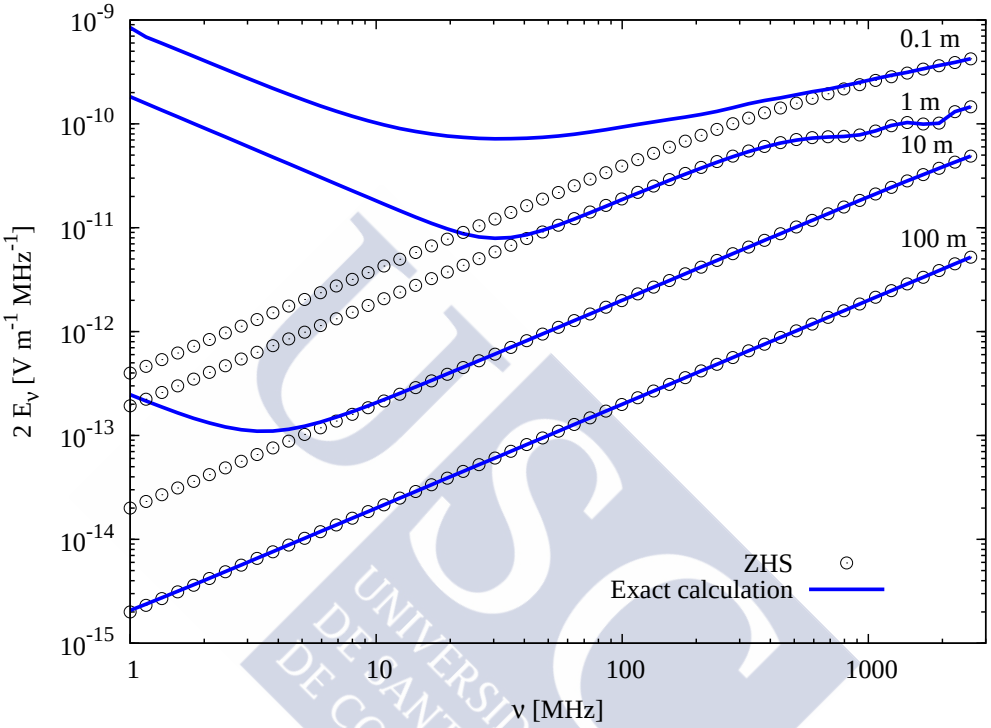

Figure 3.4: Fourier components of the electric field modulus for a single particle track as obtained with the exact calculation of Eqs. (3.34) and (3.36) (solid lines) and with the ZHS algorithm of Eq. (3.52) (open symbols). The length of the track is $L = 1.2$ m, the speed is $v \approx c$ and the field is shown for observers at distances (from top to bottom lines) $R = 0.1$ m, 1 m, 10 m and 100 m, with respect to the center of the track, and placed at the Cherenkov angle in ice.

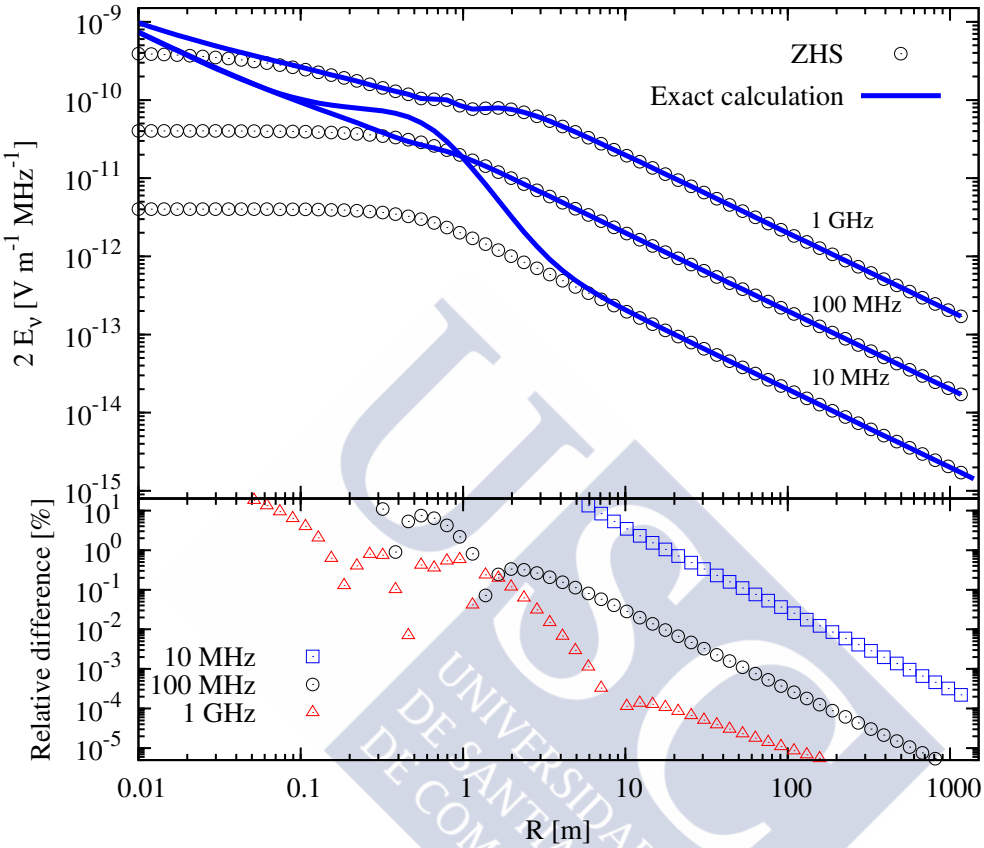

Figure 3.5: Top: Fourier components of the electric field modulus at $\nu = 1$ GHz, 100 MHz and 10 MHz (from top to bottom lines) for a single particle track as a function of the distance to the track, as obtained with the exact calculation (Eqs. (3.34) and (3.36), solid lines) and with the ZHS algorithm (Eq. (3.52), open symbols). The length of the track is $L = 1.2$ m, the speed is $v \approx c$ and the observers are placed at the Cherenkov angle. Bottom: Relative difference (in percentage) between the exact solution and that obtained with the ZHS algorithm for the same frequencies.

Behaviour of the field with frequency

As we show in Fig. 3.3, the exact solution for the modulus of the electric field scales linearly with frequency as long as $kR \gg 1$, in agreement with the ZHS formula. For an observer close to the Cherenkov angle, the factor $(\omega - \mathbf{k}\cdot\mathbf{v}) \ll 1$ and the term in brackets in Eq. (3.52) can be approximated by

$$\left[\frac{e^{i(\omega-\mathbf{k}\cdot\mathbf{v})t_2} - e^{i(\omega-\mathbf{k}\cdot\mathbf{v})t_1}}{i(\omega-\mathbf{k}\cdot\mathbf{v})}\right] \approx \frac{1 + i(\omega-\mathbf{k}\cdot\mathbf{v})t_2 - 1 - i(\omega-\mathbf{k}\cdot\mathbf{v})t_1}{i(\omega-\mathbf{k}\cdot\mathbf{v})} = t_2 - t_1, \tag{3.56}$$

making the dependence of the field with the frequency ω apparent:

$$\mathbf{E}_{\rm ZHS}(\theta = \theta_c, \omega) = \frac{q\mu_r i}{4\pi\epsilon_0 c^2}\frac{e^{ikR}}{R}\omega(t_2 - t_1). \tag{3.57}$$

In an idealised medium with constant permittivity if the field grows linearly with frequency the power radiated per unit area is

$$\frac{{\rm d}\langle P\rangle}{{\rm d}t} = \frac{1}{\Delta t}\int_{-\infty}^{\infty}{\rm d}\nu\sqrt{\frac{\epsilon(\nu)}{\mu(\nu)}}|\mathbf{E}(\nu)|^2, \tag{3.58}$$

where Δt is the total time when the radiation exists, and is infinite at the Cherenkov angle. In a real medium, however, ϵ and μ depend on ω and this dependence controls the apparent ultraviolet divergence. In particular, absorption at high frequencies will tame the growth with frequency of the electric field.

When $kR < 1$ the field behaves with frequency as ω^{-1}, as can be seen in Fig. 3.3. In the model of a charged particle at rest for $t \leq t_1$, moving with a constant speed v between t_1 and t_2 and becoming again at rest for $t \geq t_2$, the Coulomb field dominates at small distances to the track and/or low frequencies. Let us consider an atom 1 with total charge q_1 and an electron of charge q that emerges from it at a time t_1. Neglecting the recoil, the Coulomb electric field of the atom 1 is

$$\mathbf{E}_1(\mathbf{x}, t) = \frac{\hat{r}_1}{4\pi\epsilon r_1^2}(q_1 - q\Theta(t - t_{\rm obs,1})). \tag{3.59}$$

The step function accounts for the loss of the electron. We have defined $\mathbf{r_1} = \mathbf{x} - \mathbf{x}_1$, where $\mathbf{x}_1$ is the position of the atom 1 and $\mathbf{x}$ is the position of the observer. Since the signal of the Coulomb field travels through the medium at the speed of light, $t_{\rm obs,1}$ is the time when the observer realises a change in the Coulomb field of the atom,

$$t_{\rm obs,1} = t_1 + \frac{c}{n}r_1 \tag{3.60}$$

The electron is abosrbed in another atom 2 at time t_2 and we can similarly write the Coulomb field for the atom 2 as

$$\mathbf{E}_2(\mathbf{x},t) = \frac{\hat{r}_2}{4\pi\epsilon r_2^2}(q_2 + q\Theta(t - t_{\text{obs},2})). \tag{3.61}$$

Eqs. (3.59) and (3.61) must be transformed to the frequency domain. The transform of a Heaviside function with our definition (Eq. (3.5)) is

$$\text{FT}[\Theta(t)] = \frac{i}{\omega} + \frac{1}{2}\delta(\omega), \tag{3.62}$$

while making a temporal translation we add a phase to the transform as follows:

$$\text{FT}[\Theta(t - t_{\text{obs}})] = e^{i\omega t_{\text{obs}}}\left(\frac{i}{\omega} + \frac{1}{2}\delta(\omega)\right). \tag{3.63}$$

With the aid of Eq. (3.63), Eqs. (3.59) and (3.61) are readily transformed into the frequency domain,

$$\mathbf{E}_1(\mathbf{x},\omega) = \frac{\hat{r}_1}{4\pi\epsilon r_1^2}\left(2\pi q_1\delta(\omega) - e^{i\omega t_{\text{obs},1}}\frac{iq}{\omega} - e^{i\omega t_{\text{obs},1}}\frac{q}{2}\delta(\omega)\right), \tag{3.64}$$

$$\mathbf{E}_2(\mathbf{x},\omega) = \frac{\hat{r}_2}{4\pi\epsilon r_2^2}\left(2\pi q_2\delta(\omega) + e^{i\omega t_{\text{obs},2}}\frac{iq}{\omega} + e^{i\omega t_{\text{obs},2}}\frac{q}{2}\delta(\omega)\right). \tag{3.65}$$

The δ-functions only have effect at zero frequency, so we might as well ignore them. We see then that the fields have a ω^{-1} frequency dependence. Adding the two fields,

$$\mathbf{E}_1(\mathbf{x},\omega) + \mathbf{E}_2(\mathbf{x},\omega) = \frac{q}{4\pi\epsilon}\frac{i}{\omega}\left[\frac{\hat{r}_2}{r_2^2}e^{i\omega t_{\text{obs},2}} - \frac{\hat{r}_1}{r_1^2}e^{i\omega t_{\text{obs},1}}\right]. \tag{3.66}$$

Eq. (3.66) explains the behaviour of the field in the low-frequency limit. It is important to remark that it is not a radiation field, and therefore cannot be reproduced by the ZHS algorithm.

One might be tempted to reason that Eq. (3.58) implies that the ω^{-1} dependence must change at low frequency so that the mean power is finite. However, Eq. (3.58) is the integral of the Pointyng vector, that is zero for a static field (the magnetic field $\mathbf{B}$ is zero), and therefore the ω^{-1} dependence poses no problem. Besides, the electric field in the time domain is bound, since we started from a bound field in Eqs. (3.59) and (3.61).

Behaviour of the field with distance

In Fig. 3.5 we show the dependence of the Fourier components of the field modulus with distance. At sufficiently large distances to the track the electric field behaves as $1/R$ for all the frequencies shown, as expected by conventional radiation theory [2].

If the observer is placed at very small distances compared to the length of the track, the situation resembles that of an infinite track, which we will address in Section 3.2. The field behaves as $1/\sqrt{R}$ at distances much smaller than the length of the track $R \ll L$ provided the frequency is large enough to satisfy

$$|u\rho| = \rho\frac{\omega}{v}\sqrt{|n^2\beta^2 - 1|} \gg 1, \tag{3.67}$$

with ρ the radial distance to the track. We will derive this condition in Section 3.2, see Eqs. (3.96) and (3.97). This behaviour with $1/\sqrt{R}$ be seen at $\nu = 1$ GHz for $R \lesssim 0.5$ m.

When $|u\rho| \ll 1$, at small distances and sufficiently low frequencies, the field becomes proportional to $1/R$ and independent of the frequency, as we will show in Section 3.2, see Eq. (3.99). This feature can be appreciated in Fig. 3.5, at distances below 0.1 m and frequencies 10 and 100 MHz.

The ZHS algorithm reproduces the exact calculation provided $kR \gg 1$, reproducing both the $1/R$ and $1/\sqrt{R}$ behaviour depending on the frequency of observation.

3.2 Exact, ZHS formulations and classical radiation fields

The exact formulas Eqs. (3.34) and (3.36) provide the field at all frequencies and distances. The radiation field is given by the ZHS formula (3.52), which is what is needed for practical applications. Now, we can turn our attention to classical problems with known solutions. In the following, we will derive the classical formula for Cherenkov radiation (Tamm problem [9]) using as starting point both the exact and ZHS formalisms.

3.2.1 Cherenkov radiation

Following Frank and Tamm [9] and Afanasiev [10] we define Cherenkov radiation as the radiation of a charged particle moving in a medium with constant velocity greater than the speed of light in the medium. The particle emits radiation with the shape of a conical wavefront, analogously to a body moving faster than the speed of sound in a medium.

This conflicts with the old adagio "radiation from a point charge is produced by acceleration", but we must remember that this is only strictly true if we add "in a vacuum". An intuitive way of visualising the problem is not to think of the particle as the creator the radiation, but the medium. It is the medium that slows the speed of the electromagnetic wave and increases the field on the surface of the cone. In a sense, the medium is the one that takes the field of the particle and "transforms" it into radiation. However, and strictly speaking, both the particle *and* the medium compose the radiating system.

The most common expression for Cherenkov radiation is derived for an infinite track. Our exact expression from Eqs. (3.34) and (3.36) should contain it as a particular case if we extend the integration range to infinity (mathematical subtleties aside). To show this, we will first obtain an alternative formula for Cherenkov radiation of an infinite track based on [11] and compare it to what is obtained with the exact and ZHS formulas.

It is possible to start with our exact formula and transform it extending the integration path to infinity. However, the steps to achieve this are not trivial. We will instead take another route and operate in the Fourier momentum domain $(\mathbf{k}, \omega)$, as opposed to the $(\mathbf{x}, \omega)$ domain we have been using.

Maxwell's equations in $(\mathbf{x}, \omega)$ space can be written as

$$(\nabla^2 + \mu\epsilon\omega^2)\mathbf{A}(\mathbf{x}, \omega) = -\mu\mathbf{J}(\mathbf{x}, \omega), \tag{3.68}$$

$$(\nabla^2 + \mu\epsilon\omega^2)\phi(\mathbf{x}, \omega) = -\frac{\rho(\mathbf{x}, \omega)}{\epsilon}, \tag{3.69}$$

where $\mathbf{J}$ and ρ are the free current and free charge associated to the track, respectively. Transforming Eqs. (3.68) and (3.69) into the $(\mathbf{k}, \omega)$ space we get

$$(|\mathbf{k}|^2 - \mu\epsilon\omega^2)\mathbf{A}(\mathbf{k}, \omega) = \mu\mathbf{J}(\mathbf{k}, \omega), \tag{3.70}$$

$$(|\mathbf{k}|^2 - \mu\epsilon\omega^2)\phi(\mathbf{k}, \omega) = \frac{\rho(\mathbf{k}, \omega)}{\epsilon}. \tag{3.71}$$

In this space, Maxwell's differential equations have turned into simple algebraic equations that allow us to obtain the potentials immediately, provided we know the charges and currents. Charge distribution and current for an infinite track along the z-axis in the time domain are readily known,

$$\rho(\mathbf{x}, t) = q\delta^{(3)}(z\hat{\mathbf{z}} - vt\hat{\mathbf{z}}), \tag{3.72}$$

$$\mathbf{J}(\mathbf{x}, t) = v\rho\hat{\mathbf{z}}. \tag{3.73}$$

We can transform Eq. (3.72) into the $(\mathbf{k},\omega)$ space and we will have the transform of Eq. (3.73) automatically,

$$\begin{aligned}\rho(\omega,\mathbf{k}) &= \int \mathrm{d}^3x\ \mathrm{d}t\ e^{i(\omega t-\mathbf{k}\cdot\mathbf{x})}q\delta(x)\delta(y)\delta(z-vt)\\ &= q\int \mathrm{d}t\ e^{it(\omega-k_zv)} = 2\pi q\delta(\omega-k_zv).\end{aligned} \tag{3.74}$$

From Eq. (3.71), the scalar potential then reads:

$$\phi(\mathbf{k},\omega) = \frac{2\pi q}{\epsilon(\omega)}\frac{\delta(k_zv-\omega)}{|\mathbf{k}|^2-\mu\epsilon\omega^2}. \tag{3.75}$$

The Lorenz gauge condition (Eq. (3.12)) when transformed to $(\mathbf{k},\omega)$ space allows us to obtain the vector potential $\mathbf{A}$ from the scalar potential ϕ. In this case, only the z component is non-zero,

$$A_z(\mathbf{k},\omega) = \mu\epsilon v\ \phi(\mathbf{k},\omega); \qquad A_x = A_y = 0. \tag{3.76}$$

Since both potentials are proportional to each other, we only need to transform back to the frequency domain one of them. Take, for instance, Eq. (3.75).

$$\begin{aligned}\phi(\mathbf{x},\omega) &= \frac{1}{(2\pi)^3}\int \mathrm{d}^3k\ e^{i\mathbf{k}\cdot\mathbf{x}}\frac{2\pi q}{\epsilon}\frac{\delta(\omega-k_zv)}{|\mathbf{k}|^2-\mu\epsilon\omega^2}\\ &= \frac{1}{(2\pi)^2}\int \mathrm{d}k_x\mathrm{d}k_y\ e^{i(k_xx+k_yy+\omega z/v)}\frac{q}{v\epsilon}\frac{1}{|\mathbf{k}|^2-\mu\epsilon\omega^2}\\ &= \frac{1}{(2\pi)^2}\frac{q}{v\epsilon}e^{i\frac{\omega}{v}z}\int k_\rho\mathrm{d}k_\rho\mathrm{d}k_\varphi\frac{e^{ik_\rho\rho\cos(k_\varphi-\varphi)}}{k_\rho^2+(\frac{\omega}{v})^2(1-\mu\epsilon v^2)},\end{aligned} \tag{3.77}$$

where we have used that

$$\delta(ax-x_0) = \frac{1}{|a|}\delta(x-x_0/a) \tag{3.78}$$

and changed $\mathbf{k}$ to polar coordinates (k_ρ,k_φ). The integral in k_φ can be done using the following integral representation for the first species Bessel functions [12].

$$J_n(z) = \frac{1}{2\pi i^n}\int_0^{2\pi}\mathrm{d}\varphi\ e^{iz\cos\varphi}e^{in\varphi}. \tag{3.79}$$

For $n=0$,

$$J_0(z) = \frac{1}{2\pi}\int_0^{2\pi}\mathrm{d}\varphi\ e^{iz\cos\varphi} = \frac{1}{2\pi}\int_0^{2\pi}\mathrm{d}\varphi\ e^{iz\cos(\varphi-\varphi_0)}. \tag{3.80}$$

Identifying $\varphi \to k_\varphi$ and $\varphi_0 \to \varphi$ in Eq. (3.77) we can introduce the definition of J_0 in Eq. (3.77) and obtain

$$\phi(\mathbf{x},\omega) = \frac{1}{2\pi}\frac{q}{v\epsilon}e^{i\frac{\omega}{v}z}\int k_\rho \mathrm{d}k_\rho \frac{J_0(k_\rho\rho)}{k_\rho^2 + (\frac{\omega}{v})^2(1-\mu\epsilon v^2)}. \tag{3.81}$$

From [13] and [14], we obtain the following integral,

$$\int_0^\infty \frac{k\ \mathrm{d}k}{k^2+u^2}J_0(k\rho) = K_0(u\rho), \tag{3.82}$$

where K_0 is the modified Bessel function of the second kind. This is the same integral as in Eq. (3.81) with the definition

$$u^2 = \frac{\omega^2}{v^2}(1-\mu\epsilon v^2) = \frac{\omega^2}{v^2}(1-n^2\beta^2), \tag{3.83}$$

and $u = \sqrt{u^2}$ is in general a complex number such as Re[z] > 0. Let us assume that ϵ and μ are real (the medium has no absorption), and write the speed of light in the medium as

$$c_n = \frac{c}{n} = \frac{1}{\sqrt{\mu\epsilon}}, \tag{3.84}$$

then, we have two different cases depending on whether the argument of the Bessel function $K_0(u\rho)$ is real or imaginary:

- If $u^2 > 0$, which corresponds to the case $v/c_n = n\beta < 1$, *i.e.* subluminal speed, it does not matter which sign we take for $\sqrt{u^2}$, since $u\rho$ is real and $K_0(x) = K_0(-x)$ for real x, so we take the positive sign:

  $$u = \frac{\omega}{v}\sqrt{1-n^2\beta^2}. \tag{3.85}$$

- If $u^2 < 0$, which corresponds to the superluminal case when $v/c_n = n\beta > 1$, the poles of the integrand in Eq. (3.82) lie on the real axis and the value of the integral depends on the contour we use (see [14]). The Bessel function we use can be either $K_0(ix)$ or $K_0(-ix)$, with real x. It also happens that $K_0(ix) = K_0^*(-ix)$. In our case, we will choose

  $$u = -i\frac{\omega}{v}|\sqrt{n^2\beta^2-1}|, \tag{3.86}$$

  because this is the choice that makes the phase of the field consistent with our exact solution for a finite track (see Fig. 3.7). Using the other contour for the integration could yield a very different function in time domain that violates causality, although the modulus in frequency domain remains unaffected.

Eqs. (3.76), (3.81) and (3.82) result in the following potentials,

$$\phi(\rho, z, \omega) = \frac{q}{2\pi\epsilon v} e^{i\frac{\omega}{v}z} K_0(u\rho), \tag{3.87}$$

$$A_z(\rho, z, \omega) = \frac{\mu q}{2\pi} e^{i\frac{\omega}{v}z} K_0(u\rho). \tag{3.88}$$

We must perform the derivatives in Eq. (3.9) to calculate the fields. In order to do that, we can use the following property of the K_0,

$$\frac{\mathrm{d}K_0(x)}{\mathrm{d}x} = -K_1(x), \tag{3.89}$$

$$E_z = -\partial_z\phi + i\omega A_z, \tag{3.90}$$

$$-\partial_z\phi = -\frac{q}{2\pi\epsilon v} i\frac{\omega}{v} e^{i\frac{\omega}{v}z} K_0(u\rho), \tag{3.91}$$

$$i\omega A_z = \frac{i\omega\mu q}{2\pi} e^{i\frac{\omega}{v}z} K_0(u\rho), \tag{3.92}$$

$$E_\rho = -\partial_\rho\phi. \tag{3.93}$$

These equations allow us to write the fields as:

$$\boxed{E_z(\rho, z, \omega) = \frac{i\omega\mu q}{2\pi} e^{i\frac{\omega}{v}z} \left(1 - \frac{1}{\mu\epsilon v^2}\right) K_0(u\rho)} \tag{3.94}$$

$$\boxed{E_\rho(\rho, z, \omega) = \frac{q}{2\pi\epsilon v} e^{i\frac{\omega}{v}z} u K_1(u\rho)} \tag{3.95}$$

Keeping in mind that u in Eqs. (3.94) and (3.95) is defined, for real μ and ϵ, as

$$n\beta < 1 \;\Rightarrow\; u = \frac{\omega}{v}\left|\sqrt{1 - n^2\beta^2}\right|, \tag{3.96}$$

$$n\beta > 1 \;\Rightarrow\; u = -i\frac{\omega}{v}\left|\sqrt{n^2\beta^2 - 1}\right|. \tag{3.97}$$

It follows that if the particle travels below the speed of light in the medium, the argument $u\rho$ of the Bessel functions is real and the particle does not radiate, as shown in [10], because the amplitude of the electric field decreases exponentially for $\rho \to \infty$ (see below in Eq. (3.100)). On the contrary, if the speed of the particle is larger than the speed of light, $u\rho$ is imaginary and the particle radiates (see below in Eqs. (3.100), (3.101) and (3.102)). The latter case corresponds to pure Cherenkov radiation [10].

With the help of the asymptotic forms for the Bessel functions found in [12], we can obtain the limits for Eqs. (3.94) and (3.95) when $|u\rho| \ll 1$, that is, for small distances to the track compared to the radiation wavelength, and for $|u\rho| \gg 1$.

- If $|u\rho| \ll 1$, the K_1 function dominates over the K_0 and only the radial component of the field (E_ρ) matters. The limit of the $K_1(x)$ when $x \ll 1$ is

$$K_1(x) \approx \frac{1}{x}, \tag{3.98}$$

so the asymptotic field in Eq. (3.95) has a simple form:

$$|E_\rho|(|u\rho| \to 0) \approx \frac{|q|}{2\pi\epsilon v}\frac{1}{\rho}, \tag{3.99}$$

where a $1/\rho$ dependence with distance is obtained, as well as no dependence with frequency.

- If $|u\rho| \gg 1$, and remembering that when $v > c/n$, the argument u is imaginary, the asymptotic expression for the field is [12],

$$K_0(z) \sim K_1(z) \sim \sqrt{\frac{\pi}{2z}}e^{-z}, \qquad |\arg z| < \frac{3}{2}\pi, \tag{3.100}$$

and the fields in Eqs. (3.94) and (3.95) can be written as

$$|E_\rho|(u\rho \to -i\infty) \approx \frac{|q|}{2\pi\epsilon\nu}\sqrt{\frac{\pi}{2}}\left|(n^2\beta^2-1)^{1/4}\sqrt{\frac{\omega}{v\rho}}\right|, \tag{3.101}$$

$$|E_z|(u\rho \to -i\infty) \approx \frac{\mu|q|}{2\pi}\left(1-\frac{1}{\mu\epsilon v^2}\right)\sqrt{\frac{\pi}{2}}\left|(n^2\beta^2-1)^{-1/4}\sqrt{\frac{v\omega}{\rho}}\right|. \tag{3.102}$$

In this case, the field is proportional to $\sqrt{\omega/\rho}$. This is in agreement with [5], where the same behaviour is deduced using simple arguments of energy conservation through a cylindrical surface surrounding the infinite track.

In Fig. 3.6 the Fourier components of the modulus of the electric field for an infinite track as obtained from Eqs. (3.94) and (3.95) are shown as a function of ρ, the radial distance to the track, and for several frequencies. The particle speed is $v \approx c > c/n$, travelling in homogeneous ice with refractive index $n = 1.78$. Under these circumstances the quantity $|u\rho|$ can be approximated as

$$|u\rho| \approx 3\left(\frac{\nu}{100\ \text{MHz}}\right)\left(\frac{\rho}{1\ \text{m}}\right). \tag{3.103}$$

At large distances to the track when $|u\rho| \gg 1$ the fields in Fig. 3.6 scale as $1/\sqrt{\rho}$ and with frequency as $\sqrt{\omega}$, in agreement with the asymptotic field components in Eqs. (3.101) and

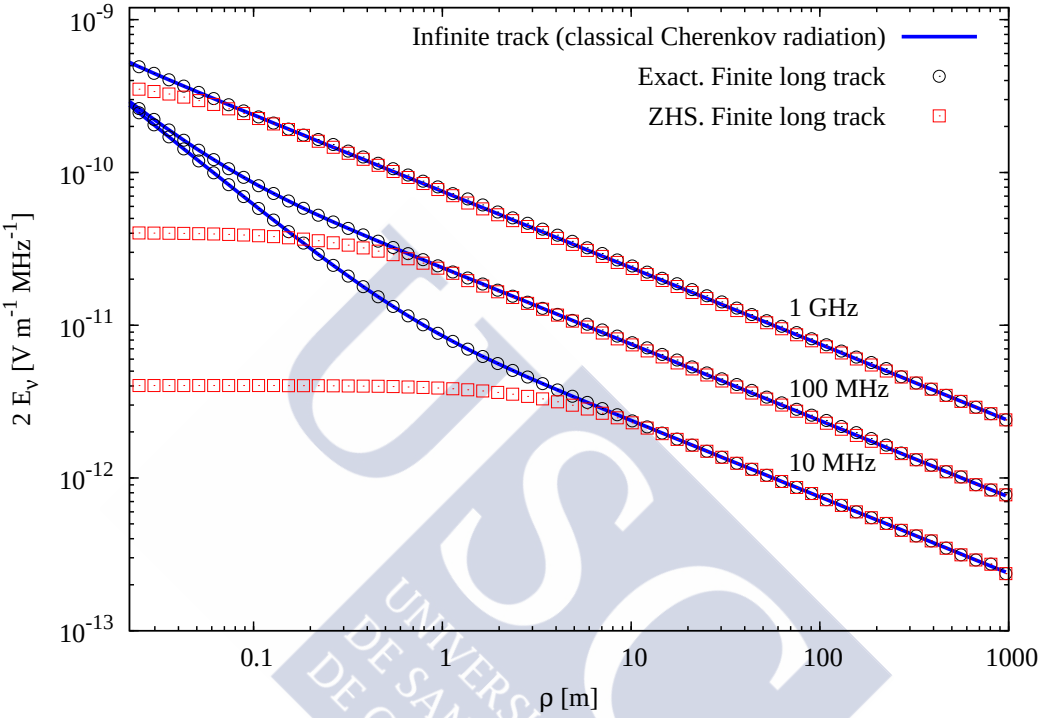

Figure 3.6: Fourier components of the electric field modulus as a function of distance to the particle track for an infinite track travelling at $v \approx c$ in ice ($n = 1.78$) as obtained from the classical equations of Cherenkov radiation Eqs. (3.94) and (3.95), (solid line) and for a (long) track of length $L = 1200$ m as obtained with the exact formulas [Eqs. (3.34) and (3.36)] (open circles) and with the ZHS algorithm [Eq. (3.52)] (open squares). From top to bottom, the observation frequencies are 1 GHz, 100 MHz and 10 MHz. The $1/\rho$ and $1/\sqrt{\rho}$ regimes are apparent depending on frequency and distance.

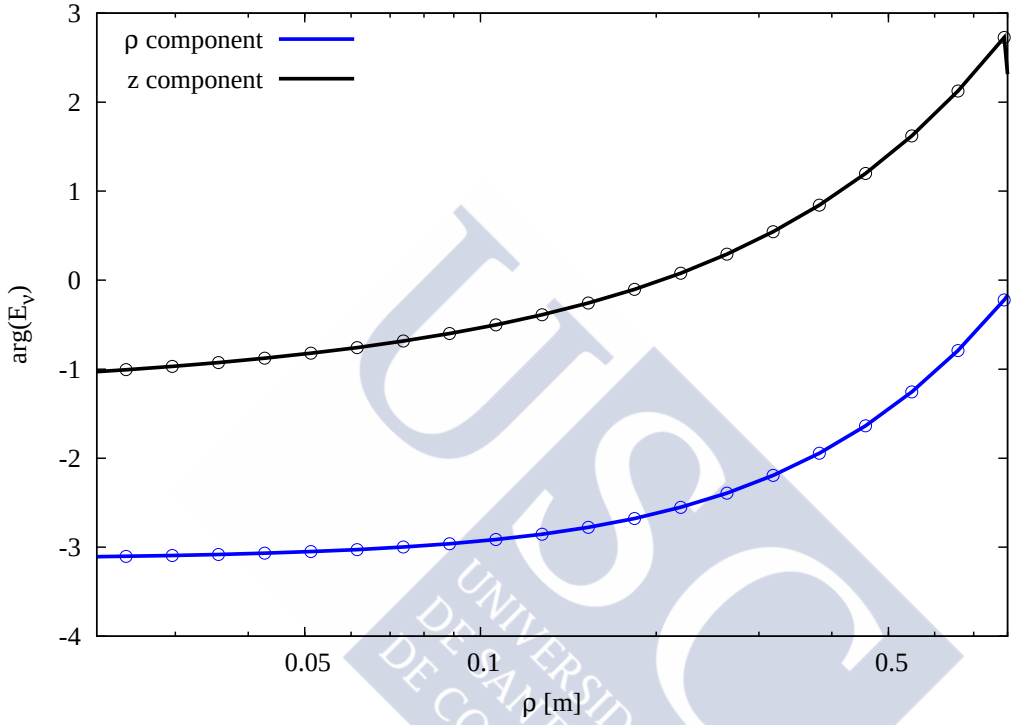

Figure 3.7: Phase of the Fourier transform of the ρ and z components of the electric field as a function of distance to the particle track for an infinite track travelled at $v \approx c$ in ice ($n = 1.78$) as obtained from the classical equations of Cherenkov radiation Eqs. (3.94) and (3.95) (solid line) and for a track of length $L = 1200$ m as obtained with the exact formulas [Eqs. (3.34) and (3.36)] (open circles). The observation frequency is 100 MHz. The phases of both approaches match.

(3.102). The scaling of the field with $\sqrt{\omega/\rho}$ occurs $\rho > 0.1$, 1 and 10 m for frequencies 1 GHz, 100 MHz and 10 MHz respectively, in agreement with Eq. (3.103), as can be seen in Fig. 3.6.

As the distance to the track decreases and the condition $|u\rho| \ll 1$ starts to be valid, the field behaves as $1/\rho$ and does not depend on frequency, as expected from Eq. (3.99). As it can be clearly seen in Fig. 3.6, the transition from the $1/\rho$ behaviour to $\sqrt{\omega/\rho}$ occurs at a distance that depends on frequency because $|u\rho|$ involves frequency (Eq. (3.103)). For instance, at distances $\rho < 0.01$ m the condition $|u\rho| \ll 1$ applies for both $\nu = 100$ and 10 MHz. The Fourier component of the field scales with $1/\rho$ and has the same value for the two frequencies as seen in Fig. 3.6, while this is not the case for a frequency of $\nu = 1$ GHz.

Also shown in Fig. 3.6 is the modulus of the field as obtained with the exact calculation (Eqs. (3.34) and (3.36)) and with the ZHS formula (Eq. (3.52)) for a finite but very long track. The exact calculation agrees perfectly well with the result of Eqs. (3.94) and (3.95), while the ZHS formula reproduces the exact calculation and classical formulas for Cherenkov radiation as long as $k\rho \gg 1$.

In Fig. 3.7 we show the phases of the Fourier transform of the ρ and z components of the field at 100 MHz for a track similar to that of Fig. 3.6, calculated with both the infinite track expression and the exact field for a long track. The z coordinate is fixed, so the phase comes from the argument of the Bessel function in Eqs. (3.94) and (3.95). Since the two approaches result in the same phases, it means we have chosen the right sign for u. Otherwise, the fields would be each other's conjugate.

In Fig. 3.8 the modulus of the electric field for a charged particle in an infinite track is shown as a function of frequency for an observer at a fixed radial distance. At large enough frequencies so that the condition $|u\rho| \gg 1$ applies, the field scales as $\sqrt{\omega}$ as expected from Eqs. (3.101) and (3.102), while it is constant with frequency for small enough frequencies so that $|u\rho| \ll 1$ as predicted from Eq. (3.99). More quantitatively, since the observer in Fig. 3.8 is located at $\rho \sim 10$ m, the field should behave as $\sqrt{\omega}$ for $\nu \gtrsim 10$ MHz. This is approximately the case in Fig. 3.8.

The result of the exact calculation for a track of length $L = 1.2$ km is also shown in Fig. 3.8. The agreement between Eqs. (3.94) and (3.95) and the exact formalism is excellent. The ZHS formalism (Eq. (3.52)) agrees with the exact formalism (Eqs. (3.34) and (3.36)) and with the classical equations of Cherenkov radiation (Eqs. (3.94) and (3.95)) as long as $k\rho \gg 1$. As can be appreciated in Fig. 3.8, the exact results and the classical Cherenkov formulas only differ, as expected, for wavelengths larger than the length of the (long but still finite) track —frequencies typically below $\nu_0 \sim (c/n)/\lambda$ with $\lambda \sim L = 1.2$

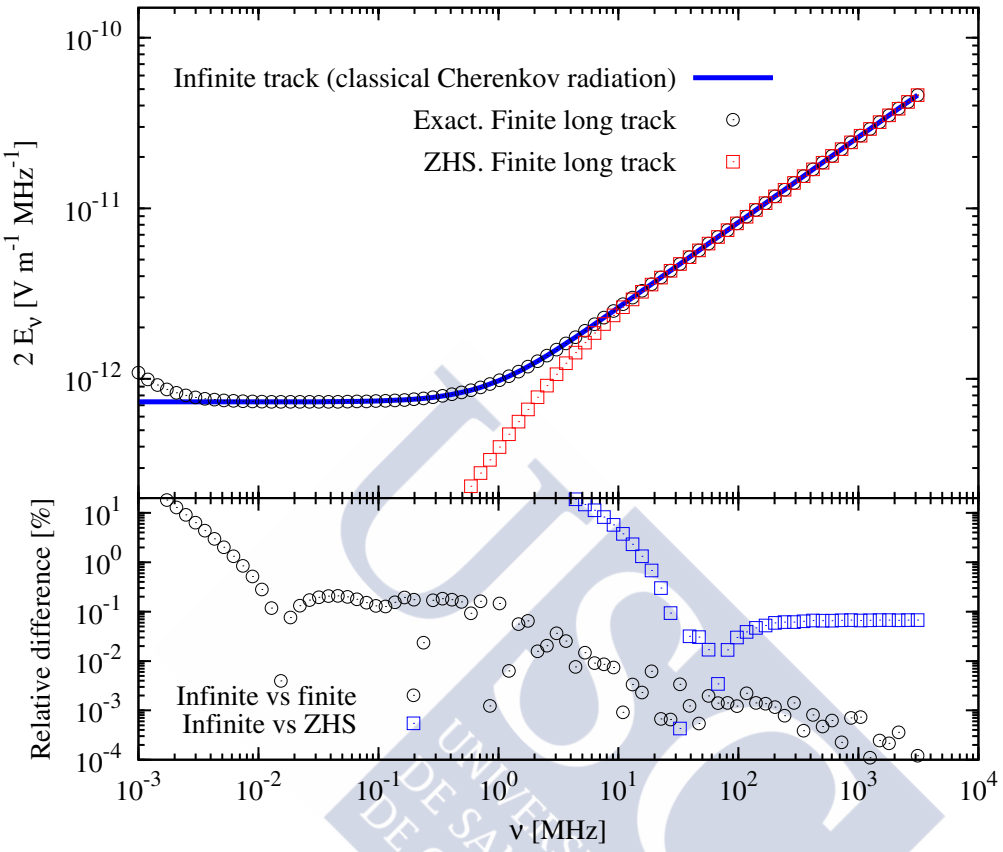

Figure 3.8: Top: Fourier components of the electric field modulus as a function of frequency for an infinite track travelling at $v \approx c$ in ice ($n = 1.78$) as obtained from the classical equations of Cherenkov radiation Eqs. (3.94) and (3.95) (solid line) and for a track of length $L = 1200$ m as calculated from Eqs. (3.34) and (3.36) (open circles). The observer is placed at a lateral distance to the infinite track $\rho = 8.27$ m. Also shown is the modulus of the field for the same finite track ($L = 1200$ m) as obtained with the ZHS algorithm, Eq. (3.52) (open squares). At high frequencies, the field behaves with $\sqrt{\omega}$ (see text for explanations). Bottom: Relative difference (in percentage) between the solution for an infinite track and the exact solution for a finite long track (open circles) and between the solution for an infinite track and that obtained with the ZHS algorithm (open squares).

km, which gives $\nu \lesssim 0.1$ MHz.

The comparisons in Figs. 3.6 and 3.8 clearly demonstrate that the ZHS algorithm can account for the classical Cherenkov radiation.

3.2.2 The Frank-Tamm formula

The Frank-Tamm formula is an expression for the energy lost per unit length and unit frequency ($\mathrm{d}^2E_{\rm rad}/\mathrm{d}z\ \mathrm{d}\omega$) by a charged particle moving along a track when it emits Cherenkov radiation. We will derive it in a similar way to [10] and [2], using Eqs. (3.88) and (3.94). We start with the Poynting vector integrated on a surface ($\mathbf{a}$) and time, which gives the energy carried to infinity by the electromagnetic field,

$$\begin{aligned} E_{\rm rad} &= \int (\mathbf{E}(t)\times\mathbf{H}(t))_{\rm rad}\cdot \mathrm{d}\mathbf{a}\ \mathrm{d}t = \frac{1}{2\pi}\int e^{-i\omega t}(\mathbf{E}(\omega)\times\mathbf{H}(t))_{\rm rad}\cdot \mathrm{d}\mathbf{a}\ \mathrm{d}t\ \mathrm{d}\omega \\ &= \frac{1}{2\pi}\int (\mathbf{E}(\omega)\times\mathbf{H}(-\omega))_{\rm rad}\cdot \mathrm{d}\mathbf{a}\ \mathrm{d}\omega \\ &= \frac{1}{2\pi}\int (\mathbf{E}(\omega)\times\mathbf{H}^*(\omega))_{\rm rad}\cdot \mathrm{d}\mathbf{a}\ \mathrm{d}\omega, \end{aligned} \tag{3.104}$$

where we have used the definition of the Fourier transform and the fact that $\mathbf{H}(-\omega) = \mathbf{H}^*(\omega)$, since $\mathbf{H}(t)$ is real. Let us calculate the magnetic field from the vector potential obtained in Eq. (3.88).

$$\mathbf{B} = \nabla\times\mathbf{A} = \nabla\times A\ \hat{\mathbf{z}} = -\frac{\partial A_z}{\partial\rho}\hat{\varphi} = \frac{\mu q}{2\pi}e^{i\frac{\omega}{v}z}uK_1(u\rho)\hat{\varphi}. \tag{3.105}$$

If we take as an integrating surface for the Poynting vector the lateral area of a cylinder, we need to know only the radial component of the Poynting vector.

$$(\mathbf{E}\times\mathbf{H}^*)\cdot\hat{\rho} = \frac{-E_z B_\varphi^*}{\mu(\omega)}. \tag{3.106}$$

If the speed of the particle is greater than the speed of light, the variable u is imaginary as discussed before, and the particle radiates. From Eqs. (3.104) and (3.106) we can obtain the energy per unit length $\mathrm{d}E_{\rm rad}/\mathrm{d}z$ passing through the lateral surface of a cylinder. We use that $\mathrm{d}\mathbf{a} = \rho\ \mathrm{d}z\ \mathrm{d}\varphi\ \hat{\rho}$ and multiply Eq. (3.104) by 2π to integrate in azimuth obtaining,

$$\begin{aligned} \frac{\mathrm{d}E_{\rm rad}}{\mathrm{d}z} &= -\int_{-\infty}^{\infty}\frac{1}{\mu}E_z B_\varphi^*\rho\ \mathrm{d}\omega \\ &= -2\int_0^\infty \frac{i\omega\mu q}{2\pi}e^{i\omega z/v}\left(1-\frac{1}{\mu\epsilon v^2}\right)K_0(u\rho)\times \\ &\times\ \frac{q}{2\pi}e^{-i\omega z/v}u^*K_1^*(u\rho)\ \rho\mathrm{d}\omega. \end{aligned} \tag{3.107}$$

Taking the limit $u\rho \to -i\infty$ and using the approximation in Eq. (3.100),

$$\begin{aligned}\frac{\mathrm{d}E_{\mathrm{rad}}}{\mathrm{d}z} &= -2\int_0^\infty \frac{i\mu q\omega}{2\pi}\left(1-\frac{1}{\mu\epsilon v^2}\right)\sqrt{\frac{\pi}{2}}(n^2\beta^2-1)^{-1/4}\sqrt{\frac{v}{(-i)\rho\omega}}\times \\ &\times \frac{q}{2\pi}\sqrt{\frac{\pi}{2}}i(n^2\beta^2-1)^{1/4}\sqrt{\frac{\omega}{vi\rho}}\rho\ \mathrm{d}\omega \\ &= \int_0^\infty \frac{\mu q^2}{4\pi}\left(1-\frac{1}{\mu\epsilon v^2}\right)\omega\ \mathrm{d}\omega. \end{aligned} \tag{3.108}$$

Performing the derivative with respect to ω,

$$\frac{\mathrm{d}^2E_{\mathrm{rad}}}{\mathrm{d}\omega\ \mathrm{d}z} = \frac{\mu q^2}{4\pi}\omega\left(1-\frac{1}{n^2v^2}\right). \tag{3.109}$$

we obtain the well-known Frank-Tamm formula.

3.3 A comprehensive comparison between the exact, ZHS and endpoints approaches in showers

Due to the large number of particles in a shower and their stochastic nature, the preferred method nowadays for calculating shower development is through the use of Monte Carlo (MC) simulations. Take, for instance, the CORSIKA [15] or AIRES [16] MCs. Using the primary particle as an input, these programs keep track of the trajectories and energies of the secondary particles present in the shower. All this information can be used to estimate the fluorescence yield, the signal on the surface detectors, or, in our case, the electric field seen by an antenna.

Despite the difficulties, analytical models for the showers have also been developed [5, 17]. While these models provide insight and constitute a sanity check for the Monte Carlo programs, the analytical approach can become rather cumbersome to work with. Besides, all the important features of the medium and the shower are very hard to take into account and a MC simulation of these features is usually performed.

In this section we will describe the ZHS and ZHAireS Monte Carlo and compare the electric field emitted in showers using both the ZHS formula and the exact formula. After that, we will deal with other formalisms to obtain the electric field of a single track, namely, the endpoints formalism [18].

3.3.1 ZHS and ZHAireS Monte Carlos

ZHS [4], created by E. Zas, F. Halzen and T. Stanev, is one of the first Monte Carlo codes that simulates the properties of a shower in a dense medium (density ~ 1 g/cm^3). It can simulate electromagnetic showers only, initiated by a positron, an electron or a photon. Due to the nature of the electromagnetic showers, the ZHS program took into account the processes of bremsstrahlung, pair production, Moller, Bhabha and Compton scattering, while including multiple elastic scattering, LPM effect and a continuous slowing down approximation. The ZHS code treats the shower as a set of particle tracks and then uses the eponymous ZHS formula (Eq. (3.52)) in order to calculate the electric field. ZHS describes well electromagnetic showers in dense media, where other effects like the geomagnetic field are negligible (see Chapter 2). The ZHS code predicts reasonably well the electric field in showers in ice, sand and salt as measured in accelerator experiments [19, 20, 21].

ZHAireS [22] combines the full shower simulations capabilities of AIRES [16] with the ZHS algorithm for the calculation of the electric field. AIRES is capable of simulating hadronic interactions for many kinds of particles and nuclei by means of several hadronic interaction models, and takes into account the atmospheric properties and the geomagnetic field, among many other features. ZHAireS uses AIRES as a tool for describing in detail the shower and obtain the tracks that are comprised in it, and then uses the ZHS algorithm to obtain the electric field. ZHAireS can also be used to create showers in dense media through its extension code named TIERRAS [23].

Both codes (ZHS and ZHAireS) behave differently when dealing with the tracking of the shower particles, but the calculation of the electric field is very similar and in fact they both use the ZHS formula. We are interested in comparing the performance of our exact formula (Eqs. (3.34) and (3.36)) with the ZHS formula (Eq. (3.52)) in a Monte Carlo program, *i.e.* in a simulated shower. We will choose ZHS in ice to test the validity of these formulas and the ZHS algorithm. ZHAireS and ZHS yield close results for electromagnetic showers in dense media [24], as shown in Fig. 3.9.

ZHS *vs* exact calculation in showers

We have applied the exact solutions of the field for a track given in Eqs. (3.34) and (3.36) in the ZHS Monte Carlo code for the simulation of electron and photon-induced showers in ice. The ZHS Monte Carlo calculates the tracks of the charged particles (electrons and positrons) in an electromagnetic shower and divides them in smaller subtracks if it is required for the electric field computation (ZHS algorithm). The particles are followed down

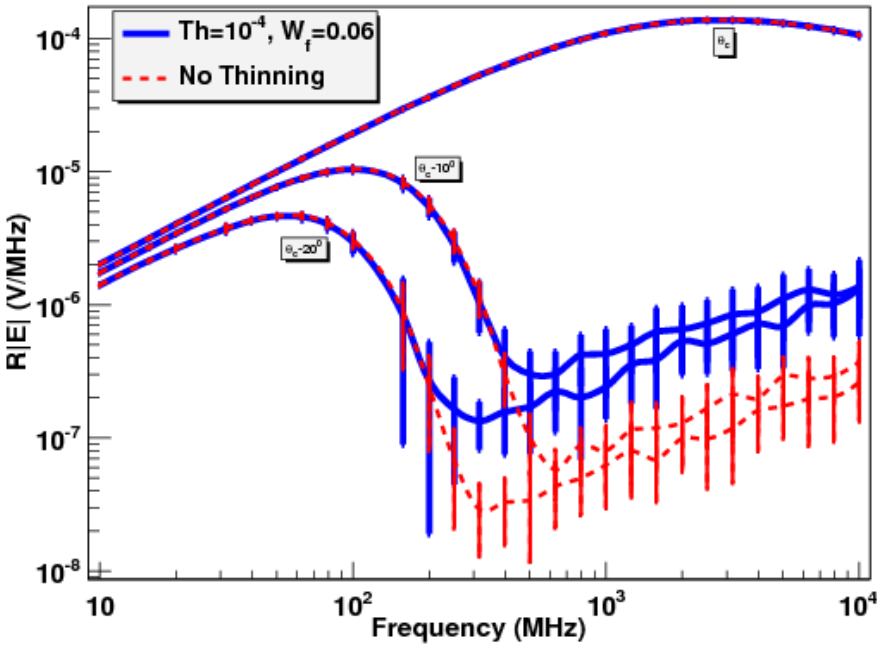

Figure 3.9: Average frequency spectrum of the Cherenkov radiation obtained in simulations of 20 electron-induced showers with primary energy $E_0 = 1$ PeV, using ZHS (blue solid line) and ZHAireS (red dashed line). The spectrum is shown at three observation angles with respect to the shower axis from top to bottom (at $\nu = 100$ MHz), θ_c, $\theta_c - 10°$ and $\theta_c - 20°$. The RMS of the 20 simulated showers is also shown. Taken from [24].

to a kinetic energy threshold of ~ 100 keV. With these we can calculate the exact electric field produced by each single subtrack and add the fields up accounting for interference between tracks. Since Eqs. (3.34) and (3.36) are only valid for a charged particle travelling along the z axis, we perform the necessary rotations of Eqs. (3.34) and (3.36) to obtain the field for a particle track moving along an arbitrary direction.

Simultaneously with the exact calculation, we also obtain the field as predicted by the ZHS algorithm for exactly the same shower (i.e., the same set of tracks and subtracks). As previously explained, the divisions are such that the conditions in Eqs. (3.38), (3.39) and (3.41) are fulfilled for all the subtracks in the shower.

The result is qualitatively the same as in the case of single tracks. As long as the condition $kR \gg 1$ is met, the ZHS algorithm gives an accurate prediction for the Fourier components of the electric field with a difference of less than a few percent relative to those obtained with the exact calculation. As can be seen in Figs 3.10, 3.11 and 3.12, this occurs for distances to the shower axis as small as $R = 1$ m and frequencies above $\nu \sim 10$ MHz, well in the distance and frequency ranges relevant for experiments looking for particle shower-induced radio pulses in dense media [8, 25, 26].

We stress here that the accuracy reported above refers to the approximation of using the ZHS formula applied to the standard subdivision of tracks in the ZHS code, instead of the exact expression for the radiation emitted by the same particle subtracks. By comparing the results obtained in the Fraunhofer limit with the standard subdivision of tracks to those obtained with a much finer subdivision, it was determined that the accuracy of the ZHS code is $\sim 10\%$ at frequencies ~ 5 GHz, improving significantly at lower frequencies. We do not further address this uncertainty in this thesis, nor the uncertainty due to the shower simulation itself.

It is also worth remarking that in terms of computing time, the exact calculation is roughly a factor ~ 5 slower than the calculation performed with the ZHS algorithm, though this depends on the distance and frequency of observation. Better integration methods could improve the performance, but the exact calculation is mainly for illustrative purposes to show that the ZHS algorithm works as long as $kR \gg 1$. For practical purposes, the far-field condition is true, and the ZHS formula returns the same result in a much faster way.

As already discussed in Chapter 2, since the ZHS algorithm can only be applied in a limited range of frequencies, an accurate representation of the electric field in the time domain cannot be obtained with an inverse Fourier transform of Eq. (3.52). The low frequency components that do not satisfy the condition $kR \gg 1$ are not accurately described

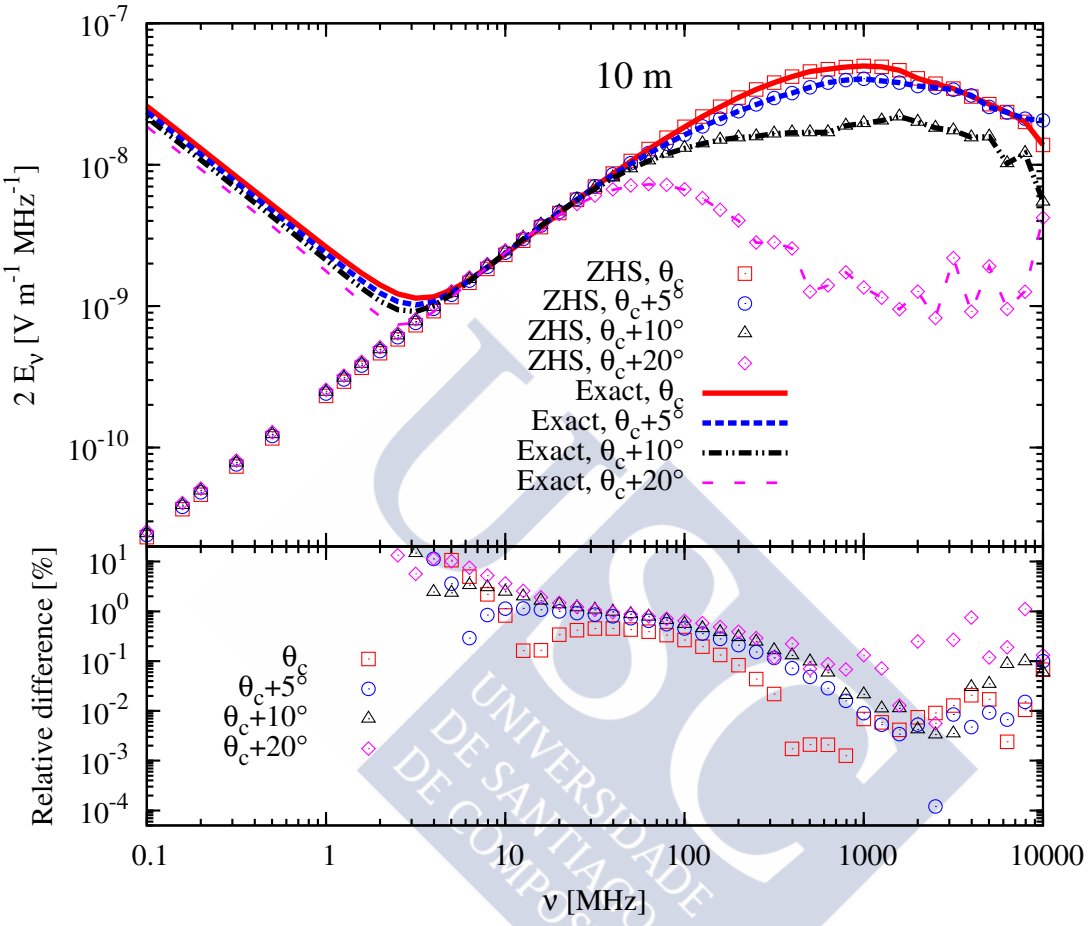

Figure 3.10: Fourier components of the electric field modulus as obtained in Monte Carlo simulations of a 10 TeV electron-induced shower in ice, with the exact calculation (lines) and with the ZHS algorithm (symbols). The observer lies at a distance of $R = 10$ m, placed at different observation angles with respect to the shower maximum. We also show the relative difference (in percentage) between the electric field modulus as obtained with the exact solution and with the ZHS algorithm for the various observation angles depicted.

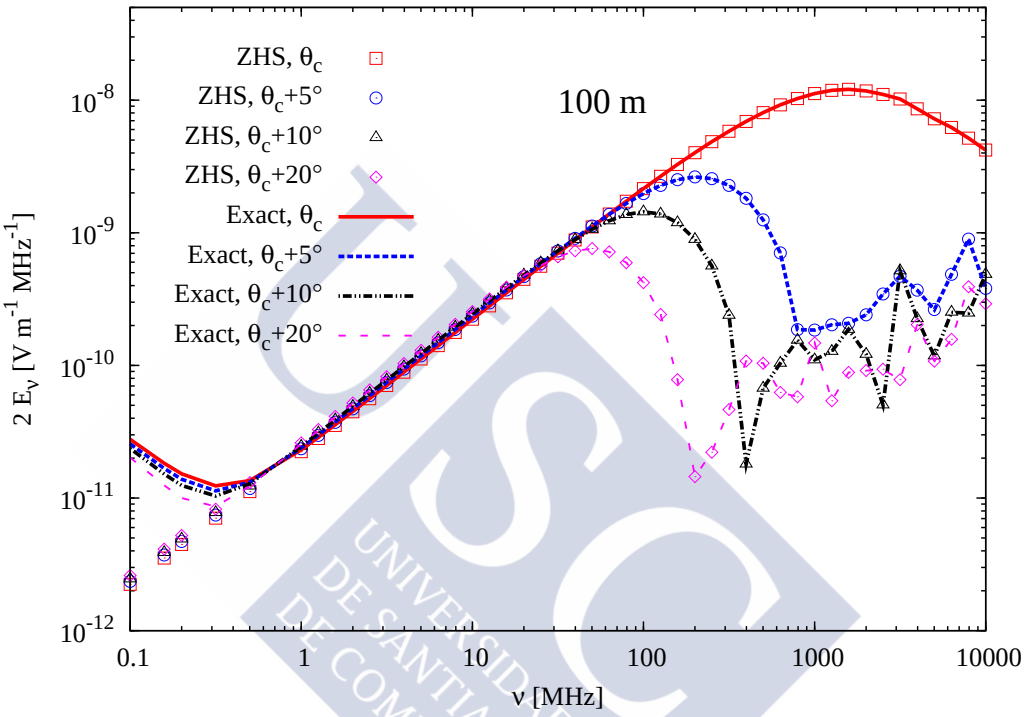

Figure 3.11: Fourier components of the electric field modulus as obtained in Monte Carlo simulations of a 10 TeV electron-induced shower in ice, with the exact calculation (lines) and with the ZHS algorithm (symbols). The observer lies at a distance of $R = 100$ m, placed at different observation angles with respect to the shower maximum.

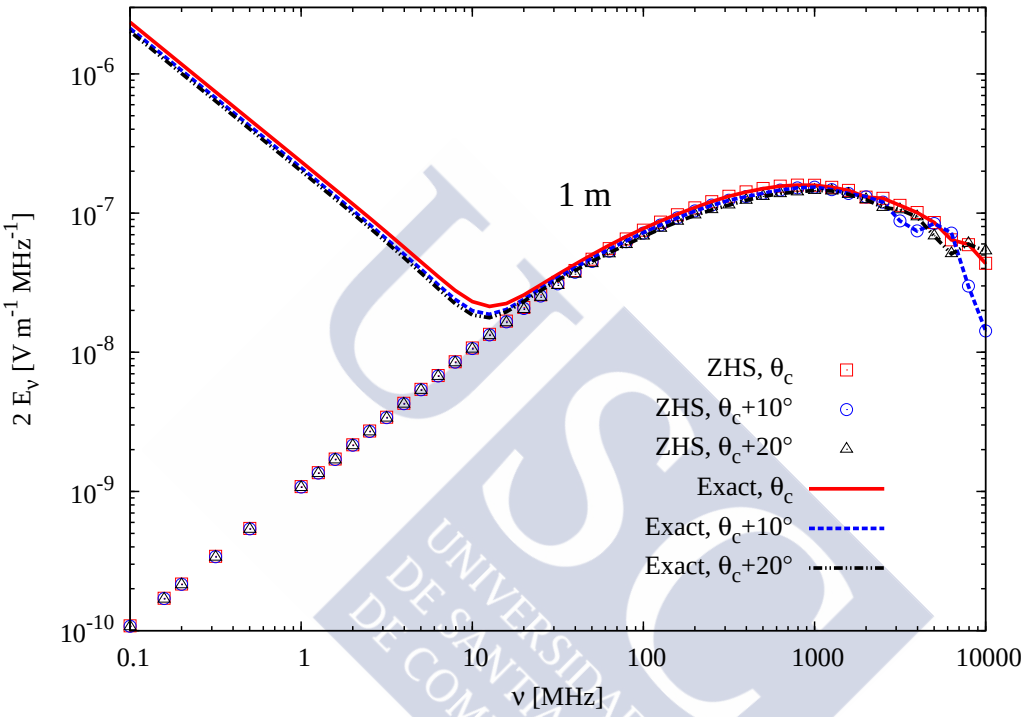

Figure 3.12: Fourier components of the electric field modulus as obtained in Monte Carlo simulations of a 10 TeV electron-induced shower in ice, with the exact calculation (lines) and with the ZHS algorithm (symbols). The observer lies at a distance of $R = 1$ m, placed at different observation angles with respect to the shower maximum.

by the ZHS algorithm. Also, at very high frequencies the number of steps in which the tracks have to be divided in order to fulfil Eqs. (3.38), (3.39) and (3.41) can become prohibitively large from a computational point of view. However, if we want the electric field in time but filtering out the frequencies where ZHS is not applicable, we can transform back Eq. (3.52). Most antennas respond only to frequencies where the ZHS is applicable, and they have to be in the far-field of the sources (see the Intermission chapter).

In practice, the ZHS algorithm provides a fast and accurate calculation of the electric field in the region of interest to ultrahigh energy neutrino and cosmic ray detection. For experiments with typical time resolutions of the order of 1 ns, and which are only sensitive to frequencies greater than 10 MHz up to a few GHz, the ZHS formula has been shown to give a very accurate representation of the Fourier components of the electric field (Fig. 3.10) [19, 20, 21, 27].

3.3.2 Endpoints formula: ZHS *vs* endpoints in ice

The endpoints formula [18] is an alternative expression to calculate the radiation field from a charged particle track. However, it presents some problems that we will highlight here.

In [18], the field is obtained from the Liénard-Wiechert potentials and their corresponding fields. These fields are only valid in vacuum, where $n = 1$. To obtain the field from a track using the Liénard-Wiechert potentials for a medium of constant refractivity n, we should take into account that, for superluminal motion ($v > c/n$), the electric field at one point in space can come from two different points of the same particle track, as it has been done in [10]. We can still use Liénard-Wiechert potentials with these modifications, but in [18], the standard Liénard-Wiechert fields were taken and the refractive index $n \neq 1$ was introduced *ad hoc*.

According to [18], the radiation electric field in time can be written as a sum of the radiation of the endpoints of the track where a particle suddenly appears and disappears (denoted with a "+" and a "−" symbol). The field of each end point can be written as

$$\mathbf{E}_{\pm}(\mathbf{x}, t) = \pm \frac{q}{4\pi\epsilon_0 c\ \Delta t} \frac{\beta \sin\theta_{\pm}}{R(1 - n\beta\cos\theta_{\pm})} \hat{\mathbf{E}}_{\pm}. \tag{3.110}$$

Δt is the time the particle takes to accelerate or decelerate, R_+ (R_-) is the distance from observation point to the initial (ending) point of the track, θ_+ (θ_-) stands for the observation angle of the beginning (end) of the track and $\hat{\mathbf{E}}_{\pm}$ are the unit polarization vectors, perpendicular to the line of sight for each end point of the track.

The endpoints field in time is quite similar to the time domain expression of the ZHS field [28]. The huge difference lies in the fact that the field in Eq. (3.110) treats the

radiation as the consequence of the instantaneous acceleration of the charged particle, but we know that superluminal motion can produce radiation without acceleration (Cherenkov radiation), as we have proven in Section 3.2 and has been proven in [10] or [2]. Besides, let us take the field for superluminal motion of Eq. (2.23) from [10],

$$\begin{aligned} 4\pi\epsilon\mathbf{E}(\mathbf{x},t) &= -\frac{\delta(c_n(t+t_0)-r_1)}{\beta_n(z+z_0)-r_1}\frac{q\rho\beta_n}{r_1}\hat{\mathbf{n}}_\theta^1 + \frac{c_n(t-t_0)-r_2}{\beta_n(z-z_0)-r_2}\frac{q\rho\beta_n}{r_2}\hat{\mathbf{n}}_\theta^2 \\ &+ \delta(c_nt-R_m)\frac{2q}{r_m\gamma_n}\times \\ &\times \Theta(\rho\gamma_n+z_0-z)\Theta(z+z_0-\rho\gamma_n)\hat{\mathbf{n}}_m, \end{aligned} \tag{3.111}$$

where $c_n = c/n$ is the speed of light in the medium, $\beta_n = v/c_n$, $\gamma_n = \sqrt{|\beta_n^2-1|}$, the track starts at $(0,0,-z_0)$ with $t=-t_0$ and ends at $(0,0,z_0)$ with $t=t_0$, r_1 and r_2 are the distances to the end points of the track, $\hat{\mathbf{n}}_\theta^1$ and $\hat{\mathbf{n}}_\theta^2$ are the unit polarization vectors perpendicular to the line of sight of the end points, $r_m = \sqrt{(z-vt)^2+\rho^2(1-\beta_n^2)}$, $R_m = (z+\rho/\gamma_n)/\beta_n$ and $\hat{\mathbf{n}}_m$ is a unit vector tangent to the surface of the Cherenkov cone.

We see that the fields in Eqs. (3.110) and the first two terms in (3.111) are quite similar, but the endpoints formula lacks the last term of the latter that accounts for Cherenkov radiation.

These fields and even the time domain version of the ZHS formula have infinities that can give problems, a result of using an unrealistic medium with a constant refractivity, independent of the frequency. But while the ZHS formula can be used in frequency and it does not ever blow up, the endpoints formula can blow up regardless of the frequency dependence of the medium. What is even worse, the endpoints formula blows up for observers at the Cherenkov angle, where the bulk of the radiation comes from and therefore of utmost importance from the experimental point of view. To illustrate this, let us take the endpoints field in frequency, according to [18],

$$\mathbf{E}_\pm(\mathbf{x},\nu) = \pm\frac{q}{4\pi\epsilon_0 c}\frac{e^{ikR_\pm}}{R_\pm}\frac{\beta\sin\theta_\pm e^{2\pi i\nu t_\pm}}{1-n\beta\cos\theta_\pm}\hat{\mathbf{E}}_\pm. \tag{3.112}$$

t_+ (t_-) is the time when the particle accelerates (decelarates). Eq. (3.112) has the problem that the denominator $[1-n\beta\cos\theta_\pm]$ is zero at the Cherenkov angle, which makes the field go to infinity. This is not acceptable from a theoretical and experimental point of view, since the field (or energy) at a fixed frequency must be finite for all angles.

On the other hand, the ZHS formula (Eq. (3.52)) has a finite value after we take the limit $\theta\to\theta_c$ (let us assume $\mu_r = 1$),

$$\mathbf{E}_{\mathrm{ZHS}}(\theta_c,\omega) = \frac{qi\omega}{4\pi\epsilon_0 c^2}\frac{e^{ikR}}{R}\mathbf{v}_\perp(t_2-t_1), \tag{3.113}$$

which is finite, as shown in Chapter 2.

Another issue with Eq. (3.112) is that it cannot be used in the near-field regime despite the claims in [18]. The main reason for this is that the Liénard-Wiechert fields, one cannot always neglect the term that falls with $1/R^2$ when transforming to frequency as done in [18], since for low values of kR (*i.e.* in the near-field) this is the part of the field that dominates. In particular, Eq. (3.112) results in a flat spectrum at low frequencies, which is unphysical, as shown below in Fig. 3.13. We have shown that for low frequencies but still in the far-field (ZHS formula), the depencence is linear with frequency, and for very low-frequencies the Coulomb field dominates and the spectrum falls with ω^{-1}.

We can obtain an expression more similar to the ZHS formula starting with Eq. (3.112) for the Fraunhofer regime and outside the Cherenkov angle, with the following approximations.

$$e^{ikR_+} \approx e^{ikR_-} \approx e^{ikR}, \tag{3.114}$$

$$\frac{1}{R_+} \approx \frac{1}{R_-} \approx \frac{1}{R}, \tag{3.115}$$

$$\theta_+ \approx \theta_- \approx \theta, \tag{3.116}$$

$$\frac{1}{1-n\beta\cos\theta_+} \approx \frac{1}{1-n\beta\cos\theta_+} \approx \frac{1}{1-n\beta\cos\theta}. \tag{3.117}$$

Adding the contributions of both endpoints,

$$\begin{aligned} \mathbf{E}_{\mathrm{EP}}(\mathbf{x},\nu) &\approx \frac{q}{4\pi\epsilon_0 c^2}\frac{e^{ikR}}{R}\frac{i\omega}{i(\omega-\mathbf{k}\cdot\mathbf{v})}(e^{i\omega t_+}-e^{-i\omega t_-})\mathbf{v}_\perp \\ &= \frac{qi\omega}{4\pi\epsilon_0 c^2}\frac{e^{ikR}}{R}\mathbf{v}_\perp\frac{e^{i\omega t_+}-e^{-i\omega t_-}}{i(\omega-\mathbf{k}\cdot\mathbf{v})}, \end{aligned} \tag{3.118}$$

where we have used that $\mathbf{v}_\perp = \beta\sin\theta\hat{\mathbf{E}}_\pm$. Eq. (3.118) is very similar to (3.52), differing only in two phase factors that can be negligible for certain frequencies in the far-field. The main problem is that this formula cannot be used for the Cherenkov angle, and most of the radiation of a particle comes from the emission at that angle.

We can compare both approaches in a more realistic situation. We can place ourselves outside the Cherenkov angle to avoid the endpoints formula from blowing up. Let us consider an electron-induced shower in ice, with an observer at $R = 100$ m and $\theta = \theta_c + 10°$. We show the result in Fig. 3.13. Although we are far from the Cherenkov angle, some particles of the shower will be seen near the Cherenkov angle, and their contribution to the field as predicted by the endpoints formula is not bound, so the resulting field makes

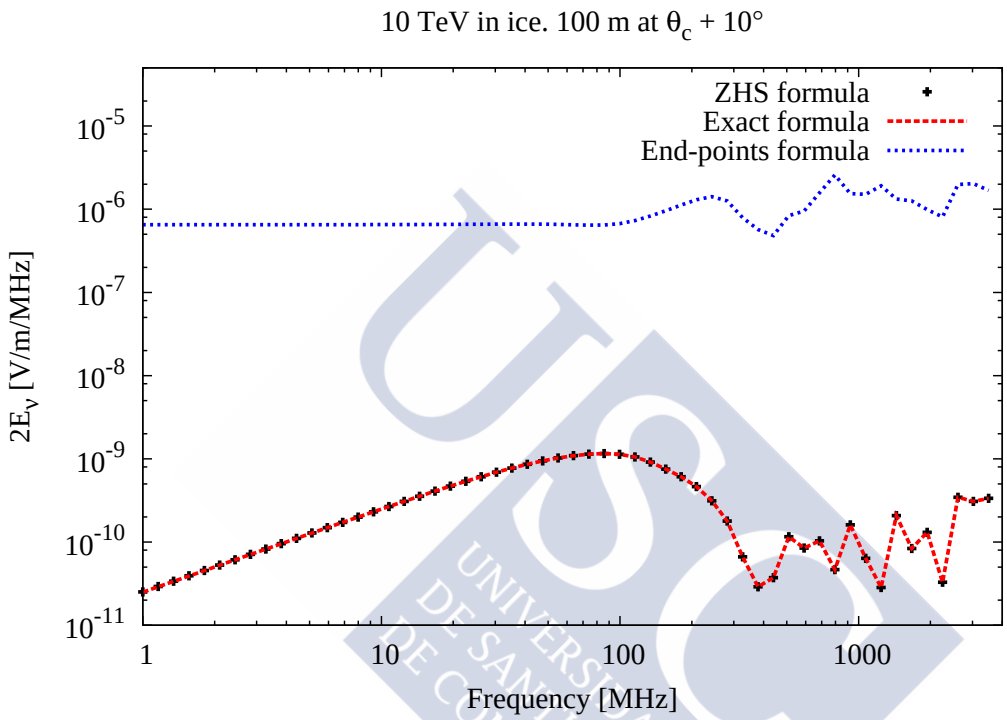

Figure 3.13: Fourier components of the electric field modulus as obtained in Monte Carlo simulations of a 10 TeV electron-induced shower in ice, as a function of the frequency. The observer lies at a distance of $R = 100$ m, placed at an angle of $\theta_c + 10°$. The ZHS formula (points), the exact formula (red line) and the end-points formula (blue line) are plotted. See text for details.

no physical sense. We can also see at low frequency the constant spectrum predicted by the endpoints formula and discussed before.

In conclusion, the endpoints formula (Eq. (3.112)) cannot be applied for calculating the field near the Cherenkov angle, where an important part of the radiation comes from. Patching the endpoints formula with the ZHS formula in the region where it breaks down (as done in [29]) is not advisable, since the physics can depend on the patch. Most of the radiation comes from the Cherenkov angle in many experimental situtations, and if we apply the patch, the main contribution to the final field will typically come from the ZHS formula and not from the endpoints formula. Due to the many problems of the endpoints formula, we strongly discourage its use.

3.4 Saddle-point approximation: ZHS *vs* saddle-point approaches in showers

Several alternative calculations of the field emitted by showers developing in dense media can be found in the literature. In [30] the finite difference time domain method is used for calculating the field of a pancake-like shower with a Gaussian longitudinal development and Gaussian radial profile in the time domain that is then transformed to the frequency domain. In [5], using the saddle-point approximation, the electric field of a charge distribution exhibiting a longitudinal profile with a well-pronounced maximum is derived. The result is factorised into an integral accounting for the longitudinal variation of the charge and a form factor that accounts for the lateral spread of the shower, a procedure revisited in [31] for realistic showers. Assuming a Gaussian longitudinal and lateral development for the charge distribution, both results were directly compared and turned out to be in good overall agreement as shown in [30]. Minor differences could be attributed to the form factors used.

This section is devoted to the comparison of the ZHS algorithm and the exact formula applied to a Gaussian longitudinal profile with the semi-analytical approach based on the saddle-point approximation developed in [5].

- **Exact calculation of the field of a Gaussian profile**

With the exact formula for the electric field obtained in this work, the field of a Gaussian profile can also be calculated. The electric current for a shower with a Gaussian profile is given by Eq. (3.15) making the following replacements,

$$Z(t) = 1; \qquad q = |e|. \tag{3.119}$$

$$P(\mathbf{x},t) = \frac{N}{2\pi\sigma_r^2} e^{-(x^2+y^2)/2\sigma_r^2} e^{-z^2/2\sigma_l^2} \delta(z-vt). \tag{3.120}$$

The shower develops in the longitudinal direction parallel to the z coordinate (shower axis) and radially along the x and y coordinates. N is a normalization constant, σ_l characterises the width of the shower along the shower axis and σ_r the corresponding lateral width. After substituting this current in the vector potential in Eq. (3.19), one finds out that, since the derivatives affect the observer coordinates and not the coordinates of the shower current, the expression for the field is the same as in Eqs. (3.34) and (3.36) but accounting for the shower development with the following modification,

$$\int \mathrm{d}t' \to \int \mathrm{d}t' \ \mathrm{d}x' \ \mathrm{d}y' \frac{N}{2\pi\sigma_r} e^{-(x'^2+y'^2)/2\sigma_r^2} e^{-v^2t'^2/2\sigma_l^2} \tag{3.121}$$

After this, the equations can still be solved numerically.

- **ZHS calculation of the field of a Gaussian profile**

The ZHS algorithm can also be applied to this situation as long as the far-field condition $kr \gg 1$ is valid for all distances r to the shower. In order to do so, we must divide the shower into a collection of tracks, so we use the procedure of "slicing" the volume occupied by the bulk of the shower in small cubes and approximating each cube as a track with a charge given by the Gaussian distribution of Eq. (3.120).

- **Saddle-point calculation**

Comparison of the result of the exact calculation (or the ZHS algorithm) with the saddle point calculation in [5] requires knowing the form factor F for a Gaussian profile. F is defined in Eq. (9) of [5] as

$$F(\mathbf{q}) = \int \mathrm{d}x' \ \mathrm{d}y' \ \mathrm{d}s' e^{-i\mathrm{q}\cdot\mathrm{x}'} f(s',x',y'), \tag{3.122}$$

with $\mathrm{q} = (\omega/v, k\rho/R)$ and $\rho = (x,y)$ the radial position of the observer. Also, $\mathrm{x}' = (s',x',y')$ with $s' = z' - vt'$. R is the distance from the maximum of the shower to the observer. The function f represents the charge density of the travelling pancake normalised to 1, and is defined in a way that the current in time can be written as

$$\mathbf{J}(\mathbf{x}',t') = \mathbf{v}n(z')f(z'-vt',\rho) \tag{3.123}$$

This means that f has no information about the longitudinal development, that is all contained in $n(z')$. Assuming a Gaussian for f of the form

$$f(s', x', y') = \frac{1}{2\pi\sigma_r^2}\delta(s')e^{-(x'^2+y'^2)/2\sigma_r^2}, \tag{3.124}$$

and substituting f into Eq. (3.122), we arrive at

$$F(\mathbf{q}) = e^{-\frac{1}{2}\left(\frac{n\omega}{c}\frac{\rho}{R}\right)^2}. \tag{3.125}$$

This must be plugged in Eq. (15) in [5] that gives the electric field in the radiation zone:

$$\begin{aligned}\mathbf{E}(R,\theta,\omega) &= \frac{i\omega|e|}{4\pi\epsilon_0 Rc^2}F(\mathbf{q})I^{FF}(\eta,\theta)\Bigg[(\cos\theta-\cos\theta_c)\hat{\mathbf{r}}+\\ &- \left(1-i\eta\frac{\cos\theta_c}{\sin^2\theta}\frac{\cos\theta-\cos\theta_c}{1-i\eta}\right)\sin\theta\;\hat{\theta}\Bigg],\end{aligned} \tag{3.126}$$

with η defined as

$$\eta = \frac{k\sigma_l^2}{R}\sin^2\theta, \tag{3.127}$$

where we have included the charge of the electron (in absolute value) so that the formula is dimensionally correct and a $4\pi\epsilon_0$ factor to convert from the CGS to SI system of units. $\hat{\mathbf{r}}$ is the radial unit vector in spherical coordinates and $\hat{\theta}$ is the unit vector of the θ coordinate. I^{FF} is defined as

$$\begin{aligned}I^{FF}(\eta,\theta) &= e^{ikR}\sigma_l\sqrt{2\pi}\left[1-i\eta\left(1-3i\eta\frac{\cos\theta}{\sin^2\theta}\frac{\cos\theta-\cos\theta_c}{1-i\eta}\right)\right]^{-1/2}\times\\ &\times \exp\left[-\frac{1}{2}(ka)^2\frac{(\cos\theta-\cos\theta_c)^2}{1-i\eta}\right].\end{aligned} \tag{3.128}$$

- **Comparison of the three approaches**

We set $N = 1$ in Eq. (3.120), $\sigma_l = 20$ m, $\sigma_r = 1$ m and $R = 300$ m with the refractive index of ice being $n = 1.78$. The electric fields for a Gaussian charge profile were calculated using Eq. (3.126) and compared to the ones obtained with the exact formula and with the ZHS algorithm. The results are shown in Fig. 3.14. Since R is large, the condition $kR \gg 1$ is satisfied for frequencies above $\nu \sim 1$ MHz and the agreement between the ZHS and the exact calculation presented in this work is almost perfect (not shown in Fig. 3.14 for clarity, since both curves would overlap). The saddle-point approach is also in very good agreement with both the exact and ZHS calculations. Finally, the results of the field for a Gaussian profile are also in good agreement with those obtained in [30] using the finite difference time domain method.

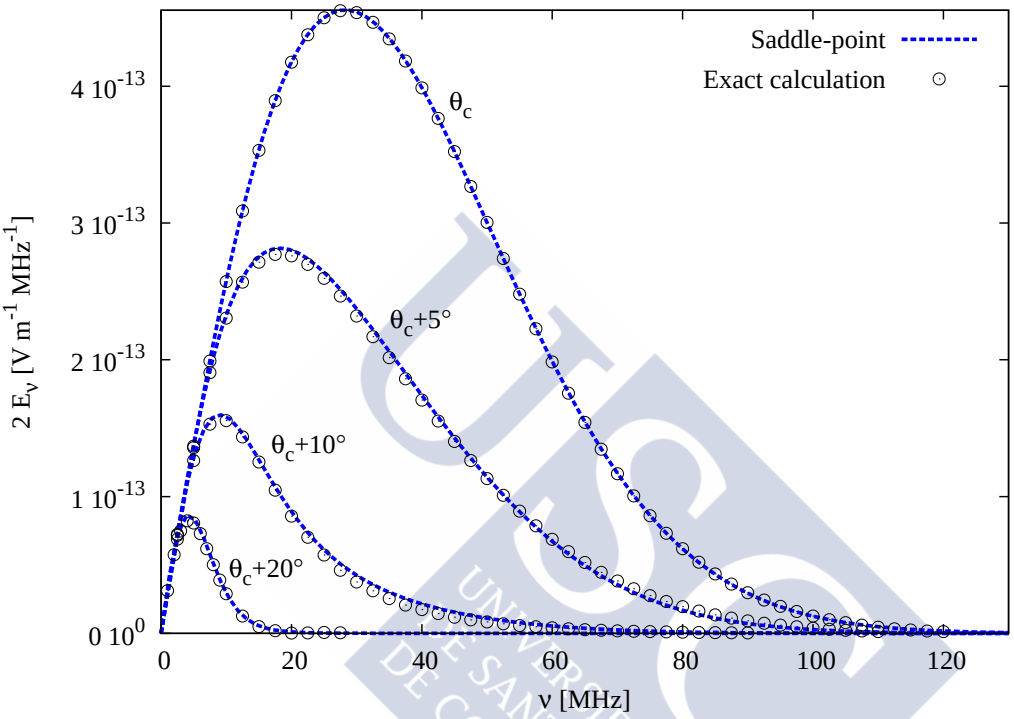

Figure 3.14: Fourier components of the modulus of the electric field for a Gaussian charge profile with $\sigma_l = 20$ m and $\sigma_r = 1$ m for an observer at $R = 300$ m with respect to the peak of the Gaussian longitudinal profile. The observation angles are, from top to bottom, θ_c, $\theta_c + 5°$, $\theta_c + 10°$ and $\theta_c + 20°$. Fields are calculated with the saddle-point approach of Eq. (3.126) and with the exact formula of Eqs. (3.34) and (3.36). The result obtained with the ZHS algorithm is on top of the exact calculation and it is not plotted here for clarity.

3.5 Conclusions and summary of this chapter

- We have derived an exact expression for the electric field of a particle track (Eqs. (3.34) and (3.36)) in the frequency domain.
- We have obtained the ZHS formula (Eq. (3.52)) from the exact expression for the far-field regime ($kR \gg 1$) and under the Fraunhofer approximation ($kL^2 \sin^2\theta/R \ll 1$).
- We have presented the ZHS algorithm, which consists in dividing a particle track so that each division is under the assumptions for applying the ZHS formula, and then add up the contributions. The ZHS algorithm works as long as $kR \gg 1$ (far-field condition) is met, and we have checked that it reproduces the field of the exact formula when applied to particle showers.
- The ZHS formula has been proven to account for the Cherenkov radiation, created by the motion of a particle at constant speed greater than the speed of light in a medium.
- We have shown that the endpoints formalism presents several problems and it does not agree with the exact calculation or the ZHS formula.
- The ZHS formula agrees with FDTD methods and the saddle-point semi-analytical calculation.

Bibliography

[1] M. E. Peskin and D. V. Schroeder. *An Introduction to Quantum Field Theory*. Perseus Books Publishing, 1995.

[2] J. D. Jackson. *Classical Electrodynamics*. Wiley, New York, 3rd edition, 1998.

[3] D. García-Fernández, J. Alvarez-Muñiz, W. R. Carvalho Jr., A. Romero-Wolf, and E. Zas. Calculations of electric fields for radio detection of ultrahigh energy particles. *Physical Review D*, **87**(023003), 2013.

[4] E. Zas, F. Halzen, and T. Stanev. Electromagnetic pulses from high-energy showers: Implications for neutrino detection. *Physical Review D*, **45**:365, 1992.

[5] R. V. Buniy and J. P. Ralston. Radio detection of high energy particles: Coherence versus multiple scales. *Physical Review D*, **65**(016003), 2001.

[6] A. Taboada Núñez. Descripción de procesos de emisión electromagnética en Astrofísica de Partículas por medio del algoritmo Zas-Halzen-Stanev. Master's thesis, Universidade de Santiago de Compostela, 2015.

[7] P. Motloch *et al.* Transition radiation at radio frequencies from ultra-high energy showers. In *Proceedings of the 34th International Cosmic Ray Conference (ICRC 2015)*, number 478.

[8] P. Allison *et al.* Design and initial performance of the Askaryan Radio Array prototype EeV neutrino detector at the South Pole. *Astroparticle Physics*, **35**:457, 2012.

[9] I. M. Frank and I. E. Tamm. Coherent radiation of fast electron in medium. *Doklady Akademii Nauk SSSR*, **14**:107, 1937.

[10] G. N. Afanasiev. *Vavilov-Cherenkov and Synchrotron Radiation: Foundations and Applications*. Kluwer Academic, Dordrecht, The Netherlands, 2004.

[11] G N Afanasiev and V M Shilov. Cherenkov radiation versus bremsstrahlung in the Tamm problem. *Journal of Physics D: Applied Physics*, **35**:854, 2002.

[12] M. Abramowitz and I. A. Stegun. *Handbook of Mathematical Functions with Formulas, Graphs, and Mathematical Tools*. National Bureau of Standards, 1964.

[13] Gradshteyn I.S. and Ryzik I.M. *Tables of Integrals, Series and Products*. Academic Press, New York, 1965.

[14] G. N. Watson. *A Treatise on the Theory of Bessel Functions*. Cambridge, 2nd edition, 1966.

[15] D. Heck *et al. FZKA Report*, (6019), 1998. Forschungszentrum Karlsruhe.

[16] S. Sciutto. <http://www.fisica.unlp.edu.ar/auger/aires/>.

[17] K. Werner and O. Scholten. Macroscopic treatment of radio emission from cosmic ray air showers based on shower simulations. *Astroparticle Physics*, **29**:393, 2008.

[18] C. W. James, H. Falcke, and T. Huege. General description of electromagnetic radiation processes based on instantaneous charge acceleration in "endpoints". *Physical Review E*, **84**(056602), 2011.

[19] D. Saltzberg *et al.* Observation of the Askaryan effect: Coherent microwave Cherenkov emission from charge asymmetry in high-energy particle cascades. *Physical Review Letters*, **86**:2802, 2001.

[20] P. W. Gorham *et al.* Observations of the Askaryan effect in ice. *Physical Review Letters*, **99**(171101), 2007.

[21] P. W. Gorham *et al.* Accelerator measurements of the Askaryan effect in rock salt: A roadmap toward teraton underground neutrino detectors. *Physical Review D*, **72**(023002), 2005.

[22] J. Alvarez-Muñiz, W. R. Carvalho Jr., and E. Zas. Monte Carlo simulations of radio pulses in atmospheric showers using ZHAireS. *Astroparticle Physics*, **35**:325, 2012.

[23] M. Tueros and S. Sciutto. TIERRAS: A package to simulate high energy cosmic ray showers underground, underwater and under-ice. *Computer Physics Communications*, **181**:380, 2010.

[24] J. Alvarez-Muñiz, W. R. Carvalho Jr., M. Tueros, and E. Zas. Coherent Cherenkov radio pulses from hadronic showers up to EeV energies. *Astroparticle Physics*, **35**:287, 2012.

[25] I. Kravchenko *et al.* RICE limits on the diffuse ultrahigh energy neutrino flux. *Physical Review D*, **85**(062004), 2012.

[26] P. W. Gorham *et al.* The Antarctic Impulsive Transient Antenna ultra-high energy neutrino detector: Design, performance, and sensitivity for the 2006–2007 balloon flight. *Astroparticle Physics*, **32**:10, 2009.

[27] F. G. Schröder *et al.* Radio detection of air showers with Auger Engineering Radio Array. In *Proceedings of the 33rd International Cosmic Ray Conference (ICRC 2013)*, number 0899.

[28] J. Alvarez-Muñiz, A. Romero-Wolf, and E. Zas. Cerenkov radio pulses from electromagnetic showers in the time domain. *Physical Review D*, **81**(123009), 2010.

[29] C. W. James. Electromagnetic radiation in the Tamm problem. In *Proceedings of the 5th Acoustic and Radio EeV Neutrino Detection Activities (ARENA 2012).*

[30] C.-Y. Hu, C.-C. Chen, and P. Chen. Near-field effects of Cherenkov radiation induced by ultra high energy cosmic neutrinos. *Astroparticle Physics*, **35**:421, 2012.

[31] J. Alvarez-Muñiz, A. Romero-Wolf, and E. Zas. Practical and accurate calculations of the Askaryan effect. *Physical Review D*, **84**(103003), 2011.

USC
UNIVERSIDADE
DE SANTIAGO
DE COMPOSTELA

Chapter 4

A model for radio emission in air showers

4.1 Motivation for the model

While Monte Carlo simulation packages such as ZHAireS [1] or CoREAS [2] provide a state-of-the-art, reliable way of computing the radio emission induced in an air shower, the time necessary to do so becomes prohibitively large for ultra high energy showers. In order to circumvent this, statistical methods such as the thinning algorithm [3, 4, 5] have to be used. The thinning algorithm samples the shower particles, ignoring certain particles in a random way, and weighting the ones that are followed to compensate for those being ignored. Both ZHAireS and CoREAS have versions of the thinning algorithm built in. However, even with thinning methods, the computational time is typically large. For instance, for a 10^{18} eV proton shower with a relative thinning level of 10^{-6}, the CPU time per antenna in an average processor is ~ 3 hours.

If one wishes to make a comprehensive study of the radio emission in cosmic ray shower for several shower geometries, several depths of the shower maximum and several observer positions for instance, the simulations can take up to several days or even weeks, despite an appropiate choice of thinning and using a large computer cluster ($\sim$ 500 nodes). It would be desirable to develop a tool that can predict some qualitative aspects of the radio emission with a minimal computational cost, so that interesting properties of a cosmic ray shower can be probed with little time, paving the way for more accurate simulations using Monte Carlo codes.

In this chapter we develop a simple model with which we can predict the spatial and temporal features of the radio emission in air showers. The model is based on geometrical grounds with a minimal dash of electrodynamics. We have applied it to several relevant physical cases and compared it with full Monte Carlo simulations performed with ZHAireS.

4.2 Description of the model

Our goal is to develop a simple model in order to predict mainly the spatial (angular) distribution of the electric field of a shower, both on the ground and after reflection. The latter case is relevant for cosmic-ray detection in the ANITA experiment [6], as will be addressed in chapter 6.

We start by modelling a shower with zenith angle θ as a one-dimensional charge distribution varying with time $N(t)$ as the shower propagates along a given direction (shower axis) at the speed of light [7]. In the Fraunhofer approximation and including a longitudinal profile $N(t)$, we can write the radial (perpendicular to shower axis) component of the electric field induced by $N(t)$, given in Eq. (3.34), as

$$E_\rho(\mathbf{x},\omega) \approx -\frac{cq}{4\pi i\epsilon\omega}\int \mathrm{d}t\ N(t)e^{i\omega t}\frac{e^{ikr(t)}}{r(t)}(ik)^2\sin\psi(t)\cos\psi(t), \tag{4.1}$$

while the longitudinal component given in Eq. (3.36) reads

$$E_z(\mathbf{x},\omega) \approx \frac{cq}{4\pi i\epsilon\omega}\int \mathrm{d}t\ N(t)e^{i\omega t}\frac{e^{ikr(t)}}{r(t)}(ik)^2[\sin\psi(t)]^2. \tag{4.2}$$

c is the speed of light in vacuum, ϵ is the permittivity of the medium, $k = \omega n/c$ is the wavenumber, t is the coordinate time for the shower, $r(t)$ gives the distance between the emitting and the observation points and $\psi(t)$ represents the angle between the shower axis and the line formed by the emission and observation points. The fields in Eqs. (4.1) and (4.2) have an integrand that is proportional to the observation frequency ω, the longitudinal profile $N(t)$, the inverse of the distance $r(t)$ and contain a phase term. This suggests a simple model for the modulus of the field dropping the proportionality constants and ignoring the angular terms:

$$E \sim \int \mathrm{d}t\ N(t)\frac{e^{i\omega t+ikr(t)}}{r(t)}. \tag{4.3}$$

We deliberately ignore the factor proportional to ω and refuse to predict the spectrum because this one-dimensional model lacks the lateral and shower width scales, of great importance to calculate the spectrum of air showers [8]. The normalisation for each frequency will be inserted *ad hoc*. Taking into account that the arrival time t_a of the wave at the observer is given by

$$t_a(t) = t + \frac{n}{c}r(t), \tag{4.4}$$

and including it in Eq. (4.3), the modulus of the field takes the form,

$$E \sim \int \mathrm{d}t \; N(t) \frac{e^{i\omega t_a(t)}}{r(t)}. \tag{4.5}$$

Eq. (4.5) has the fewest quantities that a pulsed wave in frequency can have, namely charge (represented by $N(t)$), a phase with the arrival time, distance between the source and the observer and frequency.

Eq. (4.5) has been derived for a homogeneous, isotropic and non-conductive medium but it can be extended to the atmosphere accounting for the time delays from propagation in the altitude-dependent index of refraction. t_a is, in this case, the arrival time of the electromagnetic wave taking into account that the speed of light depends on the position. Also, $r(t)$ must be calculated as the length of the path travelled by the ray between the emission and observation points, keeping in mind that the trajectory is now a curve due to the variable refractive index. This will be addressed later in this chapter.

Eq. (4.5) can be discretised in order to perform a numerical integration. The discretisation must be performed in a way such that the 1D shower is divided in pieces of a constant time difference Δt, or, equivalently, constant length.

$$E \sim \Delta t \sum_j N(j\Delta t) \frac{e^{i\omega t_a(j\Delta t)}}{r(j\Delta t)}. \tag{4.6}$$

Another important feature is that this model can be extended for rays reflected on ground and travelling to a high altitude observer, simply by calculating the arrival time and path distance of the reflected ray to the observer. This has important applications as described in Chapter 6.

For the model to work we need a fast ray tracing algorithm in order to account for the curvature of the path followed by radio waves in a non-homogeneous medium such as the Earth's atmosphere.

4.2.1 Ray tracing algorithm

We assume the exponential model for the refractivity of the atmosphere as a function of height[1] used in the ZHAireS code, known to reproduce the refractivity calculated in [9] up to 10 km of altitude above sea level with a relative accuracy of less than $\sim 1\%$.

$$n(h) = 1 + 10^{-6} R_0 e^{-k_0 h} \tag{4.7}$$

[1]The model is not limited by the atmospheric model for the refractivity adopted.

$$R_0 = 325 \qquad k_0 = 0.1218 \text{ km}^{-1}, \tag{4.8}$$

with h being the altitude above sea level. In the implementation of the ray-tracing algorithm the atmosphere is discretised in radial layers centered at the centre of the Earth, chosen so that the radial distance between two consecutive interfaces remains constant[2]. We consider only showers that lie in a plane with the center of the Earth in it, and observation points that lie in the same plane, see Fig. 4.1.

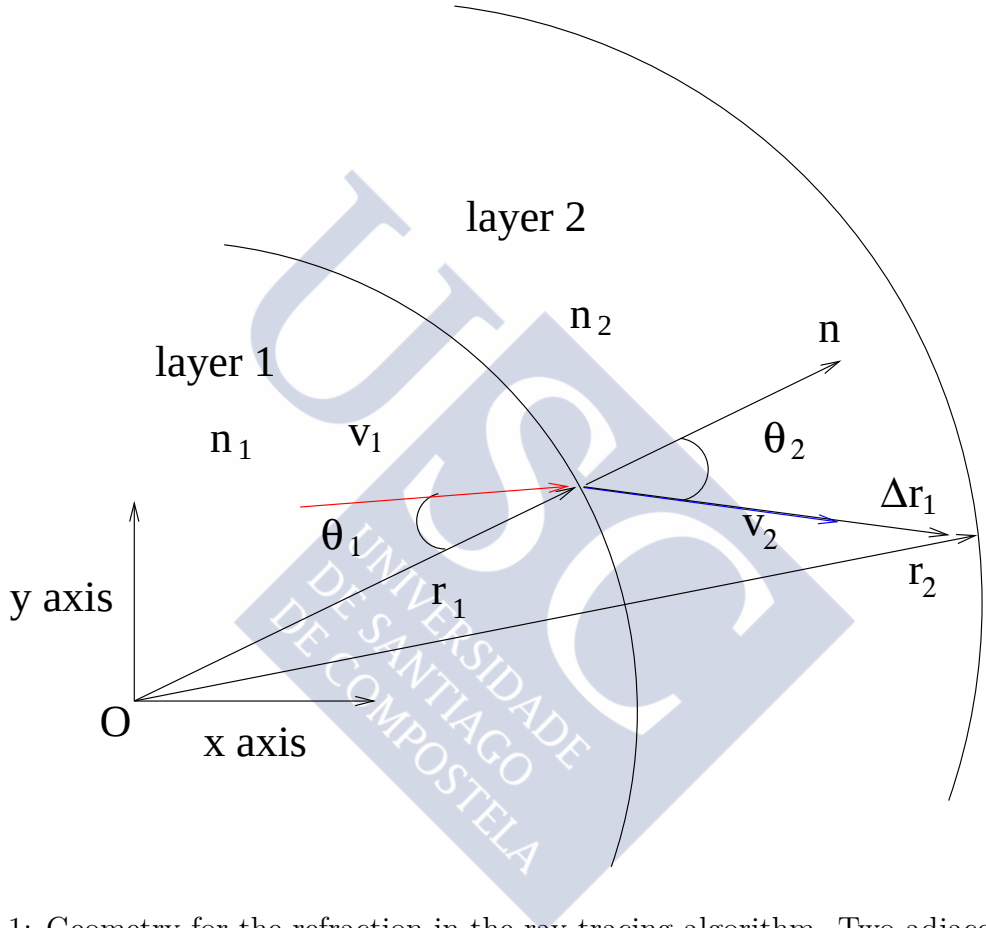

Figure 4.1: Geometry for the refraction in the ray tracing algorithm. Two adjacent layers are plotted. We show the incident ($\mathbf{v}_1$), refracted ($\mathbf{v}_2$) and normal ($\mathbf{n}$) vectors. Point O is the origin of the coordinate system and is located at the center of the Earth.

As sketched in Fig. 4.1, at the interface between layer 1 and layer 2 there are three relevant unitary vectors for any ray: the incident vector ($\mathbf{v}_1$), the refracted vector ($\mathbf{v}_2$), and the normal vector ($\mathbf{n}$). If (x_1, y_1) is the point where the ray hits the interface in a

[2]A much more efficient approach is to choose layers with a constant refractive index difference.

reference frame with origin at the centre of the Earth, the normal to the interface at that point is given by

$$\mathbf{n} = \frac{x_1}{r_1}\hat{\mathbf{x}} + \frac{y_1}{r_1}\hat{\mathbf{y}}, \tag{4.9}$$

where

$$r_1 = \sqrt{x_1^2 + y_1^2}. \tag{4.10}$$

The incident angle (first quadrant) is given by:

$$\theta_1 = \arccos\left(\mathbf{n} \cdot \mathbf{v}_1\right). \tag{4.11}$$

We can perform a rotation to a frame where the normal vector $\mathbf{n}$ has no x component. In that frame we have for the incident vector,

$$\mathbf{u}_1 = \mathbf{R}\mathbf{v}_1 = (s_x \sin\theta_1, s_y \cos\theta_1), \tag{4.12}$$

with $\mathbf{R}$ the rotation matrix, and s_x and s_y the signs of the components. Since the refractive indexes on both sides of the interface are known, the calculation of the refracted angle is straightforward,

$$\theta_2 = \arcsin\left(\frac{n_2}{n_1}\sin\theta_1\right), \tag{4.13}$$

and then the refracted vector in the new frame is,

$$\mathbf{u_2} = (s_x \sin\theta_2, s_y \cos\theta_2). \tag{4.14}$$

Rotating back, the refracted vector in the original frame is obtained:

$$\mathbf{v_2} = \mathbf{R}^{-1}\mathbf{u_2}. \tag{4.15}$$

Knowing the point at the interface where the ray hits ($\mathbf{r}_1$) and the refracted vector $\mathbf{v}_2$ we can calculate the point on the next interface ($\mathbf{r}_2$) and repeat the algorithm. For each layer, we calculate the distance the ray travels (Δr_i) and the travel time (Δt_i):

$$\Delta r_i = |\mathbf{r}_{i-1} - \mathbf{r}_i|, \tag{4.16}$$

$$\Delta t_i = \frac{n_i}{c}\Delta r_i. \tag{4.17}$$

Δr_i is the distance between the in and out points of the ith layer for a ray, and n_i is the refractive index of the ith layer (assumed constant). Fresnel coefficients are also calculated

at each interface, but in the atmosphere the effect on the refracted field across the interface is very small, with a typical difference between the fields on both sides of the interface $\sim 10^{-3}$.

We iterate until the ray arrives at the observer position. It is usually easier to do the ray tracing backwars starting at the observer position. Once the ray tracing ends we know the initial and end points of the ray, the distance $\sum_i \Delta r_i$ and the total travel time $\sum_i \Delta t_i$. The ray tracing algorithm can also be used to propagate rays to the ground and then reflect them until a high altitude observer is reached.

Finally, the ray tracing algorithm also allows the propagation using straight lines. This is done in order to compare with the simulations performed with ZHAireS, since ZHAireS does not take into account the curved ray propagation because it is only relevant for high zenith angle showers ($\gtrsim 80°$) as will be shown later in this chapter.

4.2.2 Geometry for the model

Throughout the next sections we use the following geometry. We define the off-axis angle ψ as that formed by the shower axis and the line connecting $X_{\max}$ and the observer position. This angle is indicated in the sketch in Fig. 4.2. Observers can be placed at different off-axis angles on the ground or at an altitude[3]. We distinguish between the height of the observer above the horizon h_z (see Fig. 4.3) and the actual height with respect to the ground h_a (Fig. 4.3).

When the curvature of Earth can not be neglected *i.e.* for very inclined showers, h_a will not be similar to h_z. For zenith angles $> 75°$, the difference between h_z and h_a is already noticeable.

4.3 Comparison of the model to ZHAireS simulations

Two immediate applications of the model for observers at the ground will be studied in this section - the dependence of the radio signal on ground altitude, and its zenith angle dependence. We will compare the results of the model and those obtained with the ZHAireS Monte Carlo. Throughout this section, all calculations with the model have been done using the ray tracing algorithm explained in section 4.2.1, and accounting for the

[3]Although the model was only implemented in software and discussed in this chapter for observers lying in the early-late region of the shower, Eq. (4.5) is also valid for observers in other regions on the ground, and the code can be expanded to calculate two-dimensional patterns of the electric field.

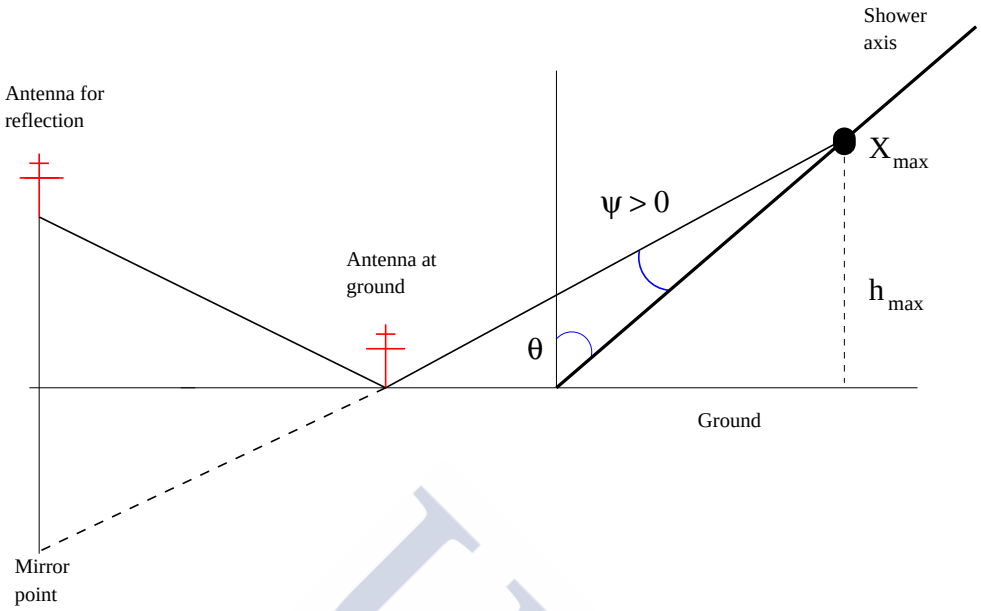

Figure 4.2: Geometry for the placement of the antennas. The sign convention for the off-axis angle is shown - positive (negative) values correspond to larger (smaller) distances from the shower maximum $X_{\max}$ to the observers, also called the late (early) region.

curved trajectories of rays. The comparison between straight and curved ray tracings can be seen in Chapter 6, where it is relevant for the physics of the ANITA experiment in discussion.

The comparison is made by confronting the radio signals simulated with ZHAireS with those obtained with the model. In order to do so, we first simulate the shower with AIRES and obtain the shower maximum. Once the maximum is known, we place antennas at different off-axis angles and calculate the field both with ZHAireS and our model. The model however does not predict the absolute value of the electric field and for this reason its predictions are scaled up or down to those of the full ZHAireS simulation.

4.3.1 Dependence of radio signal on ground altitude

We have studied the variation of the signal with the altitude of the ground where the array is located. We have used two ground altitudes - 0 m, which corresponds to sea level, and 1400 m, which corresponds to the altitude of the Pierre Auger Observatory. We simulate the same showers with the same parameters (energy, θ, random seed...), so that the difference between the fields comes mainly from the difference in the altitude of the

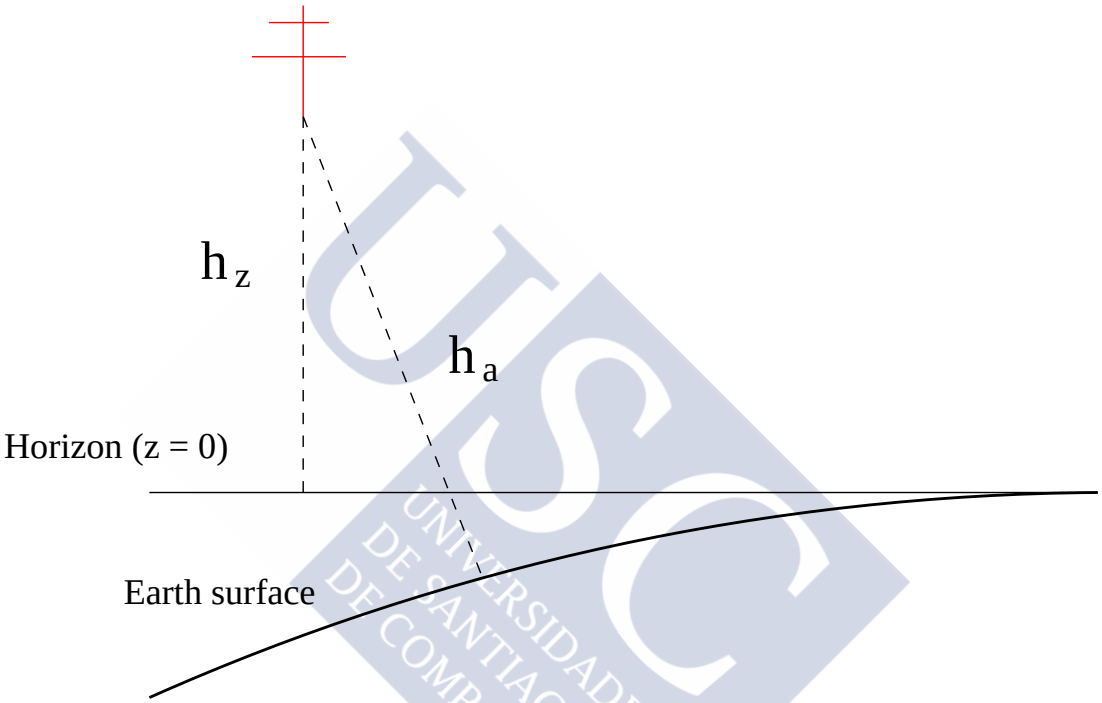

Figure 4.3: Geometry for the altitude of the antennas. The height used in this chapter (h_z) corresponds to the altitude for a *flat Earth*, while the true altitude (h_a) must be calculated taking into account the curvature of the Earth if this is not negligible.

ground only. We choose a $\theta = 60°$ shower with a vertical $X_{\rm max}$ of 424 g/cm^2. We use as input to the model the number of electrons and positrons $N(t)$ obtained in the ZHAireS simulations[4]. In Fig. 4.4 we show the radio signal *vs* off-axis angle ψ (see Fig. 4.2) for the two altitudes comparing the results of the model and ZHAireS simulations at a frequency of 300 MHz. The agreement between the model and the Monte Carlo is better at 0 m than at 1400 m. This is understandable, since the model has been derived in the Fraunhofer regime and at 0 m of ground altitude the array is further away from the shower than at 1400 m. The position of the peak of the ψ distribution of the field is not reproduced exactly by the model, but this is due to the fact that the model is one-dimensional and the lateral structure of the shower is crucial for computing the fields, especially for the observer at the peak whose off-axis angle is typically the Cherenkov angle at the position of $X_{\rm max}$ (see Section 2.3.2 in Chapter 2). In any case and despite the fact that for a ground at 1400 m of altitude the observer is closer to the near-field zone, the qualitative aspects of the off-axis angle distribution of the signal are reasonably well predicted by the model. One can see in Fig. 4.4 that the position of the peak of the field is further away from shower core ($r = 0$) for the ground at 0 m than at 1400 m, a geometrical effect that is due to the larger distance from $X_{\rm max}$ to ground for a ground at sea level altitude. This will be further explored in Section 4.4.

4.3.2 Frequency and zenith angle dependences

We have simulated showers with zenithal angles $\theta = 60°$, $70°$ and $80°$, initiated by a primary proton of energy 10^{19} eV. The ground is placed at an altitude of 2800 m, similar to the altitude of the South Pole. The magnetic field has a magnitude of $B = 54$ μT with an inclination of $I = -73°$.

We compare the results of the ZHAireS simulations and those of the model in Figs. 4.5, 4.6 and 4.7, where it can be seen that the overall shape of the off-axis angular distributions of the radio signal is well reproduced by the model. Although the quantitative aspects are not exactly reproduced, the agreement is better for high zenith showers, since for those showers the observer lies more in the Fraunhofer zone given by the condition $kR \gg 1$. It is also worth noting that a larger frequency implies a larger value of kR, and because of that the predictions of the model for 300 MHz and 900 MHz tend to be closer to the ZHAireS predictions than the 50 MHz ones. This tendency continues until the frequency is

[4]Note that one can obtain a good estimate of $N(t)$ without investing a large CPU time using an appropriate thinning level in the ZHAireS simulations.

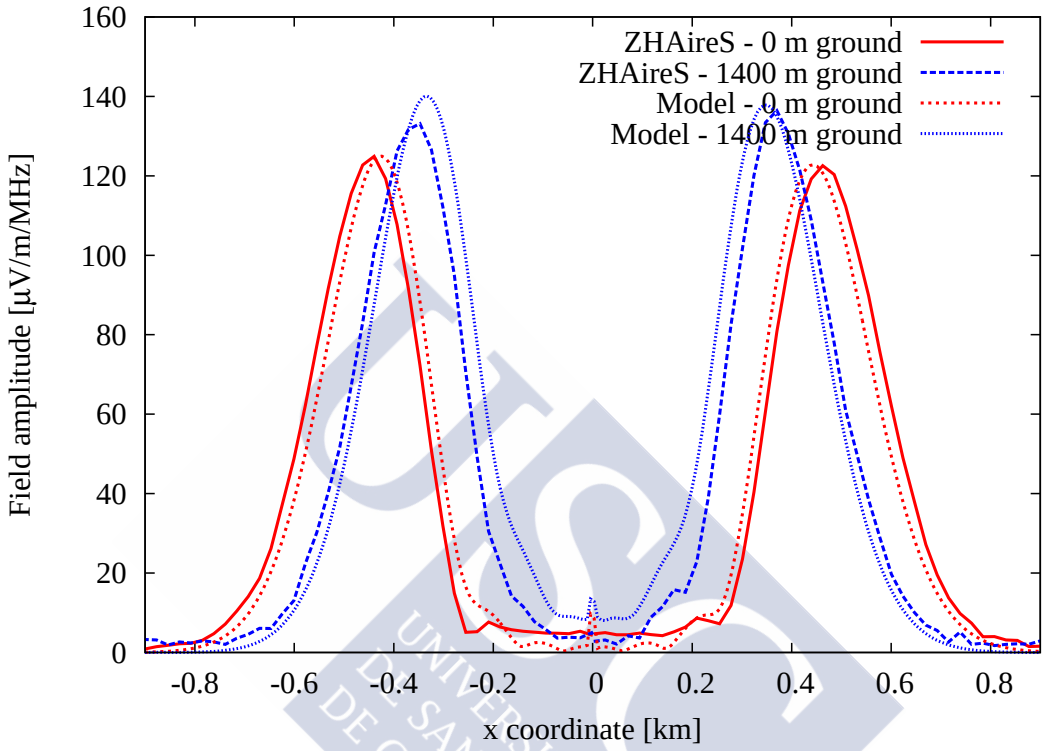

Figure 4.4: Field amplitude in frequency domain as a function of the x coordinate on the ground for 0 m (red lines) and 1400 m (blue lines) of ground altitude. ZHAireS and the model predictions are shown. The model predictions have been rescaled (the model predicts no normalization). The shower has 60° of zenithal angle, its primary is a proton of 10^{19} eV of energy and comes from the North, whereas the observer antennas are placed on the North-South (also called early-late) line (positive x means South side of the line). The observation frequency is 300 MHz. The magnetic field is 54 μT with $-73°$ of inclination. The shower maximum corresponds to a vertical depth of 424 g/cm^2. See text for details.

sufficiently large that treating the shower as a one-dimensional object is no longer a good approximation.

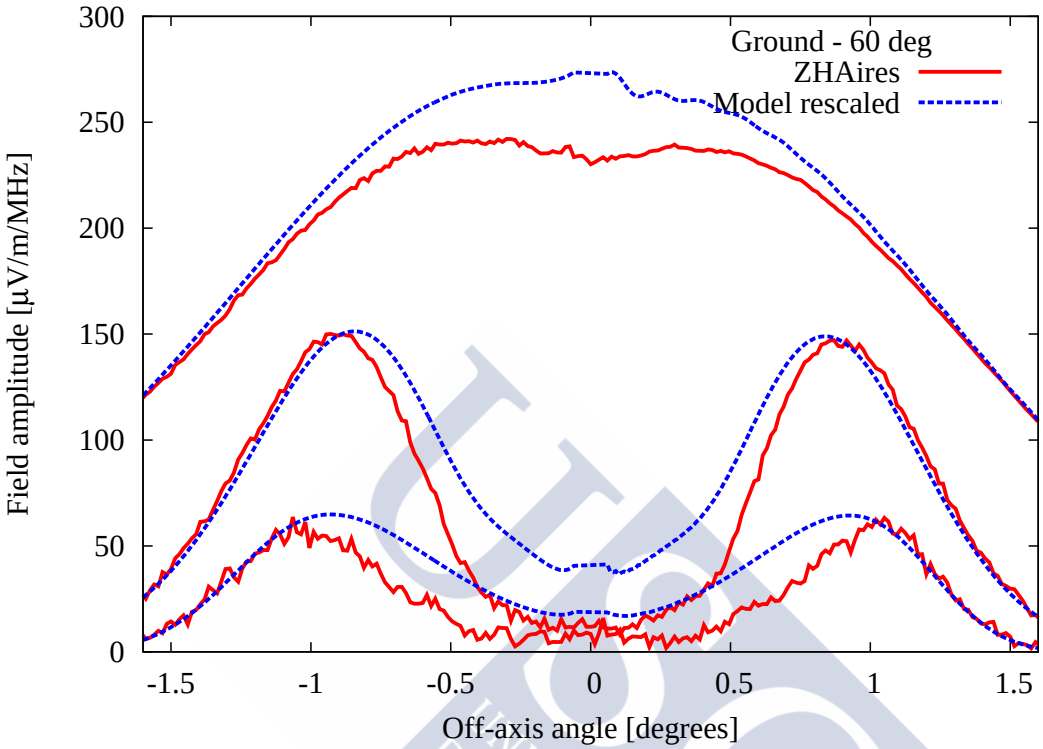

Figure 4.5: Field amplitude in frequency domain as a function of the off-axis angle ψ (see Fig. 4.2). ZHAireS (red solid lines) and the model predictions (blue dashed lines) are shown. The model predictions have been rescaled. The observation frequencies are, from top to bottom, 50, 300 and 900 MHz. The shower has 60° of zenithal angle, initiated by a proton of energy 10^{19} eV arriving from the magnetic North. The antennas are placed on the North-South (also called early-late) line (positive ψ corresponds to the South side of the line). The magnetic field is 54 μT with $-73°$ of inclination.

While we have shown that the model predictions are closer to the Monte Carlo ones for observers in the Fraunhofer regime, the shape of the off-axis angle distribution of the radio signal is qualitatively reproduced even for a 30° zenith angle proton shower at a ground of 1400 m of altitude, as shown in Fig. 4.8.

As a general conclusion, despite its simplicity, the model predictions for the off-axis distribution of the field are in qualitative agreement with sophisticated and accurate simulations performed with ZHAireS for many shower geometries, altitudes of ground level

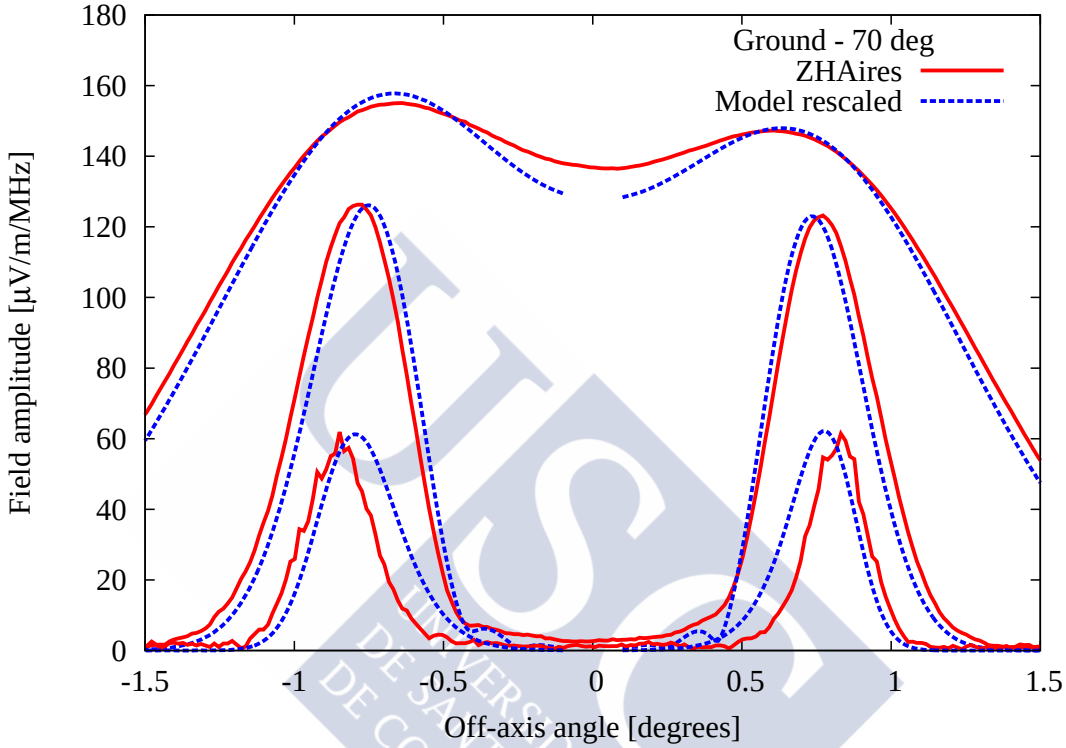

Figure 4.6: Field amplitude in frequency domain as a function of the off-axis angle ψ (see Fig. 4.2). ZHAireS (red solid lines) and the model predictions (blue dashed lines) are shown. The model predictions have been rescaled. The observation frequencies are, from top to bottom, 50, 300 and 900 MHz. The shower has 70° of zenithal angle, initiated by a proton of energy 10^{19} eV arriving from the magnetic North. The antennas are placed on the North-South line (positive ψ corresponds to the South side of the line). The magnetic field is 54 μT with $-73°$ of inclination.

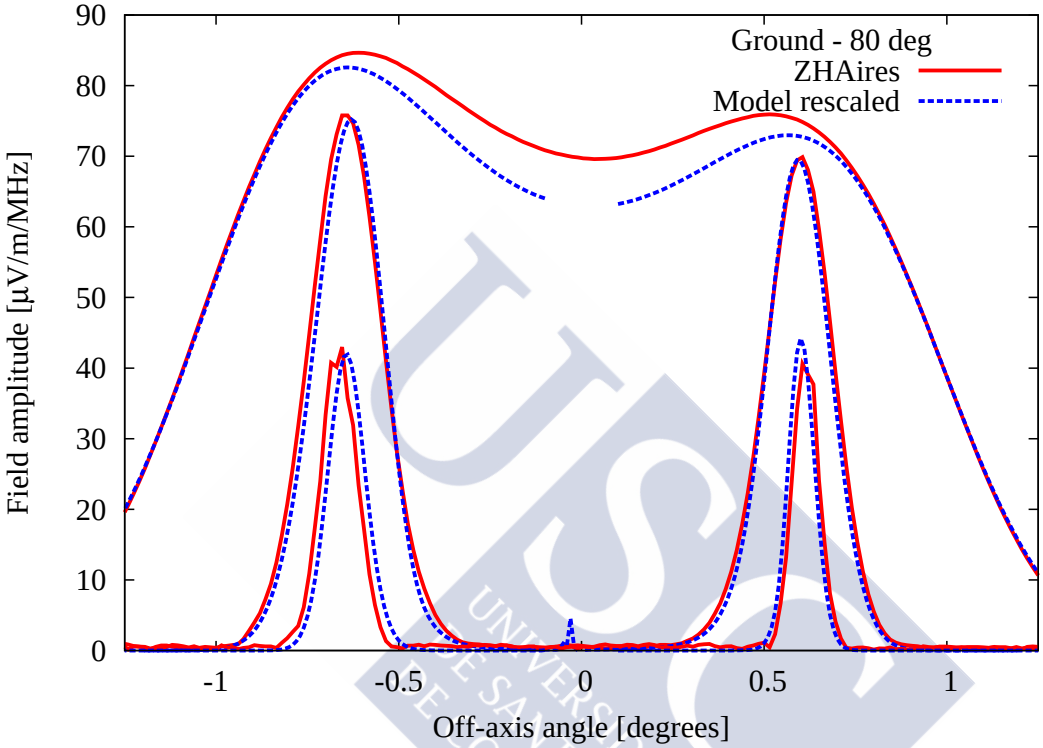

Figure 4.7: Field amplitude in frequency domain as a function of the off-axis angle ψ (see Fig. 4.2). ZHAireS (red solid lines) and the model predictions (blue dashed lines) are shown. The model predictions have been rescaled. The observation frequencies are, from top to bottom, 50, 300 and 900 MHz. The shower has 80° of zenithal angle, inititated by a proton of energy 10^{19} eV arriving from magnetic the North. The antennas are placed on the North-South line (positive ψ corresponds to South side of the line). The magnetic field is 54 μT with $-73°$ of inclination.

and frequencies of observation.

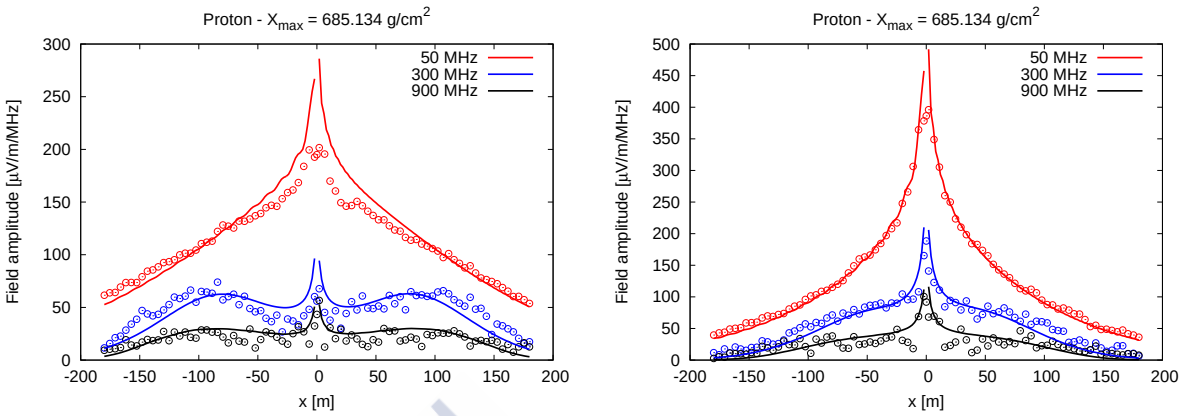

Figure 4.8: Field amplitude as a function of the x coordinate at ground level for a 10^{19} eV and 30° proton shower coming from the North with 685 g/cm^2 of vertical depth. ZHAireS simulations (points) and model predictions (lines) are shown. The magnetic field is 54 μT with $-73°$ of inclination. The plotted frequencies are, from top to bottom, 50 (red), 300 (blue) and 900 MHz (black). Left: ground at 0 m (sea level). Right: Ground at 1400 m.

4.4 Applications of the model

The 1D model developed in Section 4.2 can be applied to many physical situations to predict in a fast and accurate manner the spatial distribution of the electric field as a function of frequency and for a variety of shower geometries. There are many applications one can foresee, for instance:

- For the design and study of the feasibility of an array of antennas for UHECR detection with the radio technique.

- Since the model can also be applied to predict the radio pulses that arrive at a high altitude detector after reflecting on the ground, it can be used in the interpretation of data collected in experiments such as the ANITA balloon payload that has recently detected 14 UHECRs using this technique or in the design of new experiments using the same concept (see Chapter 6).

- The model can also be applied to search for observables that are sensitive to shower

parameters, such as the nature of the primary particle initiating the shower, without the need to perform time-consuming Monte Carlo simulations.

- Eq. (4.6) can also be easily adapted to predict the modulus of the field in a 3D array of antennas buried in a dense medium such as ice, a concept detector exploited in many initiatives such as the ARA and ARIANNA experiments. Either the field from air showers or that from in-ice showers could be in principle predicted with the model.

For these applications, once the array layout and arrival directions of the CRs are known, the only input needed is $N(t)$, the shower profile, in the form of a parameterization such as the Gaisser-Hillas function [10], where parameters such as the primary energy, the depth of shower maximum $X_{\max}$, *etc.*, can be varied at will.

In the following we concentrate on using the model for the study of the sensitivity of the radio signal to $X_{\max}$ and hence to primary CR composition.

4.4.1 Searching for radio observables sensitive to composition with the model

The variation of the depth of the position of shower maximum and its impact on the electric field pattern is capital for the radio technique. The understanding of this relation can open the door to measuring the composition of the cosmic rays using radio.

The main question can be posed as: "is there any measurable property of the electric field that is sensitive to the $X_{\max}$ of the shower?" Finding a quantity or a method that allows us to determine the composition of the cosmic rays could consolidate radio as an experimental technique.

We will study two promising observables, namely: the position of the peak of the lateral distribution of the signal and the ratio of the electric field at two different locations and we will their address their viability as composition observables. Similar methods were also exploited in [11, 12].

Other methods, such as a global fit to the 2D lateral distribution of the signal using $X_{\max}$ as a parameter, are being studied [13]. However, they require many MC simulations as an input, and for this reason it is worth studying the problem with our model and trying to obtain observables more simple or more direct than a 2D fit.

4.4.2 Position of the peak of the electric field in the radio lateral distribution function ($r_{\max}$)

In principle, there is an obvious quantity that depends on $X_{\max}$, and that is the position of the maximum of the radio lateral distribution function ($r_{\max}$) at a given frequency. The possibility of using it as a tool for knowing the composition of a shower has been addressed in [11].

We begin our study with 60°, 70° and 80° zenith angle showers, where the $X_{\max}$ is farther away from the ground and we could expect that the changes in the position of $X_{\max}$ induce a bigger change on the position $r_{\max}$ of the maximum field on the ground. We use the model to predict the field as a function of the radial distance to the shower core varying the slant depth of shower maximum $X_{\max}$ from 550 to 950 g/cm^2, although the experimental region for inclined showers is narrower than that [14]. We change the position of the shower maximum in a standard Gaisser-Hillas function for the longitudinal shower profile, and the rest of the parameters[5] are fixed to those of a mean 10^{19} eV shower. Then, we calculate the field with the model, find the position of the maximum of the field ($r_{\max}$) along the early and late lines of the shower at ground and plot $r_{\max}$ as a function of $X_{\max}$.

We show the results in Figs. 4.9, 4.10 and 4.11. As seen for instance in Fig. 4.4, the lateral distribution of the signal exhibits 2 maxima, one in the early region and one in the late region of the shower, where the early (late) refers to the region on the ground where the signal arrives first (last). In both regions, $r_{\max}$ exhibits a monotonously growing behaviour with $X_{\max}$ except for the 80° shower in the late region. The maximum slope of an $r_{\max}$ *vs* $X_{\max}$ linear fit is achieved in the early region of the 80° shower and amounts to a value of 0.5 m/(g/cm^2). This means that, to measure $X_{\max}$ with a precision of 20 g/cm^2, we should reconstruct the position of the maximum field with a precision of $\sim$ 10 m. In LOFAR [15] the distance between antennas is less than $\sim$ 10 m within each antenna cluster and the typical number of antennas per event is $\sim$ 200, which may allow to reconstruct $r_{\max}$ with enough precision [13]. AERA [16], with a typical distance between antennas of 100 m, and a typical number of less than $\sim$ 10 antennas per event will have more difficulties in using the $r_{\max}$ observable for an accurate determination of $X_{\max}$. This serves as a good

[5]The Gaisser-Hillas function is

$$N(X) = N_{\max}\left(\frac{X - X_0}{X_{\max} - X_0}\right)^{(X_{\max}-X_0)/\lambda} \exp\left(\frac{X_{\max}-X}{\lambda}\right), \tag{4.18}$$

where X is the slant depth and $X_{\max}$, X_0, $N_{\max}$ and λ are parameters.

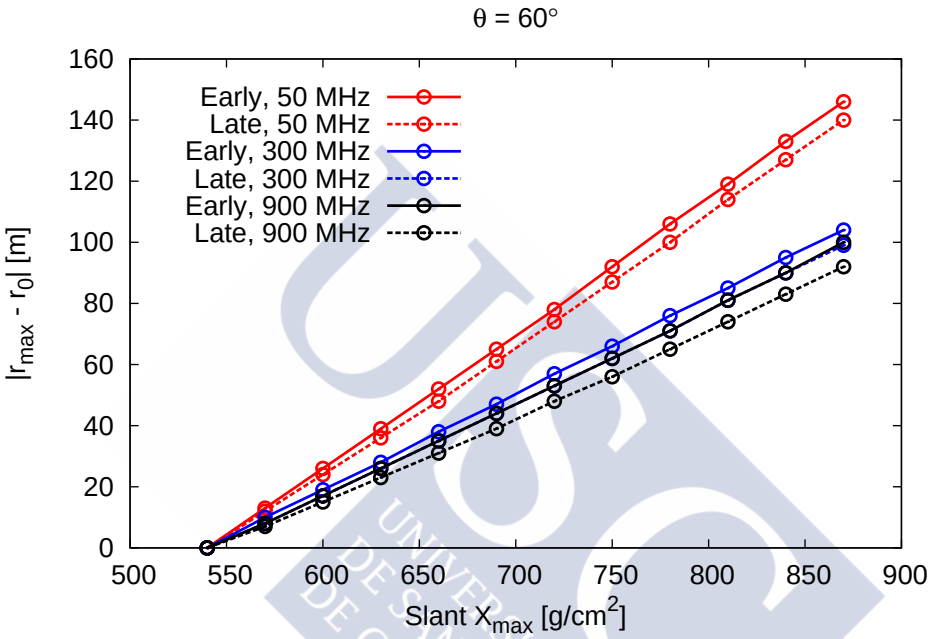

Figure 4.9: Position of the peak value of the electric field $r_{\max}$ minus r_0 ($r_0 = r_{\max}$ for a shower with $X_{\max} = 550$ g/cm^2) as a function of the $X_{\max}$ slant depth for a 60° shower. Solid lines represent the early region of the shower and dashed lines represent the late region. The values of $r_{\max}$ are shown for frequencies 50 MHz (red), 300 MHz (blue) and 900 MHz (black).

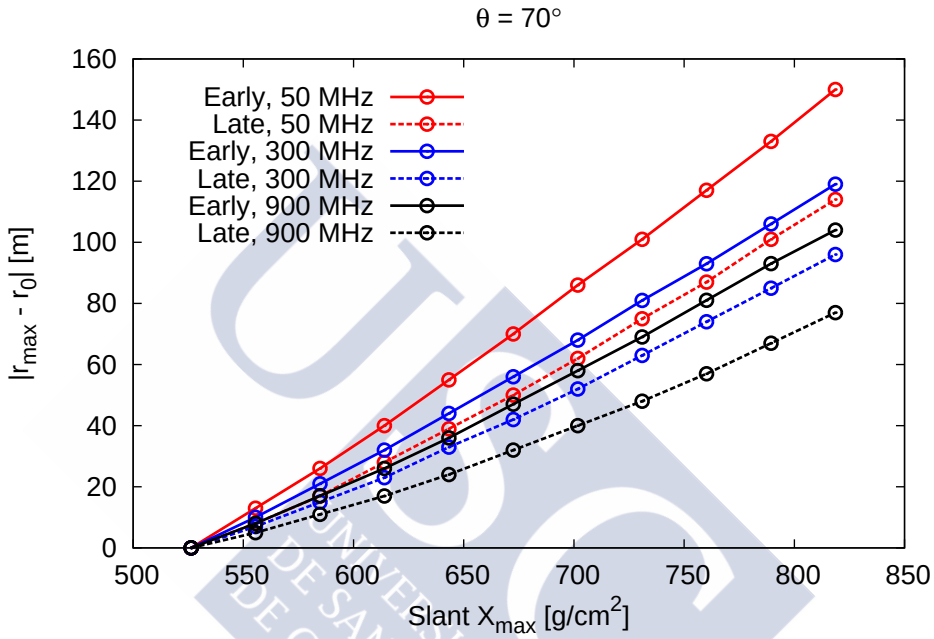

Figure 4.10: Position of the peak value of the electric field $r_{\max}$ minus r_0 ($r_0 = r_{\max}$ for a shower with $X_{\max} = 550$ g/cm^2) as a function of the $X_{\max}$ slant depth for a 70° shower. Solid lines represent the early region of the shower and dashed lines represent the late region. The values of $r_{\max}$ are shown for frequencies 50 MHz (red), 300 MHz (blue) and 900 MHz (black).

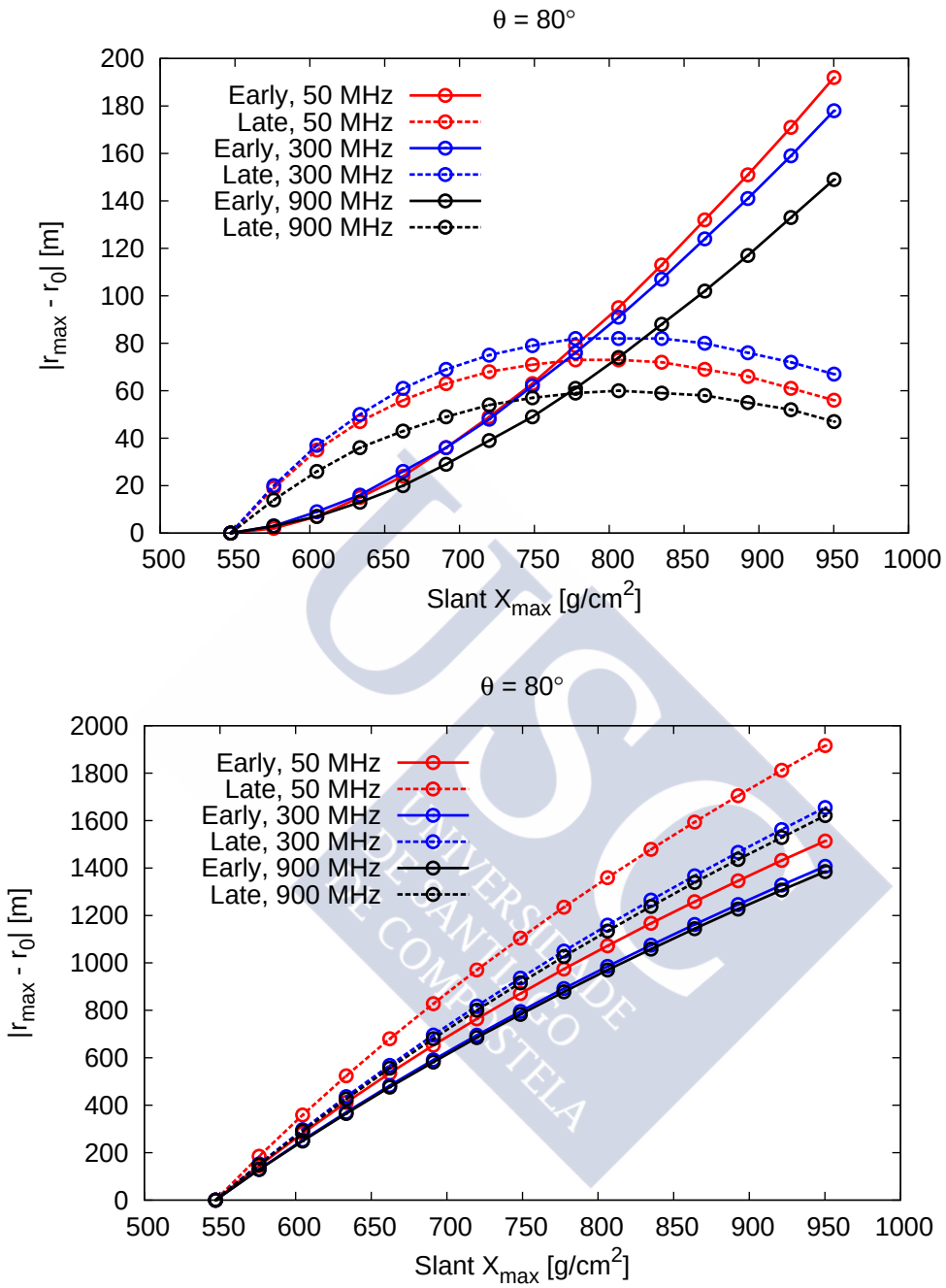

Figure 4.11: Position of the peak value of the electric field $r_{\max}$ minus r_0 ($r_0 = r_{\max}$ for a shower with $X_{\max} = 550$ g/cm^2) as a function of the $X_{\max}$ slant depth for a 80° shower. Solid lines represent the early region of the shower and dashed lines represent the late region. The values of $r_{\max}$ are shown for frequencies 50 MHz (red), 300 MHz (blue) and 900 MHz (black). Top: $r_{\max}$ calculated with the usual ZHAireS altitude-dependent refractive index. Bottom: $r_{\max}$ calculated with a constant refractive index $n = 1.0001$.

illustration of the type of conclusions one can obtain in a short time applying the model developed in this chapter.

The sensitivity to $X_{\max}$ is poor for the late region of the 80° shower in Fig. 4.11 (top), since it exhibits a "plateau" around 750 g/cm^2, where the mean $X_{\max}$ measured at 10^{19} eV of primary energy by the Auger observatory lies. That plateau is created by the variable refractive index present in the atmosphere, as it is evidenced by the fact that in model calculations with a constant refractive the plateau disappears, see Fig. 4.11 (bottom).

While our analysis was limited to inclined showers, model calculations indicate that vertical showers have less variation on the $r_{\max}$ position when changing the depth of shower maximum. This implies that using the position of the peak electric field in the radio signal lateral distribution as an observable is less viable for vertical showers than for inclined showers.

4.4.3 Ratio of the electric field at two different positions

As discussed in Chapter 2, the electric field at low frequencies (few tens of MHz) is coherent and scales with shower energy and with $\sin\alpha$, with α the geomagnetic angle (the angle between $\mathbf{v}$ and $\mathbf{B}$ with $\mathbf{v}$ parallel to shower axis and $\mathbf{B}$ the geomagnetic field). Due to this scaling, a convenient quantity to work with is the normalised field ϵ (the electric field divided by $\sin\alpha$).

The electric field as a function of distance to the core d for showers of fixed zenith angle exhibits a distance to the core d_0 where the normalised field $\epsilon(d_0)$ depends very weakly on the energy and $X_{\max}$ of the showers. In contrast, the fields at $d > d_0$ are highly dependent on the depth of shower maximum $X_{\max}$ as shown in [11]. We can define a distance $d_s > d_0$ and a ratio:

$$r = \frac{\epsilon(d_0)}{\epsilon(d_s)}, \tag{4.19}$$

that we expect to depend on the shower maximum.

In [12], the method is applied to experimental data in the frequency band of the LOPES experiment ($\sim$ 40-80 MHz), yielding promising results. However, the precision was still very low to claim that the ratio r is a feasible observable sensitive to $X_{\max}$.

We will now use the model developed in Section 4.2 to study the parameter r as an estimator of $X_{\max}$. LOPES explored showers with less than 40°, and we will use our model to test this approach at higher angles. We use a fixed frequency of 50 MHz and place the observers on the ground along the early-late line (see Fig. 4.2). In Fig. 4.12 we show the

electric field ϵ predicted by the model[6] as a function of d for showers with zenith angle 40 and 50°. The existence of a region where the curves cross each other and hence ϵ is less sensitive to $X_{\max}$ is apparent, and we choose the crossing point as the location of the distance d_0 that is marked in the plot by the vertical dashed black lines[7]. The blue lines indicate the location of the distance d_s at which the sensitivity of ϵ to $X_{\max}$ is large.

The trend of having a distance d_0 where the lines intersect clearly continues in 60° showers as shown in Fig. 4.13. At larger zenith angles such as $\theta = 70°$ and 80° the trend is however less clear.

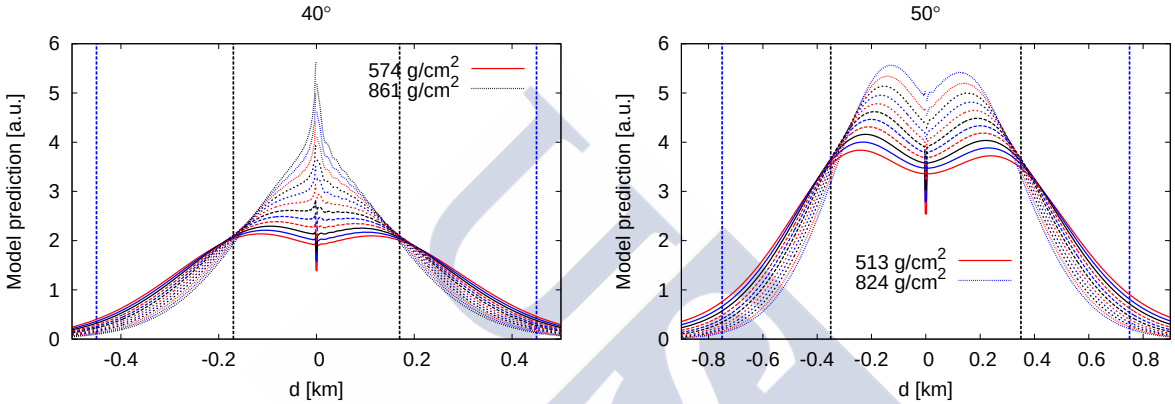

Figure 4.12: Electric field predicted by the model as a function of the distance d to the core in showers with different $X_{\max}$. Vertical black lines mark the distance d_0 and vertical blue lines mark the distance d_s where the sensitivity to $X_{\max}$ is weak and large respectively. The observation frequency is 50 MHz. Left: $\theta = 40°$ shower. $d_0 = 0.17$ km. $d_s = 0.45$ km. Contiguous lines have a slant depth difference of ~ 25 g/cm^2 decreasing from top to bottom at $d \approx 0$. Right: $\theta = 50°$ shower. $d_0 = 0.35$ km. $d_s = 0.75$ km. Contiguous lines have a slant depth difference of ~ 30 g/cm^2 decreasing from top to bottom at $d \approx 0$.

The ratio r in Eq. (4.19) is sensitive to the chosen distances d_0 and d_s that depend on the shower zenith angle. Our model allows us to choose the optimal distances at which r is maximum (exhibits the maximum sensitivity to $X_{\max}$) for each zenith angle. In Figs. 4.15 and 4.16 we show the sensitivity of r to $X_{\max}$ for the distances d_0 and d_s indicated in Figs. 4.12, 4.13 and 4.14. A sensitivity of $X_{\max}$ of ~ 20 g/cm^2 (comparable to that of the

[6]Since the model does not take into account the geomagnetic effect, we will use the electric field from the model and the normalised field ϵ indistinctively.

[7]Being the model mainly qualitative, we will refrain from performing a rigorous calculation for obtaining d_0. The analysis presented here is mainly for illustrative purposes of the possible applications of the model.

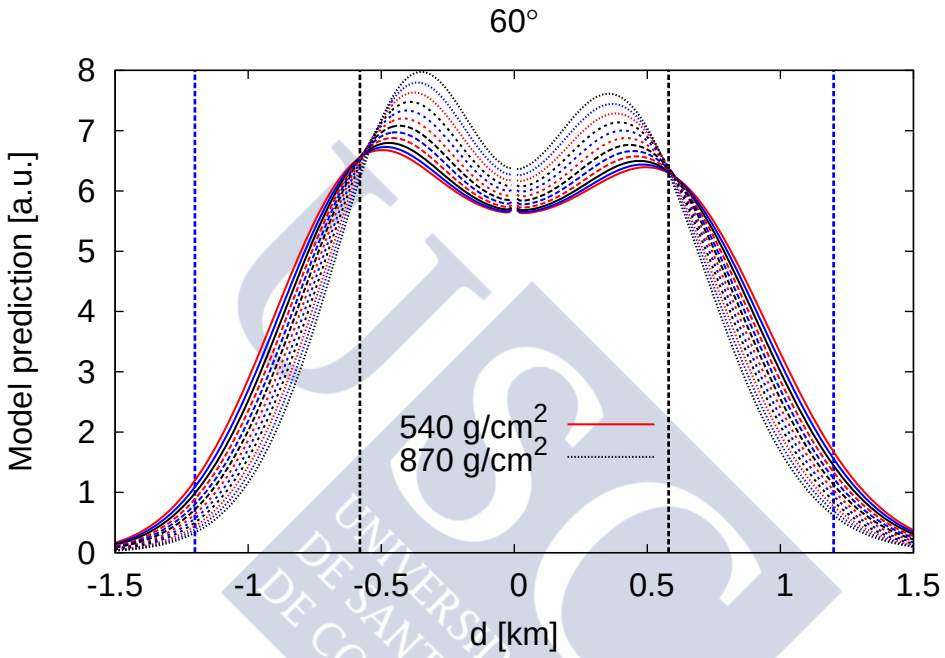

Figure 4.13: Electric field predicted by the model as a function of the distance d to the core in showers with different $X_{\max}$. Vertical black lines mark the distance d_0 and vertical blue lines mark the distance d_s where the sensitivity to $X_{\max}$ is weak and large respectively. The observation frequency is 50 MHz. $\theta = 50°$ shower. $d_0 = 0.58$ km. $d_s = 1.2$ km. Contiguous lines have a slant depth difference of ~ 25 g/cm^2 decreasing from top to bottom at $d \approx 0$.

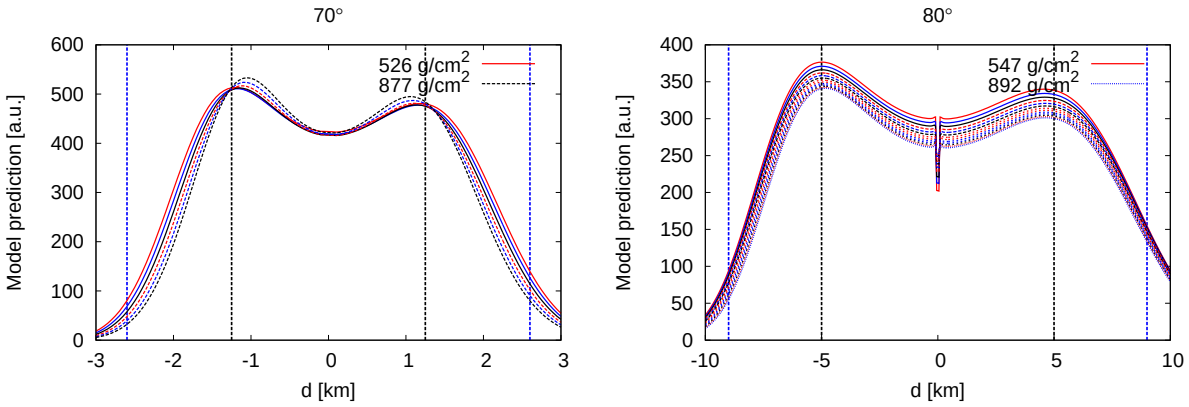

Figure 4.14: Electric field predicted by the model as a function of the distance d to the core in showers with different $X_{\max}$. Vertical black lines mark the distance d_0 and vertical blue lines mark the distance d_s where the sensitivity to $X_{\max}$ is weak and large respectively. The observation frequency is 50 MHz. Left: $\theta = 70°$ shower. $d_0 = 0.75$ km. $d_s = 2.6$ km. Contiguous lines have a slant depth difference of ~ 59 g/cm^2 decreasing from top to bottom at $d \approx 0$. Right: $\theta = 80°$ shower. $d_0 = 5$ km. $d_s = 9$ km. Contiguous lines have a slant depth difference of ~ 29 g/cm^2 decreasing from top to bottom at $d \approx 0$.

FD detector) can be achieved if the ratio can be measured with an uncertainty $\sigma(r) \sim 2$, which seems plausible in current radio experiments.

At least for intermediate zenith angles, r appears to be sensitive to $X_{\max}$, a fact that is worth exploring further in dedicated simulations that take into account the response of the detector and discrete sampling of the electric field at a limited number of positions around the shower core. Our results seem to suggest that at least for intermediate angle showers the ratio could suffice to distinguish a mean proton shower from a mean iron shower. Nevertheless, a better account of the features of the ongoing experiments and a more serious study of the detectors is needed to verify such a claim.

4.4.4 Limitations of the model

The simplified model presented here fails at reproducing all the features of the frequency spectrum seen in Monte Carlo simulations performed with ZHAireS (see for instance Fig. 2.12). It is clear from the discussion of the box model of shower development in Section 2.1.3 that accounting only for the longitudinal shower development and neglecting the other relevant shower dimensions is not a good approximation when trying to reproduce

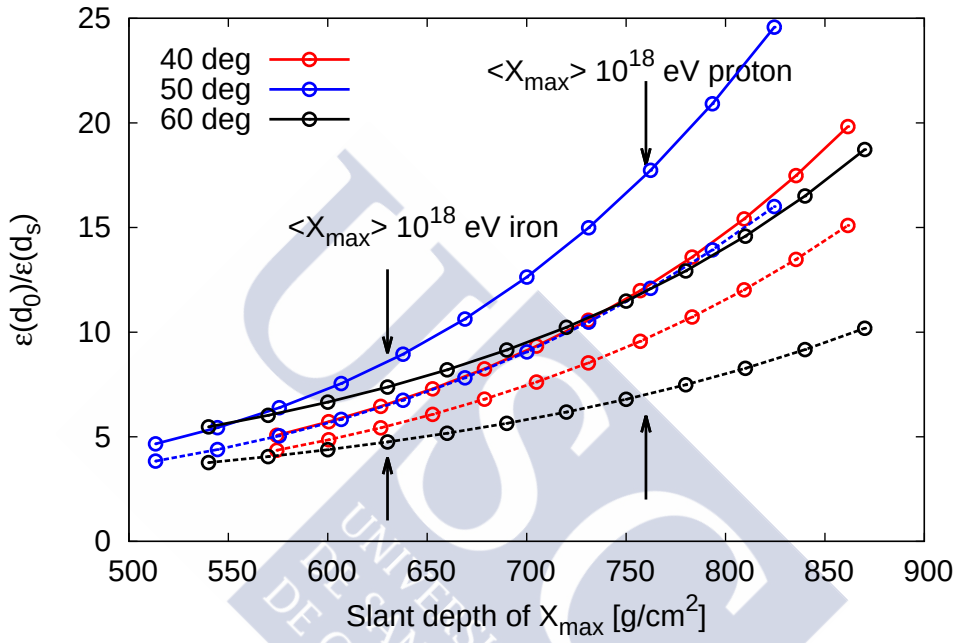

Figure 4.15: Ratio $r = \epsilon(d_0)/\epsilon(d_s)$ as a function of the shower maximum slant depth. The curves correspond to showers of $\theta = 40°$ (red), $\theta = 50°$ (blue) and $\theta = 60°$ (black). Solid (dashed) lines correspond to the early (late) region of the corresponding showers. Arrows indicate the mean $X_{\max}$ for 10^{18} eV proton and iron showers predicted in shower simulations with the QGSJETII model.

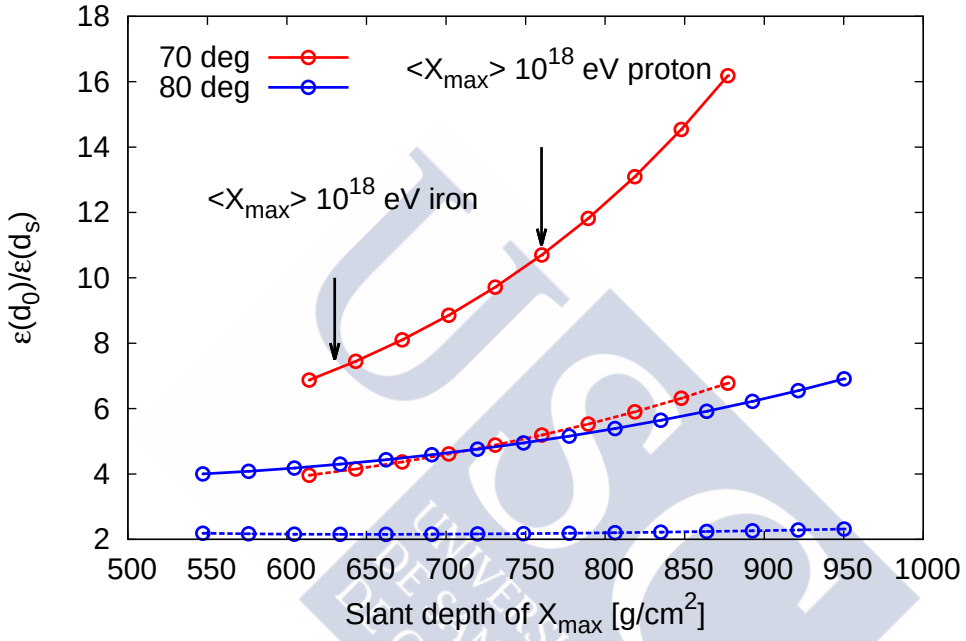

Figure 4.16: Ratio $r = \epsilon(d_0)/\epsilon(d_s)$ as a function of the shower maximum slant depth. The curves correspond to showers of $\theta = 70°$ (red) and $\theta = 80°$ (black). Solid (dashed) lines correspond to the early (late) region of the corresponding showers. Arrows indicate the mean $X_{\max}$ for 10^{18} eV proton and iron showers predicted in shower simulations with the QGSJETII model.

the richness of the frequency spectrum of the emitted radiation in air showers. Moreover, Eq. (4.5) was derived using the Fraunhofer approximation and ignoring the polarisation of the electric field, which is usually not an accurate approximation for air showers. We have checked that accounting for the angular factors in Eqs. (4.1) and (4.2) does not improve significantly the agreement between the results of the model and those of the ZHAireS Monte Carlo. The lateral distribution and the directions of the particles in the shower are important for accurately computing the spectrum even for large off-axis angles [8], and they are not present in our one-dimensional model.

Bibliography

[1] J. Alvarez-Muñiz, W. R. Carvalho Jr., and E. Zas. Monte Carlo simulations of radio pulses in atmospheric showers using ZHAireS. *Astroparticle Physics*, **35**:325, 2012.

[2] T. Huege, M. Ludwig, and C. W. James. Simulating radio emission from air showers with CoREAS. *AIP Conference Proceedings*, **1535**:128, 2012.

[3] J. Alvarez-Muñiz, C. W. James, R. J. Protheroe, and E. Zas. Thinned simulations of extremely energetic showers in dense media for radio applications. *Astroparticle Physics*, **32**:100, 2009.

[4] A. M. Hillas. Shower simulation: lessons from MOCCA. *Nuclear Physics B (Proceedings Supplements)*, **52**(3):29, 1997.

[5] M. Kobal. A thinning method using weight limitation for air-shower simulations. *Astroparticle Physics*, **15**:259, 2001.

[6] S. Hoover *et al.* Observation of ultrahigh-energy cosmic rays with the ANITA balloon-borne radio interferometer. *Physical Review Letters*, **105**(151101), 2010.

[7] J. Alvarez-Muñiz, R. A. Vázquez, and E. Zas. Calculation methods for radio pulses from high energy showers. *Physical Review D*, **105**(063001), 2000.

[8] J. Alvarez-Muñiz, A. Romero-Wolf W. R. Carvalho Jr., M. Tueros, and E. Zas. Coherent radiation from extensive air showers in the ultrahigh frequency band. *Physical Review D*, **86**(123007), 2012.

[9] N. C. Gerson. Variation in the index of refraction of the atmosphere. *Pure and Applied Geophysics*, **13**:3, 1948.

[10] T.K. Gaisser and A.M. Hillas. Reliability of the method of constant intensity cuts for reconstructing the average development of vertical showers. In *Proceedings of the 15th International Cosmic Ray Conference (ICRC 1977)*, volume 8, page 353.

[11] K.D. de Vries, O. Scholten, and K. Werner. The air shower maximum probed by Cherenkov effects from radio emission. *Astroparticle Physics*, **45**:23, 2013.

[12] W. D. Apel *et al.* Reconstruction of the energy and depth of maximum of cosmic-ray air-showers from LOPES radio measurements. *Physical Review D*, **90**(062001), 2014.

[13] S. Buitink *et al.* Method for high precision reconstruction of air shower $X_{\max}$ using two-dimensional radio intensity profiles. *Physical Review D*, **90**(082003), 2014.

[14] J. Abraham *et al.* Measurement of the depth of maximum of extensive air showers above 10^{18} eV. *Physical Review Letters*, **104**(091101), 2010.

[15] P. Schellart *et al.* Detecting cosmic rays with the LOFAR radio telescope. *Astronomy and Astrophysics*, **A98**:560, 2013.

[16] F. G. Schröder *et al.* Radio detection of air showers with Auger Engineering Radio Array. In *Proceedings of the 33rd International Cosmic Ray Conference (ICRC 2013)*, number 0899. arXiv:1307.5059.

USC
UNIVERSIDADE
DE SANTIAGO
DE COMPOSTELA

Chapter I

Intermission
Antennas for particle detection

So far, we have focused our attention on the calculation of electric fields. However, in order to link the electric field with the experimental results, we need to understand how the electric field of a particle shower interacts with a receiving antenna.

Most antenna books (for instance, [1]) do not treat the case of several sources at different angles emitting radiation (far-field zone) at a fixed frequency towards the antenna. Engineering applications usually deal with a point source in the far field and use the electric field from the source to calculate the voltage at the receiving antenna. This is not the case for a typical shower. Particle showers subtend a vast angular region, in general, and have a large number of tracks emitting radiation. We need a formula to relate the field emitted by the particles of the shower with the voltage at the antenna, which is usually the quantity that is measured in the experiments. The calculation of this formula is the objective of this intermission that links the radio theory with the radio applications.

I.1 The reciprocity theorem

We begin by deriving the reciprocity theorem, needed to obtain an equation for the voltage received at an antenna. Derivations of the reciprocity theorem can be found in [1] and [2].

Let us consider a volume of space that can have an arbitrary shape, finite or infinite, simply or multiply connected... Now, a configuration of total current and electric field is considered $(\mathbf{J}_1, \mathbf{E}_1)$. Then, a different configuration is placed in the same volume $(\mathbf{J}_2, \mathbf{E}_2)$. Both configurations can represent different physical situations, but as long as they both verify Maxwell's equations, the reciprocity theorem states that they have to verify

$$\boxed{\int_V (\mathbf{E}_1 \cdot \mathbf{J}_2 - \mathbf{J}_1 \cdot \mathbf{E}_2)\, \mathrm{d}V = \oint_S (\mathbf{E}_2 \times \mathbf{H}_1 - \mathbf{E}_1 \times \mathbf{H}_2) \cdot \mathrm{d}\mathbf{S}}, \tag{I.1}$$

where the first integral is performed in the volume of space and the second in the (closed)

surface enclosing the volume. $\mathbf{H}_{1,2}$ are the auxiliary magnetic fields $\mathbf{H}$ for each configuration, which can be written in frequency domain as

$$\mathbf{H}_{1,2} = \frac{1}{i\omega\mu}\nabla \times \mathbf{E}_{1,2}. \tag{I.2}$$

Let us prove Eq. (I.1). The medium is parametrised by the permittivity $\epsilon(\mathbf{x},\omega)$, permeability $\mu(\mathbf{x},\omega)$ and conductivity $\sigma(\mathbf{x},\omega)$. Keep in mind that, in general, they have a spatial dependence and they do not commute with the nabla operators. For instance,

$$\nabla \times \frac{\mathbf{E}}{\mu(\mathbf{x},\omega)} = \frac{1}{\mu(\mathbf{x},\omega)}\nabla \times \mathbf{E} - \mathbf{E} \times \left(\nabla \frac{1}{\mu(\mathbf{x},\omega)}\right) \neq \frac{1}{\mu(\mathbf{x},\omega)}\nabla \times \mathbf{E}. \tag{I.3}$$

Maxwell's curl equations in Fourier space state that,

$$\mathbf{B} = \frac{1}{i\omega}\nabla \times \mathbf{E}, \tag{I.4}$$

$$\nabla \times \frac{\mathbf{B}}{\mu} = \mathbf{J}_f - i\omega\epsilon\mathbf{E}, \tag{I.5}$$

where $\mathbf{J}_f$ stands for the *free* current, created by the free electrons, not bound to the medium [3]. The free current is any current that is not the polarisation current, magnetisation current or displacement current, all of them associated to the movement of bound atoms in the medium. Let us combine both equations in order to eliminate the explicit dependence on the magnetic field,

$$\frac{1}{i\omega}\nabla \times \left(\frac{1}{\mu}\nabla \times \mathbf{E}\right) = \mathbf{J}_f - i\omega\epsilon\mathbf{E}. \tag{I.6}$$

We can divide the free current in ohmic ($\mathbf{J}_{\mathrm{o}}$) and non-ohmic ($\mathbf{J}_{\mathrm{n-o}}$) terms. We can think of the non-ohmic term as an imposed, *impressed* current existing in our problem and not affected by the macroscopic fields. For instance, the particle tracks we are interested in, or the currents generated by the power source of the antenna, can be regarded as this kind of current.

$$\mathbf{J}_f = \mathbf{J}_{\mathrm{n-o}} + \mathbf{J}_{\mathrm{o}}, \tag{I.7}$$

with $\mathbf{J}_{\mathrm{o}} = \sigma\mathbf{E}$ the ohmic current. From now on, to simplify the notation of the non-ohmic free current, we will call

$$\mathbf{J} \equiv \mathbf{J}_{\mathrm{n-o}}. \tag{I.8}$$

This convenient division allows us to rewrite (I.6) as an expression for the non-ohmic free current,

$$\mathbf{J} = \frac{1}{i\omega}\left[\nabla \times \left(\frac{1}{\mu}\nabla \times \mathbf{E}\right) - \omega^2\epsilon\mathbf{E} - i\omega\sigma\mathbf{E}\right]. \tag{I.9}$$

Defining $\kappa = \omega^2\epsilon + i\omega\sigma$ and realising that the current is a function of the electric field, we can write the expression above as an operator acting on $\mathbf{E}$.

$$\mathbf{J} = O\mathbf{E} = \frac{1}{i\omega}\left[\nabla \times \frac{1}{\mu}\nabla \times -\kappa\right]\mathbf{E}. \tag{I.10}$$

Coming back to the volume with two different sets of physical fields, we define the product of the electric field of the first set with the non-ohmic free current of the second set, integrated over the volume,

$$\tau_{12} = \int (\mathbf{E}_1 \cdot \mathbf{J}_2)\, \mathrm{d}V. \tag{I.11}$$

Let us expand this,

$$\begin{aligned}
\tau_{12} &= \frac{1}{i\omega}\int \left(\mathbf{E}_1 \cdot \nabla \times \frac{1}{\mu}\nabla \times \mathbf{E}_2\right)\, \mathrm{d}V - \frac{\kappa}{i\omega}\int (\mathbf{E}_1 \cdot \mathbf{E}_2)\, \mathrm{d}V \\
&= \frac{1}{i\omega}\int \left[\left(\frac{1}{\mu}\nabla \times \mathbf{E}_1\right) \cdot (\nabla \times \mathbf{E}_2)\right]\, \mathrm{d}V - \frac{1}{i\omega}\oint \left[\mathbf{E}_1 \times \left(\frac{1}{\mu}\nabla \times \mathbf{E}_2\right)\right] \cdot \mathrm{d}\mathbf{S} \\
&\quad -\frac{\kappa}{i\omega}\int (\mathbf{E}_1 \cdot \mathbf{E}_2)\, \mathrm{d}V,
\end{aligned} \tag{I.12}$$

where we have used the vectorial identity

$$\int_V \mathbf{F} \cdot (\nabla \times \mathbf{G})\, \mathrm{d}V = \int_V (\nabla \times \mathbf{F}) \cdot \mathbf{G}\, \mathrm{d}V - \oint_S (\mathbf{F} \times \mathbf{G}) \cdot \mathrm{d}\mathbf{S}. \tag{I.13}$$

We must apply Eq. (I.13) one more time and use the definition of the auxiliary field $\mathbf{H}$,

$$\mathbf{H} = \frac{1}{\mu}\mathbf{B} = \frac{1}{i\omega\mu}\nabla \times \mathbf{E}, \tag{I.14}$$

to obtain

$$\begin{aligned}
\tau_{12} &= \frac{1}{i\omega}\int \left[\left(\nabla \times \frac{1}{\mu}\nabla \times \mathbf{E}_1\right) \cdot \mathbf{E}_2\right]\, \mathrm{d}V - \frac{1}{i\omega}\oint \left[\left(\frac{1}{\mu}\nabla \times \mathbf{E}_1\right) \times \mathbf{E}_2\right] \cdot \mathrm{d}\mathbf{S} \\
&\quad -\frac{1}{i\omega}\oint \left[\mathbf{E}_1 \times \left(\frac{1}{\mu}\nabla \times \mathbf{E}_2\right)\right] \cdot \mathrm{d}\mathbf{S} - \frac{\kappa}{i\omega}\int (\mathbf{E}_1 \cdot \mathbf{E}_2)\, \mathrm{d}V.
\end{aligned} \tag{I.15}$$

Joining the first and the last integral we retrieve the current operator after using Eq. (I.14), this time applied on $\mathbf{E}_1$,

$$\tau_{12} = \int \mathbf{J}_1 \cdot \mathbf{E}_2 \, \mathrm{d}V - \oint (\mathbf{E}_1 \times \mathbf{H}_2 - \mathbf{E}_2 \times \mathbf{H}_1) \cdot \mathrm{d}\mathbf{S}. \tag{I.16}$$

This result can be rearranged using Eq. (I.11) to yield the general reciprocity theorem:

$$\boxed{\int_V (\mathbf{E}_1 \cdot \mathbf{J}_2 - \mathbf{J}_1 \cdot \mathbf{E}_2) \, \mathrm{d}V = \oint_S (\mathbf{E}_2 \times \mathbf{H}_1 - \mathbf{E}_1 \times \mathbf{H}_2) \cdot \mathrm{d}\mathbf{S}} \tag{I.17}$$

Let us remind ourselves that the current $\mathbf{J}_i$ we are using is the non-ohmic free current in our problem. What is remarkable about this theorem is that, given an inhomogeneous linear medium and an arbitrary volume within that medium, two totally different sets of non-ohmic free currents and fields must verify an identity that involves both of them. This may help us in finding a relationship between problems that at first seem quite different, like the situations when an antenna is emitting and receiving.

It is also important to note that, in order to apply correctly the theorem, the medium must have the same permittivity, permeability and conductivity in both configurations (1 and 2), implying that the radiator elements of the antennas must be in the same places. If we want to have different locations for the conductive media in cases 1 and 2, Eq. (I.1) is still valid provided we interpret the current as the *total free* current and not only the non-ohmic free part.

In a medium with non-zero conductivity or dielectric attenuation (as every real medium has), we can guarantee that the fields at a very large distance tend to zero. In other words, at a sufficiently large distance even the radiation fields fade out,

$$\lim_{|\mathbf{x}|\to\infty} |\mathbf{E}| = 0; \qquad \lim_{|\mathbf{x}|\to\infty} |\mathbf{H}| = 0. \tag{I.18}$$

With this, if we extend part or all the enclosing surface S to infinity, we get that for those parts the surface integral is zero, and the reciprocity theorem reads:

$$\oint_\infty (\mathbf{E}_2 \times \mathbf{H}_1 - \mathbf{E}_1 \times \mathbf{H}_2) \cdot \mathrm{d}\mathbf{S} = 0 = \int_\infty (\mathbf{E}_1 \cdot \mathbf{J}_2 - \mathbf{J}_1 \cdot \mathbf{E}_2) \, \mathrm{d}V. \tag{I.19}$$

I.2 Reciprocity applied to an antenna and a charged particle track

Let us think of an antenna in an homogeneous, isotropic medium. The volume is chosen in such a way that the radiating elements and the transmission line formed by the antenna

terminals are contained in the volume[1]. We define a reference plane RP (see Figs. I.1 and I.2) that cuts the transmission line perpendicularly. The surface is extended to infinity except for a patch surrounding the isolating conductors of the antenna.

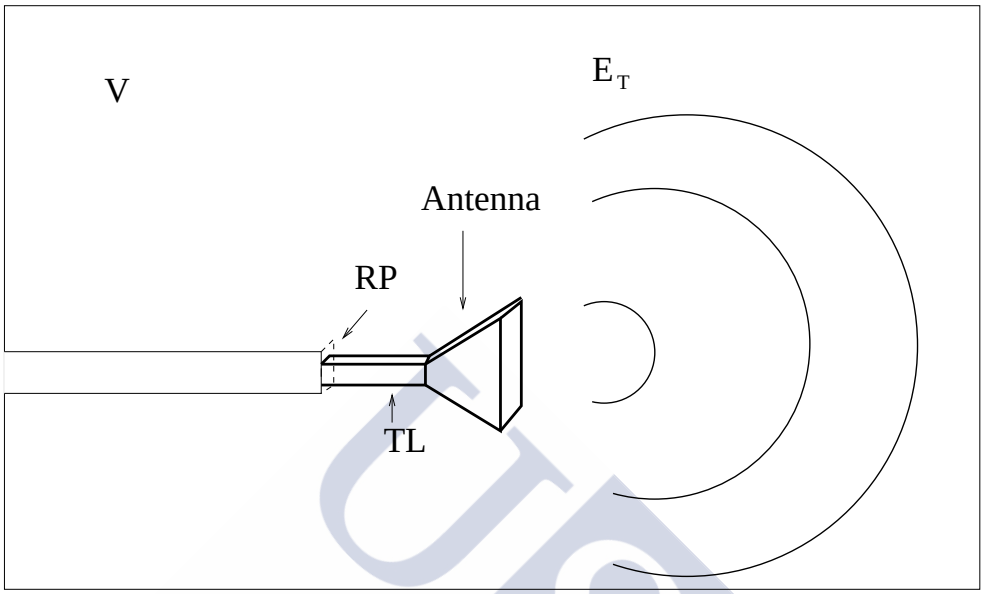

Figure I.1: Antenna in transmission mode. The chosen volume has its surface at infinity and on the rectangle on the left, in such a way that the antenna radiator and the transmission line (TL) are contained in it. RP denotes a reference plane (see text).

To apply the reciprocity theorem, we choose two situations. In situation T (transmission, see Fig. I.1) the antenna is emitting radiation $\mathbf{E}_T$ into the medium. In situation R (reception, see Fig. I.2), a charged particle current $\mathbf{J}_R$ creates a field $\mathbf{E}_R$ that arrives at the antenna. The antenna absorbs some and rescatters some, but this does not affect the track current. Since the antenna elements contained in the volume are considered ohmic, the only non-ohmic current to take into account is the particle track. The left-hand side of Eq. (I.1) then reads:

$$\int_V (\mathbf{E}_T \cdot \mathbf{J}_R - \mathbf{E}_R \cdot \mathbf{J}_T)\, \mathrm{d}V = \int_{\text{track}} \mathrm{d}V\ \mathbf{E}_T \cdot \mathbf{J}_{\text{track}}. \tag{I.20}$$

We will also suppose that the isolating conductors are good enough so that the surface integral in Eq. (I.1) results in an important contribution in the RP only. We choose the

[1]That is, we assume that the antenna terminals behave as a transmission line with an impedance that is, by definition, the antenna impedance (Z_A). The terminals are connected in general to another transmission line that can have a different impedance, creating an impedance mismatching, but we are not interested in it.

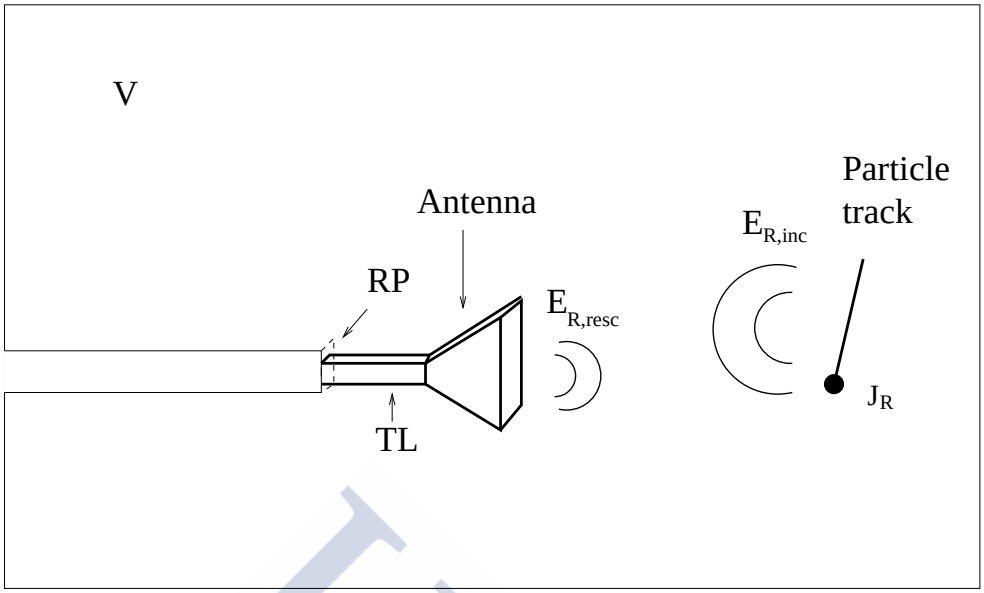

Figure I.2: Antenna in reception mode. The volume is identical to that in Fig. I.1, but now contains a track creating a field that arrives at the antenna and gets reflected.

medium so that at large distances it has a small conductivity, but enough to vanish the radiation fields. Therefore, the only contribution to the surface integral will be given by the RP in Fig. I.1, since at large distances the field is zero and in a perfect conductor the field is also zero, *i.e.*,

$$\oint_S (\mathbf{E}_R \times \mathbf{H}_T - \mathbf{E}_T \times \mathbf{H}_R) \cdot \mathrm{d}\mathbf{S} \approx \int_{RP} (\mathbf{E}_R \times \mathbf{H}_T - \mathbf{E}_T \times \mathbf{H}_R) \cdot \mathrm{d}\mathbf{S}. \tag{I.21}$$

We impose now an open-circuit condition at the RP for the receiving situation. The transmission line is supposed to operate with its TEM mode[2], which means that at the RP, where the voltage is being measured, the evanescent modes play no role. The open circuit condition for the RP implies that the current intensity is zero. For a TEM transmission line, the **H** field at any point is proportional to the current intensity that goes through each conductor [2, 4],

$$|\mathbf{H}_R| \propto I_R. \tag{I.22}$$

[2]The transverse electromagnetic mode or TEM mode of a waveguide is a configuration of the electric and magnetic fields inside a waveguide in such a way that the electric and magnetic fields are perpendicular to the direction of propagation of the electromagnetic wave. In a TEM transmission line the electromagnetic wave usually propagates in the fundamental TEM mode below the threshold frequency of TE and TM modes [4]. TEM modes cannot occur in a hollow waveguide [3], and several conductors inside the waveguide are necessary for them to exist, as it is the case for coaxial cables.

Therefore, a zero current intensity I_R at the RP implies,

$$\mathbf{H}_R|_{RP} = 0. \tag{I.23}$$

Eq. (I.21) can then be written as

$$\int_{RP} (\mathbf{E}_R \times \mathbf{H}_T - \mathbf{E}_T \times \mathbf{H}_R) \cdot \mathrm{d}\mathbf{S} = \int_{RP} \mathbf{E}_R \times \mathbf{H}_T \cdot \mathrm{d}\mathbf{S}. \tag{I.24}$$

The next step is to write the $\mathbf{E}_R$ and $\mathbf{H}_T$ fields for reception and transmission mode, respectively. We will introduce $\mathbf{e}_0$ as the TEM mode of a TEM transmission line evaluated on the reference plane. $\mathbf{e}_0$ is a function of the transverse coordinates for the transmission line and must be normalised, in the sense that

$$\int_{RP} \mathbf{e}_0 \cdot \mathbf{e}_0 \, \mathrm{d}S = 1. \tag{I.25}$$

$\mathbf{e}_0$ allows us to write the electric field in receiving mode as,

$$\mathbf{E}_R|_{RP} = V_{oc}\mathbf{e}_0, \tag{I.26}$$

where V_{oc} stands for the open-circuit voltage in receiving mode. Defining $\hat{z}$ as the direction of the TEM line on the RP (*i.e.* perpendicular to $\mathbf{e}_0$, for we have a TEM transmission line) and knowing that the transmission current is I_T, the transmission $\mathbf{H}_T$ field is equal to

$$\mathbf{H}_T|_{RP} = I_T(\hat{z} \times \mathbf{e}_0). \tag{I.27}$$

This expression does not imply that we must have a single wave propagating along the $\hat{z}$ direction. If we have an I_{+z} current and a I_{-z} current propagating in opposite directions, the equation is valid provided we write $I_T = I_{+z} - I_{-z}$.

Eq. (I.21) becomes very simple using the properties of the TEM modes.

$$\int_{RP} \mathbf{E}_R \times \mathbf{H}_T \cdot \mathrm{d}\mathbf{S} = V_{oc} I_T \int_{RP} \mathbf{e}_0 \times (\hat{z} \times \mathbf{e}_0) \cdot \mathrm{d}\mathbf{S} = V_{oc} I_T. \tag{I.28}$$

Reciprocity for an antenna and a charged particle track finally yields

$$\boxed{\int \mathrm{d}V \ \mathbf{E}_T \cdot \mathbf{J}_{\mathrm{track}} = V_{\mathrm{oc}} I_T} \tag{I.29}$$

We usually know the particle current $\mathbf{J}_{\mathrm{track}}$ in our theoretical problems, or we can simulate it with a Monte Carlo for practical purposes. We need to find out the general transmission field $\mathbf{E}_T$ for the antenna.

I.3 Far-field for an (almost) arbitrary antenna

A common feature of most antennas is that they have one of their dimensions much smaller than the wavelength of the fields in consideration and the observation distance (even in near field). For instance, a wire (or loop) antenna usually has a small cross section diameter, and aperture antennas are built from plates whose thickness is low. Provided that, we can ignore one or two of the dimensions of the antenna and treat the antenna ohmic current as an *impressed* surface or linear current embedded in a medium that we are going to assume homogeneous and isotropic[3].

From now on, we will assume we are working in the far-field (Fraunhofer) regime. Calculations using the Coulomb gauge ($\nabla \cdot \mathbf{A} = 0$) show that for $kr \gg 1$ the vector potential can be written as

$$\mathbf{A}(\mathbf{x},\omega) = \frac{\mu}{4\pi}\int \mathrm{d}^3x' \frac{\mathbf{J}_t}{|\mathbf{x}-\mathbf{x}'|} e^{ik|\mathbf{x}-\mathbf{x}'|}, \tag{I.30}$$

where $\mathbf{x}$ is the position of the observer and $\mathbf{x}'$ is the position of a point of the radiating antenna (see Fig. I.3). $\mathbf{J}_t$ corresponds to the transverse current of Coulomb gauge. In the Fraunhofer regime, the transverse current can be approximated by the current perpendicular to the line of sight, called $\mathbf{J}_\perp$. The approximations for Fraunhofer regime are the following (see Section 3.1.2).

- $k|\mathbf{x}| \gg 1$,
- $1/|\mathbf{x}| \approx 1/R$,
- $\frac{k}{2}\frac{(\mathbf{x}\cdot\mathbf{x}')^2}{|\mathbf{x}|^3} \ll 1 \qquad \Rightarrow \qquad e^{ik|\mathbf{x}-\mathbf{x}'|} \approx e^{ikR}e^{-ikr'\cos\tilde{\theta}}$,

where the angle $\tilde{\theta}$ is a function of the source coordinates and the angle formed by the position vector with the polar angle, sketched in Fig. I.3.

$$\tilde{\theta} = \tilde{\theta}(\mathbf{x}',\theta,\phi). \tag{I.31}$$

These approximations can be plugged into the vector potential,

$$\mathbf{A} \approx \frac{\mu}{4\pi R} e^{ikR}\int \mathrm{d}^3x'\ \mathbf{J}_\perp(\mathbf{x}') e^{-ikr'\cos\tilde{\theta}(\mathbf{x}',\theta,\phi)}. \tag{I.32}$$

This integral for computing the field will be a function of the observation angles (θ,ϕ) only (assuming R is constant) after we integrate away the $\mathbf{x}'$ dependence. Experimentally,

[3] Attenuation due to dielectric absorption and electrical conduction can be included imposing an imaginary part for the permittivity and the wavenumber.

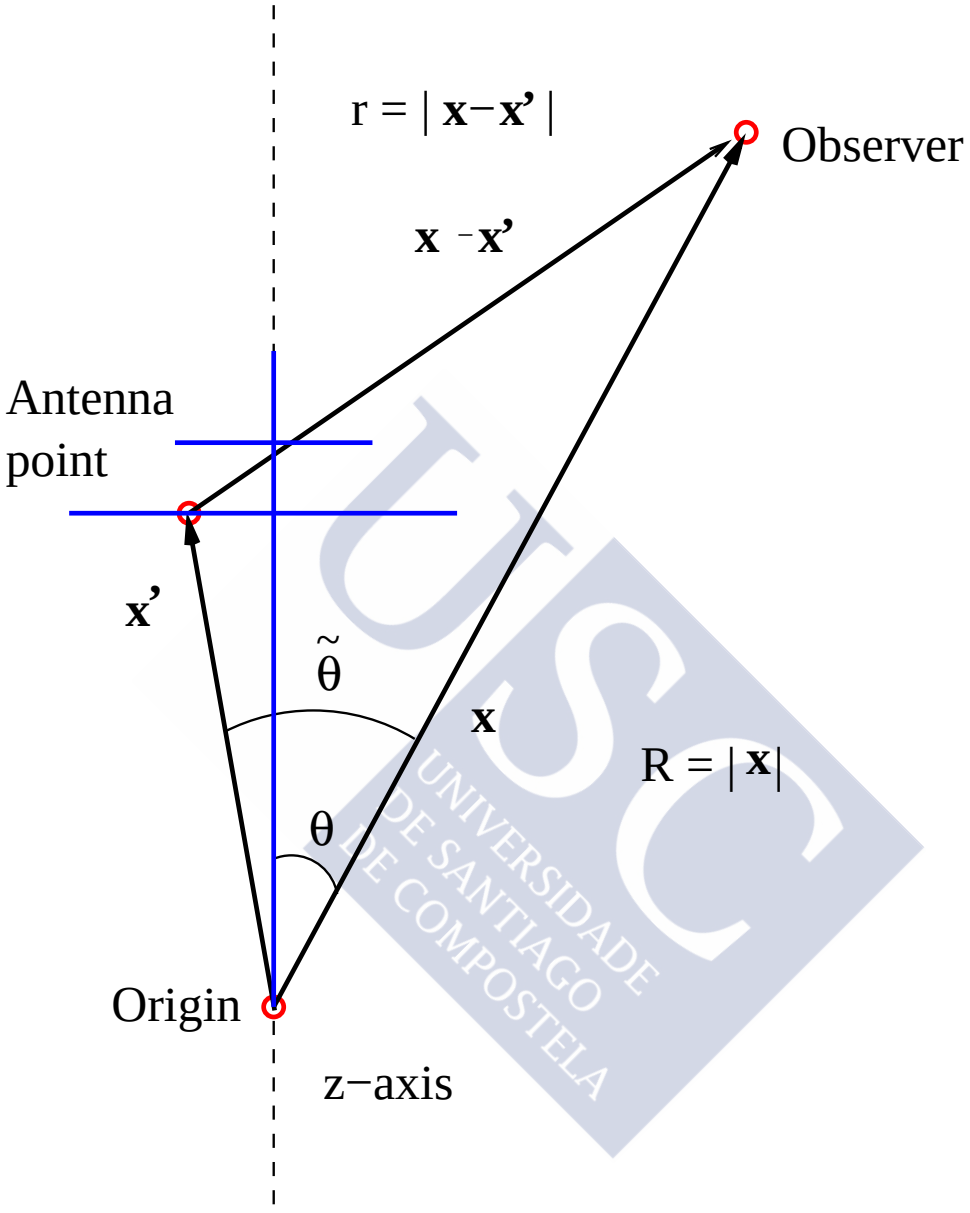

Figure I.3: Sketch of the emitting antenna. The antenna is drawn in blue. $\mathbf{x}$ is the position vector of the observer and $\mathbf{x}'$ is the position vector of an arbitrary point of the antenna. θ is the observation angle with respect to the z-axis, while $\tilde{\theta}$ is the angle formed by $\mathbf{x}$ and $\mathbf{x}'$.

we expect for most antennas a proportionality between the the current density and the current at the antenna terminals I_T, which is what can be controlled in practice,

$$|\mathbf{J}_\perp| \propto I_T. \tag{I.33}$$

This leads us to expect that the vector potential is proportional also to the current in the antenna terminals and to a function of the angles,

$$\mathbf{A} = \frac{\mu}{4\pi R} e^{ikR} I_T \, \mathbf{l}(\theta, \phi), \tag{I.34}$$

where $\mathbf{l}$ is called the *antenna effective length*. Note that its value depends on the medium in which the antenna is located. That is, the radiation pattern and the receiving properties of an antenna depend on the chosen medium. From Eq. (I.34),

$$\mathbf{l}(\theta, \phi, \omega) \equiv \frac{1}{I_T} \int \mathrm{d}^3 x' \; \mathbf{J}_\perp(\mathbf{x}') e^{-ikr' \cos\tilde{\theta}}. \tag{I.35}$$

Since the $\mathbf{J}_\perp(\mathbf{x}')$ is perpendicular to the line of sight (as is the case with the usual radiation fields), the effective length has no radial component,

$$\mathbf{l} = l_\theta \hat{\theta} + l_\phi \hat{\phi}. \tag{I.36}$$

One advantage of using the Coulomb gauge is the possibility of obtaining the radiation field through $\mathbf{A}$ alone,

$$\boxed{\mathbf{E}_T = i\omega \mathbf{A} = \frac{i\omega\mu}{4\pi R} e^{ikR} I_T \mathbf{l}} \tag{I.37}$$

Eq. (I.37) is valid for every antenna used in a laboratory or experiment. Even when having a ground below the antenna, its effect on the radiation pattern can be plugged into the effective length.

I.4 Voltage as a function of the incident field

Eqs. (I.29) and (I.37) can be used to obtain the open-circuit voltage for the antenna in receiving mode. We must picture a charged particle track, small and far enough for the track to "inhabit" the Fraunhofer regime of the antenna and viceversa. The frequency current of the track is written in the frequency domain as,

$$\mathbf{J}(\mathbf{x}', \omega) = \int_{t_1}^{t_2} \mathrm{d}t \; e^{i\omega t} q \mathbf{v} \delta(\mathbf{x}' - \mathbf{v}t). \tag{I.38}$$

Eqs. (I.29) and (I.37) imply that

$$\begin{aligned} V_{oc}I_T &= \int \mathrm{d}^3x' \ \mathrm{d}t \ \frac{i\mu\omega q}{4\pi r'} e^{i\omega t} e^{ikr'} I_T \ \mathbf{l}\cdot\mathbf{v} \ \delta(\mathbf{x}' - \mathbf{v}t) \\ &= \frac{i\mu\omega q}{4\pi} I_T \int \mathrm{d}t \ e^{i\omega t} e^{ikr'(t)} \left[\mathbf{l}(\theta'(t), \phi'(t))\cdot\mathbf{v}\right] \frac{1}{r'(t)}. \end{aligned} \tag{I.39}$$

If the antenna is placed in the far-field region of the track, the usual ZHS approximations can be made to simplify the integral (see Chapter 3). Also, since the effective length has no radial component, we can substitute the velocity with its projection perpendicular to the line of sight (from the point of view of the antenna).

$$\begin{aligned} V_{oc}I_T &\approx \frac{i\mu\omega q}{4\pi R} I_T e^{ikR} \left[\mathbf{v}_\perp \cdot \mathbf{l}(\theta,\phi)\right] \int_{t_1}^{t_2} \mathrm{d}t \ e^{i\omega t} e^{-ikvt\cos\tilde{\theta}} \\ &= \frac{i\mu\omega q}{4\pi R} I_T e^{ikR} \left[\mathbf{v}_\perp \cdot \mathbf{l}(\theta,\phi)\right] \frac{e^{i(\omega - \mathbf{k}\cdot\mathbf{v})t_2} - e^{i(\omega-\mathbf{k}\cdot\mathbf{v})t_1}}{i(\omega - \mathbf{k}\cdot\mathbf{v})} \end{aligned} \tag{I.40}$$

But this is just the ZHS field for the track evaluated at the antenna position and multiplied by the effective length at the angle where the track field is seen to come from and then,

$$V_{\mathrm{oc}} = \mathbf{E}_{\mathrm{ZHS}} \cdot \mathbf{l}(\theta,\phi). \tag{I.41}$$

If we have a collection of tracks, each one at a different angle, we must multiply each track by the corresponding effective length.

$$\boxed{V_{\mathrm{oc}} = \sum_i \mathbf{E}_{\mathrm{ZHS,i}} \cdot \mathbf{l}(\theta_i,\phi_i)} \tag{I.42}$$

Let us remember that the condition for Eq. (I.42) to work is that track and antenna must lie in each other's Fraunhofer regime. This means in practice that $kr \gg 1$ and the antenna must verify

$$\eta = \frac{k}{2}\frac{(\mathbf{x}'\cdot\mathbf{x})^2}{r^3} \ll 1 \tag{I.43}$$

with the unprimed coordinates referring to the track position and the prime coordinates referring to the antenna points. Although the track can be subdivided as many times as we want, the above condition places a limitation on the minimum distance the track can have to the antenna.

Eq. (I.42) is also valid for antennas over ground, as long as the ground is present in transmission mode and therefore affects the effective length shape.

I.5 Short-circuit voltage and time-domain voltage

Radio wavelengths are usually small enough so that we have to consider their wave nature when travelling in electronic circuits. But for simple antennas modeled just by an antenna impedance Z_A and a load impedance Z_L, the short-circuit voltage is known by applying the tension divider formula,

$$V = \frac{Z_L}{Z_A + Z_L} V_{oc}. \tag{I.44}$$

However, since we are using a transmission line in most experimental situations, the use of this formula implies that the line is properly matched at both ends. One way of doing it is by making the antenna have the conjugate impedance of the line, and the load to have the same impedance as the antenna, $Z_A = Z_L$ (in many cases, purely resistive with 50 Ω).

$$V = \frac{1}{2} V_{oc}. \tag{I.45}$$

For a real antenna, we must face the losses in the transmission line, the impedance mismatchings, the reflections in dielectric parts of the antenna and the electronics related limitations (see [5]). These effects can be very difficult to take into account.

Precisely because of their difficulty, for most practical applications (e.g. telecommunications) it is enough to know the antenna *gain*, a quantity that relates the power radiated by the antenna to the power consumed by the antenna and that is easily measured. With the gain, we can compute the *effective area* [1], which is the ratio of the received power at the load and the power of an incoming plane wave. The problem is that in an accelerator or shower experiment the waves come from multiple places and their fields are added. The effective area deals with power, and powers cannot be added. Another way to realise this is that the effective area is a real scalar quantity, while the effective length is a complex vectorial quantity (with two dimensions). We are missing three real numbers if we are only provided with the gain for a particular antenna.

Finally, we should keep in mind that what we tipically measure is a time-domain voltage, while the present calculations are performed in frequency domain. Therefore, we must transform back to time domain our voltage,

$$V(t) = \frac{1}{2\pi} \int \mathrm{d}\omega \; e^{-i\omega t} V(\omega). \tag{I.46}$$

Bibliography

[1] C. A. Balanis. *Antenna Theory, Analysis and Design.* John Wiley and Sons, 2nd edition, 1997.

[2] R. York. Antenna theory, ece 201c. http://my.ece.ucsb.edu/York/Bobsclass/201C/.

[3] D. J. Griffiths. *Introduction to Classical Electrodynamics.* Prentice Hall, 3rd edition, 1999.

[4] S. J. Orfanidis. Electromagnetic waves and antennas. http://www.ece.rutgers.edu/ orfanidi/ewa/orfanidis-ewa-book.pdf.

[5] F. G. Schröder *et al.* Radio detection of air showers with Auger Engineering Radio Array. In *Proceedings of the 33rd International Cosmic Ray Conference (ICRC 2013)*, number 0899.

USC
UNIVERSIDADE
DE SANTIAGO
DE COMPOSTELA

Chapter 5

Radiation in accelerator experiments

This chapter is devoted to the study of *molecular bremsstrahlung radiation* (MBR) as a potential technique for UHECR detection analog to the fluorescence technique, but using radio frequencies, as proposed in [1]. MBR is caused when free electrons scatter in the field of the molecules of the ambient medium, and it is expected to create an unpolarised electric field. At SLAC [1], the electric field of an electron beam that enters an anechoic chamber filled with air after interacting with some alumina targets was measured. The polarisation of the field in the plane containing the beam and the observer and perpendicular to the line of sight indicated the presence of (expected) Cherenkov radiation. However, an electric field polarised perpendicularly to the Cherenkov field was also measured and interpreted as MBR. The flux of the electric field scaled quadratically with beam energy and it was concluded that MBR could be used to detect air showers after extrapolating the measured flux to UHECR energies. With the aim of trying to reproduce the results of the SLAC experiments several other electron-beam experiments were designed.

In this chapter we concentrate on the AMY and MAYBE experiments devoted to the measurement of the MBR yield. We use the ZHS formula derived in Chapter 3 to predict the observed electric field in these setups that is not due to MBR (*i.e.* the background). We also develop a model for MBR based on that in [2]. We implement the model in the ZHS Monte Carlo for electromagnetic showers that can also handle beams of electrons, and give upper bounds on the amount of the MBR in these experiments. We also briefly review the status of the MBR yield measurements and theoretical calculations at the end of this chapter.

5.1 The AMY experiment

AMY (Air Microwave Yield) [3] is an experiment located at the BTF (Beam Test Facility) in the Frascati INFN National Laboratory. Its aim is to test the SLAC results in [1] with the electron beam of the DAΦNE accelerator and with a wide frequency range. So far, the results of the SLAC experiment could not be reproduced in AMY that measured a more

limited emission of MBR (if any). The results of AMY jeopardise the future of the MBR technique as a viable technique for the detection of UHE cosmic rays.

5.1.1 Description of the experimental setup

In the AMY experiment, an electron beam collides with an interaction target of a variable thickness and enters an anechoic Faraday chamber filled with air where antennas sensitive in the GHz range observed the emitted electric field. The variable target thickness allows to study MBR as a function of the shower age and the energy deposit within the chamber. According to [1], MBR should be proportional to the energy deposit, analogously to fluorescence. A sketch of the experiment is shown in Fig. 5.1.

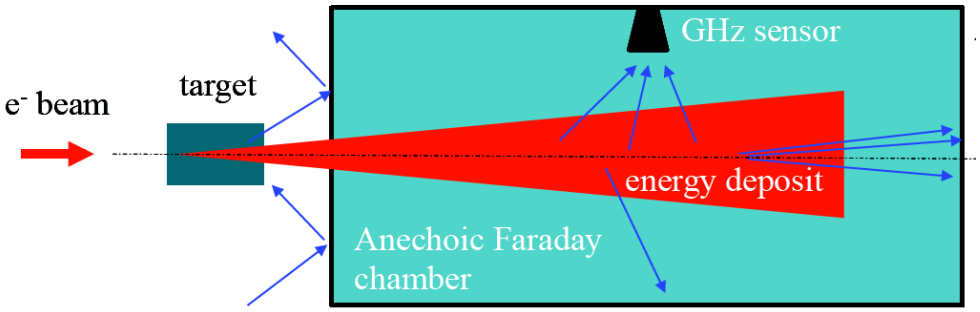

Figure 5.1: Sketch of the AMY experiment. The electron beam collides with the target and enters the anechoic chamber. The emitted radiation is detected by the GHz antenna. Figure taken from [3].

The BTF is a part of DAΦNE, the LINAC that provides the beam for the experiment. The beam for the AMY runs consists on 510 MeV kinetic energy electrons with a total charge up to 10^{10} electrons per pulse and a bunch length of 1.5, 3 or 10 ns (see Fig. 5.2). The bunches are composed of several microbunches with a FWHM of 14 ps separated by 0.35 ns. The microbunches were initially thought to have the same amount of charge (number of electrons), but we will show that their charge varies from microbunch to microbunch, as evidenced by the AMY data.

The interaction target is 95% pure Al_2O_3 (alumina). There are six alumina blocks. Two of them have a thickness of 10 cm, three of them have 7.5 cm and one has 2.5 cm. The thickness of them all combined is about 7 radiation lengths ($7X_0$).

The anechoic chamber has dimensions of 2 m×2 m×4 m. In its interior, pyramidal RF absorbers make the reflections off the walls drop by 35 dB at 1 GHz to 45 dB at 6 GHz

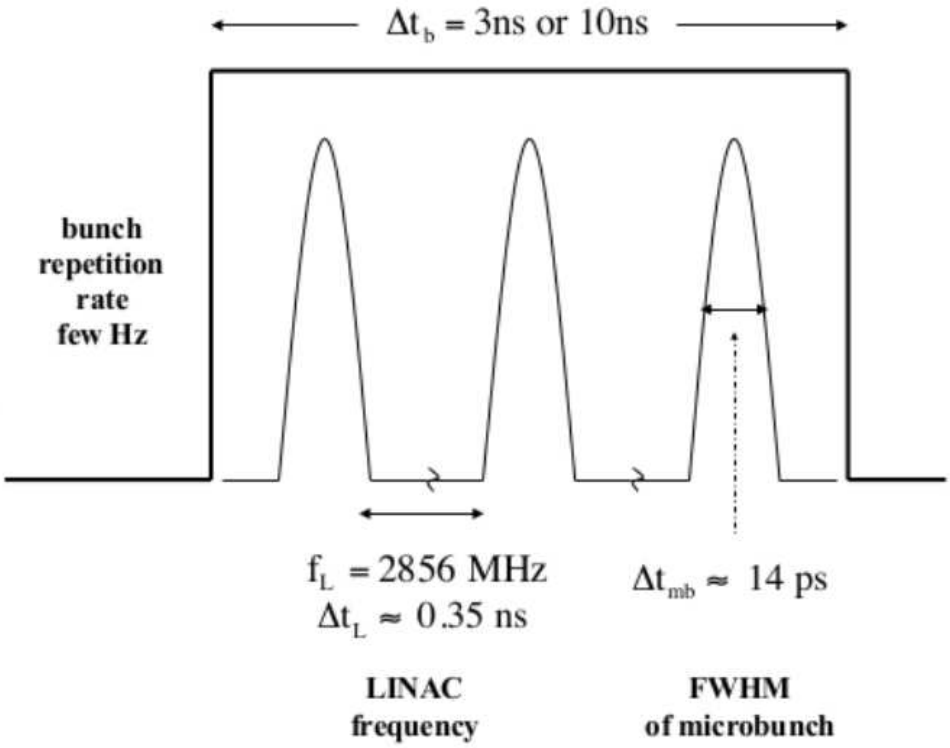

Figure 5.2: Sketch of the structure of the LINAC beam used for the AMY experiment. The horizontal axis shows the time while the vertical axis indicates the number of particles at a fixed position lying on the axis of the beam. The beam is composed by microbunches with a temporal full width at half maximum (FWHM) of 14 ps and separated 0.35 ns. The total time of the beam can correspond to 1.5 ns (not indicated in the figure), 3 ns or 10 ns. In the experimental setup the charge of each microbunch changes from microbunch to microbunch.

and 50 dB at higher frequencies. The shielding from the outside noise is more than 80 dB at 2 GHz and $\sim$ 50 dB at 1 GHz.

The antennas are two *Rhode&Schwarz HL050* log-periodic antennas and two *RF Spin Double Ridged Waveguide Horn DRH20*. The frequency band of interest for the AMY experiment ranges from 1 to 20 GHz. The data in the present work have been taken using the latter antennas. Both the log-periodic and the horn are sensitive to linear polarisation.

The signal of the antenna was amplified by a *Minicircuits* wide band amplifier *ZVA-185-S+*, passed through $\sim$ 20 m of low loss coaxial cables to the control room and read with a *Lecroy SDA 830Zi-A* oscilloscope with a sampling rate of 40 GS/s.

5.1.2 Description of experimental data

When a beam of electrons enters the chamber of the AMY experiment, we expect four different contributions to the radiation at GHz frequencies:

1. Cherenkov radiation for particles with energy higher than the Cherenkov threshold in air, $\sim$ 20 MeV.

2. Radiation from the sudden appearance of the charge in the anechoic chamber as seen by the antennas inside.

3. Radiation from the sudden acceleration of the bound electrons in air when the atoms in the chamber are ionised by the electrons in the beam, and also from hard bremsstrahlung processes.

4. Radiation from the soft collisions of the electrons with the molecules of the medium, producing bremsstrahlung photons at GHz frequency, that is, MBR.

ZHS accounts for 1, 2, partly for 3 (due to the continuous energy loss approximation for ionisation electrons emitted with energy below a few tens of keV) and, effectively but not explicitely, for 4 (due to the continuous energy loss treatment of bremsstrahlung photons of energy below a few tens of keV).

The antennas used in AMY are very sensitive to a certain polarisation of the electric field (determined by the *effective length* of the antenna) and have very little sensitivity to the corresponding perpendicular polarisation. For a perfectly collinear beam the electric field polarisation will lie in the plane formed by the beam and the antenna. We expect, therefore, two different physical situations. If we align the antenna in a way that its effective length lies in the plane containing the beam and the observer, a high signal (mainly from

Cherenkov radiation and the sudden appearance of the charge, both linearly polarised in the plane of the beam and observer) is expected. We call this case the *co-polarised* or *co-pol* case. If we rotate the antenna 90°, in a way that the effective length is perpendicular to the plane, we expect the signal to be smaller. We call this case the *cross-polarised* or *cross-pol* case. Since MBR is thought to be unpolarised [1], we expect it to induce a larger relative contribution to the signal in the cross-pol case.

We show in Fig. 5.3 two voltage traces collected at the oscilloscope after the passage of two different bunches of electrons. In the top panel, the antenna is parallel to the beam axis (co-pol), while in the bottom panel, the antenna is perpendicular to the beam axis (cross-pol). We see that the signal peak is about ~ 100 mV in the co-pol case. Turning the antenna to place it in the cross-pol case produces a dramatic decrease of the electric field, whose peak is now about ~ 5 mV.

The co-pol signal in Fig. 5.3 exhibits 9 or 10 peaks that are attributed to the signal of each microbunch. The total time of the beam is 3 ns, and the temporal separation between each microbunch is 0.35 ns. Dividing both numbers we get the number of microbunches: $3/0.35 \approx 9$ microbunches, which is also the number of peaks observed in the oscilloscope trace.

An interesting feature is the appearance in the cross-pol plot of a second set of peaks that further analysis reveals to be unpolarised, something that is expected from MBR according to [1]. While it could be generated by reflections in the chamber, the cables, or by the response of the amplifier or the antenna, the data collected at the MAYBE experiment (see next section) suggest that this is most likely the unpolarised emission of the low energy electrons of the shower, and that emission is expected to contain MBR. The gathered data can be used to obtain an experimental upper bound to the MBR.

The spectra of a typical co-pol run with a target of $0.3X_0$ and a cross-pol run with a target of $2.3X_0$ are shown in Fig. 5.4. Since the bunches are organised in microbunches separated 0.35 ns, that induces a main peak in the spectrum at a frequency $f_0 \approx (0.35\ \text{ns}^{-1}) \approx 2.86$ GHz, clearly visible in Fig. 5.4. Besides this peak, other harmonics at integer multiples of f_0 can be seen in the co-pol plot (top), whose peak amplitudes decrease with frequency as a result of the microbunch dimensions (the dimensions of the microbunch imply the existence of a cutoff frequency at which the whole microbunch ceases to create a coherent electric field, much alike the box model described in Section 2.1.3) and the response of the detectors, cables and amplifiers. In the cross-pol plot (bottom) a reduction of the received power can be seen, as expected. The $2.3X_0$ target also suppresses the harmonics by scattering the particles in the beam and preventing the coherence at higher frequencies

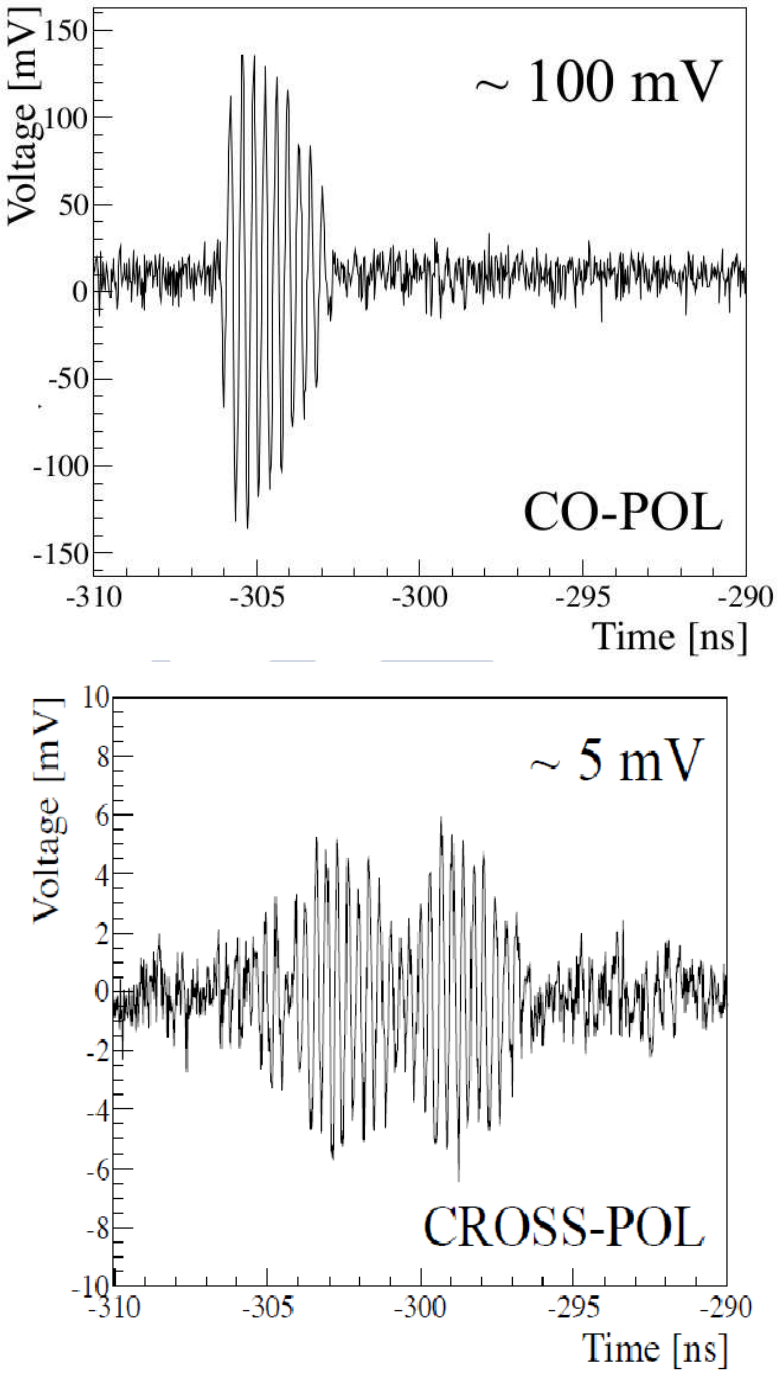

Figure 5.3: Voltage measured at the oscilloscope as a function of time for a typical 3 ns bunch without targets. Top: antenna in co-pol position. Bottom: antenna in cross-pol position. Figure taken from [4].

than the fundamental one.

5.1.3 Bound to the MBR emission

For completitude we give here the preliminary bound on the flux of MBR obtained with the AMY experiment. For that purpose the spectrum for a cross-pol configuration with several targets has been used. This setup should have the least possible amount of Cherenkov emission (*i.e.* background). Since particles are scattered and act less coherently, their energy is on average smaller (and even below the Cherenkov threshold), and the bulk of the Cherenkov contribution is polarised in the co-pol direction.

Taking the power of the first harmonic in an average of runs similar to the one at the bottom of Fig. 5.4, but with a $4.7X_0$ target, and after a simple calculation, the power flux per frequency unit was estimated in [4],

$$\langle F \rangle_{\rm AMY} \lesssim 5 \times 10^{-17} \text{ W m}^{-2}\text{Hz}^{-1}. \tag{5.1}$$

This is an upper bound since not all the emission can be attributed to MBR because we still expect some contamination in the cross-pol channel from Cherenkov radiation. However, what is important is to realise that $\langle F \rangle_{\rm AMY}$ is an order of magnitude smaller than the previous measurement in the SLAC experiment [1].

5.1.4 Simulating the observed radiation

We have modified the ZHS program so that it can calculate the field of a beam of particles inside a chamber of given dimensions and in particular inside the one used in AMY. We create an electron beam as described below, pass it through the GEANT4 package to obtain the tracks at the entrance of the chamber after the beam has gone through the alumina target [5] and then use ZHS to compute the electric field. The conditions for the application of the ZHS formula ($kR \gg 1$ and $\eta \ll 1$, see Eq. (I.43) from the Intermission) are met. The ZHS code accounts for the sudden charge and the Cherenkov contributions (*i.e.* the background to MBR), while due to the approximations in the code for low momentum transfer collisions, we do not expect the MBR contribution to be faithfully reproduced. For this we develop and implement in the ZHS code a model for MBR described later in this chapter. However, whereas the MBR model does not include the radiation due to the sudden accelerations in the ionisation process, the ZHS formula for the electric field does. This process is very important for the energy loss of the beam particles at energies below the critical energy, where ionisation dominates over bremsstrahlung. This could

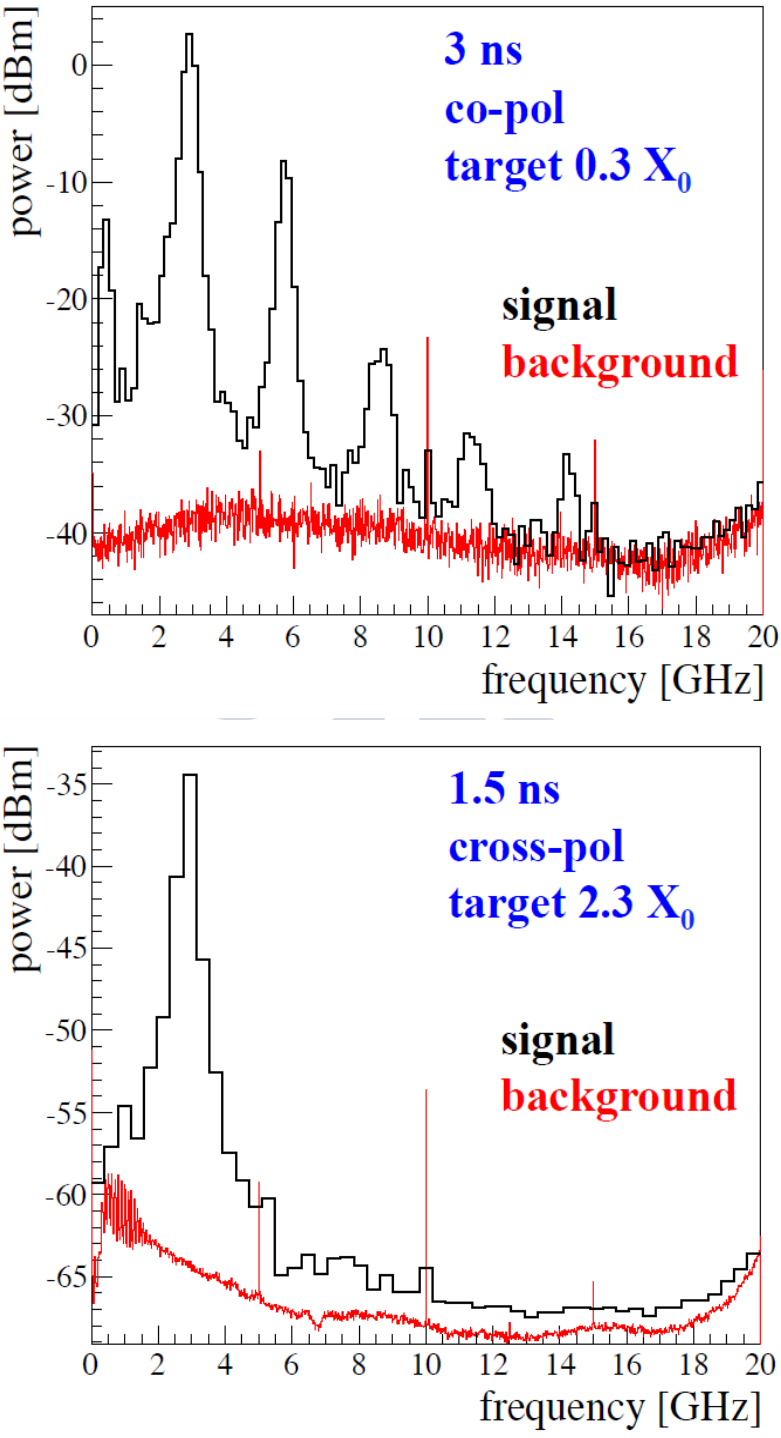

Figure 5.4: Fourier transform of the power at the oscilloscope as a function of frequency averaged over many triggers. Top: Average spectrum of a 3 ns bunch with a $0.3X_0$ depth target in co-pol configuration. Note the harmonics structure matching the 2.86 GHz frequency of the LINAC. Bottom: Average spectrum of a 1.5 ns bunch with a $2.3X_0$ depth target in cross-pol configuration. Background for the two configurations (taken with the beam off) is also shown. Figure taken from [4].

also explain the fact that the MC simulations in [2] are systematically below the data by a factor of 1.37.

Recreating the beam

In the AMY experiment, the LINAC creates an electron beam that penetrates through a copper anechoic chamber and several alumina targets (or none). One way of simulating the beam is injecting electrons into the GEANT4 package and collecting the resulting particles that enter the chamber. The outputs of GEANT4 are the energy, spacetime position and direction of these particles, which are then used as an input to the ZHS code.

The bunch produced by the LINAC can last 10, 3 or 1.5 ns. It is divided in microbunches separated 0.35 ns in time, each microbunch having a time width of 14 ps. The kinetic energy of the electrons in the bunch is 510 MeV.

The beam coming from the LINAC also posseses a certain intrinsic lateral spread, large enough so that it matters for the calculation of the field at GHz frequencies. We imitate this by displacing the injection point of the particles sampling a gaussian distribution with a lateral deviation of $\sigma_r = 0.5$ cm [5]. A sketch of the bunch and microbunches is shown in Fig. 5.2.

There is also another important factor to correctly recreate the beam. If the beam had constant charge in each microbunch, the fields induced by each bunch would look very similar. This is not what is seen in the data (Fig. 5.5). The changing height of the peak voltages at the oscilloscope can be attributed to a modulation of the charge in the bunch, that is, each microbunch has a different charge. This modulation may also change from bunch to bunch. Unfortunately, the amount of electrons in each microbunch cannot be measured directly, only the total number of electrons in the bunch is known. We will assume that the microbunches have different numbers of electrons and these are responsible for the different heights of the observed peaks in the time voltage traces. This can be confirmed with simulations (Fig. 5.6), where the charge in the beam used as input to the ZHS code was modulated matching a function similar to the envelope of the voltage traces in real data, and as a result the simulated voltages follow the same envelope.

As a consequence and in order to recreate the beam for a certain run, we first look at the height of the peaks of the time voltage and create a beam made of electrons put together to form microbunches, where the number of electrons in each microbunch is proportional to the height of the corresponding peak. The total number of electrons in the bunch is known from the monitoring of the LINAC beam.

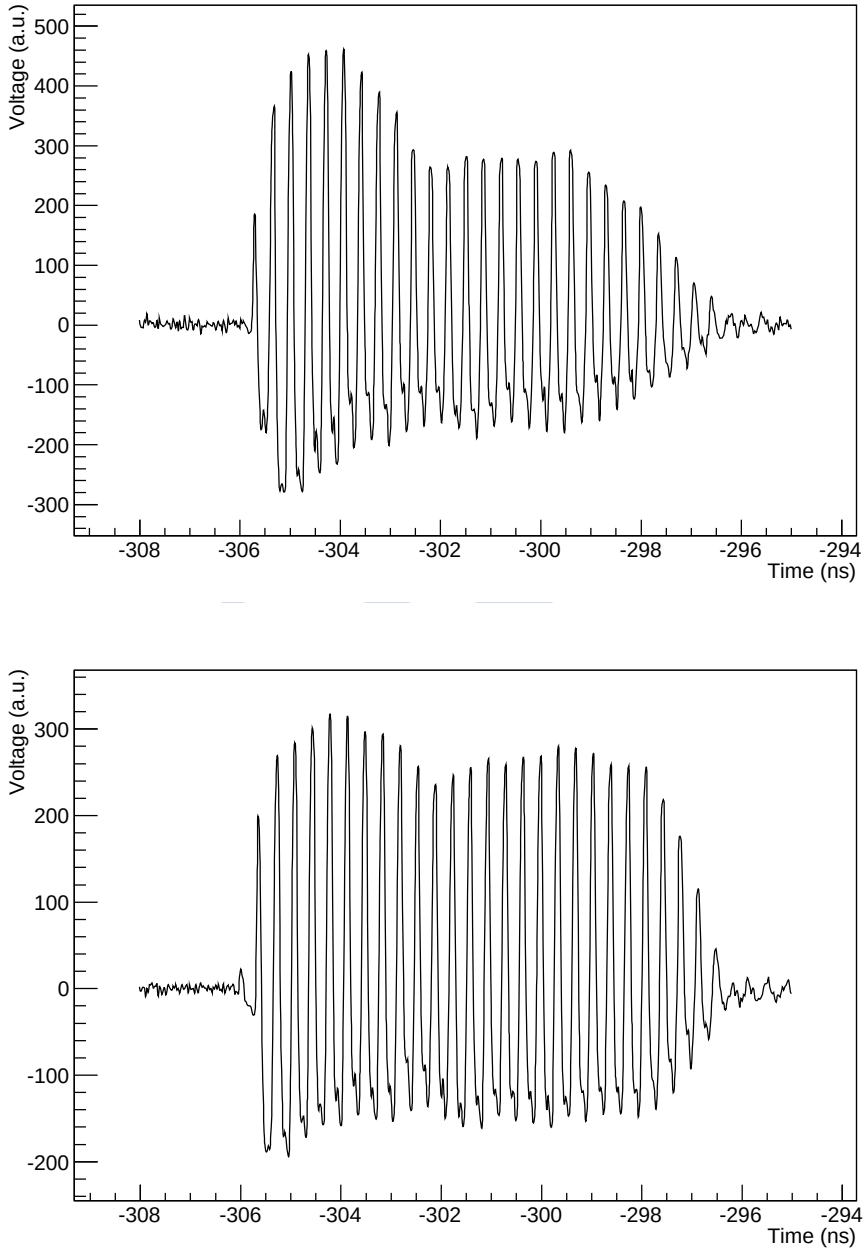

Figure 5.5: Time voltage for the run DST201212071436. The bunch lasts 10 ns and has 30 microbunches, and hence 30 peaks are seen. The upper plot represents the 6th bunch in the run and the lower one the 201st. As can be seen, both signals are different, and within each signal the peaks have different height, pointing to a different number of electrons in each of the microbunches, inducing a bunch modulation that varies from bunch to bunch.

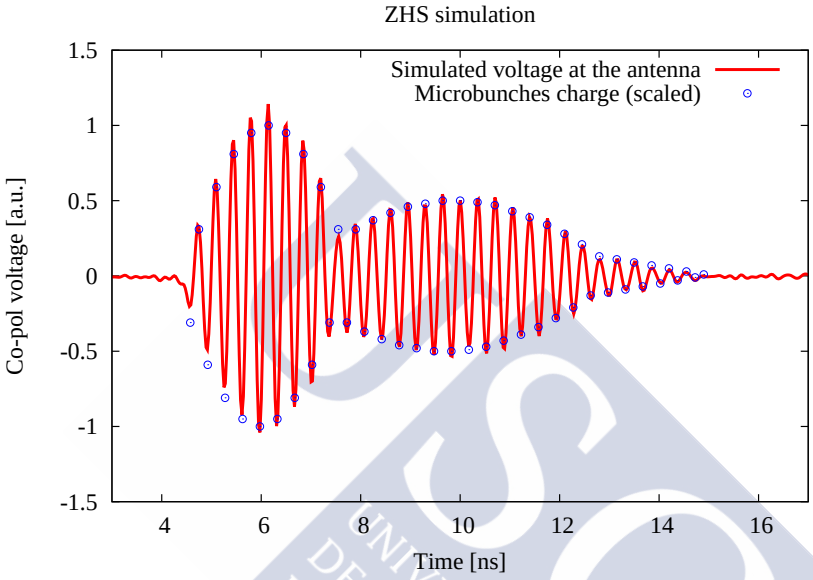

Figure 5.6: Simulated voltage as a function of time for a bunch made of 30 microbunches (solid line). The charge of each microbunch (points) used in the ZHS simulation is plotted in arbitrary units on top of the voltage. The microbunches are separated 0.35 ns in time. The voltage has been obtained from the frequency field given by ZHS convoluted with a simple antenna model (linear up to 2 GHz, falling with $1/\nu$ from 2 GHz) and then transformed to time. A two-blob charge modulation, similar to the voltage envelope seen in the top panel of Fig. 5.5, has been used in this simulation.

Calculating the field and the voltage at the antenna

The particles simulated using GEANT4 are then passed through the ZHS program, that recreates their trajectories through the chamber with small straight line segments called *tracks*. The depth of air in the chamber is ~ 0.48 g cm^{-2}, which is much smaller than a radiation length in air $X_0 \sim 37$ g cm^{-2}, and therefore most electrons do not experience hard bremsstrahlung emission or Møller interactions. Each one of these tracks creates a field in their Fraunhofer zone well approximated by the ZHS formula (Eq. (3.52)), as demonstrated in Chapter 3. Each field induces a different voltage in the antenna, depending on its polarisation and the incoming angle of the radiation as seen by the antenna. The relevant quantity is the *effective length* of the antenna $\mathbf{l}_{\text{eff}}$ that gives the open circuit voltage V_{oc} at the antenna when a plane wave $\mathbf{E}_{\text{inc}}$ (from the Fraunhofer zone of a certain radiating source) reaches it from a direction (θ, ϕ) (see the Intermission chapter for more details),

$$V_{\text{oc}} = \mathbf{E}_{\text{inc}} \cdot \mathbf{l}_{\text{eff}}(\nu, \theta, \phi). \tag{5.2}$$

The effective length is a vectorial, complex quantity. Four real or two complex numbers are needed to fully characterise a conventional antenna at a given direction (θ, ϕ) and frequency ν. Unfortunately, in the calibration available for the horn antenna [6] only two real numbers have been measured, namely, the *realised power gains* in transmission mode $G_\theta^{\text{cal}}(\theta, \phi)$ and $G_\phi^{\text{cal}}(\theta, \phi)$[1]. Information on the orientation of the effective length and the complex phase is not available, so we are forced to work with the calibration data for the co-polarised plane[2], where the orientation for the horn can be assumed to be similar to that of a dipole antenna and the phase can be ignored. See Appendix A for more details.

The realised gain is defined as the transmission gain when the antenna is fed by a 50 Ω generator. This choice turns the realised gain into a useful quantity, since it makes safe to ignore the antenna impedance, as long as the antenna is connected to a 50 Ω transmission line and the oscilloscope is matched to the same line [7].

If the ith electron track creates an electric field $\mathbf{E}_i$ on the antenna, the resulting voltage

[1] $G_\theta^{\text{cal}}(\theta, \phi)$ is the realised gain of the antenna in the direction (θ, ϕ) for an electric field polarised in the $\hat{\theta}$ direction. $G_\phi^{\text{cal}}(\theta, \phi)$ is the same as $G_\theta^{\text{cal}}(\theta, \phi)$ for an electric field polarised in the $\hat{\phi}$ direction. See Appendix A.

[2] For an almost linearly polarised antenna such as the horn antenna, the co-polarised plane (or copol plane or E plane) is the plane centered at the antenna that contains the electric field vector and emits the most electric field. The cross-polarised (or copol or H) plane is the plane perpendicular to that. See the sketch in Fig. (5.7). Since, by definition, the copol plane emits more radiation than any other plane, the received signal will be the highest when the incoming electric field lies on that plane, by reciprocity.

in a 50 Ω equivalent circuit coupled to the antenna can be expressed as

$$V(\nu) = \sum_i \mathbf{E}_i \cdot \mathbf{l}_{\rm load}(\nu, \theta_i, \phi_i), \tag{5.3}$$

where $\mathbf{l}_{\rm load}$ is written with the help of the realised gains $G_\theta^{\rm cal}$ and $G_\phi^{\rm cal}$ (see Appendix A),

$$\mathbf{l}_{\rm load}(\nu, \theta, \phi) = \frac{c_n}{2\sqrt{\pi}\nu}\sqrt{\frac{R_L}{Z_n}}\left[\sqrt{G_\theta^{\rm cal}}\,\hat{\theta} + \sqrt{G_\phi^{\rm cal}}\,\hat{\phi}\right], \tag{5.4}$$

c_n stands for the speed of light in the medium the antenna is inserted in, Z_n is its impedance and R_L is the impedance of the oscilloscope, assumed to be purely resistive (real) and equal to 50 Ω in order to work with the realised gains $G_\theta^{\rm cal}$ and $G_\phi^{\rm cal}$. A sketch of the reference frame, the relevant angles and planes is shown in Fig. 5.7. The reference frame of the antenna must be chosen in such a way that the unit vectors $\hat{\theta}$ and $\hat{\phi}$ are continuous in the co-polarised and cross-polarised planes, provided we take the positive square root for the gain. A global phase is irrelevant except for an inversion of the oscilloscope voltage. Eq. (5.3) is all we would need if we measured directly the voltage at the antenna with a 50 Ω resistance. However, in practice, we need to use coaxial cables, amplifiers and an oscilloscope.

In Fig. 5.8 we show the antenna gain $G_\theta^{\rm cal}$ as a function of frequency for the angle $\theta = 0°$, where the emission and therefore the reception is largest. Although the gain increases for the horn antenna with frequency as seen in Fig. 5.8, this will be partly compensated by the fact that the effective length in Eq. (5.4) has a $1/\nu$ dependence.

As mentioned before, we also need to take into account the influence of the cables and the amplifier on the antenna signal. First, the electric field wave reaches the antenna and creates a voltage between its terminals. This voltage will then feed the coaxial, amplifier and oscilloscope system, which form the rest of the measurement device. For a certain input voltage between the antenna terminals at a given frequency, we need to know the output voltage at the oscilloscope. The easiest way to figure it out experimentally is to use a test voltage at the input and measure the output.

Several different configurations for the cables and amplifiers have been used in the AMY experimental setup, so different calibrations have to be used in the simulations. In Fig. 5.9 several calibrations for the ratio of output and input power vs. frequency are plotted. Again, we lack information on the phase, but a global phase is irrelevant besides a voltage inversion, and we will consider it constant through all the frequency region relevant for the experiment. One remark about Fig. 5.9 is that it holds only for the regime where the amplifier operates in linear mode. When saturation is reached, the calibration is no longer valid.

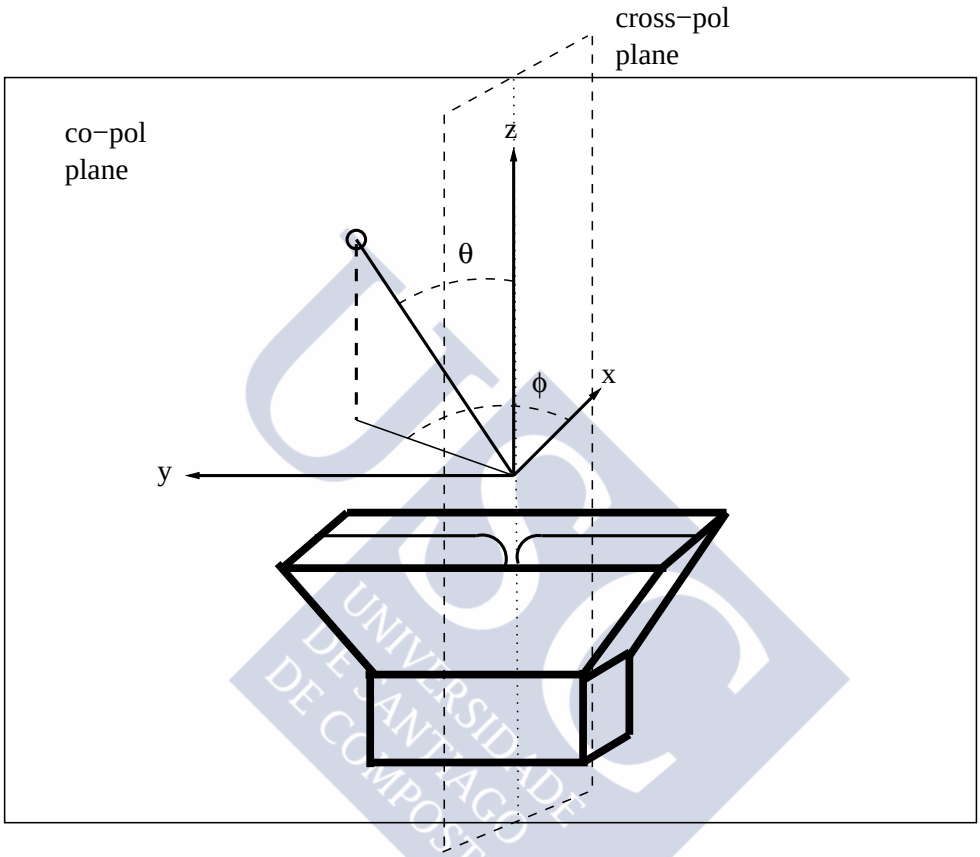

Figure 5.7: Sketch for the calibration reference frame of the antenna. θ and ϕ angles are shown. A horn antenna is depicted at the bottom. The co-pol plane is defined as the yz plane, while the cross-pol plane corresponds to the xz plane.

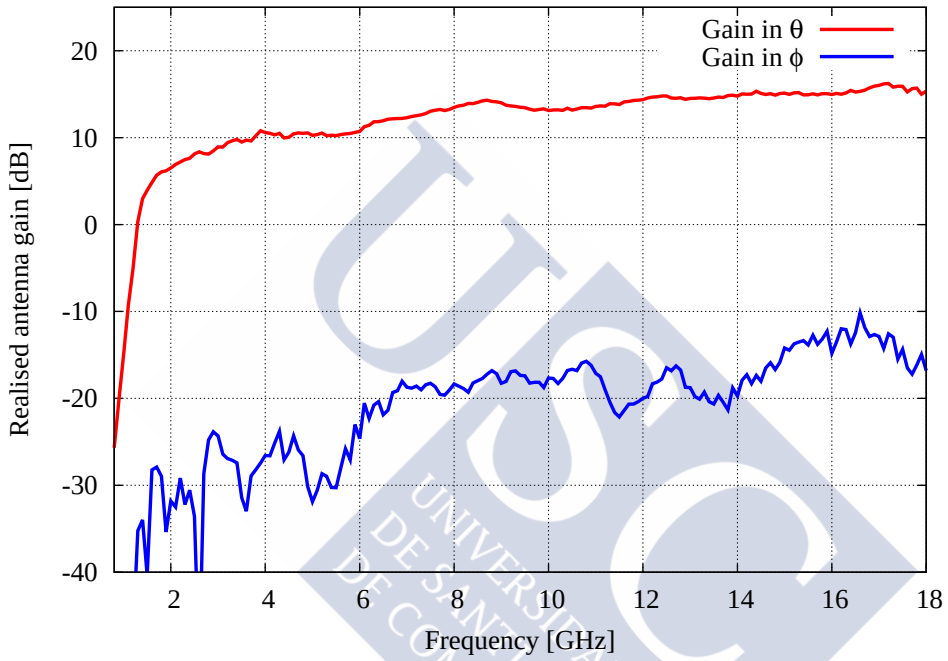

Figure 5.8: Realised gain $G_\theta^{\rm cal}$ for the horn antenna in dB for $\theta = 0°$. See sketch in Fig. 5.7. The upper curve shows the gain in the component parallel to $\hat{\theta}$ of the incident electric field arriving at $\theta = 0°$, where the emission is largest, and the lower curve shows the gain in the component parallel to $\hat{\phi}$ [5, 6].

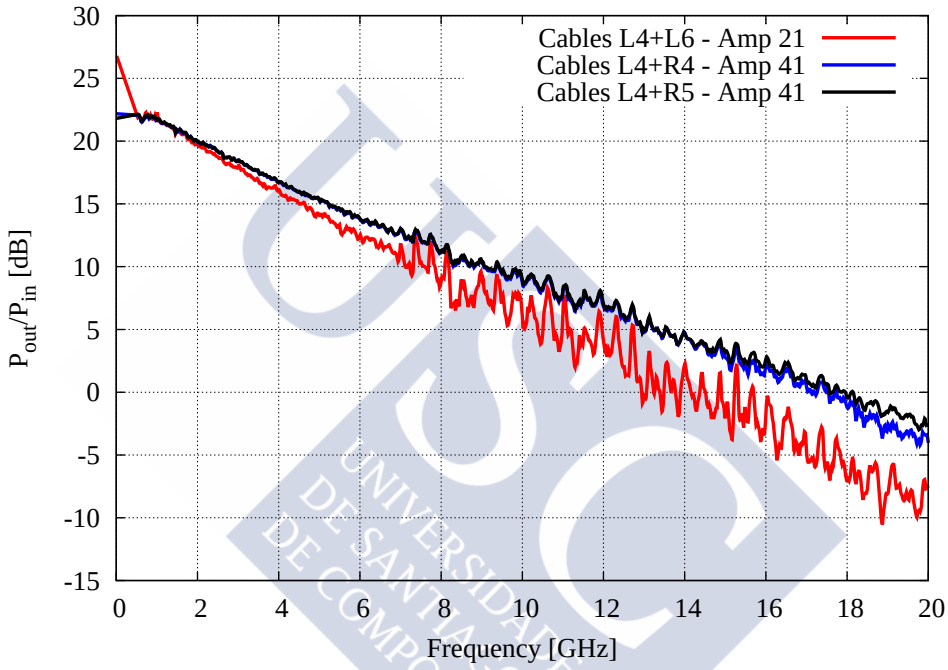

Figure 5.9: Output/Input power ratio in dB as a function of frequency for three different configurations of cables and amplifiers used in the AMY experimental setup [5].

5.1.5 Results of the simulation for a run without targets

The AMY experiment was designed to observe MBR. Since MBR is expected to be produced mainly by low energy electrons (keV-MeV) and the electrons at the LINAC have $K_e = 510$ MeV they are converted into lower energy electrons by means of interactions with targets. However, runs with 0 targets were also performed to study the background to MBR that should come mainly from Cherenkov radiation as well as from the radiation expected from the sudden appearance of the charge in the AMY camera. The ZHS code can account for these two sources of radiation and for this reason we expect to be able to reproduce the radiation collected in the AMY runs with 0 targets.

Let us remember the steps for calculating the voltage at the oscilloscope in a given run:

- GEANT4 simulation of the electron beam at the entrance of the chamber after passing through the targets.
- Addition of the beam lateral spread and distribution of electrons into microbunches replicating the modulation of the field seen in the run.
- Propagation of the beam inside the chamber and calculation of the field with the ZHS code and use of the antenna gain to obtain the input voltage.
- Use of the measurement setup calibration of cables and amplifiers to get the output voltage from the input voltage at the antenna.

As stated before, due to the lack of information on the phases of the effective length, we can only do simulations for a beam that lies approximately in a plane. For this reason we expect our simulation to give realistic results only in the runs without targets where the spread of the particles is expected to be small. The presence of more targets spreads the beam outside a single plane and forces us to make assumptions about the direction of the antenna effective length.

We have simulated the run DST201212140237, taken at 02:37 on the 14th of December, 2012. Characteristics for the run are given in Table 5.1.

This run is a good candidate to compare simulations to data, since we know all of its characteristics (see Table 5.1). However, the mean beam charge is $6 \cdot 10^9$ electrons, a number well beyond the saturation point of the amplifier. For this reason we cannot expect to exactly reproduce the absolute scale of the frequency spectrum of the electric field.

In Fig. 5.10 we plot the simulated voltage compared to the data. Besides the charge rescaling, we multiply the simulation by a factor 0.4 to account for the saturation of the

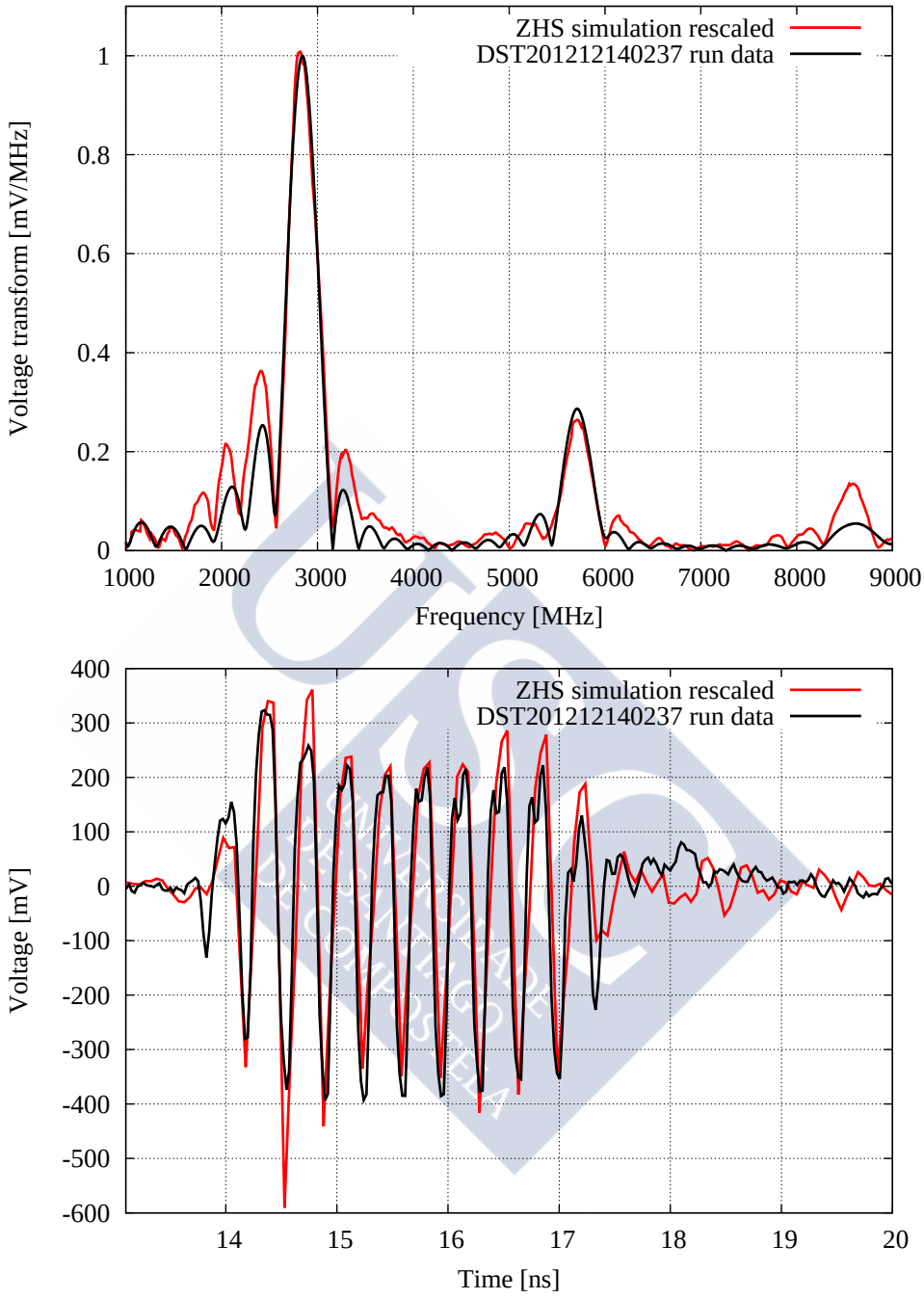

Figure 5.10: Voltage (simulation and data) for the run DST201212140237. Top: Voltage in frequency domain. Bottom: Voltage in time domain. The data are normalised to a 10^9 electron beam, and the simulation is rescaled by a factor of 10^6 due to the charge difference (we used 1000 primary electrons), and by an extra factor 0.4 due to the saturation of the amplifier. Number of electrons for the 10 simulated microbunches matching the modulation of the observed voltage traces: $\{76, 151, 117, 98, 94, 98, 103, 103, 103, 57\}$.

Mean charge (e^-)	Bunch (ns)	Calibration	Targets	polarisation	Position
$6 \cdot 10^9$	3 ns	L5+R5+AMP41	0	Co-pol	C2

Table 5.1: Features of the electron bunch and experimental setup in the DST201212140237 run of the AMY experiment. Position C2 refers to the location of the antenna the center of the chamber, on a lateral side, with coordinates $(x, y, z) = (1, 0, 2)$ m, with z parallel to the length of the chamber. The beam enters the air volume at $(x_0, y_0, z_0) = (0, 0, 0)$ m.

amplifier (see below). The shapes of both spectra (top panel) are similar, and the first and second harmonic peaks are nicely reproduced both in position and shape. The position of the lobes surrounding the first harmonic are also reproduced, although the heights are typically overestimated in the simulation. We have checked that the height of the lobes is very sensitive to the charge modulation of the beam which we introduce ad hoc in the simulation from the observed field in time in the run. The third harmonic can be suppressed with a more spread beam, with the spread of the beam being another ad hoc parameter in our simulation. It should be remarked that the unknown frequency dependence of the saturation could also change the shape of the spectrum.

Due to the large current of the beam, most of the runs without a target, including the one simulated here, suffer saturation, which renders the comparison of normalizations impossible. Since we are in saturated regime, we expect the oscilloscope signal to be lower than predicted by the simulations, and that is precisely what happens, for instance in the run in Fig. 5.10 we had to scale down the simulation by a factor of 0.4 to match the overall normalisation with our simulation.

In Fig. 5.10 bottom, we show the voltage in time domain measured by the oscilloscope compared to the voltage in time that results from transforming the spectrum in the top panel of Fig. 5.10 back to time. Since we do not have data for the phases of the effective length in Eq. (5.2), we have assumed a constant phase at all frequencies. Because of this and despite the good agreement between the simulated time voltage and the data, there are features like the two-ridged peaks that cannot be explained with the simulation.

With Fig. 5.10 we demonstrate that the background for an almost collinear beam can be well reproduced with the ZHS code and the available calibrations. This is an important result that nicely illustrates the applicability of the ZHS algorithm and code to different physical situations of experimental interest beyond those explained in [8, 9].

AMY was designed for measuring the MBR. As a result, most of the data were taken with several targets, which cannot be realistically simulated due to the incomplete calibration of the antenna. The same can be said for the cross-pol configuration.

Also we expect that a better agreement between data and simulation could be achieved with a better knowledge of the input beam (lateral spread, charge in each microbunch...) and with the measurement of the phase of the effective length.

As a general conclusion, we have proven that the ZHS algorithm is capable of reproducing the background in the AMY experiment when the effects of the instrumentation are known in full detail.

5.1.6 Model for molecular bremsstrahlung (MBR) and estimate of emission

In this section we adopt a model for MBR that reproduces experimental data and assumes MBR is due to bremsstrahlung photons emitted by low energy electrons in the field of the molecules of the medium and implement it in the ZHS code which does not account explicitely for this emission mechanism.

Firstly we will review the experiments aimed at measuring MBR and their most important results and try to shed light onto the nature of radiation.

The nature of the MBR

According to [1], MBR in weakly ionized air is created by free electrons accelerating and decelerating through collisions with the fields of molecules in the ambient medium. When an air shower is created, the particles (mainly electrons and positrons) in it ionise the surrounding medium. In [1], it is argued that the electrons (and positrons) collide many times and lose energy, and when they have low enough energy (< 10 eV) they can be treated like thermal electrons. These decelerate in the field of the molecules and emit radiation isotropically. Thus, MBR is expected to be an isotropic radiation. This starting point could lead to a new cosmic ray detection technique with similarities to the widely used fluorescence detection (FD), but with the advantages of lower price of detectors and full-time duty cycle due to the radio waves (GHz frequencies) that can be detected day and night.

In [1] an exponential dependence with time for the radiation intensity has been allegedly measured. For the 28 GeV electron beam at SLAC collisioned with alumina targets, the intensity of the observed radiation in an anechoic chamber filled with air was found to be:

$$I = I_0 e^{-t/\tau}; \qquad I_0 = 10^{-6}\ \mathrm{W/m^2}; \qquad \tau = 10\ \mathrm{ns}. \tag{5.5}$$

These results were not reproduced with the AMY [3] experimental setup. Besides,

there are some concerns about the experimental approach for the measurement of I_0. Since MBR is expected to be unpolarised and the usual Cherenkov electric field for a particle is polarised in a direction perpendicular to the line of sight that goes from the antenna to the particle [10, 8], the antennas in the SLAC experiment were set to cross-polarisation mode in order to measure the polarisation perpendicular to the beam. However, antennas cannot perfectly filter one polarisation and there is always some leakage. Moreover, particles propagating off-axis can create a Cherenkov field with a polarisation that has a sizable component in the cross-pol channel. In [1] they acknowledge the leakage, but choose to disregard it.

Another experiment called MIDAS [11, 12] tried to measure MBR in air showers. The experiment set an upper bound to the flux of incoherent emission of MBR of $3.98 \cdot 10^{-15}$ W m^{-2} Hz^{-1} with a 95% CL, and an upper limit to the totally coherent flux of $\sim 4.5 \cdot 10^{-16}$ W m^{-2} Hz^{-1}, both for a reference shower of $3.36 \cdot 10^{17}$ eV of total energy at a distance of 0.5 m from the shower axis, a configuration similar to the one at SLAC, excluding the power flux measured in [1] over a large range of partial coherence hypothesis.

An alternative semi-analytical approach for calculating the MBR flux has been discussed in [13]. They estimated a flux of $4 \cdot 10^{-26}$ W m^{-2} Hz^{-1} for a $10^{17.5}$ eV shower at a distance of ~ 10 km from the shower core, which is one order of magnitude lower than the extrapolation in [1].

In another experiment, Conti *et al.* [2] managed to measure radiation coming from a 81 keV electron beam. The energies of the particles in the beam are much lower than the Cherenkov threshold in air (~ 20 MeV), and therefore the only expected radiation should come from electrons accelerating and decelerating through collisions with the molecules in air. In [2] the radiation was found to be unpolarised (Fig. 5.11), incoherent and having the angular pattern of bremsstrahlung emission of very low energy photons (Fig. 5.12) in the field of the nuclei of the molecules, with a maximum in the direction of the beam, *i.e.* non-isotropic. A prediction using a Monte-Carlo code for tracking the particles and the standard bremsstrahlung cross section is also given, matching the observations within experimental uncertainties. There seems to be a systematic bias, though, because the Monte Carlo simulations are below the data and a correction factor ~ 0.73 to fit the data must be applied. This might be explained by the lack of the radiation from the sudden acceleration of the ionised electrons in the model. Nevertheless, the experimental data clearly clash with the experiment at SLAC [1].

So far, we have two different sources for the so-called molecular bremsstrahlung:

1. Bremsstrahlung at very low electron energies (< 10 eV), emitted isotropically, ac-

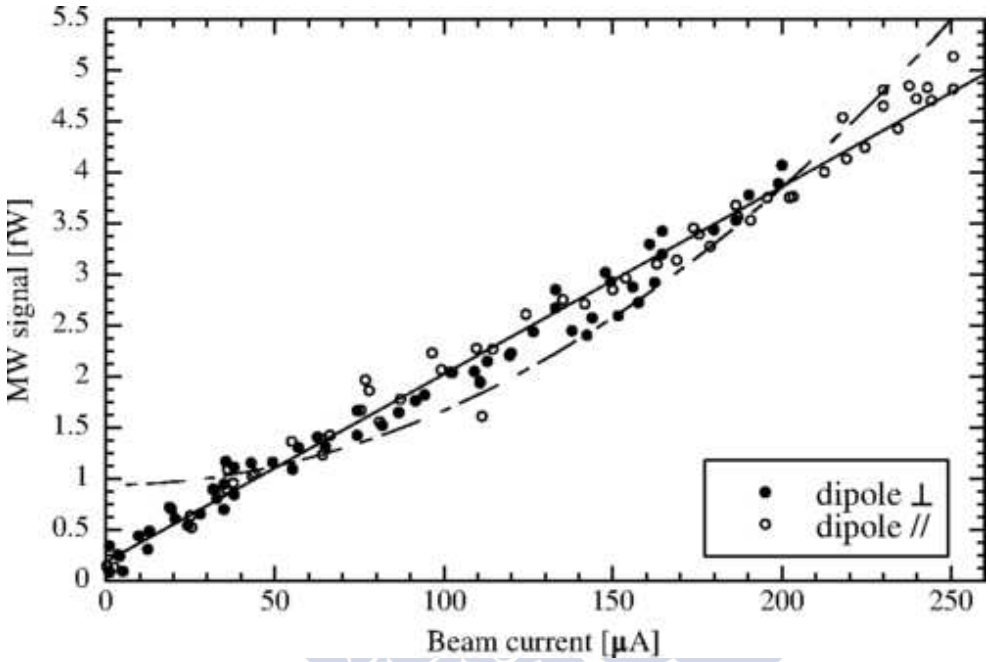

Figure 5.11: Dependence of the microwave signal in the Conti *et al.* experiment [2] for an observer at at $\theta = 25°$ from the beam axis for the co-pol (parallel) and cross-pol (perpendicular) polarisations. Linear and quadratic fits to the data are also shown. The linear fit is closer to the data, implying that the emission is incoherent.

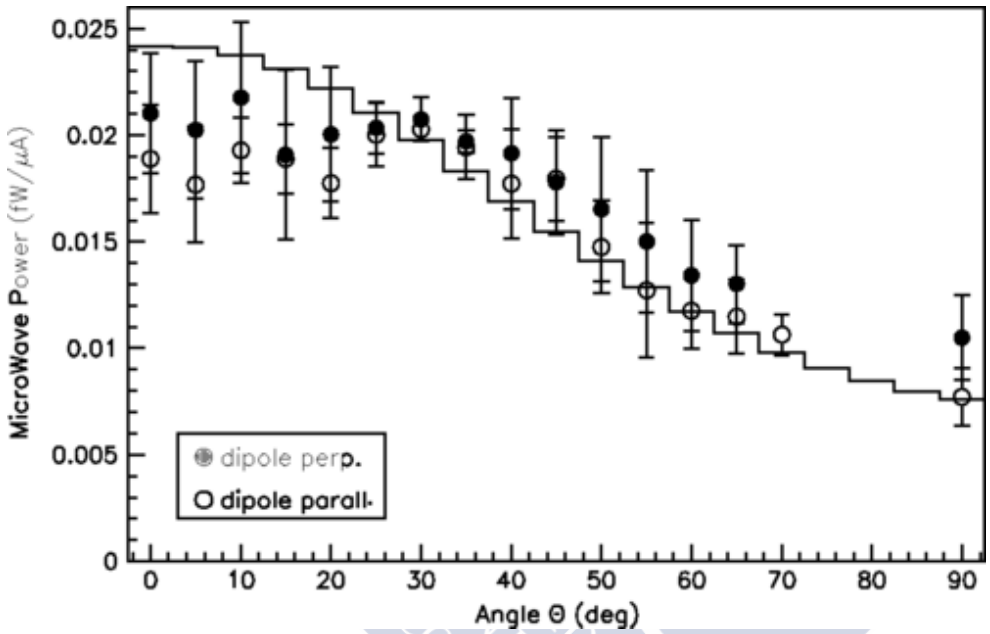

Figure 5.12: Angular dependence of the microwave emitted power in the Conti *et al.* experiment [2] for the co-pol (parallel) and cross-pol (perpendicular) polarisations, and results of simulations (full line) performed in [2]. The results of the simulations have been rescaled by a factor of 0.73 in order to fit the data.

cording to Gorham *et al.* in [1].

2. Bremsstrahlung from electrons having kinetic energies larger than 1 keV in the field of the nuclei of molecules, beamed in the forward direction, according to Conti *et al.* [2].

We will adopt the view of MBR of item 2, because it is the model that has been able to reproduce the experimental results in [2]. We will implement the model of Conti *et al.* in the ZHS Monte Carlo code (without using the ZHS formula for the electric field) and obtain in this manner an estimation of the MBR in the AMY experimental setup.

Formula for the bremsstrahlung flux

For a particle track, we can calculate the mean energy in the emitted bremsstrahlung spectrum per unit frequency and solid angle for small scattering angle collisions[3]. Using the bremsstrahlung cross section for one emitted photon ($\mathrm{d}^2\sigma/\mathrm{d}\nu\mathrm{d}\Omega$) the mean energy emitted is given by:

$$\langle \frac{\mathrm{d}^2 E}{\mathrm{d}\nu\ \mathrm{d}\Omega} \rangle = h\nu\ \frac{\rho N_A l}{A} \frac{\mathrm{d}^2\sigma}{\mathrm{d}\nu\ \mathrm{d}\Omega}, \tag{5.6}$$

where ρ is the medium density, l is the length of the particle track, N_A is Avogadro's number in mol^{-1}, A is the atomic mass in g/mol, and σ is the bremsstrahlung cross section per frequency ν and solid angle Ω (with both photon polarisations summed [14]). Eq. (5.6) is simply the energy of the emitted photon at frequency ν times the probability of emitting that photon along the electron track.

We are interested in the power emitted per unit area (flux) to compare with the AMY experiment. For an antenna in the far-field of the track the integration in solid angle can be approximated by a multiplication by $\Delta\Omega = A_{\mathrm{ant}}/R^2$, with R the distance from the track to the antenna (assumed to be in the far-field) and A_{ant} the area of the antenna. Then, we divide by the area of the antenna and the measurement time Δt to get the mean flux:

$$\begin{aligned} \langle F \rangle &= \langle \frac{\mathrm{d}^3 E}{\mathrm{d}\nu\ \mathrm{d}t\ \mathrm{d}A} \rangle \approx h\nu\ \frac{\rho N_A l}{A} \frac{\mathrm{d}^2\sigma}{\mathrm{d}\nu\ \mathrm{d}\Omega} \frac{\Delta\Omega}{\Delta t A_{\mathrm{ant}}} \\ &= h\nu\ \frac{\rho N_A l}{A} \frac{\mathrm{d}^2\sigma}{\mathrm{d}\nu\ \mathrm{d}\Omega} \frac{A_{\mathrm{ant}}}{R^2 \Delta t A_{\mathrm{ant}}} \\ &= h\nu\ \frac{\rho N_A l}{A} \frac{1}{R^2 \Delta t} \frac{\mathrm{d}^2\sigma}{\mathrm{d}\nu\ \mathrm{d}\Omega}. \end{aligned} \tag{5.7}$$

[3] In doing so, we are neglecting the radiation field at radio frequencies from hard collisions. However, this is is a higher order process and its radiation electric field is already included in the ZHS formula when the initial and final angles of the incident particle are significantly different.

To calculate the power received by an antenna from a set of tracks, we need to make some hypotheses. First of all, we assume incoherence so that we can add the energy of the radiation coming from several tracks. This is an important assumption, since coherence can play a major role depending on the beam structure and the position of the observer. We also assume an antenna with a flat angular pattern. Although this is impossible, it will give us an upper bound to the incoherent flux, since a real antenna would always receive less flux than an isotropic receiver. Under these assumptions, the flux at the antenna can be written as a sum of the contributions of each track:

$$\langle F \rangle_{\text{antenna}} \sim h\nu \frac{\rho N_A}{A\Delta t} \sum_{i,\text{tracks}} \frac{l_i}{R_i^2} \frac{\mathrm{d}^2\sigma}{\mathrm{d}\nu \mathrm{d}\Omega}(E_i). \tag{5.8}$$

We will also consider the air made of nitrogen and oxygen only and treat the molecules as separate nuclei. In the interest of simplification, and since we want to obtain an upper bound to MBR we will use the atomic mass of nitrogen (the smallest of the two) because it results in a slightly larger flux, while we will use the atomic number (Z) of the oxygen, since the cross section is proportional to the atomic number.

Another effect to consider is screening. Screening is caused by the field of the electrons surrounding the nucleus and tends to lower the cross section of the bremsstrahlung process. Screening is important when $\gamma \lesssim 1$ [14], with γ given by:

$$\gamma = \frac{100\ h\nu\ m_e c^2}{E_0 E Z^{1/3}}. \tag{5.9}$$

Here E_0 and E are the initial and final energies of the scattered electron, respectively. At low frequency, the screening is total, since a low energy photon sees the atom or molecule as a whole, and as a result the cross section is drastically reduced due to the electric field of the electrons, because the effect of the field of the nucleus is attenuated. Since we are interested in the radiation emitted at GHz frequencies, the energy of the relevant photons will always be less than 10^{-3} eV. This means that even for electrons at rest ($E \approx E_0 = m_e c^2$) γ is small in the frequency band of the AMY experiment, from ~ 1 to ~ 20 GHz,

$$\gamma < \frac{100 \cdot 4.136 \cdot 10^{-15} \cdot 20 \cdot 10^9}{0.511 \cdot 10^3 \cdot 8^{1/3}} = 8 \cdot 10^{-6}, \tag{5.10}$$

as a consequence screening of the bremsstrahlung cross section cannot be ignored if we want a precise prediction. Not taking screening into account overestimates the bremsstrahlung cross section.

Angular behaviour of the bremsstrahlung cross section

One could, in principle, use a cross section differential in photon frequency and solid angle in Eq. (5.8), such as formula 2BN in the comprehensive review on bremsstrahlung emission by Koch and Motz [14]. However, this formula may give numerical problems for a soft photon such as the GHz photons in the AMY experiment due to the presence of terms proportional to $(E_0 - E)^{-1}$ with $E = E_0 - h\nu$ and $h\nu \sim$ a few 10^{-3} eV. We may instead multiply and divide by the cross section differential in photon frequency only, to get:

$$\frac{\mathrm{d}^2\sigma}{\mathrm{d}\nu\ \mathrm{d}\Omega} = S(\nu,\theta,\beta)\frac{\mathrm{d}\sigma}{\mathrm{d}\nu}, \tag{5.11}$$

where θ is the angle between the photon and the incident electron momentum, β is the speed of the incident electron and the function S gives information about the angular distribution, defined as:

$$S(\nu,\theta,\beta) = \frac{\mathrm{d}^2\sigma}{\mathrm{d}\nu\ \mathrm{d}\Omega}\Big/\frac{\mathrm{d}\sigma}{\mathrm{d}\nu}. \tag{5.12}$$

For low photon energies, it can be demonstrated [15] that the angular distribution S can be written using the Legrendre polynomials P_l:

$$S(\nu=0,\theta,\beta) = \frac{1-\beta^4}{4\pi(1-\beta\cos\theta)^4}\left(1 - \frac{3\beta}{1+\beta^2}P_1(\cos\theta) + \frac{1}{2}P_2(\cos\theta)\right). \tag{5.13}$$

Using that $P_1(x) = x$ and $P_2(x) = \frac{1}{2}(3\cos^2 x - 1)$ we can rewrite the previous expressions.

$$\begin{aligned} S(\nu=0,\theta,\beta) &= \frac{(1-\beta^2)(1+\beta^2)}{4\pi(1-\beta\cos\theta)^4}\left(1 - \frac{3\beta}{1+\beta^2}\cos\theta + \frac{1}{4}(3\cos^2\theta - 1)\right) \\ &= \frac{1-\beta^2}{4\pi(1-\beta\cos\theta)^4}\left(1+\beta^2 - 3\beta\cos\theta + \frac{1}{4}(1+\beta^2)(3\cos^2\theta - 1)\right) \\ &= \frac{1-\beta^2}{4\pi(1-\beta\cos\theta)^4}\left(\frac{3}{4}(1-\beta\cos\theta)^2 + \frac{3}{4}(\beta-\cos\theta)^2\right) \\ &= \frac{3}{16\pi}\frac{1-\beta^2}{(1-\beta\cos\theta)^2}\left(1 + \frac{(\beta-\cos\theta)^2}{(1-\beta\cos\theta)^2}\right). \end{aligned} \tag{5.14}$$

It is worth mentioning that Eq. (5.14) is precisely the classical expression for the angular distribution of radiation from a charged particle calculated by Jackson in [16]. Eq. (15.10) in [16], adding the classical intensity for both polarisations yields (in gaussian units, but this does not affect the angular distribution):

$$\lim_{\omega\to 0}\frac{\mathrm{d}^2 I}{\mathrm{d}\omega\ \mathrm{d}\Omega} = \frac{Z^2e^2}{8\pi^2 c}|\Delta\beta|^2\frac{1}{(1-\beta\cos\theta)^2}\left(1 + \frac{(\beta-\cos\theta)^2}{(1-\beta\cos\theta)^2}\right). \tag{5.15}$$

$|\Delta\beta|$ is the momentum transfer due to the collision, *i.e.* the difference between final and initial speeds of the electron. Integrating Eq. (5.15) in solid angle, we arrive at:

$$\lim_{\omega\to 0}\frac{\mathrm{d}I}{\mathrm{d}\omega}=\frac{2}{3\pi}\frac{Z^2e^2}{c}\frac{1}{1-\beta^2}|\Delta\beta|^2. \tag{5.16}$$

Taking Eq. (5.15) and dividing it by Eq. (5.16) we arrive at the angular distribution of the radiation, that is, at Eq. (5.14).

$$\lim_{\omega\to 0}\frac{\mathrm{d}^2I}{\mathrm{d}\omega\ \mathrm{d}\Omega}\Big/\lim_{\omega\to 0}\frac{\mathrm{d}I}{\mathrm{d}\omega}=\frac{3}{16\pi}\frac{1-\beta^2}{(1-\beta\cos\theta)^2}\left(1+\frac{(\beta-\cos\theta)^2}{(1-\beta\cos\theta)^2}\right). \tag{5.17}$$

For low energies (low β), the emission tends to be isotropic, while for high energies (β close to 1), the radiation is beamed in the forward direction. In Fig. 5.13 we show ($\nu=0,\theta,\beta$) as a function of θ for different values of β (kinetic energy). If MBR is produced primarily by bremsstrahlung of electrons of keV and higher energies in the molecular electric field, it cannot be isotropic. Once the angular behaviour of $\mathrm{d}^2\sigma/\mathrm{d}\nu\mathrm{d}\Omega$ is known we need an expression for $\mathrm{d}\sigma/\mathrm{d}\nu$. We will consider two options in the following.

The non-screened Born approximation cross-section

The bremsstrahlung cross section per unit frequency without screening under the Born approximation[4] corresponds to formula 3BN of Koch and Motz [14] - see Eq. (5.18). We reproduce it here to make the discussion self-contained. The cross section 3BN in [14] reads:

$$\begin{aligned}\frac{\mathrm{d}\sigma}{\mathrm{d}\nu} &= \frac{Z^2r_0^2}{137}\frac{1}{\nu}\frac{p}{p_0}\left\{\frac{4}{3}-2E_0E\left(\frac{p^2+p_0^2}{p^2p_0^2}\right)+\frac{\epsilon_0E}{p_0^3}+\frac{\epsilon E_0}{p^3}-\frac{\epsilon\epsilon_0}{pp_0}\right.\\ &+ L\left[\frac{8E_0E}{3p_0p}+\frac{k^2(E_0^2E^2+p_0^2p^2)}{p_0^3p^3}+\frac{k}{2p_0p}\left(\left(\frac{E_0E+p_0^2}{p_0^3}\right)\epsilon_0\right.\right.\\ &- \left.\left.\left.\left(\frac{E_0E+p^2}{p^3}\right)\epsilon+\frac{2kE_0E}{p^2p_0^2}\right)\right]\right\}.\end{aligned} \tag{5.18}$$

Where r_0 is the electron classical radius and L, ϵ_0 and ϵ are defined as follows:

$$L=2\log\left[\frac{E_0E+p_0p-1}{k}\right], \tag{5.19}$$

[4]The Born approximation for relativistic electron speeds applies when $\beta\gg Z/137$ or equivalently when $T\gg\left(\frac{1}{\sqrt{1-(8/137)^2}}-1\right)m_ec^2\sim 8.7$ keV.

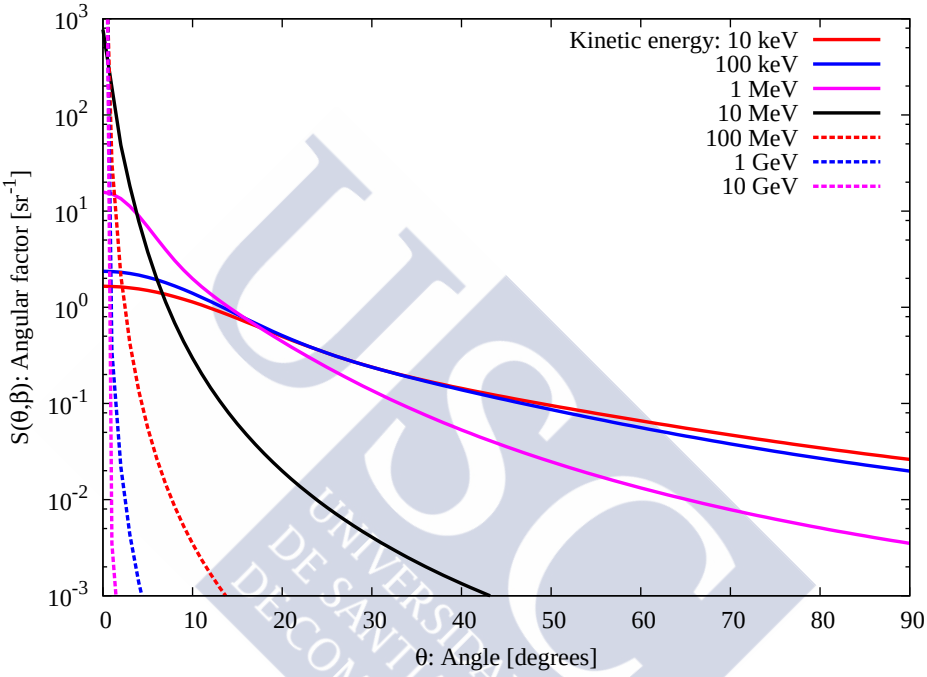

Figure 5.13: Angular distribution $S(\nu = 0, \theta, \beta)$ of the emitted photons at $\nu = 0$ as a function of the angle with respect to the direction of the electron for several electron kinetic energies (from 10 keV to 10 GeV). As the kinetic energy of the electron increases, the emitted radiation is increasingly peaked in the forward direction.

$$\epsilon_0 = \log\left(\frac{E_0 + p_0}{E_0 - p_0}\right), \tag{5.20}$$

$$\epsilon = \log\left(\frac{E + p}{E - p}\right). \tag{5.21}$$

The quantities with 0 refer to the incident electron, and the ones without 0 to the outgoing electron. k is the photon energy. Energies are given in mc^2 units and momenta in mc units, which means that to convert the equation to standard units we must make the standard changes for energies and momenta:

$$E \to \frac{E}{mc^2}; \qquad p \to \frac{p}{mc}. \tag{5.22}$$

Due to conservation of energy (ignoring the recoil of the nucleus):

$$E_0 = E + k. \tag{5.23}$$

Eq. (5.18) neglects screening and fails for non-relativistic speeds, where the Born approximation is not valid.

Tabulated screened bremsstrahlung cross sections

Another option for the cross section is to use the tabulated values of a partial wave expansion numerical calculation with screening, which will give more realistic results. As we have argued before, the photon energies ($\nu \sim$ few GHz) and electron kinetic energies in AMY are in a range where the bremsstrahlung cross section is strongly screened.

In [17] tabulated cross sections for oxygen ($Z = 8$) at low frequency ($k/T \to 0$) can be found for electron kinetic energies from $T = 1$ keV to 2 MeV (k is again the photon energy). In [18] the range covers from $T = 1$ keV to 10 GeV, but the closest to air element available is carbon ($Z = 6$). The quantity tabulated in these papers is the scaled cross section, defined as:

$$\sigma^{\text{scaled}} = \frac{k\beta^2}{Z^2}\frac{\mathrm{d}\sigma}{\mathrm{d}k} = \frac{\nu\beta^2}{Z^2}\frac{\mathrm{d}\sigma}{\mathrm{d}\nu}. \tag{5.24}$$

Values are reproduced in Table 5.2 for completitude.

As a consequence, if the kinetic energy is less than 2 MeV, we can use the cross section for oxygen. Otherwise, we have to use the carbon cross section. The method we use for the evaluation of the cross section at an arbitrary energy T from the tabulated cross section is a simple linear interpolation. If $T_i \le T \le T_{i+1}$:

$$\frac{\mathrm{d}\sigma}{\mathrm{d}\nu} = \frac{8^2}{\beta^2(T)\nu}\left(\sigma_i^{\text{scaled}} + \frac{\sigma_{i+1}^{\text{scaled}} - \sigma_i^{\text{scaled}}}{T_{i+1} - T_i}(T - T_i)\right). \tag{5.25}$$

Table 5.2: Tabulated scaled (see Eq. (5.24)) bremsstrahlung cross sections ($k/T = 0$) for various electron kinetic energies. Left: in carbon, $Z = 6$, taken from [18]. Right: in oxygen, $Z = 8$, [17].

T [MeV]	σ^{scaled} [mb]	T [MeV]	σ^{scaled} [mb]
0.001	5.335	0.001	4.762
0.002	6.495	0.0025	6.328
0.005	8.014	0.005	7.534
0.01	9.135	0.01	8.671
0.02	10.19	0.025	10.112
0.05	11.50	0.050	10.978
0.1	11.91	0.075	11.366
0.2	12.17	0.1	11.535
0.5	12.63	0.2	11.881
1.0	13.22	0.3	12.059
2.0	13.78	0.4	12.234
3.0	14.04	0.5	12.363
4.0	14.19	0.6	12.452
5.0	14.16	0.8	12.762
6.0	14.24	1.0	12.971
8.0	14.34	1.2	13.234
10.0	14.40	1.4	13.418
15.0	14.47	1.6	13.428
20.0	14.50	1.8	13.573
30.0	14.52	2.0	13.543
40.0	14.52		
50.0	14.52		
60.0	14.50		
80.0	14.53		
100.0	14.53		
200.0	14.51		
500.0	14.51		
1000.0	14.51		
2000.0	14.53		
5000.0	14.51		
10000.0	14.51		

Comparison of bremsstrahlung cross sections

We show in Fig 5.14 the non-screened Born approximation and the tabulated screened bremsstrahlung cross sections for the emission of photons at fixed frequency, $\nu = 2.8$ GHz, corresponding to the frequency of the first harmonic observed in the AMY experimental setup. The Born approximation is always above the screened tabulated cross section by an order of magnitude. For low kinetic energies (~ 8.7 keV and smaller), the Born approximation ceases to be valid and predicts a steeper curve than the partial wave expansion method.

We will use both cross sections in order to have two different results, the one using the larger non-screened cross section will naturally lead to a larger upper bound to the intensity of the emitted radiation.

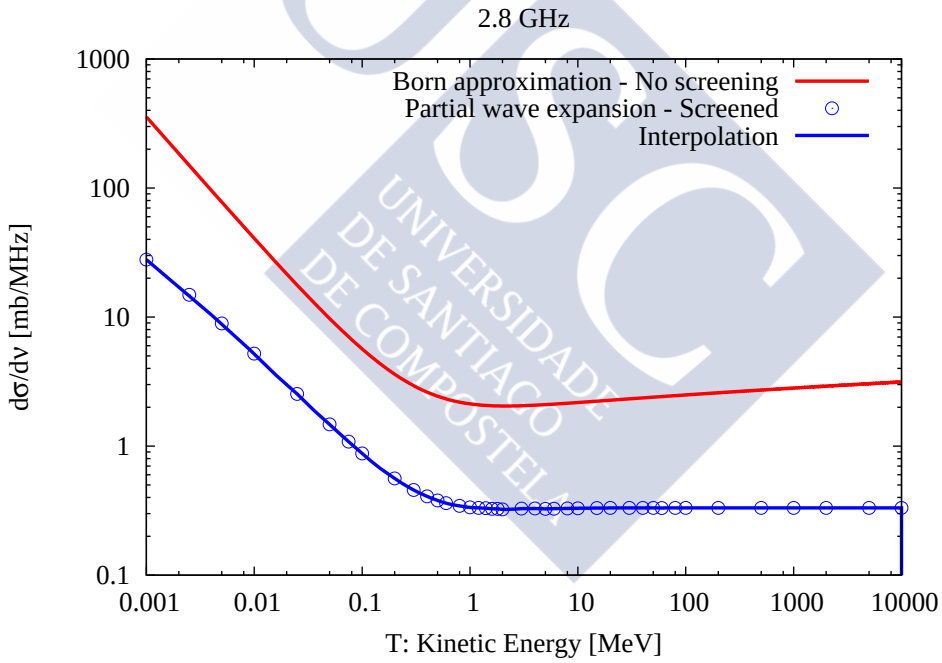

Figure 5.14: Bremsstrahlung cross section per unit frequency ($d\sigma/d\nu$) as a function of the kinetic energy of the electron. The non-screened Born approximation (red) and screened partial wave expansion (blue) are shown. The frequency of emission is $\nu = 2.8$ GHz.

Explicit expression for the flux

The radiated flux is given in Eq. (5.8). Separating explicitly the cross section into the angular part and the frequency part, we have:

$$\langle F \rangle_{\text{antenna}} \sim h\nu \frac{\rho N_A}{A\Delta t} \sum_{i,\text{tracks}} \frac{l_i}{R_i^2} S(\theta_i, \beta_i) \frac{\mathrm{d}\sigma_i}{\mathrm{d}\nu}. \tag{5.26}$$

Eq. (5.26) can be implemented either with the analytical non-screened Born formula for $\mathrm{d}\sigma/\mathrm{d}\nu$ or the tabulated partial wave expansion that accounts for screening (see Fig. 5.14). We must remember that both cross sections yield the spectrum of both polarisations combined. We will use both in the next section.

Implementation in ZHS

As already mentioned, ZHS [19] is a code for the simulation of the interactions and trajectories of electrons, positrons and photons in a medium. The ZHS code can provide us with a set of tracks representing the trajectory of a propagating electron in air. In particular the ZHS code gives the velocity and position of each track from which θ_i, the angle to the antenna, can be calculated. With this information along with the bremsstralung cross section in Eqs. (5.11), (5.14) and either Eq. (5.18) or Eqs. (5.24) and (5.25) for $\mathrm{d}\sigma/\mathrm{d}\nu$ we can calculate the emitted flux with the aid of Eq. (5.26). We follow the electrons until a threshold kinetic energy of 1 keV.

In this modified version of ZHS, the particles are injected into a rectangular chamber. Upon exiting the chamber, a particle ceases to exist and is not taken into account for further calculations. We also ignore the particles once their kinetic energy is less than $T_{\text{threshold}} = 1$ keV, following [2].

After embedding the Born approximation cross section in ZHS, the first task to perform was to check the behaviour of the yield of MBR emission as a function of the length l_i of the tracks modelling the trajectory of each particle. This length can be chosen by increasing or decreasing the number of steps in which the electron track is divided[5]. In Fig. 5.15 we show the results for a beam comprised of 1000 collinear electrons of 1 MeV of kinetic energy injected all at the same time. The chamber is finite with dimensions of 2x2x4 m^3 and the antenna is placed at $(x, y, z) = (1, 0, 2)$ m, with $(0, 0, 0)$ the entrance point of the beam in the chamber. We have used three different seeds to show the typical difference due to the random development of the shower. As it can be seen, as the number of steps increases

[5]This is controlled internally with a parameter called $nsteps\_fac$.

(the length of tracks decreases) the curve tends to increase for the three different seeds, and around 1000 steps it reaches a plateau where the seeds produce a bigger change in yield than increasing the number of steps. We must also note that increasing the number of steps does not lead to a convergent value for the yield, since a different number of steps creates a different shower as the random numbers for the interactions change as well. From now on, we will use 1000 steps, which corresponds to a maximum length of the tracks of ~ 1 mm.

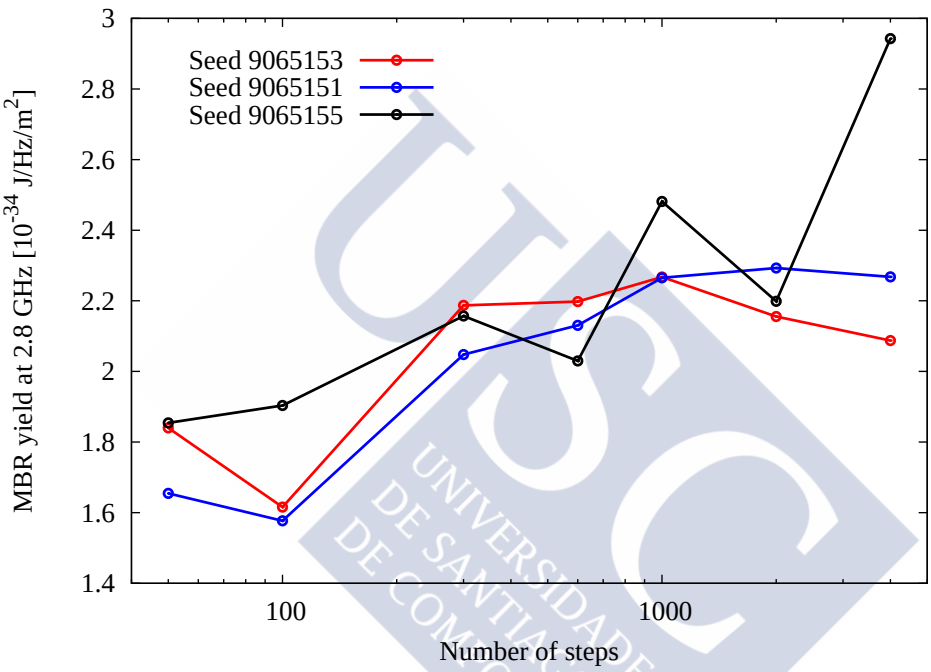

Figure 5.15: MBR yield at 2.8 GHz (Born approximation) for a shower of 1000 collinear electrons of 1 MeV of kinetic energy as a function of the number of steps in which the electron trajectories are divided. Three different seeds for random number generation in the ZHS code have been used.

After studying the dependence with the number of steps, we perform a check of the implementation of the MBR model in the ZHS code. For that purpose we calculate the energy E_{MBR} emitted thorugh bremsstrahlung at a fixed frequency ν_0 and in all directions, as a function of electron kinetic energy and compare it with the energy obtained with the simulation performed in [2]. For a very big chamber, electrons of several kinetic energies

were injected, and the emitted energy calculated according to the formula:

$$E_{\mathrm{MBR}}(\nu_0) \approx h\nu_0 \frac{\rho N_A}{A} \Delta\nu \sum_{i,\mathrm{tracks}} l_i \frac{\mathrm{d}\sigma}{\mathrm{d}\nu}(E_i, \nu_0). \tag{5.27}$$

This equation is similar to Eq. (5.26), but without geometric factors and eliminating the Δt since we are now calculating energy instead of power. We also include a bandwidth $\Delta\nu = 0.75$ GHz similar to that used in [2]. The calculation was performed at a frequency $\nu_0 = 11.325$ GHz as done in [2]. We have performed this calculation with two choices for $\mathrm{d}\sigma/\mathrm{d}\nu$: the Born approximation formula in Eq. (5.18) and the tabulated screened cross sections in Eq. (5.24) (see also Fig. 5.14).

Our results and comparison with the calculations in [2] are shown in Fig. 5.16. Born approximation (red dots) gives a larger energy than the tabulated screened cross sections (blue dots), as expected. A linear fit of the radiated energy *vs* kinetic electron energy $E = aT$ as obtained with the tabulated cross section data is in good agreement (within 15% in the slope) with Conti's fit [2] for electron energies above 10 MeV and below 10 GeV. However, for low energies, ZHS deviates from linearity and predicts a larger emission. This can be caused by approximations in the ZHS code, which was never intended to be used for non-relativistic kinetic energies. For instance, ZHS does not accurately take into account processes at keV energies such as the scattering with the atoms of the surrounding medium, while the PENELOPE code used in [2] uses numerical cross sections for collisions with atoms at low energies. Despite this clear discrepancy at $T < 1$ MeV the agreement with an independent simulation gives us confidence in our implementation of the MBR model in the ZHS code. We will apply the MBR model implemented in the ZHS to the AMY experiment in a configuration with 5 alumina targets. $\sim 99.5\%$ of the electrons that enter the chamber in that case have kinetic energies larger than 1 MeV, and lie in the region where the results of the ZHS code for the total radiated energy agree with those of Conti [2].

Estimation of the MBR yield for the AMY experiment

We firstly recall again that the AMY experiment (see [3] and previous subsections) consists on an anechoic chamber of 2x2x4 m^3 filled with air and a LINAC (DAΦNE) that injects a beam of electrons into the chamber. A horn antenna is placed inside (at position $(1, 0, 2)$ m) and its signal is amplified and read by an oscilloscope at the output.

Before entering the chamber, the beam can go through a variable depth of alumina targets. The experimental bound given by AMY (see section 5.1.3) has been obtained

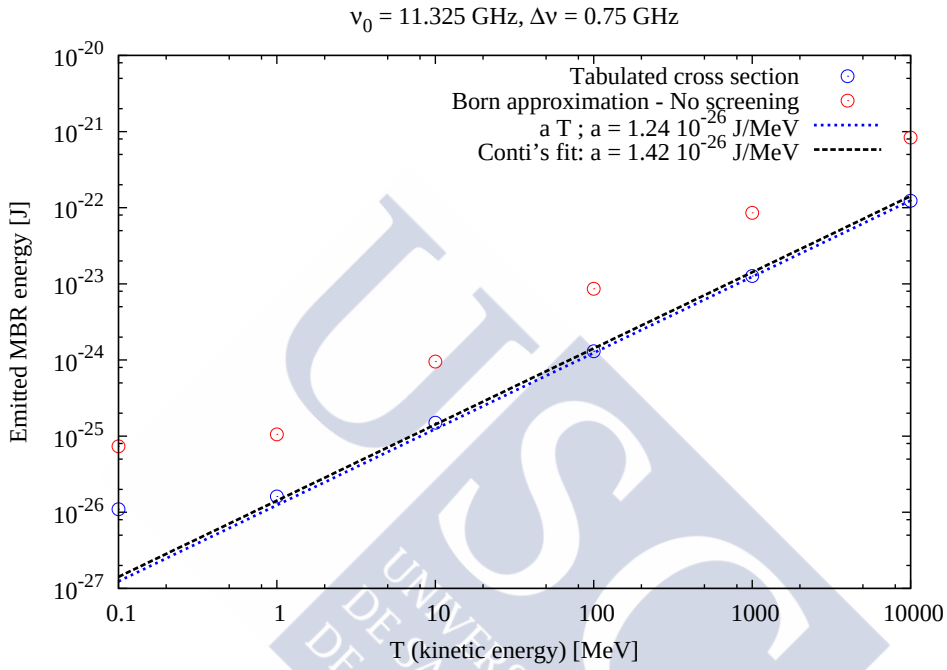

Figure 5.16: Energy E_{MBR} (in joules) radiated in a bandwidth $\Delta\nu = 0.75$ GHz centered at $\nu_0 = 11.325$ GHz by an electron as a function of its kinetic energy. Points for 0.1, 1 and 10 MeV are averaged over a 1000 electron sample. The 100 MeV point corresponds to a 100 electron sample, the 1 GeV from a 10 electron sample, and the 10 GeV to just 1 electron. Red dots correspond to the Born approximation for $\mathrm{d}\sigma/\mathrm{d}\nu$ and blue dots correspond to the tabulated screened cross sections. A linear fit to the points with $T > 1$ MeV is also shown, as well as a fit to previous results by Conti *et al.* in [2].

using 4.7 radiation lengths of alumina (5 targets) and a beam of 1.5 ns, so we will use as input to the ZHS code the output of a GEANT4 simulation of electrons traversing the same amount of alumina. After interacting with the alumina, there will be secondary photons, electrons and positrons, with a distribution of energies and momenta. The three kinds of particles are included in our simulations.

We use 1000 primary electrons distributed in 5 microbunches set apart 0.35 ns, with a lateral deviation of $\sigma_r = 0.5$ cm and a temporal FWHM of $\sigma_t = 14$ ps. The charge in each microbunch is modulated according to the height of the peaks in the time voltage created by the beam as explained in section 5.1.4. We rescale the total charge of the bunch to the actual number of electrons (10^9) used in the AMY runs.

We use Eq. (5.26) to calculate the MBR yield for $\nu = 2.8$ GHz and $\Delta\nu = 0.5$ GHz, which are the experimental values. Also, we use as the time interval, $\Delta t = 1.5$ ns, *i.e.* the time duration of the bunch. The MBR field could last more time were the emission actually isotropic, because the pulse time would then be the difference between the arrival of the signal produced when the head of the beam enters the chamber and the arrival of the signal produced when the tail of the beam leaves the chamber. However this only means that the upper bound we calculate will be overestimated. The frequency dependence of the MBR is rather flat for the given bandwidth because the energy of the radiated photons increases with ν but this is compensated by the behaviour of the bremsstrahlung cross section $\mathrm{d}\sigma/\mathrm{d}\nu$ as ν^{-1}. For this reason it suffices to calculate $F(\nu = 2.8\ \mathrm{GHz})$ and multiply by the bandwidth $\Delta\nu$.

We have used four different distributions of secondary particles after 1000 primary electrons pass through the 5 alumina targets (4.7 radiation lengths), and we have used four different seeds in the ZHS simulation for each one as an attempt to quantify the statistical deviation of the flux. Results can be found in Fig. 5.17. The mean value of the MBR flux with its variance estimator when using the Born approximation for the cross section is:

$$\langle F \rangle_{\mathrm{Born}} \sim (2.04 \pm 1.36) \cdot 10^{-18}\ \mathrm{W\ m^{-2}\ Hz^{-1}}. \tag{5.28}$$

The tabulated screened cross section results in a lower number, as expected,

$$\langle F \rangle_{\mathrm{screened}} \sim (2.91 \pm 2.00) \cdot 10^{-19}\ \mathrm{W\ m^{-2}\ Hz^{-1}}. \tag{5.29}$$

The experimental bound to the flux obtained in AMY [4],

$$\boxed{\langle F \rangle_{\mathrm{AMY}} \leq 5 \cdot 10^{-17}\ \mathrm{W\ m^{-2}\ Hz^{-1}}}, \tag{5.30}$$

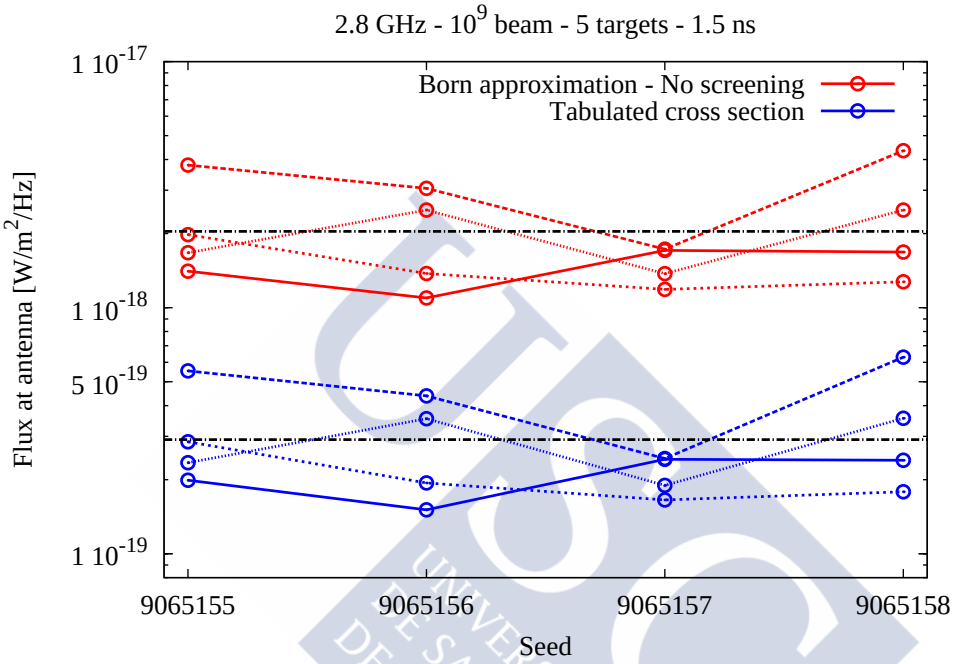

Figure 5.17: MBR flux prediction for the AMY experiment in $W/m^2/Hz$ as obtained with the ZHS simulation with the MBR model of [2] implemented. Several random seeds have been used (x axis) in the simulation, as well as several sets of 1000 primary electrons (rescaled with a factor of 10^6 to emulate a 10^9 electron beam) that cross 4.7 radiation lengths in alumina, indicated by the different line styles. The observation frequency is 2.8 GHz. Red (blue) lines represent the Born (tabulated, screened) approximation, while black lines represent the mean for each of the two cross sections. See text for details.

is higher than the flux predicted in our simulations by one to two orders of magnitude. This is not surprising since we have assumed that photons of GHz frequencies are emitted in a completely incoherent fashion (*i.e.* we have added the energies of the photons) while some degree of coherence might be expected in a pulsed beam. Also the experimental bound $\langle F \rangle_{\mathrm{AMY}}$ was obtained using the power in the first harmonic beam, where coherence is clearly present. Moreover, the model does not take into account the radiation from the sudden acceleration of the ionised electrons which should contribute to the radiation observed in AMY.

As a general conclusion, our bound to the MBR emission $\langle F \rangle_{\mathrm{screened}}$ using the screened cross section and assuming full incoherence is below the experimental bound $\langle F \rangle_{\mathrm{AMY}}$. $\langle F \rangle_{\mathrm{screened}}$ sets the sensitivity that needs to be achieved in AMY to be able to observe MBR if it behaves the same way as in the experiment by Conti *et al.* [2].

Experiments and simulations cannot account for the large flux of MBR obtained in the SLAC experiment [1]. If we scale the reference flux in [1] with the ratio of the total energy of the beams at DAΦNE and SLAC, the SLAC results would correspond to a flux of $\sim 6 \cdot 10^{-16}$ W m^{-2} Hz^{-1}, which is higher than the AMY experimental bound. It is not clear yet if MBR can be detected at AMY. New runs performed in AMY and new future experiments must shed light on this matter.

The flatness of the MBR emission with frequency implies that these estimations are also valid for the frequency regions that lie outside the harmonics, where the emission is clearly incoherent.

5.2 The MAYBE experiment

The Microwave Air Yield Beam Experiment (MAYBE) [20, 12] was carried out at the Argonne National Lab with the goal of measuring the MBR yield. They observed an unpolarised emission, expected for MBR, with a 3 MeV electron beam. From these results a bound to the MBR yield was obtained that lies below the measurements in [1], as it was the case with AMY [4] and the experiment in [2]. This reinforces the conclusion that the MBR yield measured at SLAC [1] was indeed overestimated.

5.2.1 Description of the experimental setup

The accelerator used is a 3 MeV Van de Graaff generator from the Argonne National Lab Chemistry Division. As pointed out in [20], the electrons are below the Cherenkov

threshold in air ($\sim$ 20 MeV), so this eliminates the main radiation background that comes from Cherenkov radiation. Any acceleration or deceleration of the electrons will produce radiation, in particular, the scattering with the molecules of the medium (MBR). The beam has a pulse length of 1-2 μs, with electrons uniformly distributed in time.

The setup is similar to the one used in AMY (Fig. 5.1), although without targets and a cubic anechoic chamber of 1 m^3. The attenuation of the signal reflected off the walls is $\geq$ 30 dB above 1 GHz. The chamber is instrumented with three antennas, a dual polarised commercial C-band LNBF (3.4-4.2 GHz), a circular polarised commercial Ku-band LNBF (12.2-12.7 GHz) and a 850 MHz to 26.5 GHz R&S log-periodic antenna. Each one of them is placed at the center of one of the sides of the cube, and they are capable of measuring in co-pol and cross-pol modes.

The antennas are coupled to three Miteq amplifiers and low loss coaxial cables that operate well up to 18 GHz. The oscilloscope is a Tektronix TDS6154C of 40 GS/s with 15 GHz analog bandwidth for the time domain. The spectrum is taken with the R&S FSV 30.

5.2.2 Experimental data

Similarly to what we have discussed for the AMY experiment in Section 5.1.2, when a beam of electrons enters the chamber of the MAYBE experiment, we could expect four[6] different contributions to the radiation:

1. Cherenkov radiation for particles with energy higher than the Cherenkov threshold in air, $\sim$ 20 MeV. We do not expect Cherenkov radiation in this case because the kinetic energy of the electrons is 3 MeV, lower than the Cherenkov threshold in air $\sim$ 20 MeV.

2. Radiation from the sudden appearance of the charge in the anechoic chamber as seen by the antennas inside.

3. Radiation from the sudden acceleration of the bound electrons in air when the atoms in the chamber are ionised by the electrons in the beam.

4. Radiation from the collision with the molecules of the medium, that is, MBR.

[6]One could also think about transition radiation. However, the chamber had a hole for the beam to enter, and it was found [12] that changing the material at the entrance did not significantly change the observed radiation.

In order to calculate the flux of the electric field at a certain frequency, first the voltage time trace $\langle V_{\rm rms}\rangle$ is collected from the oscilloscope and filtered to a certain frequency band. Then, the power received at the oscilloscope is calculated by substracting the mean of the power with signal and without signal,

$$\langle P_{\rm sgn}\rangle = \left(\frac{\langle V_{\rm rms}\rangle^2}{R_L}\right)_{\rm sgn+bkg} - \left(\frac{\langle V_{\rm rms}\rangle^2}{R_L}\right)_{\rm bkg}. \tag{5.31}$$

R_L is the resistance of the oscilloscope. It can be shown (see Appendix B) that the mean power received by the oscilloscope is related to the mean flux of the incoming radiation in the following way,

$$F_\nu = \frac{\langle P_{\rm sgn}\rangle}{\Delta\nu A_{\rm eff}}, \tag{5.32}$$

where F_ν is the mean flux (mean power per frequency and area), $\Delta\nu$ is the bandwidth and $A_{\rm eff}$ is the effective area of the antenna, related to the gain $G(\theta,\phi)$ through (see Appendix A)

$$A_{\rm eff}(\theta,\phi) = \frac{c^2}{\nu^2}\frac{G(\theta,\phi)}{4\pi}. \tag{5.33}$$

The resulting power spectrum $\langle P_{\rm sgn}\rangle(\nu)$ averaged over tens of thousands of runs shows a quite flat behaviour with frequency and no sign of polarisation (see Fig. 5.18), with a mean flux of $\sim 0.3\cdot 10^{-18}$ W m^{-2} Hz^{-1} for each polarisation. This is what is expected for the MBR, understood as a deceleration in the electric field of the molecules. In the experiment in [2] the angular pattern of the radiation resembles that of usual bremsstrahlung, but this could not be studied with the setup of the MAYBE experiment.

From the measured spectrum, an extrapolation to extended air showers (EAS) can be made, resulting in an estimated flux of a few 10^{-20} W m^{-2} Hz^{-1} for a $3\cdot 10^{17}$ eV shower, assuming linear scaling. This estimate is much smaller than the value of $4\cdot 10^{-16}$ W m^{-2} Hz^{-1} in the SLAC experiment [1], agreeing with the most recent experiments AMY [3] and Conti *et al.* [2].

Further studies are needed to confirm whether the unpolarised emission measured by MAYBE can be attributed to MBR or not.

5.2.3 Simulations using the MBR model

We could, in principle, use the ZHS code to give an estimation to the flux measured at MAYBE, since ZHS accounts for the fields arising from Cherenkov radiation (not present

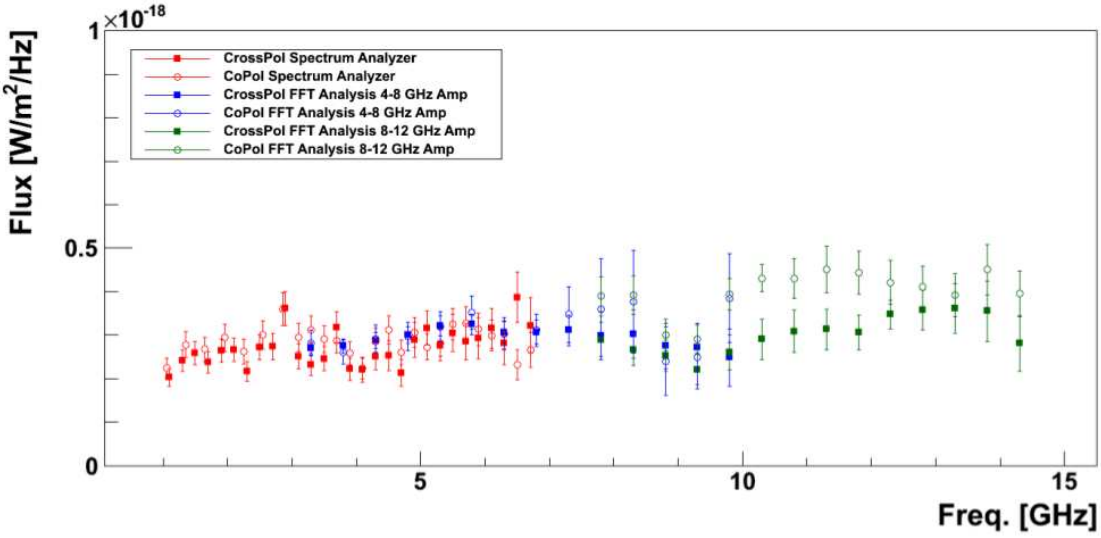

Figure 5.18: Mean flux (power per unit area and frequency) as a function of frequency, measured by the MAYBE experiment. Co-pol and cross-pol data are shown. Results are mostly compatible with a rather flat spectrum and with an unpolarised emission, although around 11 GHz the copolarised field seems to dominate. Taken from [12].

in MAYBE), sudden appearance of charge in the chamber, partly for the accelerations and decelerations caused by ionisation and hard bremsstrahlung (due to the continuous energy loss approximation for ionisation electrons emitted with energy below a few tens of keV) and, effectively but not explicitely, for MBR (due to the continuous energy loss treatment of bremsstrahlung photons of energy below a few tens of keV). However, at low energies below a few tens of keV, relevant for MAYBE, the tracking of the ZHS is not accurate enough for a precise electrodynamical calculation of the electric field. The particle deflections at these energies are of utmost importance to obtain the polarisation and magnitude of the electric field, and ZHS at low energies is not well suited for this task. This is because ZHS was never intended to be used for non-relativistic kinetic energies. Let us remember that it does not accurately take into account processes at keV energies, while the PENELOPE code used in [2] does.

For this reason, and since the model by Conti *et al.* reproduces the experimental data in [2] and gives a reasonable bound to the MBR flux in AMY, we calculate the MBR flux in MAYBE with the MBR model discussed in Section 5.1.6. The assumption of incoherence is true for MAYBE, since the beam is not modulated, lasts for 1 μs = 1 MHz^{-1} and in MAYBE measurements are performed at GHz frequencies.

We have performed a simulation in a similar fashion to those done for the AMY experiment, but this time with 3 MeV electrons following a uniform distribution in time for a time interval of 1 μs and distributed laterally using a Gaussian of standard deviation $\sigma_r = 0.25$ cm [21]. A total of 10^4 electrons are injected in constant density air and the MBR flux is computed. As already mentioned, the MAYBE chamber is a cube of 1 m^3 and the antenna is placed on the centre of one of the lateral faces. The radiated energy is calculated using only the tabulated screened cross section. The energy is rescaled to the typical beam in MAYBE of $4.15 \cdot 10^{12}$ electrons and then divided by the pulse time in order to get the flux. Finally, we divide the number obtained by two, since the cross section takes into account both polarisations and we are interested in comparing data measured with a definite polarisation. We have used Eq. (5.8) but including the charge rescaling, the 1/2 factor from the polarisation and the antenna gains in cross-pol mode,

$$\langle F \rangle_{\text{antenna}} \sim \frac{4.15 \cdot 10^{12}}{10^4} \frac{1}{2} h\nu \frac{\rho N_A}{A \Delta t} \sum_{i,\text{tracks}} \frac{l_i}{R_i^2} \frac{\mathrm{d}^2\sigma}{\mathrm{d}\nu \mathrm{d}\Omega}(E_i) \frac{G(\theta_i)}{G(\pi/2)}, \tag{5.34}$$

so that we account for the antenna angular response. The angle θ is defined in Fig. 5.19 and the gain $G(\theta)$ used is the one used by the MAYBE collaboration [21]. The observation frequency is fixed to 5 GHz, although the model predicts no significant flux difference in the MAYBE frequency range. The results of the simulations are shown in Fig. 5.20.

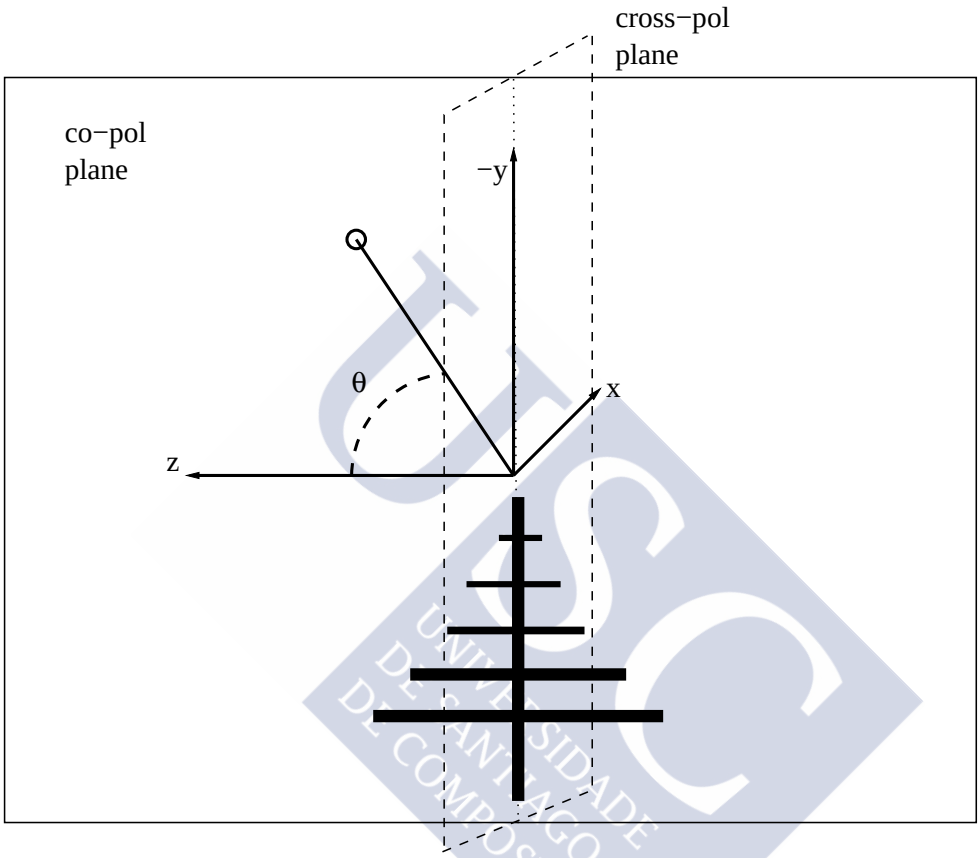

Figure 5.19: Sketch of a log-periodic antenna and definition of the antenna reference frame for MAYBE. The θ angle is the angle that a position vector forms with the z axis parallel to the direction of the dipoles. Co-pol and cross-pol planes are also shown. Note that the $-y$ axis is shown, and not the y axis.

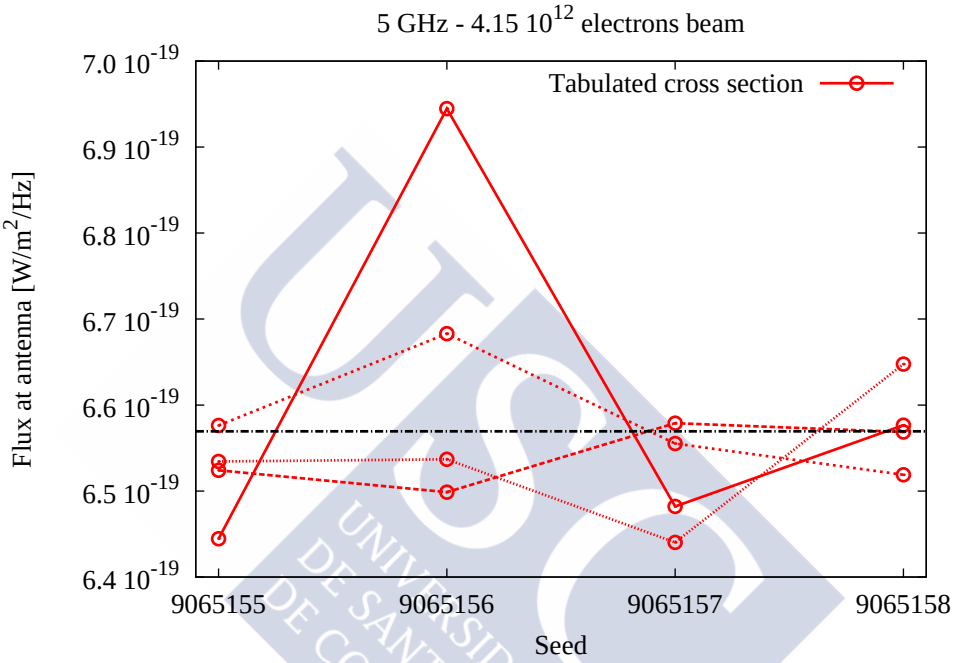

Figure 5.20: MBR flux prediction for the MAYBE experiment in $\mathrm{W/m^2/Hz}$. Several seeds for random number generation in the ZHS Monte Carlo have been used (x axis), as well as several 10^4 electron beams (rescaled with a factor of $4.15 \cdot 10^8$ to emulate a $4.15 \cdot 10^{12}$ electrons beam). The observation frequency is 5 GHz. The black line (dash-dotted) represents the mean flux. See text for details.

We compare the results of the MBR model with MAYBE data in Table 5.3. The uncertainty of the model is statistical only, not taking into account the uncertainties in the antenna pattern or those due to the approximations of the MBR model. The simulation is a factor of ~ 2 above the data. This is consistent with the fact that the ZHS code predicts more MBR emission than PENELOPE [2] at low energies (Fig. 5.16). The unknown uncertainties in the antenna pattern, as well as in the MBR model, do not allow us to conclude if the results are in agreement within uncertainties. In any case, the order of magnitude is reproduced by means of MBR emission only.

$F_\nu/10^{-18}$ W m^{-2} Hz^{-1}			
MBR simulations	MAYBE data		
5 GHz	1.5-1.75 GHz	5-5.25 GHz	8-8.25 GHz
0.657 ± 0.003	0.24 ± 0.02	0.31 ± 0.03	0.3 ± 0.06

Table 5.3: Mean value of the radiated flux as obtained with the MBR model and the tabulated screened cross section for the MAYBE experiment and data from Fig. 5.18. Cross-polarised fluxes are given. For the simulation, the uncertainty due to the beam is less than $\sim 1\%$, and the uncertainty of the antenna pattern is the one that dominates, although it is not known accurately.

5.3 Comparison of experiments and theoretical calculations

For the sake of completeness, we include a comparison of the measurements and theoretical calculations for the MBR flux. As a way to establish a fair comparison, we normalise the values of the flux to a reference $E_0 = 10^{18}$ eV shower and for an observer at a distance of $d_0 \sim 1$ km from the depth shower maximum. In order to do so, we assume the following:

- MBR is incoherent and its flux is proportional to the total energy of the shower.
- The flux (proportional to the electric field squared) is inversely proportional to the square of the distance to the shower maximum.

Under these hypotheses, we only have to rescale the flux to the reference energy E_0 and distance,

$$F_0 = F \frac{E_0}{E} \frac{d^2}{d_0^2}, \tag{5.35}$$

where F_0 is the flux for our reference shower, F is the measured or calculated flux, and E and d are the energy and distance used in the measurement or calculation, respectively.

The prediction using the simulations from the experiment in [2] must be treated in a different way in this comparison. From Fig. 5.16 we get that the total MBR energy emitted in the band from 10.95 GHz to 11.70 GHz is linear with the total energy of the shower,

$$E_{\mathrm{MBR}} = E \cdot 1.42 \cdot 10^{-23}\ \mathrm{J\ eV^{-1}}. \tag{5.36}$$

We also assume a pulse length of 10 ns, which is a short time for detection and therefore will enhance the estimated flux. In the interest of simplification, we will also assume that the emission is isotropic, as done in [13]. We must also take into account the solid angle subtended by the antenna and its area to obtain the flux,

$$F_0 \sim \frac{E_{\mathrm{MBR}}}{\Delta\nu\Delta t}\frac{\Delta\Omega_{\mathrm{ant}}}{4\pi}\frac{1}{A_{\mathrm{ant}}} \sim \frac{E_{\mathrm{MBR}}}{\Delta\nu\Delta t}\frac{1}{4\pi}\frac{1}{4\pi d_0^2}. \tag{5.37}$$

In Table 5.4, the fluxes scaled to the reference shower of energy E_0 and distance d_0 are listed. The extrapolations from the AMY and MAYBE experiments agree that the result at SLAC is indeed overestimated. The theoretical calculations of Al-Samarai *et al.* [13] and the estimation derived from the fit by Conti *et al* [2] agree surprisingly well, and also indicate that the expected MBR flux is lower than that measured at SLAC.

Experiment/calculation	E [eV]	d [m]	F [W m^{-2} Hz^{-1}]	F_0 [W m^{-2} Hz^{-1}]
SLAC [1]	10^{18}	~ 0.5	$4 \cdot 10^{-16}$	$2.98 \cdot 10^{-22}$
AMY [3]	$5.1 \cdot 10^{17}$	~ 1	$< 5 \cdot 10^{-17}$	$< 9.80 \cdot 10^{-23}$
MAYBE [12]	$2.49 \cdot 10^{19}$	~ 0.5	$3 \cdot 10^{-19}$	$3.01 \cdot 10^{-27}$
MIDAS [11] (95% CL)	$3.36 \cdot 10^{17}$	~ 0.5	$< 3.98 \cdot 10^{-15}$	$< 2.96 \cdot 10^{-21}$
Conti *et al.* [2] (theory)				$1.20 \cdot 10^{-23}$
Al-Samarai *et al.* [13] (theory)	$3.16 \cdot 10^{17}$	$\sim 10^4$	$4 \cdot 10^{-26}$	$1.26 \cdot 10^{-23}$

Table 5.4: MBR flux F_0 for a reference shower of $E_0 = 10^{18}$ eV at a distance of ~ 1 km from the shower maximum (rightmost column). The columns also show the shower energy E, distance d and flux F for each experiment (SLAC, AMY, MAYBE, MIDAS) or calculation (Conti *et al.*, Al-Samarai *et al.*).

5.4 Conclusions

We have reviewed the AMY experiment and confirmed that the ZHS algorithm can reproduce with high level of detail the background radiation of the experiment. After re-deriving

the MBR model in [2], we have applied it to the AMY setup in order to get an upper bound for an incoherent flux. The bound from the model is two or three orders of magnitude below the experimental bound. Although AMY uses a coherent beam and there is a strong presence of Cherenkov radiation, the MBR bound obtained by AMY is one order of magnitude below the SLAC result.

MAYBE solves the problem of the Cherenkov radiation by using an electrom beam with kinetic energy smaller than the Cherenkov threshold in air. They found an unpolarised emission ranging from 1 GHz to 15 GHz, and assuming it was due to MBR, calculated a bound. The bound to MBR in MAYBE is also several orders of magnitude below the SLAC result. We have also applied the MBR model, whose result is a factor of ~ 2 larger than the measured flux. This discrepancy could be due to an unaccurate tracking of the particles at low energies below a few tens of keV by the ZHS code. The ZHS code predicts more MBR flux at low energies than what was obtained in [2]. Besides, the uncertainty in the antenna gain is not known.

Conti *et al.*, with a 81 keV electron beam, detected an unpolarised radiation with an angular dependence compatible with bremsstrahlung. Despite the fact that the MC simulations are systematically below the data and there could be other processes at work, the experiment remains the most enlightening one about the nature of the microwave emission of showers. Their prediction of the MBR for air showers is also more pessimistic than the one in [1].

Although there could be more details, [2] points that bremsstrahlung of electrons in the field of the molecules is present in the microwave emission of a shower. The emission at the experiments AMY and MAYBE is not completely understood, however, there is an agreement that the MBR flux is much lower than what was initially proposed in [1], jeopardising the future of the technique of using MBR for the detection of air showers.

Bibliography

[1] P. Gorham *et al.* Observations of microwave continuum emission from air shower plasmas. *Physical Review D*, **78**(032007), 2008.

[2] E. Conti, G. Collazuol, and G. Sartori. Experimental study of the microwave emission from electrons in air. *Physical Review D*, **90**(071102(R)), 2014.

[3] J. Alvarez-Muniz *et al.* The Air Microwave Yield (AMY) experiment - a laboratory measurement of the microwave emission from extensive air showers. In *Proceedings of The European Physical Society Conference 2013*.

[4] V. Verzi. The AMY (Air Microwave Yield) experiment to measure the GHz emission from air shower plasma. In *Proceedings of Acoustic and Radio EeV Neutrino Detection Activities (ARENA) 2014*.

[5] G. Rodríguez. AMY Collaboration, private communication.

[6] SATIMO. Antenna measurement report, Ref. MR.333.4.12.SATI.A. Calibration of the Dual Ridge Horn antenna DRH20-120401A20 used at the AMY experiment.

[7] R. York. Antenna theory, ece 201c. http://my.ece.ucsb.edu/York/Bobsclass/201C/.

[8] D. García-Fernández, J. Alvarez-Muñiz, W. R. Carvalho Jr., A. Romero-Wolf, and E. Zas. Calculations of electric fields for radio detection of ultrahigh energy particles. *Physical Review D*, **87**(023003), 2013.

[9] A. Taboada Núñez. Descripción de procesos de emisión electromagnética en Astrofísica de Partículas por medio del algoritmo Zas-Halzen-Stanev. Master's thesis, Universidade de Santiago de Compostela, 2015.

[10] J. Alvarez-Muñiz, A. Romero-Wolf, and E. Zas. Cerenkov radio pulses from electromagnetic showers in the time domain. *Physical Review D*, **81**(123009), 2010.

[11] J. Alvarez-Muñiz *et al.* Search for microwave emission from ultrahigh energy cosmic rays. *Physical Review D*, **86**(051104(R)), 2012.

[12] C. Williams. *A search for microwave emission from cosmic ray showers*. PhD thesis, University of Chicago, Illinois, 2013.

[13] I. Al Samarai *et al.* An estimate of the spectral intensity expected from the molecular Bremsstrahlung radiation in extensive air showers. *Astroparticle Physics*, **67**:26, 2015.

[14] H. W. Koch and J. W. Motz. Bremsstrahlung cross section formulas and related data. *Reviews of Modern Physics*, **31**:920, 1959.

[15] H. K. Tseng *et al.* Electron bremsstrahlung angular distributions in the 1-500 kev energy range. *Physical Review A*, **19**:187, 1979.

[16] J. D. Jackson. *Classical Electrodynamics*. Wiley, New York, 3rd edition, 1998.

[17] R. H. Pratt *et al.* Bremsstrahlung energy spectra from electrons of kinetic energy 1 keV $\leq T_1 \leq$ 2000 keV incident on neutral atoms $2 < Z < 92$. *Atomic Data and Nuclear Data Tables*, **20**:175, 1977.

[18] S. M. Seltzer and M. J. Berger. Bremsstrahlung spectra from electron interactions with screened atomic nuclei and orbital electrons. *Nuclear Instruments and Methods in Physics*, **12**:95, 1985.

[19] E. Zas, F. Halzen, and T. Stanev. Electromagnetic pulses from high-energy showers: Implications for neutrino detection. *Physical Review D*, **45**:365, 1992.

[20] C. Williams. First results from the Microwave Air Yield Beam Experiment (MAYBE). In *Proceedings of Intertational Symposium on Future Directions in UHECR Physics (UHECR 2012)*.

[21] MAYBE Collaboration, private communication.

USC
UNIVERSIDADE
DE SANTIAGO
DE COMPOSTELA

Chapter 6

Radiation in UHECR experiments. The ANITA experiment

We are witnessing the revival of the interest in using the radio technique to detect extensive air showers induced by Ultra-High Energy Cosmic Rays (UHECR). Among the experiments dedicated to that goal we find CODALEMA [1], LOFAR [2], AERA [3], LOPES [4] and Tunka-Rex [5], whose instrumentation is far superior to the one available in the early days of radio detection [6], and have stimulated an impressive progress in the field. As a result, the use of the radio technique as a stand-alone method or as a complement to other techniques is being seriously considered [7].

The ANITA experiment at the South Pole discovered by chance 16 radio pulses from air showers extending up to the GHz range with its first balloon borne antenna system [8]. 14 of those 16 events were compatible with an electric field of UHECR shower origin reflected on ice, while the other 2 were compatible with an electric field coming directly from a UHECR shower. ANITA, operating within a frequency band between 200 and 1200 MHz, had been conceived for detecting radio emission from neutrino interactions.

In this chapter we review the ANITA experiment and discuss the results of simulations with the ZHAireS Monte Carlo codes for physical situations that are relevant to the ANITA experiment.

6.1 Description of the ANITA experiment

The Antarctic Impulse Transient Antenna detector (ANITA) is an antenna array carried by a balloon that is flying over Antarctica and optimised to detect impulsive radio frequency events that match the expected signature of known high-energy particle showers, such as neutrino-induced showers.

The ANITA I payload is an octogonally symmetric gondola made of aluminum that supports three cluster rings where the antennas are set. The two upper clusters have eight antennas each, while the lower cluster has sixteen. See Fig. 6.1.

Figure 6.1: ANITA I payload in flight-ready configuration. Taken from [8].

Each antenna is a horn type antenna custom designed for ANITA by Seavey Engineering Inc. The average FWHM of the antennas is about 45° of approximately 10 dBi average across the 200-1200 MHz band. The design of the antenna allows a good overlap between the response of adjacent antennas while mantaining a reasonable directivity. The azimuthally symmetric antenna array achieves a complete coverage of the horizon down to 40° of the nadir angle.

The RF front end of ANITA is composed of a band-pass filter followed by a combination of a low-noise-amplifier (LNA) and a power limiter, then followed by a second stage booster amplifier. Once the signals are amplified, they are transmitted to the trigger system. If the trigger is passed, the data are digitised and stored.

This payload is mounted on a long-duration balloon at an altitude of 35-37 km. The objective of using a balloon is both to cover a vast area (~ 1.5 Mkm^2) and to reduce the anthropogenic noise from the base camps on Antarctica.

Further details on ANITA I can be found in [9].

6.2 Experimental data: reflected events

While trying to detect upward-going neutrino-induced cascades from neutrino interactions in the Antarctic ice, that have a characteristic vertical (with respect to the ground) polarisation, ANITA I found 16 events with horizontal polarisation, which is typical of the geomagnetic emission from air showers when the magnetic field is almost vertical to ground as happens in the South Pole[1]. The polarisations of the electric fields of these events were found to be perpendicular to the local geomagnetic field [8]. Let us place ourselves in the plane formed by the local geomagnetic field and the polarisation vector (See Fig. 6.2), and define as 0° the angle of the vector in that plane that is horizontal (has no z component, being z the direction of the gravitational field). Let us define Θ_B, the angle of the local geomagnetic field, and Φ, the angle of the (electric field) polarisation vector. Since the geomagnetic component of the electric field of an air shower is proportional to $\mathbf{v} \times \mathbf{B}$, with $\mathbf{v}$ the vector parallel to the shower axis and $\mathbf{B}$ the geomagnetic field, the polarisation must be perpendicular to the geomagnetic field. If we define the positive sense of the angles properly, then,

$$\Phi = \Theta_B - \frac{\pi}{2}. \tag{6.1}$$

[1]The inclination of the geomagnetic field at the South Pole is $I \approx -76°$.

This is supported by data collected by ANITA I, shown in Fig. 6.3, where there is a strong correlation between both angles. This is a strong indication of the geomagnetic origin of the 16 radio pulses detected with ANITA I.

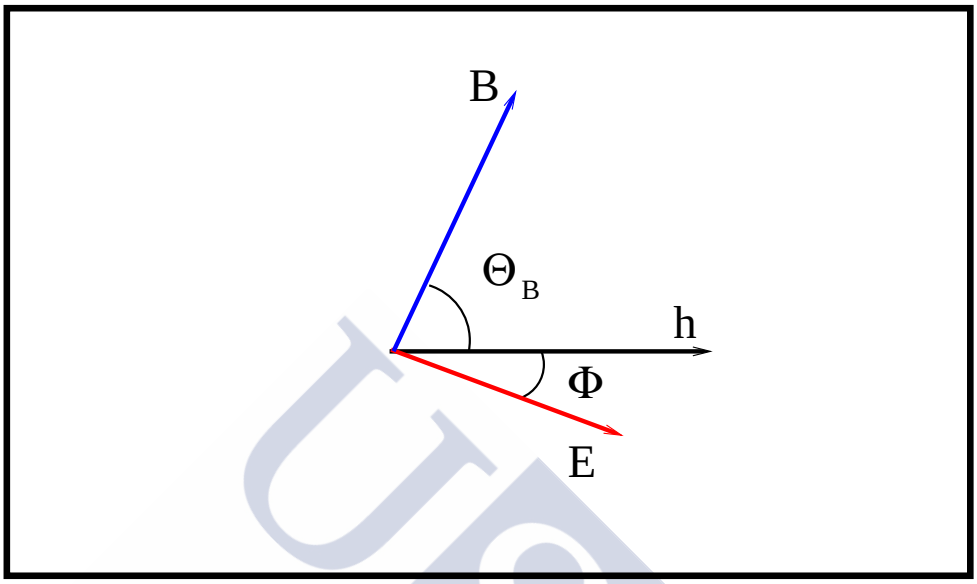

Figure 6.2: Sketch of the plane formed by the electric field polarisation vector **E** and the geomagnetic field **B**. In that plane lies a horizontal vector **h**. The angles Θ_B and Φ are measured with respect to **h**.

With two exceptions, the events pointed to locations on the surface of the ice. The two exceptional cases had an origin above Earth's horizon (*direct* events). Satellite noise was discarded since coherence at the ns scale cannot be mantained, due to dispersion, after the wave crosses the ionospheric plasma. Besides, the 14 below-horizon events are phase inverted with respect to the 2 above-horizon events (see Fig. 6.4). Since the Fresnel coefficient for the horizontal polarisation predicts a phase inversion upon reflection (see section 6.3.2), these events must be induced by the field of air showers that gets reflected on the ice surface (*reflected* events).

The spectrum of the events can be described with an exponential function $e^{-\nu/\nu_0}$, with the falloff ν_0 being (197 ± 15) MHz^{-1} for direct events and (180 ± 13) MHz^{-1} for reflected events (see Fig. 6.5).

The mean energy of the reflected was estimated to be $2.9 \pm 0.4(\text{individual}) \pm 0.8(\text{scale})$ EeV [10]. A sky map with a 2° uncertainty is also given in [8], with no correlation to expected source.

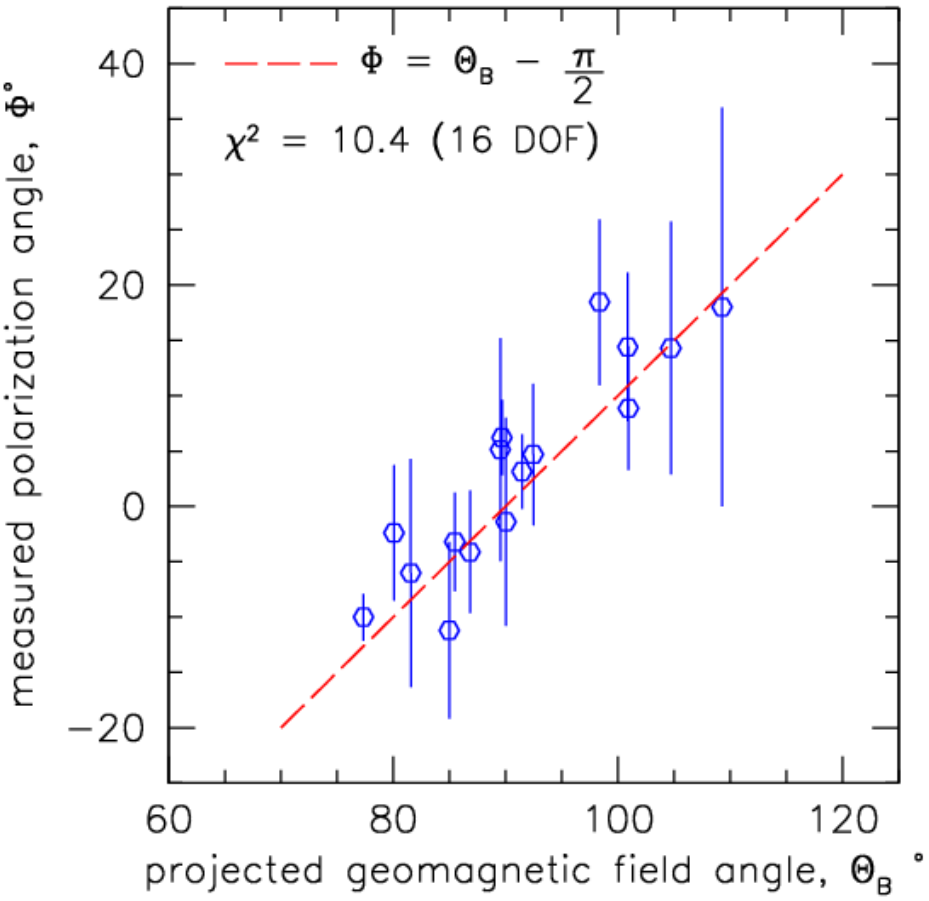

Figure 6.3: Angle of the polarisation of the electric field Φ as a function of the geomagnetic local angle Θ_B for the 16 ANITA events attributed to UHECR-induced showers. The angles are measured in the plane formed by the polarisation vector and the geomagnetic field vector, taking 0° as the angle of the horizontal vector (See Fig. 6.2). Taken from [8].

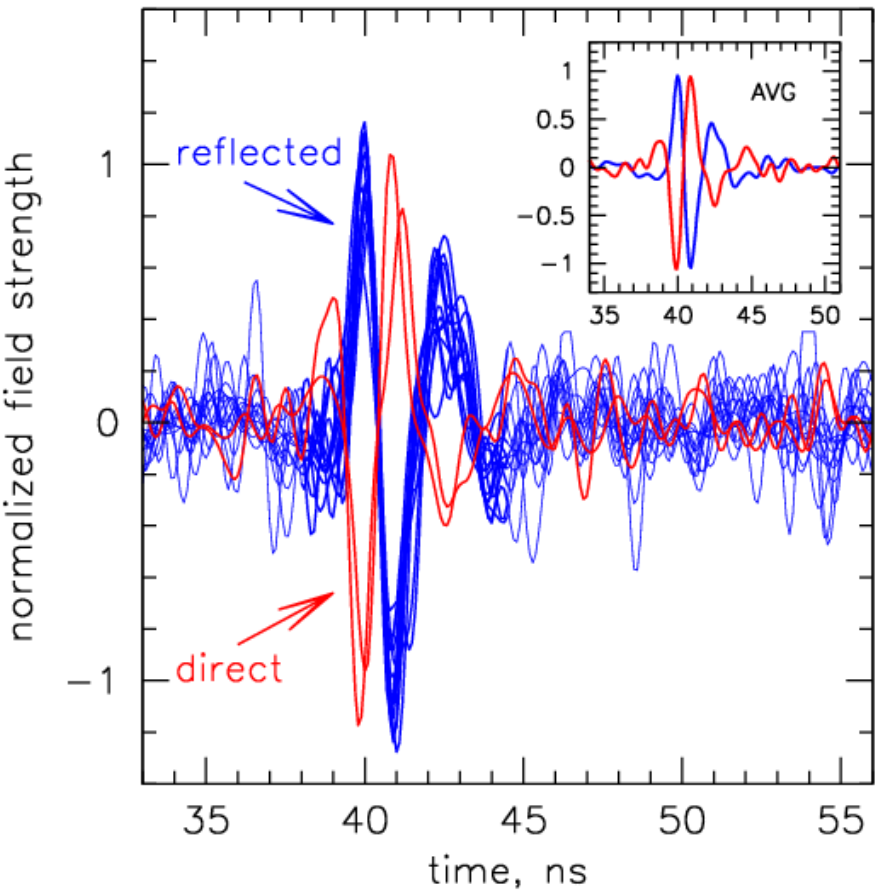

Figure 6.4: Overlay of the 16 UHECR events pulse shapes as a function of time for the horizontal polarisation, showing the two direct events (red) and fourteen reflected events (blue). Note the inversion upon reflection. In the inset, the pulse shape averaged over the 14 reflected (blue) and 2 direct (red) events respectively is also shown. Taken from [8].

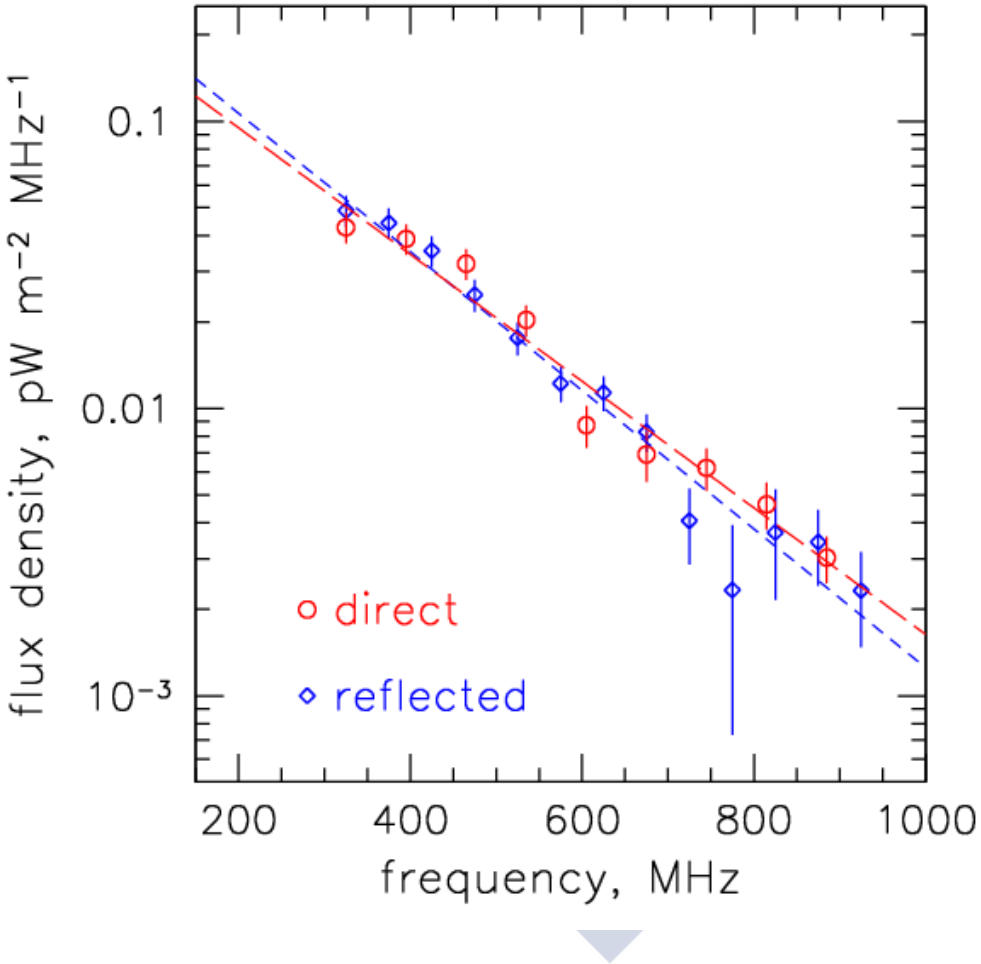

Figure 6.5: Flux density (see section 6.5.2 for definition) as a function of frequency for the averaged direct and reflected events, along with exponential fits. Taken from [8].

In what follows, we will use ZHAireS to simulate reflected events similar to the ones detected by ANITA I.

6.3 The ZHAireS-Reflex Monte Carlo

The reflection of the UHECR-induced shower radio pulses in the ice implies a reduction of the emission due to the Fresnel coefficients. Besides, upon reflection, the relative time delays with respect to detection at ground level are altered, since the pulses propagate upwards after reflection towards the top of the atmosphere along a decreasing refractive index profile. These effects have to be taken into consideration to interpret the events detected by ANITA I, and to evaluate the acceptance of experiments that rely on observing radiation induced by showers from mountain tops [11], balloon payloads [12], such as the ANITA III flight and EVA [13] or from satellites as proposed in SWORD [14].

In this chapter we simulate and describe the properties of radio pulses emitted from extensive air showers after reflection off a surface. Most of the calculations have been performed assuming a high altitude balloon flight over Antarctica, but the methods developed can be applied to to other reflective surfaces and different detector altitudes. We modified the ZHAireS code [15] to calculate the radio emission from air showers after reflection on a flat surface. The result is the so-called ZHAireS-Reflex Monte Carlo described in [16]. In the following, we first describe the geometry and explain the modifications made to adapt the program to calculate the reflected radiation. Then, we validate the straight ray-tracing embedded in ZHAireS. For this purpose we use the simplified model for the emission discussed in Chapter 4 (see also [17, 18]). After this we generate a set of simulations to investigate the signal properties as a function of the off-axis angle (see below), frequency, zenith angle, and energy of the primary particle, stressing the importance of properly accounting for the Fresnel reflection coefficients and the correct propagation of the pulses towards the top of the atmosphere. This discussion can also be found in [16].

6.3.1 Geometry for reflected events

The appealing aspect of observing radiation from air showers after reflection is that a large atmospheric volume can be monitored with a single detector. Therefore, the most interesting geometry is that of air showers that impact Earth's surface at large zenith angles. The basic geometry of the problem is sketched in Fig. 6.6. We define a rectangular coordinate system with the z-axis pointing upwards in the vertical direction and the x-y

plane tangent to the Earth's surface. The reflective surface will be approximated by this plane. The origin of the coordinate system is the point at which the shower axis intercepts the Earth's surface which is assumed to be at a ground altitude z_g above sea level. The zenith angle of the shower, θ, is defined with respect to the z-axis. We define the *off-axis* angle ψ in Fig. 6.7, to describe the angular deviation of the emitted radiation with respect to the shower axis[2].

A generic detector is positioned at a point with vertical altitude h_d. In Fig. 6.6 the detector is displayed in a special position such that it views the reflected radiation which was emitted precisely along the direction of shower axis with $\psi = 0°$. The altitude at which shower maximum ($X_{\rm max}$) is reached, $h_{X_{\rm max}}$, is also of relevance. Besides determining the angle at which the emission is largest [17], it also sets the scale of distances the pulse has to travel to reach the detector, $d_{X_{\rm max}} + d_d$, where $d_{X_{\rm max}}$ and d_d respectively denote the distances from the origin of the coordinate system to shower maximum and to the detector (See Fig. 6.6).

We illustrate the typical scales of the geometry by showing in Fig. 6.8 some parameters for a high altitude balloon over Antarctica. We take a detector at a typical altitude of $h_d = 35$ km, a ground altitude of the ice cap of $z_g = 2$ km and the Earth's radius $R_E = 6357$ km. The distance d_d becomes simply a function of the shower angle θ, which is illustrated in the top panel of Fig. 6.8. To estimate the distance to shower maximum, $d_{X_{\rm max}}$, we use the average slant depth of shower maximum $\langle X_{\rm max} \rangle$ as observed by the Pierre Auger Observatory [19, 20] together with the atmospheric density profile used in the air shower simulation package AIRES [21]. Clearly the average position of $X_{\rm max}$ depends on shower energy, but the effect is small according to the measurements at the Pierre Auger Observatory which indicate little change in $X_{\rm max}$ in the energy range from $10^{17.8}$ to $10^{19.6}$ eV [19, 20]. The results for different primary energies are shown as a function of θ in the middle panel of Fig. 6.8. It should be noted that the measured RMS fluctuations of $X_{\rm max}$ are between 20 and 60 g cm^{-2} [19, 20] corresponding to variations of $d_{X_{\rm max}}$ below 11% (3%) for a zenith angle of 60° (85°). The variation relative to the total distance travelled by the pulse $d_{X_{\rm max}} + d_d$ reduces to 1.5% (1.0%).

A relevant parameter is the Cherenkov angle $\psi_C \approx \cos^{-1}(1/n)$, at the location of $X_{\rm max}$ that is directly obtained using the refractive index n at the corresponding altitude, $h_{X_{\rm max}}$. In the following the refractive index is approximated by a simple exponential function of altitude h given by Eq. (4.7). The Cherenkov angle at $X_{\rm max}$ is shown in Fig. 6.8 (bottom) for this particular parameterization of the refractive index.

[2] ψ as depicted in Fig. 6.7 is also used to refer to the location of the observer.

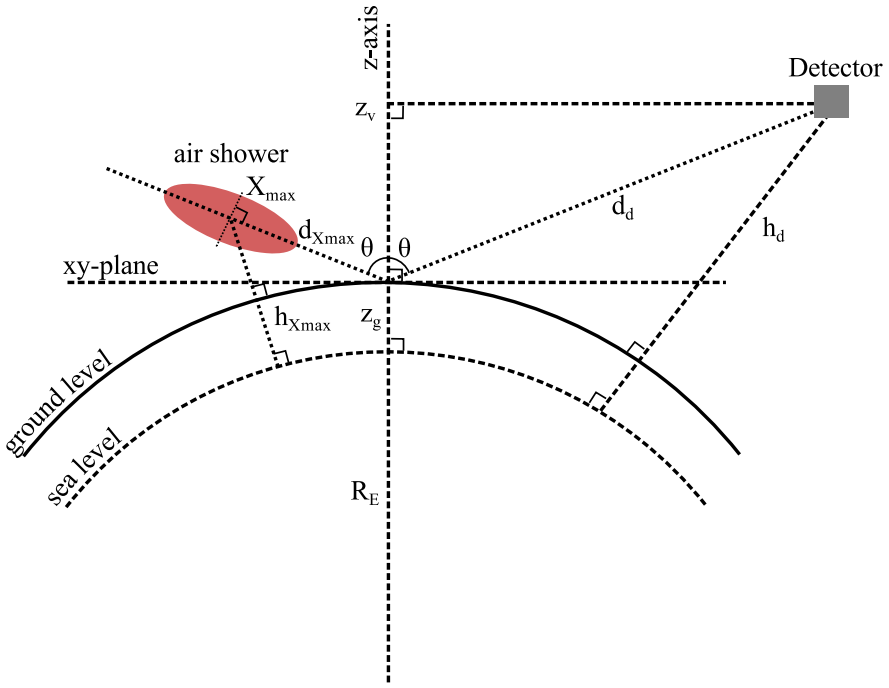

Figure 6.6: Geometry for reflected signals from air showers (see text for details). Taken from [16].

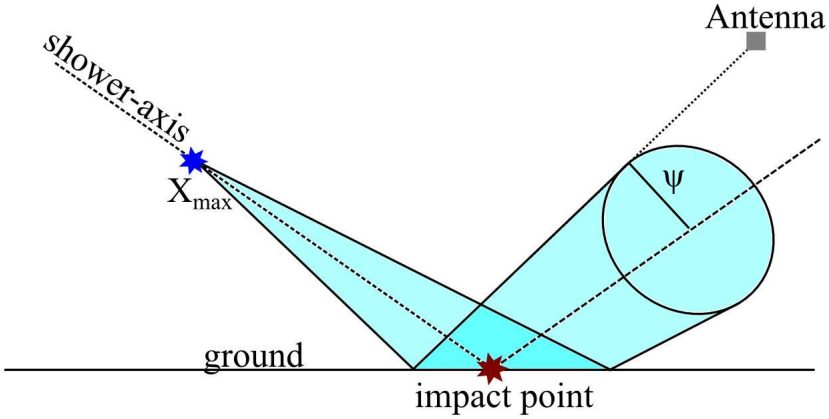

Figure 6.7: To describe a location of an observer (antenna) we use the off-axis angle ψ, defined as that between the shower axis and the line joining the location of $X_{\max}$ and the antenna position. Taken from [16].

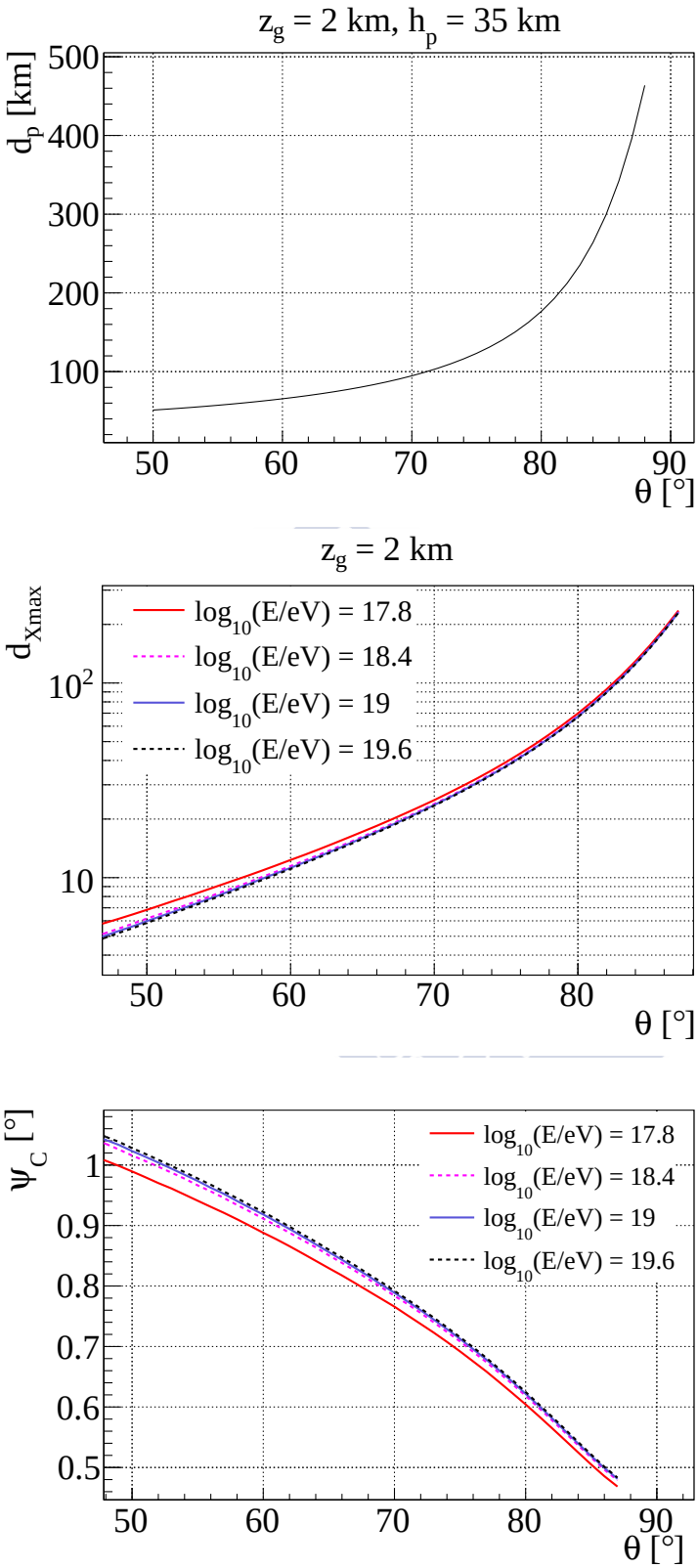

Figure 6.8: Top panel: distance from the reflection point to the detector (d_d in Fig. 6.6). Middle panel: distance to shower maximum ($d_{X_{\max}}$ in Fig. 6.6). Bottom panel: Cherenkov angle at $X_{\max}$ as a function of shower zenith angle. For the location of $X_{\max}$ we used the average value of $\langle X_{\max} \rangle$ as a function of energy measured Pierre Auger Collaboration [19, 20]. Taken from [16].

6.3.2 Introducing reflection in ZHAireS. Fresnel coefficients

The ZHAireS MC code [15] has already been introduced in Chapter 3, however it is worth pointing now that, in order to calculate travel times in ZHAireS we perform a numerical calculation accounting for the variation of the index of refraction with altitude assuming that the emission travels in straight lines to the observer. The curvature of the Earth's atmosphere is fully accounted for in AIRES.

We have modified the ZHAireS code to deal with the reflection of air shower radio emission on a surface [16]. For each rectilinear electron or positron track element we first find the point on the reflection surface and the angle of emission of radiation with respect to the track so that the emitted ray propagates first to the reflection point and then upwards towards the observer at a fixed position. Approximating the reflection surface to a plane makes it trivial to obtain this reflection point for a ray coming from any point in the atmosphere. Once this is known, the time delay due to the refractive index is easily calculated integrating the travel time over the total path of the ray before and after the reflection. We assume that the emission travels in a straight line to the observer. We have explored the validity of this approximation (see next subsection).

We approximate the reflection surface to the x-y plane in Fig. 6.6, assumed to be perfectly flat. The bulk of the emission has been shown to be concentrated in a cone that makes a small off-axis angle ψ to the shower direction [17] as shown in Fig. 6.7. This angle is very close to the Cherenkov angle (0.5°-1°) at an altitude at which the shower maximum occurs [17]. As a consequence the illuminated region on the reflective surface is relatively small, of order 0.5 km $\times$ 1 km (1.5 km $\times$ 10 km) for a $\theta = 60°$ (80°) shower. As a result it is reasonable to ignore the differences in the orientation angle and altitude of the reflecting surface at the locations of the different reflection points across the illuminated area. These differences are below 0.1° and a few meters respectively even for showers of $\theta = 80°$. There are other important aspects to the flat mirror approximation. When rays are reflected on a convex and rough surface they will diverge after reflection, and therefore the power received at a given surface element will be typically less than when a flat reflector is assumed. These effects have been studied in [14, 22], and have little impact at moderate zenith angles, however they can become significant for high zenith angles ($\theta > 80°$). Results of the simulations with the reflective surface assumed flat can be corrected *a posteriori* following the procedures outlined in [14, 22]. Such calculation is however very detector specific. Despite this, we expect the simulation method presented in this work to be very suitable for the purposes of interpreting ANITA data.

At each reflection point the Fresnel coefficients are applied to the time-domain electric

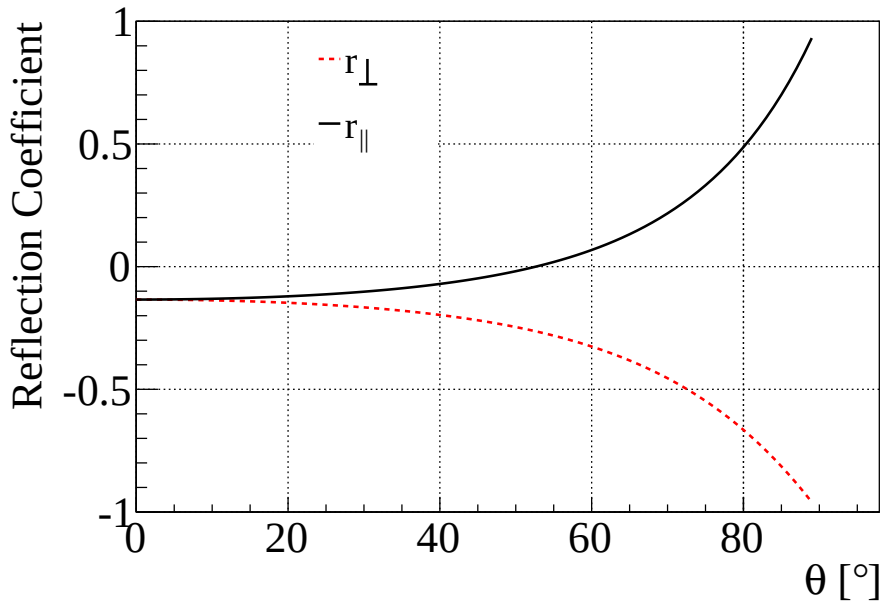

Figure 6.9: The Fresnel coefficients for an air-ice interface with refractive indices 1.0003 and 1.31 respectively, as a function of the zenith angle θ of the incident ray.

field to calculate the attenuation of the component with polarisation parallel, $r_{\parallel}$, and perpendicular, $r_{\perp}$, to the reflection plane, defined by the normal to the reflecting surface and the direction of the radiation:

$$r_{\perp} = \frac{n_1 \cos\theta - n_2\sqrt{1-\left(\frac{n_1}{n_2}\sin\theta\right)^2}}{n_1 \cos\theta + n_2\sqrt{1-\left(\frac{n_1}{n_2}\sin\theta\right)^2}}, \tag{6.2}$$

$$r_{\parallel} = \frac{n_1\sqrt{1-\left(\frac{n_1}{n_2}\sin\theta\right)^2} - n_2\cos\theta}{n_1\sqrt{1-\left(\frac{n_1}{n_2}\sin\theta\right)^2} + n_2\cos\theta}, \tag{6.3}$$

where θ is the incident angle of the ray (not the shower angle), n_1 is the refractive index of the medium where the ray propagates (air, in our case), and n_2 is the refractive index of the medium where the ray reflects off. We consider both media to be lossless and non-magnetic dielectrics.

The Fresnel coefficients for an air-ice interface are shown in Fig. 6.9 as a function of the zenith angle θ of the incident ray. A large fraction of the components of the field is

not reflected below $\theta \sim 60°$, and in fact at the Brewster angle at $\theta \sim 53°$ the parallel component is not reflected at all. The coefficients change rapidly above $\theta \sim 60°$. Clearly they have a drastic impact on the overall amplitude, the polarisation and the zenith angle dependence of the radio signal as we will show in section 6.5.2.

6.4 Straight vs curved rays

The variation with altitude of the index of refraction of the atmosphere is known to bend the trajectories followed by radio waves. It has been shown that the effects are negligible for most shower geometries and observers on ground [23], for which the propagation along straight paths is a good approximation. In the case of showers at large zenith angles and especially when accounting for reflection, the involved distances from emission to the detector become large (see Figs. 6.6 and 6.8) and the curvature of the rays can be expected to be larger.

To evaluate if the approximation of straight propagation still holds in the typical geometries involved in reflection, we have developed a simple ray tracing code presented in Chapter 4. We divide the atmosphere in many spherical layers with constant distance between them. The layers are taken sufficiently narrow so that the ray can be approximated as travelling in a straight line along a constant refractive index n in each layer given the exponential model of Eq. (4.5). The ray is refracted in each interface between two adjacent layers, taking into account the different refractive index in each layer. The total travel time of the ray is calculated as the sum of the times it takes to cross each layer. When the ray reflects on the ground, it is also propagated upwards through a decreasing refractive index profile until it reaches the detector. The arrival time assuming straight line propagation to ground and then to the same detector position is also calculated. The reflection surface is assumed to be at sea level for these calculations. Since the gradient of an exponential atmosphere is largest at sea level, it can be expected that curvature effects for reflection from surfaces at higher altitudes will have less impact than estimated here.

In Fig. 6.10 (top panel) we show the relative arrival times of radio signals emitted from different positions along the shower axis of a $\theta = 70°$ shower. They have been calculated with the straight and curved ray approximations for two particular observer positions such that the radiation arriving from shower maximum makes an off-axis angle $\psi \sim 0.77°$. One observer is located on the ground and receives the rays directly, while the other one is placed at an altitude $h_d \sim 33$ km and receives the rays after they have been reflected. The difference in the arrival times between curved and straight ray propagation is hardly

noticeable in the scale of Fig. 6.10. It is in fact below $\sim$ 50 ps on the ground, which corresponds to a frequency of $\sim$ 5 GHz when using a quarter wavelength criterion for coherence. As a result we expect the straight ray approximation to be valid below this frequency. The difference for the high altitude observer is even smaller.

Similarly in Fig. 6.10 (bottom panel) we show the arrival times of the pulses for a $\theta = 85^\circ$ shower and observation at an off-axis angle $\psi = 0.4^\circ$. Although in this case the difference between curved and straight ray propagation is sizable, it is an almost constant offset of $\sim$ 0.3 ns along shower development for the observer on the ground and $\sim$ 0.9 ns for the observer at high altitude $h_d \sim 50$ km. This global offset induces unobservable phase shifts in the field at the detector. When accounting for these offsets, the relative differences between the straight and curved propagations are $\sim$ 200 ps for the observer at ground level corresponding to a frequency of $\sim$ 1.25 GHz using a quarter wavelength criterion, while for the observer at $h_d \sim 50$ km of altitude the differences are below $\sim$ 20 ps ($\sim$ 12 GHz frequency).

In the top and bottom panels of Fig. 6.10 the relative arrival times at ground and at the high altitude observer are approximately flat within a large region ($\sim$ 10 km) around shower maximum. As a result the emission from this region is coherent up to GHz frequencies. Another interesting feature is the inversion of the arrival times at the high altitude observer position. The radio signal emitted in the Cherenkov angle (in this particular case from the region around shower maximum) arrives last at the high altitude location, contrary to what happens in an homogeneous medium. The time inversion is also seen for the observer on the ground for the 85° shower in Fig. 6.10 (bottom). The effect does not seem to have relevant implications for detection.

We can now use the simplified one-dimensional model (chapter 4) to test the effect of the straight ray approximation on the off-axis angular distribution of the signal. The arrival times t_a at the detector are now calculated using the integrated travel time along both straight and curved paths with the ray tracing algorithm and the discretised integral of Eq. (4.6).

The results using the straight and curved ray calculations are compared in Fig. 6.11 where we plot the modulus of the electric field as a function of the offset angle of the antenna ψ for showers of $\theta = 70^\circ$ (top) and $\theta = 85^\circ$ (bottom). As anticipated from Fig. 6.11, the difference in the angular distribution of the electric field between the straight and curved ray propagation is negligible for the $\theta = 70^\circ$ shower at all the frequencies being used in existing or planned radio experiments exploiting radio emission from UHECR-induced showers after reflection. It can be appreciated that even for $\theta = 85^\circ$, the difference is still

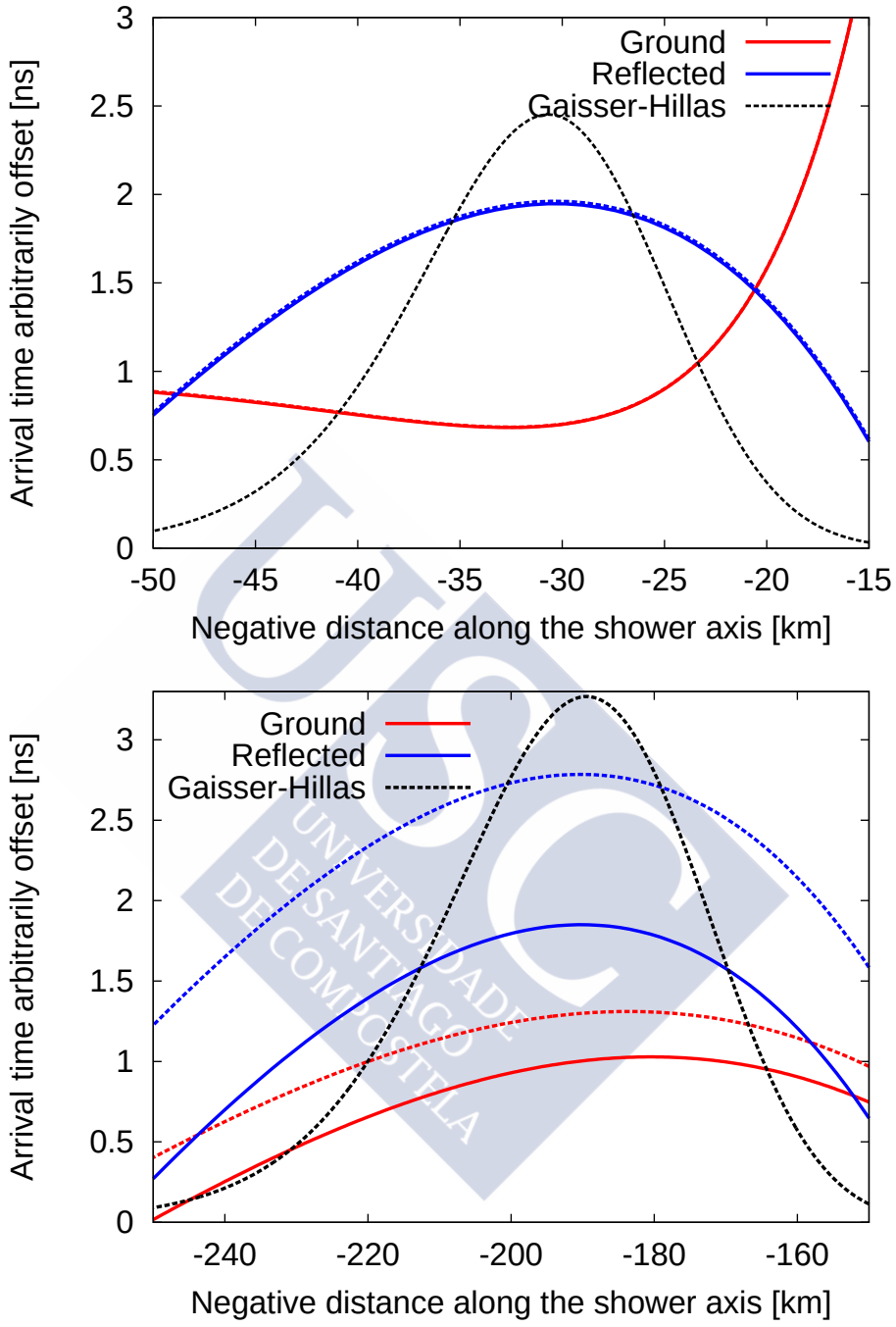

Figure 6.10: Top: Relative arrival times of rays emitted along the axis of a $\theta = 70°$ shower at two particular antenna locations: one located on the ground (red lines) and another after reflection towards a high altitude balloon (blue lines), both at an off-axis angle close to the Cherenkov angle $\psi \sim 0.77°$. The straight ray approximation (dashed lines) and the curved ray propagation (solid lines) are shown (see text for details). A 10^{19} eV, $\theta = 70°$ Gaisser-Hillas shower profile is superimposed (black line). Bottom: the same as in the top panel, but for a $\theta = 85°$ shower viewed at an off-axis angle $\psi \sim 0.40°$.

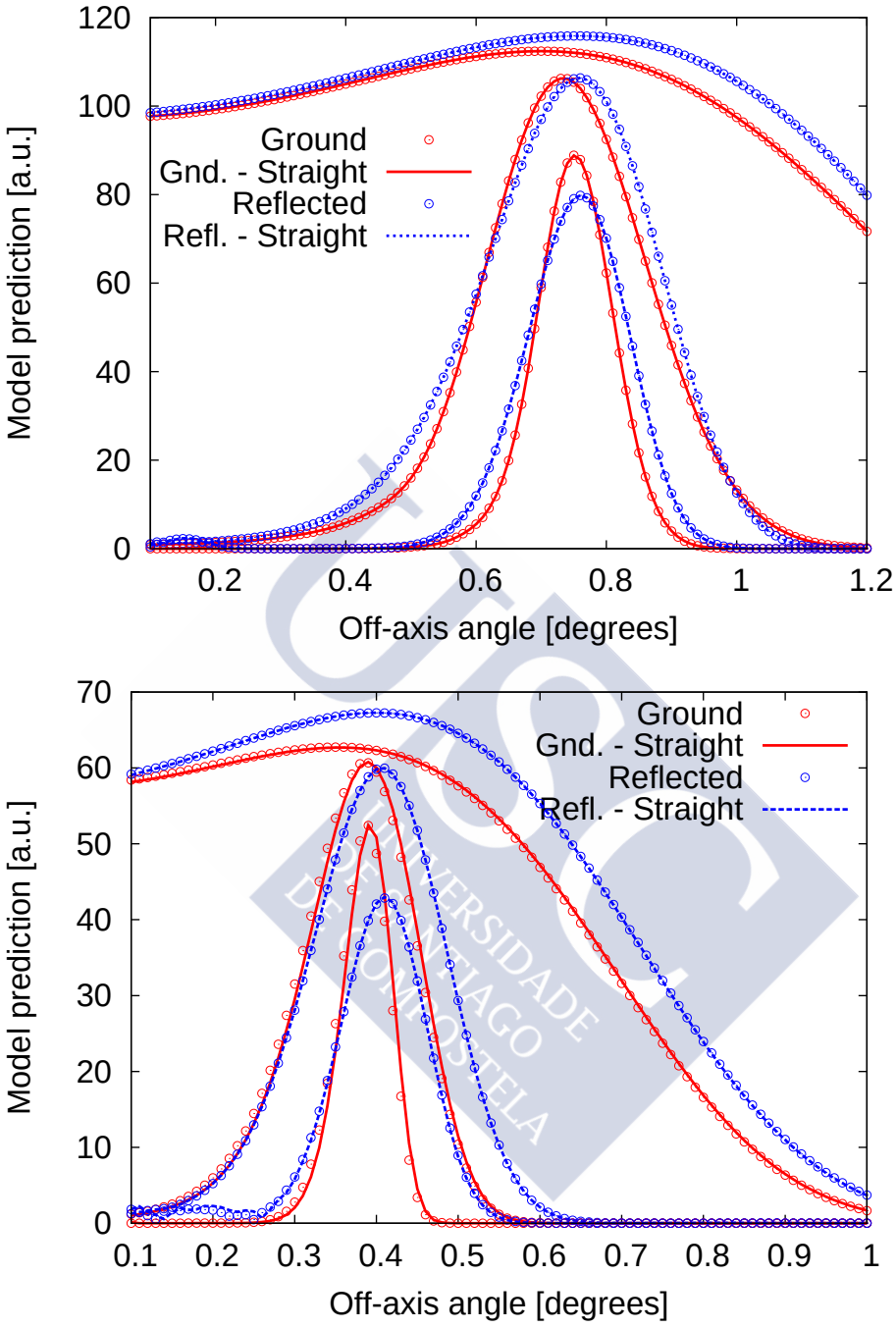

Figure 6.11: Top: electric field modulus as obtained with the model in Eq. (4.5), as a function of the off-axis angle ψ for three frequencies. The observers are located at different ψ angles on the ground (red solid lines) and at an overall distance $\sim$ 130 km to $X_{\max}$ after reflection (blue dashed lines). The shower has $\theta = 70°$ and $X_{\max}$ at an altitude above ground $h_{X\max} \sim 10.4$ km. The results of curved (points) and straight (lines) rays calculations are shown. From top to bottom, the observation frequencies are 50, 300 and 900 MHz. Bottom: the same as in the top panel with the observers located on the ground and at an overall path distance of $\sim$ 648.5 km. The shower has $\theta = 85°$ and $h_{X\max} \sim 16.5$ km. In both panels the fields on the ground are rescaled with the corresponding ratio of the distance to the ground and the total distance to the detector for visibility.

negligible up to a frequency of 900 MHz. This justifies the straight ray approximation for the calculation of the angular distribution of the field, even at high zenith angles and up to GHz frequencies.

6.5 Results of simulations with ZHAireS-Reflex

6.5.1 Simulation set and considerations

We place antennas at a fixed altitude $h_d = 36$ km above sea level (see Fig. 6.6), and choose the reflecting surface to be at $z_g = 2$ km above sea level. We adopt a refractive index for ice of $n_2 = 1.31$ [24] consistent with ANITA measurements of the reflected image of the Sun [25] on the Antarctic firn. The geomagnetic field is chosen to have a typical value of 55 μT and an inclination of $-70°$. We generated proton showers with zenith angles $\theta = \{57°, 64°, 71°, 78°, 85°\}$ and azimuth angles such that they always arrive from the geomagnetic west. For each zenith angle, we generate air showers with energies $E = \{10^{17.8}, 10^{18.4}, 10^{19}, 10^{19.6}\}$ eV [16]. We select simulations that have a shower maximum similar to the average $\langle X_{\rm max}\rangle_{\rm Auger}$ observed at the Pierre Auger Observatory. To do so, we pre-simulate seven air showers per configuration with different random seeds and we select the air shower closest to $\langle X_{\rm max}\rangle_{\rm Auger}$. This results in an average deviation of $|X_{\rm max} - \langle X_{\rm max}\rangle_{\rm Auger}| \approx 18$ g cm^{-2}, which is within the root mean square of the energy-dependent $X_{\rm max}$ distributions that have been observed. The shower simulation is run with AIRES using QGSJETTII.03 hadronic model interactions with a thinning level of 10^{-5} [21].

6.5.2 Results

To illustrate some of the typical features of the radio signal, we display in Fig. 6.12 the flux density Φ as a function of frequency and off-axis angle ψ for an air shower with zenith angle $\theta = 71°$ and an energy $E = 10^{17.8}$ eV. The flux density is defined as the power spectrum at a fixed frequency f averaged over a period of $T = 10$ ns, and is given in units of pW m^{-2} MHz^{-1} throughout this chapter.

$$\Phi \equiv \frac{c\epsilon_0}{T}|\mathbf{E}(f)|^2. \tag{6.4}$$

In the top left panel of Fig. 6.12 we show the two-dimensional distribution of Φ as a function of ψ and f which displays coherent properties and is clearly beamed around the Cherenkov angle at $\sim 0.77°$. This can be better appreciated in the bottom left panel where

we show the distributions in the off-axis angle ψ for different frequency components of the pulse. As the frequency increases the radiation adds coherently only within a smaller angle of the Cherenkov cone [17]. In the right panels in Fig. 6.12 we show the spectral shape of the flux density for a variety of observation off-axis angles. At very low frequencies ($f < 10$ MHz) the flux density increases until it reaches a maximum in the range $f \sim$ 10-150 MHz and then decreases with an exponential fall-off to first order. A very important feature is illustrated in the right panels, the steepness of the fall-off has a clear dependence on the off-axis angle ψ of the detector. This dependence is key to the energy determination of UHECRs with ANITA as will be explained later.

6.5.3 Implications of the reflection

Other efforts to simulate reflected radio signals from air showers have relied on pulses simulated at ground which were extrapolated using the attenuation of the signal with increased distance ($|\mathbf{E}| \propto 1/r$) after accounting for the loss of signal induced by the Fresnel coefficients [26]. In a homogeneous medium this "specular approach" can be expected to be a good approximation provided the pulse can be considered to be in the Fraunhofer limit. As a result it can be expected to work better for highly inclined showers, since the distance between the observer and air shower increases as the zenith angle rises.

In this work all track contributions to the pulse are reflected at the interface to account for attenuation with distance, for the Fresnel reflection coefficients that attenuate the parallel and perpendicular components of the field, and to account for the fact that reflection also alters the relative time delays of emission from different regions of the shower affecting the coherence properties of the pulses. Therefore, this method can also be applied when the reflector is not in the Fraunhofer limit.

We compare the specular approximation to the results of the full ZHAireS simulation including reflection to illustrate the difference between the two methods. For this comparison we evaluate the flux density at $f = 300$ MHz at a few ground locations scaling it to account for the distance from ground to the location of the high altitude balloon. In Fig. 6.13 we display the electric field as a function of ψ for two different zenith angles. We note that for $\theta = 57°$ (Fig. 6.13 top) the distribution in ψ is significantly wider, what can lead to orders of magnitude of over-estimation of the flux density for the larger off-axis angles. For $\theta = 71°$ (Fig. 6.13 bottom) we still see relevant deviations between the two methods, but they are significantly reduced compared to the lower zenith angle case. Significant deviations are also found at other frequencies. Moreover, the shapes of the frequency spectra obtained with the two methods also differ appreciably, as we plot in

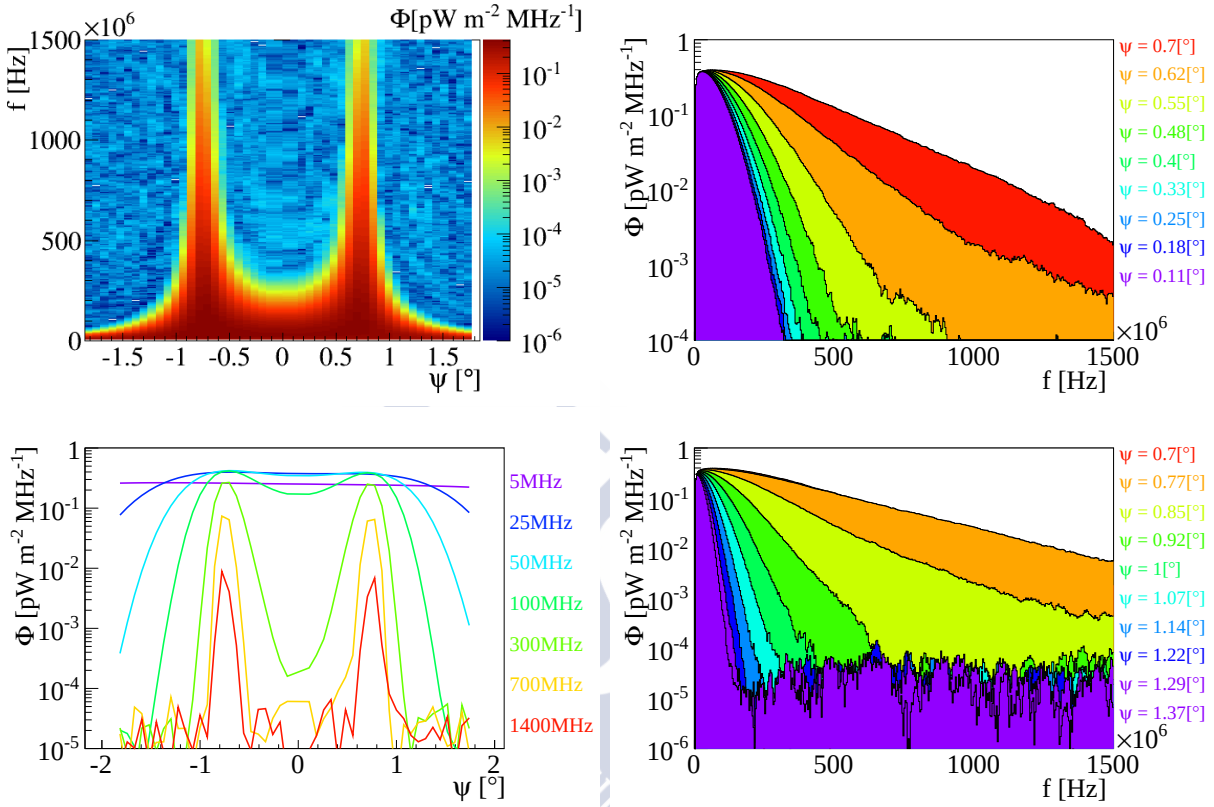

Figure 6.12: Top left panel: distribution of the radio signal (flux density Φ) as function of the off-axis angle ψ and frequency f for an air shower with $\theta = 71°$ and $\log_{10}(E/\text{eV}) = 18.4$. In the bottom left panel we show the distribution of the radio signal as a function of the off-axis angle at various frequencies. In the right panels we show the radio signal distribution as a function of frequency, in the top right panel for off-axis angles equal or smaller than the Cherenkov angle at the $X_{\max}$ of the shower, i.e. $\psi \leq 0.7°$, while in the bottom right panel for $\psi \geq 0.7°$. Taken from [16].

Fig. 6.14.

It is interesting to explore how the radiation changes with zenith angle for a primary particle with fixed energy. As the zenith angle increases the flux density Φ decreases. This can be seen in the top panel of Fig. 6.15, displaying the flux density Φ at $f = 300$ MHz as a function of the off-axis angle ψ for an air shower induced by a primary particle with energy $E = 10^{18.4}$ eV. The dominant effect in the decrease is the increasing overall distance to the detector with θ (see Fig. 6.8). Other effects however compensate the decrease in θ. The angle α of the shower axis to the Earth's magnetic field at the South Pole increases in the range of θ shown in Fig. 6.15, and the geomagnetic contribution is known to scale with $\sin\alpha$. Also, showers of increasing θ develop in a less dense atmosphere where the geomagnetic contribution to the electric field is expected to be increasingly larger [27]. The net result, including other more subtle effects such as the change in the region of the shower that emits coherently [28] is a decrease of Φ with θ.

To illustrate the importance of accounting for the Fresnel coefficients they were artificially set to 1 in the simulations shown in the top panel of Fig 6.15, while in the bottom panel they are taken into account. Comparing both panels, the peak value of the flux density is largest at relatively high zenith angles ($\theta \sim 80°$) when the Fresnel coefficients are accounted for, contrary to what is seen in the top panel where the peak value of Φ is achieved at the smallest zenith angles. This suggests that detection can be expected to be most favourable for θ around 80°. A thorough calculation of the acceptance integrating over area and solid angle [12] should also account for the reduction of the Cherenkov angle as the zenith angle rises (see Fig. 6.8) and for the directionality of the detection system.

6.5.4 Comparison with the simple model

Using Eq. (4.5) for the simple model developed in Chapter 4, we can compare the results of the model and those of a full ZHAireS simulation modified for reflection. In all the comparisons shown in the following plots, the depth of shower maximum for both the ZHAireS simulation and the model are chosen to be the same.

We calculate the amplitude of the electric field at several high altitude antennas located at different off-axis angles ψ and constant overall path distance for the ray as sketched in Fig. 6.17. We show the results in Fig. 6.16. The results from the model have been arbitrarily normalised. The shape of the angular distribution is well described by the simple model in a wide frequency range (from at least 50 to 900 MHz). It should be noted that, being one-dimensional, the approach cannot fully reproduce the frequency spectrum as obtained in the ZHAireS simulations near the Cherenkov angle, where the lateral spread is of utmost

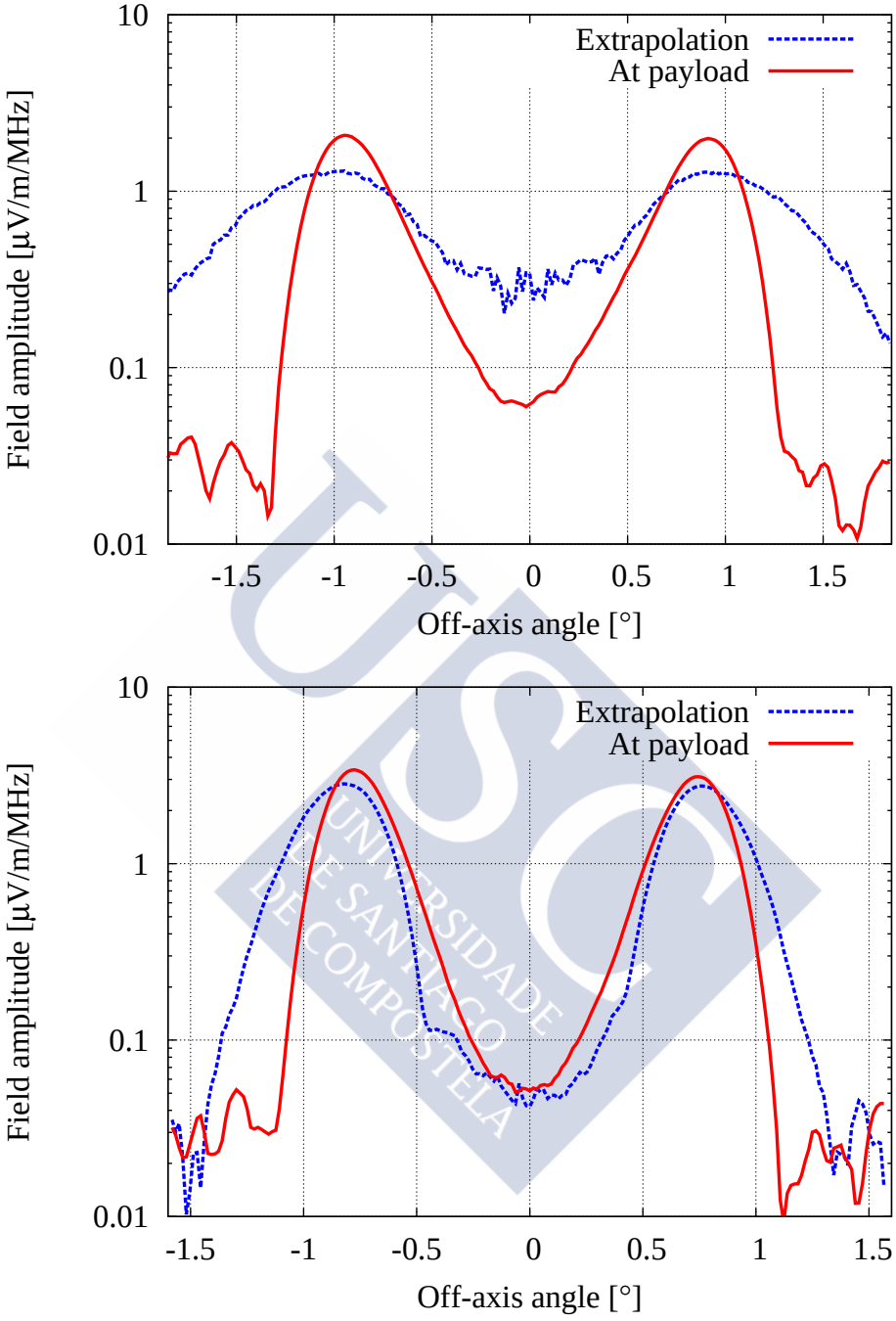

Figure 6.13: Electric field amplitude at a frequency $f = 300$ MHz as a function of off-axis angle ψ as obtained extrapolating the ZHAireS simulated signal at ground to the detector (dashed blue line), and simulating the reflection as explained in the text (solid red line). The electric field is shown for showers of $E = 10^{18.4}$ eV and two zenith angles $\theta = 57°$ (top panel) and $\theta = 71°$ (bottom panel). The Fresnel reflection coefficients are accounted for in all cases.

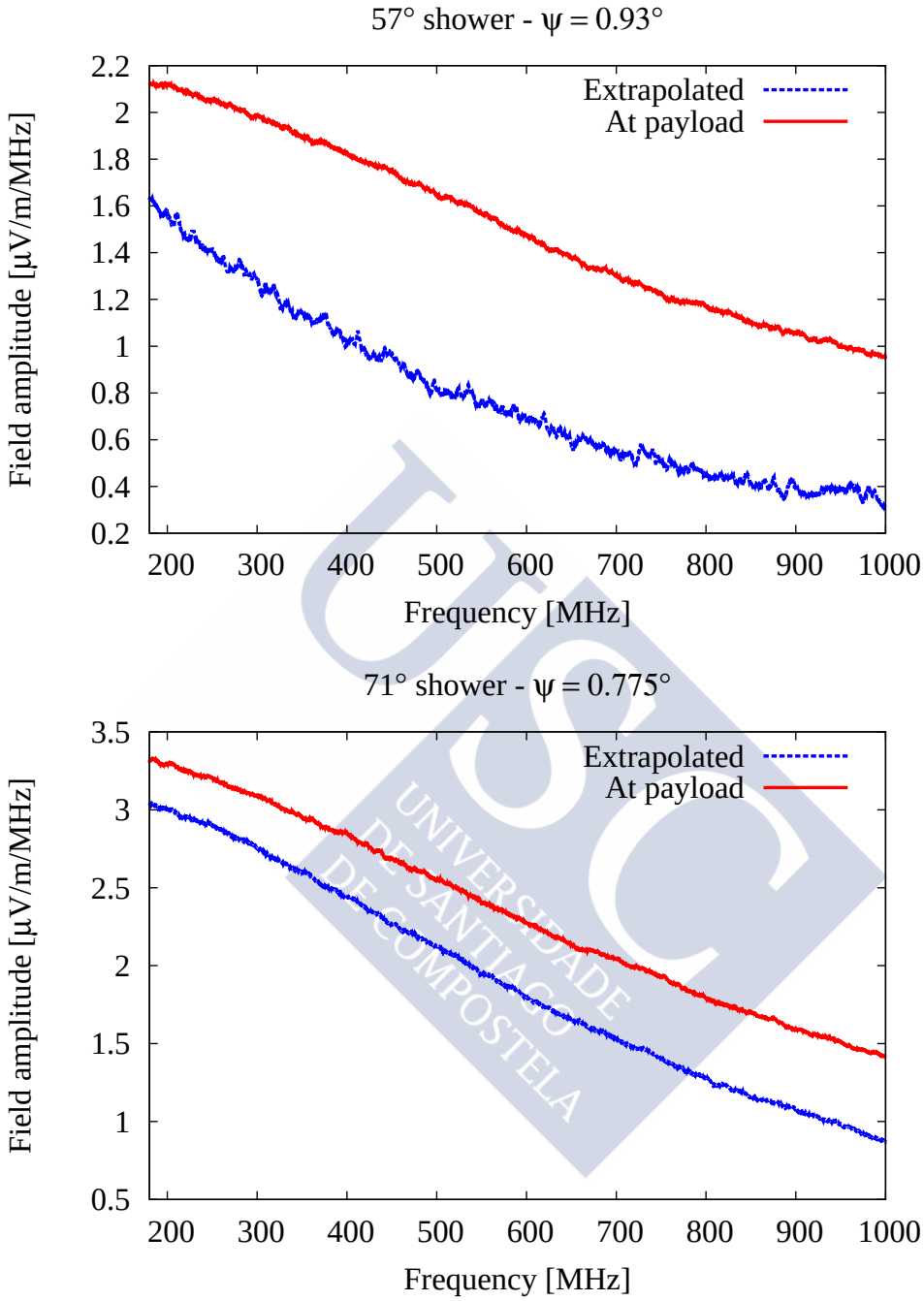

Figure 6.14: Electric field amplitude as a function of frequency (spectrum) as obtained extrapolating the ZHAireS simulated signal at ground to the detector (black dots and solid line), and simulating the reflection as explained in the text (red crosses and dashed line). The spectrum is shown for two showers of $E = 10^{18.4}$ eV. Top: Shower with 57° of zenith angle and 0.93° of off-axis angle. Bottom: Shower with 71° of zenith angle and 0.775° of off-axis angle. The Fresnel reflection coefficients are accounted for in all cases.

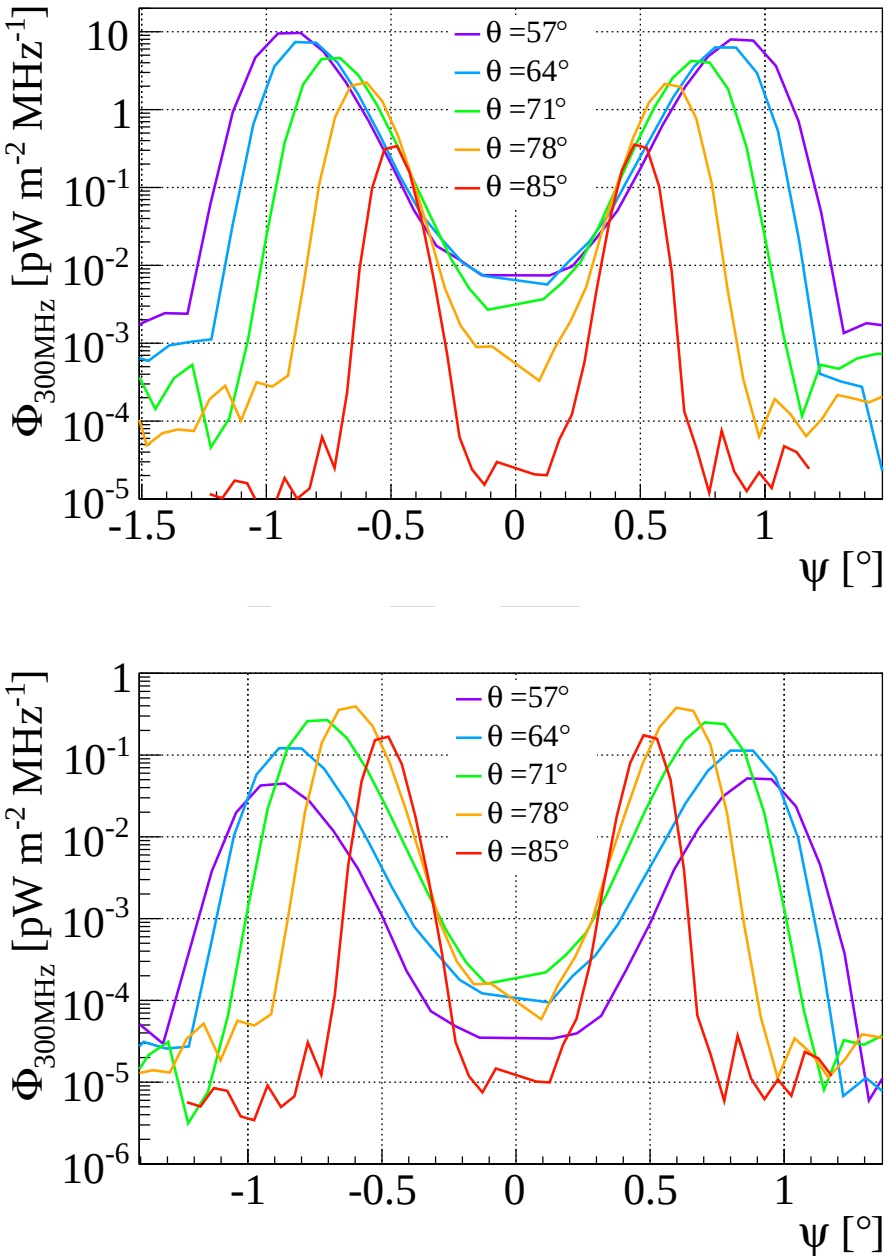

Figure 6.15: Comparison of the flux-density Φ at $f = 300$ MHz as a function of the off-axis angle ψ before (top) and after applying Fresnel reflection coefficients (bottom). Different sets of curves correspond to different zenith angles θ as labeled. The simulations have an energy of $10^{18.4}$ eV. Taken from [16].

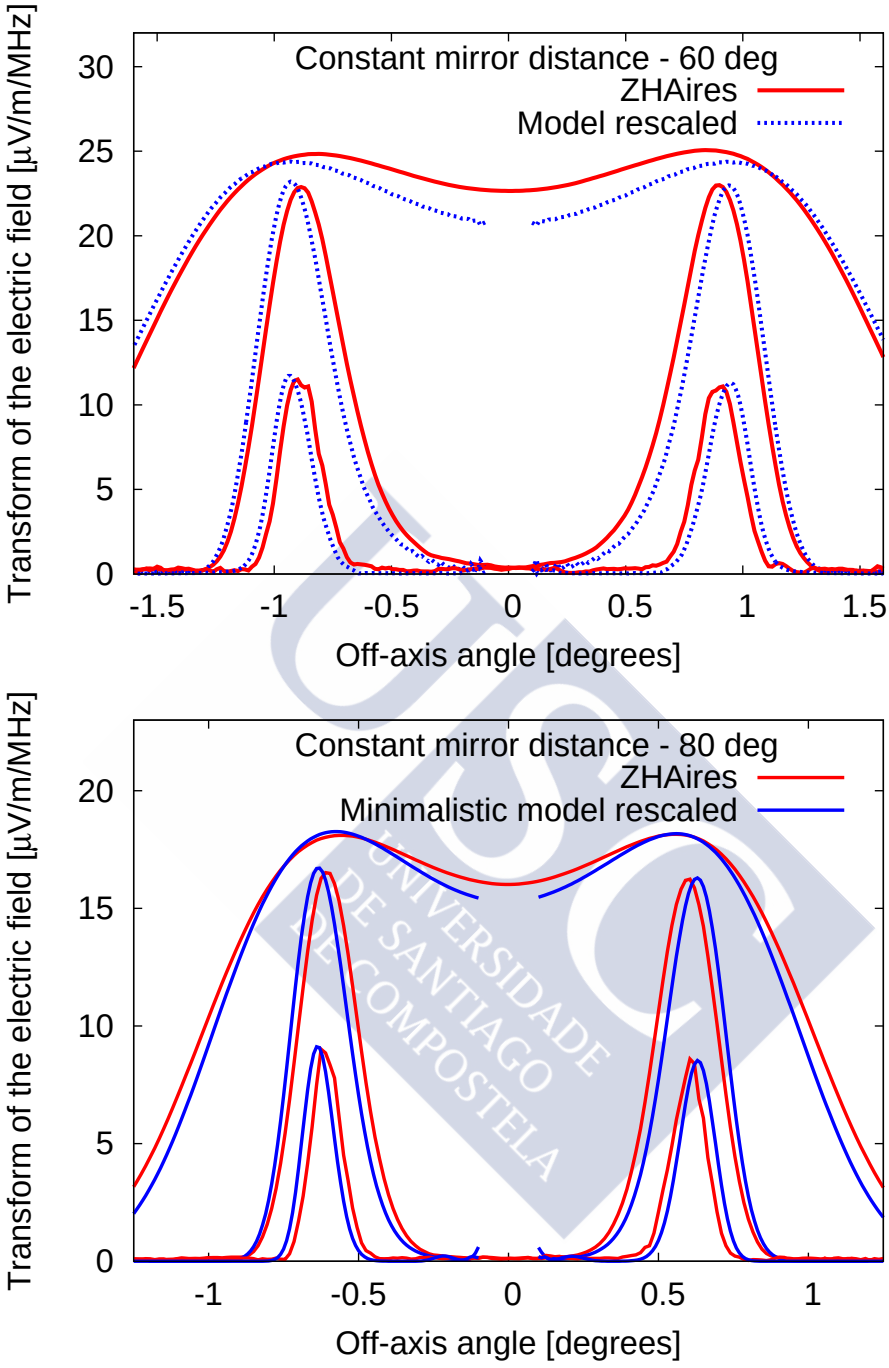

Figure 6.16: Top: amplitude of the Fourier transformed electric field as a function of the off-axis angle for different frequencies. Results from full ZHAireS simulations and the model are shown. The shower has $E = 10^{19}$ eV, $\theta = 60°$ and a height of $X_{\max}$ of ~ 83.3 km. From top to bottom the observation frequencies are 50, 300 and 900 MHz. Bottom: same as in the top panel, but for a $\theta = 80°$ shower with $h_{X\max} \sim 13.5$ km and with the observers placed at a constant distance of ~ 276.9 km.

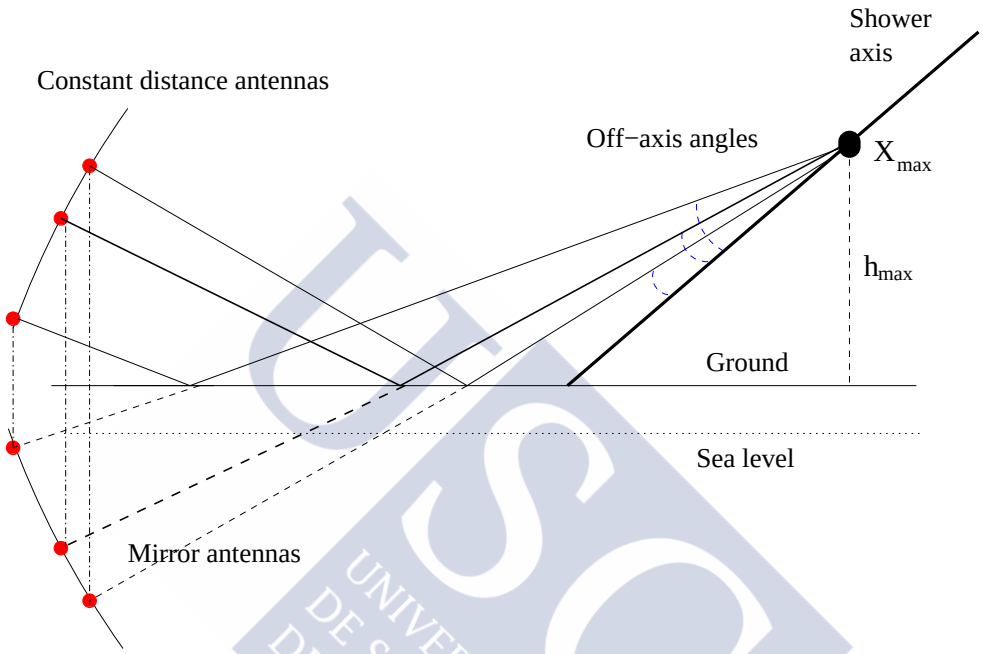

Figure 6.17: Sketch of the placement of the antennas in the simulation. We choose antennas at a constant distance from the shower maximum that lie below the ground (labeled mirror antennas) and then we invert their vertical coordinates with respect to the ground to obtain the location of the antennas that receive the reflected rays (labeled constant distance antennas), the ones that will be used for the simulation of reflected events. In doing so, the distance that a reflected ray covers from the shower maximum to these antennas is constant, independent of the off-axis angle.

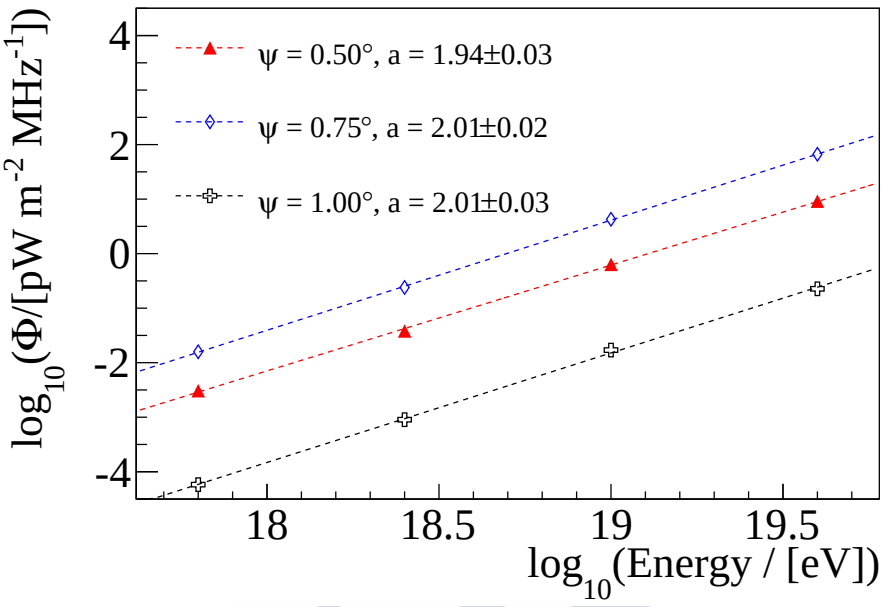

Figure 6.18: Flux density Φ at $f = 300\,\mathrm{MHz}$ as a function of the energy of the primary particle for three off-axis angles. The results of fitting a straight line $\log_{10}\Phi = a\log_{10}(E/\mathrm{eV})+b$ are shown.

importance [15]. We are however confident that the agreement between the simple model and the ZHAireS simulations strengthen the validity of the latter.

6.5.5 Energy dependence of the reflected emission

From the set of simulations we have examined the energy dependence of the radio signal. As before, we use the flux density at a reference frequency $f = 300$ MHz for a shower of $\theta = 71°$.

In Fig. 6.18 we select three off-axis angles and plot the flux density (which is proportional to the electric field squared, according to Eq. (6.4)) as a function of the primary particle energy. We fit a simple linear function to the dependence of $\log_{10}\Phi$ on $\log_{19}E$ and find a slope that is consistent with 2. This confirms that the received flux density scales quadratically with the primary energy and the amplitude of the electric field scales linearly with it. This is not surprising since for a coherent signal it is expected that the amplitude of the electric field scales with the number of electrons in the shower which is

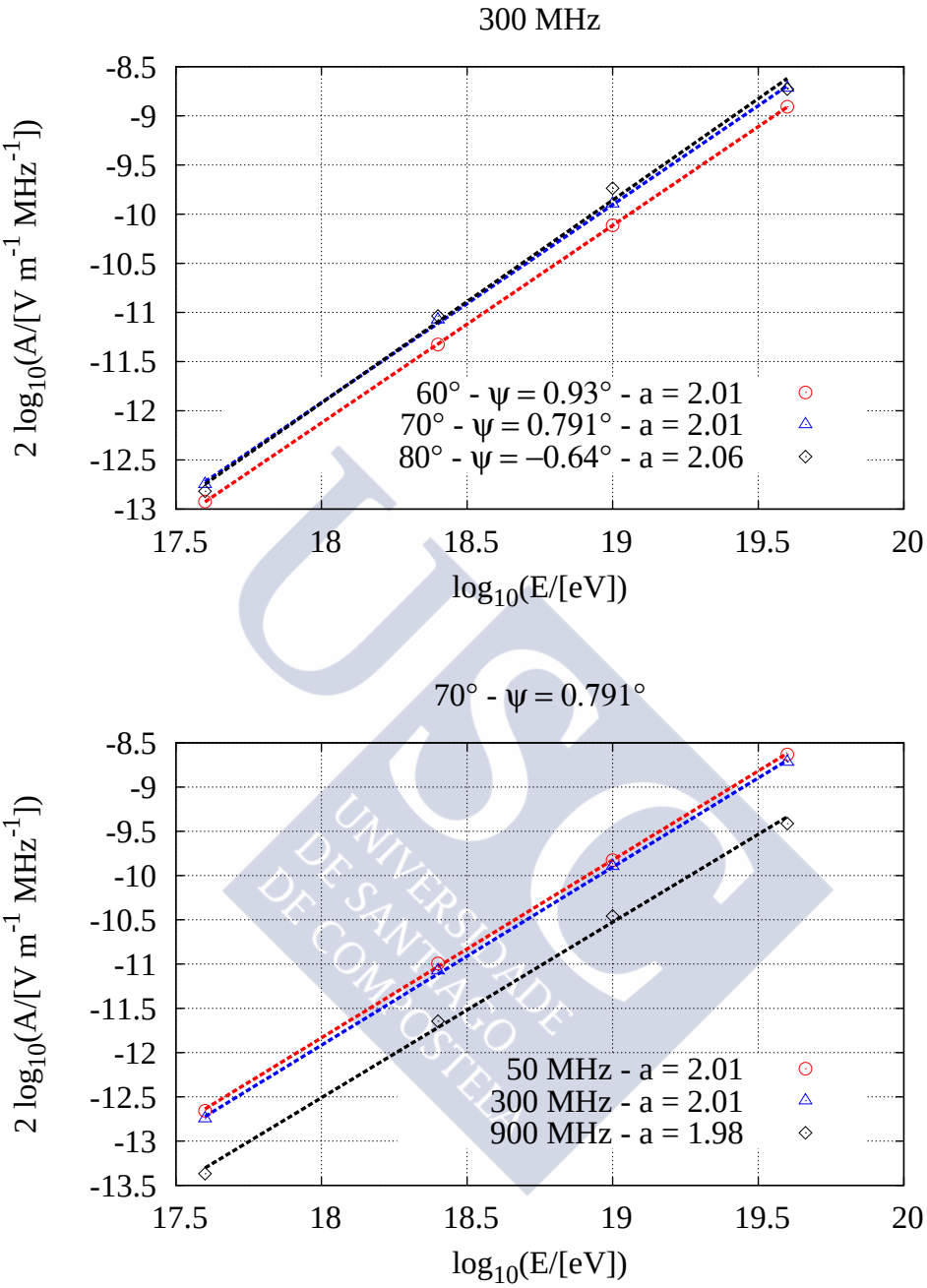

Figure 6.19: Top: Electric field amplitude at $f = 300$ MHz as a function of the energy of the primary energy particle for three shower zenith angles. Bottom: Electric field amplitude for a 70° zenith angle shower as a function of the energy of the primary energy particle for different frequencies. The results of fitting a straight line $\log_{10}\Phi = a\log_{10}(E/\mathrm{eV}) + b$ are shown.

proportional to the energy of the primary particle. We have verified that the quadratic relation between the electric field and energy of primary cosmic ray particle holds for all the zenith angles (Fig. 6.19, top panel) and all considered frequencies (Fig. 6.19, bottom panel) in our simulation set. This has important consequences since measuring the flux density at a given off-axis angle provides a measurement of the energy of the air shower. In practice the off-axis angle can be related to the exponential fall-off of the flux density as can be seen in Fig. 6.12. This relation is key to the energy determination of UHECRs with ANITA [26, 29]. This means that it is in principle possible to deduce the primary energy from the measurement of the spectrum at a single location as long as the exponential fall-off of the spectrum can be determined, as is shown in [10, 29].

6.6 Measurement of the UHECR spectrum with ANITA I

For completitude we give here a brief account of the first measurement of the UHECR spectrum with ANITA I. See [29] for further details.

It is possible to measure the energy of the primary particle of a shower by means of radio detection only, as shown in [10]. The ANITA payload can measure the angle at which the radiation is reflected, which is close to the shower zenith angle. For a given shower, the fall-off of the spectrum and its amplitude at a given frequency and off-axis angle are related to the fall-off and the amplitude at the Cherenkov angle,

$$\log_{10}(|\mathbf{E}_c|) = \log_{10}(|\mathbf{E}|) - b(\gamma - \gamma_c). \tag{6.5}$$

The amplitude at 300 MHz, $|\mathbf{E}|$, as well as the spectral fall-off, γ, can be measured experimentally. The spectral fall-off at the Cherenkov angle, γ_c, and the proportionality constant b can be obtained by fitting the ZHAireS simulations, and they happen to be energy independent. After using Eq. (6.5) to obtain the amplitude at the Cherenkov angle $|\mathbf{E}_C|$, the energy of the primary particle is obtained through another fit to ZHAireS simulations,

$$\log_{10}(E) = \frac{1}{p_1}\left[\log_{10}(|\mathbf{E}_c|) - p_0\right], \tag{6.6}$$

where E is the primary particle energy and p_0 and p_1 are the fit parameters.

There are important sources of uncertainty for the method [29]. First of all, the Fresnel coefficients, the curvature of the Earth and the roughness of the reflecting surface affect the normalization of the spectrum, while the roughness alone affects the fall-off of the

spectrum since it has an effect that is dependent on the frequency. Besides, the methods used to account for surface roughness present large uncertainties due to the limited information on the reflecting surface. Another important source of uncertainty is the current impossibility of determining the depth of shower maximum $X_{\max}$. Several showers with different angles and shower maxima are simulated in order to get an uncertainty for the energy reconstruction method.

Using the data from the 14 reflected pulses in [8], the method yields a mean energy for the detected events of $(2.9 \pm 0.4 \pm 0.8)$ EeV, with the first uncertainty due to the individual events and the second due to the normalization scale of the electric field.

The exposure of ANITA, that is, the expected number of cosmic ray events detected by ANITA at a given energy divided by the incident cosmic ray flux, was obtained with simulations [29]. With the exposure and the mean energy of the cosmic ray primaries, a measurement of the cosmic ray flux can be obtained, as shown in Fig. 6.20. This measurement constitutes the first cosmic ray flux measurement performed using radio as a stand-alone technique.

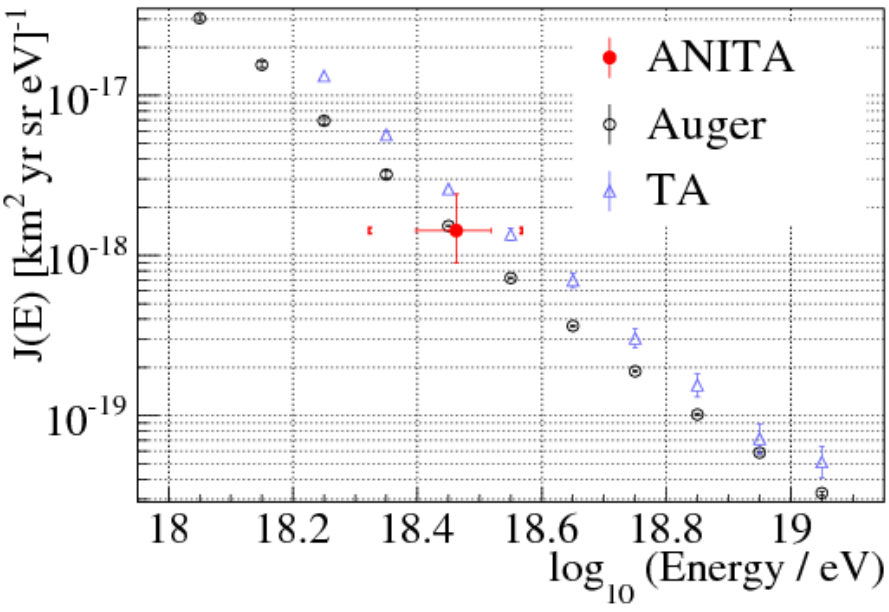

Figure 6.20: Comparison between the UHECR flux as observed by ANITA I, the Pierre Auger Observatory and the Telescope Array. Taken from [29].

Bibliography

[1] D. Ardouin *et al.* Geomagnetic origin of the radio emission from cosmic ray showers observed by codalema. *Astroparticle Physics*, **31**:192, 2009.

[2] P. Schellart *et al.* Detecting cosmic rays with the LOFAR radio telescope. *Astronomy and Astrophysics*, **A98**:560, 2013.

[3] F. G. Schröder *et al.* Radio detection of air showers with Auger Engineering Radio Array. In *Proceedings of the 33rd International Cosmic Ray Conference (ICRC 2013)*, number 0899.

[4] H. Falcke *et al.* Detection and imaging of atmospheric radio flashes from cosmic ray air showers. *Nature*, **435**:313, 2005.

[5] F. G. Schröder *et al.* The Tunka Radio Extension (Tunka-Rex): Status and first results. In *Proceedings of the 33rd International Cosmic Ray Conference (ICRC 2013)*, number 0452.

[6] H. R. Allan. *Progress in Elementary Particle and Cosmic Ray Physics*, **10**:169, 1971.

[7] T. Huege. The renaissance of radio detection of cosmic rays. In *Proceedings of the 33rd International Cosmic Ray Conference (ICRC 2013)*, number 0520.

[8] S. Hoover *et al.* Observation of ultrahigh-energy cosmic rays with the ANITA balloon-borne radio interferometer. *Physical Review Letters*, **105**(151101), 2010.

[9] P. W. Gorham *et al.* The Antarctic Impulsive Transient Antenna ultra-high energy neutrino detector: Design, performance, and sensitivity for the 2006–2007 balloon flight. *Astroparticle Physics*, **32**:10, 2009.

[10] H. Schoorlemmer *et al.* Energy and flux measurements of ultra-high energy cosmic rays observed during the first ANITA flight. In *Proceedings of the 34th International Cosmic Ray Conference (ICRC 2015)*, number 272.

[11] J. Nam. Taiwan Astroparticle Radiowave Observatory for Geo-synchrotron Emissions (TAROGE). In *Proceedings of the 34th International Cosmic Ray Conference (ICRC 2015)*, number 663.

[12] P. Motloch, N. Hollon, and P. Privitera. On the prospects of ultra-high energy cosmic rays detection by high altitude antennas. *Astroparticle Physics*, **54**:40, 2014.

[13] P.W. Gorham *et al.* The ExaVolt Antenna: A large-aperture, balloon-embedded antenna for ultra-high energy particle detection. *Astroparticle Physics*, **35**:242, 2011.

[14] A. Romero-Wolf *et al.* Concept and analysis of a satellite for space-based radio detection of ultra-high energy cosmic rays, 2013. arXiv:1302.1263 [astro-ph].

[15] J. Alvarez-Muñiz, W. R. Carvalho Jr., and E. Zas. Monte Carlo simulations of radio pulses in atmospheric showers using ZHAireS. *Astroparticle Physics*, **35**:325, 2012.

[16] J. Alvarez-Muñiz, W.R. Carvalho Jr., D. García-Fernández, H. Schoorlemmer, and E. Zas. Simulations of reflected radio signals from cosmic ray induced air showers. *Astroparticle Physics*, **66**:31, 2015.

[17] J. Alvarez-Muñiz, A. Romero-Wolf W. R. Carvalho Jr., M. Tueros, and E. Zas. Coherent radiation from extensive air showers in the ultrahigh frequency band. *Physical Review D*, **86**(123007), 2012.

[18] J. Alvarez-Muñiz, R. A. Vázquez, and E. Zas. Calculation methods for radio pulses from high energy showers. *Physical Review D*, **105**(063001), 2000.

[19] J. Abraham *et al.* Measurement of the depth of maximum of extensive air showers above 10^{18} eV. *Physical Review Letters*, **104**(091101), 2010.

[20] A. Aab *et al.* Depth of maximum of air-shower profiles at the pierre auger observatory: Measurements at energies above $10^{17.8}$ ev, 2014. arXiv1409.4809 [astro-ph].

[21] S. Sciutto. <http://www.fisica.unlp.edu.ar/auger/aires/>.

[22] A. Romero-Wolf *et al.* A passive probe for subsurface oceans and liquid water in Jupiter's icy moons. *Icarus*, **248**:463, 2015.

[23] K. Werner and O. Scholten. Macroscopic treatment of radio emission from cosmic ray air showers based on shower simulations. *Astroparticle Physics*, **29**:393, 2008.

[24] I. Kravchenko, D. Besson, and J. Meyers. In situ index-of-refraction measurements of the south polar firn with the RICE detector. *Journal of Glaciology*, **50**:171, 2004.

[25] D. Z. Besson *et al.* Antarctic radio frequency albedo and implications for cosmic ray reconstruction. *Radio Science*, **50**:1, 2015.

[26] K. Belov *et al.* Towards determining the energy of the UHECRs observed by the ANITA detector. *AIP Conference Proceedings*, **1535**:209, 2013.

[27] O. Scholten, K. Werner, and F. Rusydi. A macroscopic description of coherent geomagnetic radiation from cosmic-ray air showers. *Astroparticle Physics*, **29**:94, 2008.

[28] J. Alvarez-Muñiz, W.R. Carvalho Jr., A. Romero-Wolf, M. Tueros, and E. Zas. Ultra high frequency geomagnetic radiation from extensive air showers. *AIP Conference Proceedings*, **1535**:143, 2013.

[29] H. Schoorlemmer *et al.* Energy and flux measurements of ultra-high energy cosmic rays observed during the first ANITA flight. arxiv:1506.05396. Accepted in Astroparticle Physics in press.

USC
UNIVERSIDADE
DE SANTIAGO
DE COMPOSTELA

Chapter 7

Summary and results

Ultra-high energy cosmic rays are particles that have energies up to 10^{20} and beyondd and that arrive to the Earth after travelling the Universe. These energies are more than one million times the energies availably by means of man-made accelerators. Cosmic rays pose several questions that remain unanswered, such as which is their composition at ultra-high energies, which are their sources (the regions of the Universe where they are produced), how they are accelerated, or how they interact with the medium while they propagate towards the Earth, *etc.*

The existence of ultra-high energy cosmic rays that are protons or charged nuclei indicates that the production of neutrinos because of the interactions of the cosmic rays, limiting the distance the ultra-high energy cosmic rays can reach (GZK effect). On the other hand, neutrinos, being particles that interact only via weak force and with cross sections about 10^7 smaller than hadronic cross sections, can come from the edge of the Universe without deviating or interacting. This makes them extraordinary cosmic messengers.

The detection methods of ultra-high energy cosmic rays and neutrinos involve the creation of particle showers from the interaction of the cosmic ray with a particle in a medium (atmosphere or ice, for instance). These showers are measured with detectors such as water tanks provided with photomultipliers, or fluorescence telescopes. Through the measurable quantities of a shower several properties of the initial particle can be inferred, like the energy, the type of particle, the arrival direction...

One of the detection methods is the radio technique. This technique began to be developed in the 1960s, reaching some promising first results, but the limitations of the electronics at the time forced the research to stop. In the last years, and thanks to the advances in electronics, that now allows the measuring of voltages with temporal precision below the nanosecond, the radio technique is witnessing a renaissance, with experiments as ANITA, LOFAR, CODALEMA, ARA or ARIANNA.

The basic idea of the radio technique is the following. When a cosmic ray or a neutrino collides with a material medium in the Earth, the resulting shower contains charged

particles. These charged particles create a radiation electric field by accelerating and decelerating through the collisions in the medium, as well as by travelling faster than the speed of light in the medium (Cherenkov radiation). Due to the particle distribution and the shower scales, the resulting radiation is coherent at MHz-GHz frequencies. This radiation can be detected using radio antennas and data acquisition electronic modules, which makes the radio technique a technique with a good cost/efficiency ratio.

The emission at radio frequencies depends on the interplay of three key factors, mainly. First, the existence of a net unbalanced charge within the shower. Second, the movement of the particles in the shower. And third, the shower dimensions, that determine the frequency regions where the radiation is coherent. If the wavelength of observation is much larger than the shower size, the total field is proportional to the excess of charged particles, N, that contribute coherently, which is proportional to the energy of the primary particle, E. The power of the electric field scales with $N^2 \propto E^2$, which makes the radio technique more suitable for detecting high energy showers.

Understanding the properties of the electric field emitted by the showers, and how to reconstruct from the field the properties of the particle initiating the shower, is the key problem in radio. There are several macroscopic models that treat the shower roughly, with macroscopic currents. These models provide analytical tools that shed light on the emission of the radiation, but on the other hand, they are not very accurate. Microscopic models are based on the description of the shower through the trajectories of all the particles that constitute the shower. This modelling is achieved with the help of Monte Carlo codes, and once the trajectories are known, the electric field of each one of them can be calculated and the superposition principle applied in order to obtain the total field. Microscopic models are more accurate than the macroscopic ones, but they requiere a heavy usage of numerical calculations.

The radio technique seems appropriate for the search of neutrinos in dense media. Neutrinos could interact within a large natural volume that is also transparent at radio frequencies, possibiliting the detection of the shower at great distances. Nature offers large media transparent at radio frequencies, such as the ice at the poles. The Moon can also be used for the detection of neutrinos. In dense media, the first responsible of the electromagnetic radiation is the Askaryan effect, that consists on the entrainment of electrons in the medium by the shower particles. This creates an excess of negative charge, allowing the existence of a coherent radiation electric field. There are three experiments that use this technique in Antarctica, namely, ANITA (ANtarctic Impulsive Transient Antenna), ARIANNA (Antarctic Ross Ice-Shelf ANtenna Neutrino Array) and ARA (Askaryan Radio

Array). In Greenland, the GNO (Greenland Neutrino Observatory) is being scheduled.

In the atmosphere, the electric field of extensive air showers initiated by cosmic rays can be detected. In fact, this had already been achieved in the 1960s. In spite of dense media seeming more appropriate for detecting neutrinos with the radio technique, it is also possible, in principle, to detect neutrinos in the atmosphere. The dominant emission mechanism in the atmosphere is the geomagnetic mechanism, due to the deflection of the particles because of Earth's magnetic field. The deflection in opposite directions of the positive and negative charges creates a net current that emits radiation. The Askaryan effect is subdominant, except for several concrete geometries. However, the interplay between the two mechanisms is responsible for asymmetrical patterns of the electric field on the ground, from which information on the primary particle can be inferred. Experiments such as LOFAR (LOw Frequency ARray), AERA (Auger Radio Engineering Array), CODALEM and Tunka-Rex are currently performing radio measurements using the atmosphere as a detection volume.

The original work contained in this thesis was focused on the study of the radio technique as a technique suited for the detection of ultra-high energy cosmic rays and neutrinos. We have reviewed several formulas for the calculation of the electric field induced by ultra-high energy cosmic rays and neutrinos. We have developed a simple model for explaining the spatial properties of the electric field with the help of a ray tracing algorithm. We have also studied the molecular bremsstrahlung radiation (MBR) as an alternative mechanism for the emission of electric field by a particle shower. Finally, we have discussed what happens when the electric field of an air shower is reflected on the ground and detected at large altitude, and we have reviewed the results of the ANITA I experiment.

7.1 Calculations of radio emission

In the microscopic models, the shower modelling is made with line segments that imitate the real trajectory of a shower particle, called *tracks*. These tracks help in the construction of an electric current that is present in Maxwell's equations. In this thesis we derive an exact formula for the electric field of a track in frequency domain.

The known validity of the ZHS (Zas-Halzen-Stanev) formula for the calculation of the electric field emitted by a track has been subject to debate. It was argued that the formula was not valid for angles near the Cherenkov angle. We have shown that the ZHS formula is a good approximation to the exact formula in the far-field ($kR \gg 1$), in the Fraunhofer zone of the track, and therefore it is suited for the calculation of the electric field in many

practical applications.

When the track is too long for the application of the ZHS formula, it can be divided in smaller tracks. If each one of these verifies the conditions of the ZHS formula, it can be applied for each subtrack and add all their contributions, obtaining a good approximation to the electric field. This procedure is what we call the ZHS algorithm.

When a particle traves at superluminal speed in a material medium, even without being accelerated, it generates a radiation electric field known as Cherenkov radiation. The exact formula and the ZHS formula are in agreement with the field coming from an infinite trajectory at constant velocity, which is the classical formula for the electric field of the Cherenkov radiation.

The exact formula was embedded in the ZHS Monte Carlo to compare its predictions for a realistic shower with the predictions of the ZHS formula. The agreement is quite satisfactory as long as the observer lies in the radiation zone.

Another alternative formula for the calculation of the electric field of a track is the *endpoints* formula, where the electric field is interpreted as being due exclusively to one acceleration at the beginning of the track and one deceleration at the ending point of the track. This formula, however, presents finiteness problems at the Cherenkov angle, which is a very relevant angle since the radiation emitted at it is maximum. The use of this formula without changing its behaviour near the Cherenkov angle gives rise to unphysical predictions.

The saddle-point approach is a macroscopic approximation to the electric field of a shower that is valid not only in Fraunhofer zone, but also in Fresnel zone, closer to the shower than the previous one. The ZHS formula and the exact formula, when compared with the saddle-poing approach, give compatible results.

7.2 Model for the radio emission in air showers

The codes used for calculating the electric field according to the microscopic modelling can take a long running time. In fact, at ultra-high energies, it is not feasible to simulate a whole shower within a reasonable time frame, so a significant statistical sample of the shower particles through *thinning* algorithms has to be taken. Even with thinning, calculations can take a long time.

Because of this reason, it is useful to have a simple model that gives a first approximation to the electric field and allows to detect interesting properties that can be later studied in detail with a more precise Monte Carlo code. We have created a simple unidimensional

model for the calculation of the electric field of a shower. The relevant physical quantities for the calculation of this field are three, namely, the charge of one point in the shower, the distance between this point and the observer and the arrival time of the electromagnetic wave to the observer coming from the shower point.

Since the atmosphere has a refractive index that varies with height, the waves emitted by the shower are affected by refraction and change the direction of their trajectories. Given that, we have developed a ray tracing code that allows to obtain the curved trajectory of the rays and the time they take to get to the observer.

This model can be applied to obtain a qualitative approximation to the spatial distribution of the electric field for different frequencies. A comparison with the results from the ZHAireS Monte Carlo reveals that the shape of the distribution is predicted in a quite efficient way with a minimal number of parameters.

The model can be used as well for discussing the viability of certain observables of the electric field as indicators of the composition of the primary particle. We have studied the position of the maximum value of the electric field and the ratio of two electric fields at two different distances from the shower core. The results seem to indicate that these methods can be applied to current experiments, but their accuracy in the measurement of the depth of shower maximum can only reach about 20 g cm^{-2}.

7.3 Antennas for particle experiments

In this thesis we have also discussed the reciprocity theorem and its application for cosmic ray and accelerator experiments that involve antennas. In these experiments, the electric field is coming from multiple points that can be located at very different angles as seen from the antenna position, which is not a common situation between the usual applications of an antenna, and therefore little literature on the matter has been written. Through the reciprocity theorem, a formula for the voltage induced at an antenna by a set of tracks in radiation zone is deduced, and it is equivalent to the use of the ZHS formula in combination with the effective length (that gives the reception pattern) of the antenna.

7.4 Radiation in accelerator experiments

Within the radio field there has been a debate in the last few years about the possibility of using a technique analog to fluorescence but with radio frequencies. A type of emission candidate for this objective was the molecular bremsstrahlung (MBR). According to the

first ideas about this emission, the electric field emitted by the very low energy (< 10 eV) electrons of the shower would be isotropic and without a defined polarisation, just like fluorescence light. In an experiment at SLAC using a 28 GeV electron beam that collided with alumina targets, they tried to measure the emission yield of this mechanism by setting some antennas in an anechoic chamber, and concluded that its extension to air showers was feasible.

However, later experiments did not observe such a pronounced emission and seem to indicate that the measurements from the experiment at SLAC may have some kind of contamination due to other types of electric field, probably due to the leaking of the electric field polarised on the beam direction when trying to measure its perpendicular component.

The AMY experiment, carried out at the INFN in Frascati, tried to reproduce the results from SLAC with a 510 MeV pulsed beam. The AMY data reveal an upper bound to the MBR that lies an order of magnitude below the previous measurement at SLAC.

The MAYBE experiment, carried out at Argonne, used a 3 MeV kinetic energy electron beam produced by a Van de Graaff accelerator, in such a way that Cherenkov radiation was eliminated since the electrons possessed a speed lower than the speed of light in air. MAYBE found and unpolarised electric field from which, however, the resulting flux was an order of magnitude below that measured at SLAC.

Conti *et al.* made an experiment using a low energy electron gun, of 81 keV of kinetic energy. They discovered an incoherent and unpolarised radiation. Making the assumption that this emission is due to standard bremsstrahlung of electrons with kinetic energy larger than 1 keV, the authors created an emission model with the help of the PENELOPE code, which is compatible with the magnitude and the angular pattern of the emission. This angular pattern is focused towards the beam front direction, which means the isotropy of the emission is jeopardised. Moreover, an extrapolation of the emission yield to atmospheric showers predicts that the flux would lie one order of magnitude below the results from SLAC.

ZHS code takes into account the radiation that is emitted due to the acceleration and deceleration of particles. However, when decelerations are small and almost continuous, as it is the case with bremsstrahlung emission at GHz frequencies, the ZHS code takes only into account an effective deceleration that results in an effective electric field, that is not exactly the actual bremsstrahlung field.

In this thesis we have adapted the ZHS code for its use in an anechoic chamber and with an electron and positron beam as input. With the help of GEANT4 we have simulated

the passage of the beam through the alumina targets and given it to ZHS as input. With the ZHS formula and the antenna response pattern, we have obtained the voltage received by the antenna of the AMY experiment, and then included the effect of the coaxial cables and the amplifier. The ZHS formula is able to reproduce the behaviour in frequency and in time of the electric field at the AMY experiment, in the co-polarised plane. Were we in possession of more data about the calibration of the antenna, the prediction for the cross-polarised plane would be viable, as well as an improvement of the calculations in the co-polarised plane.

Due to the fact that the ZHS code does not take into account the incoherent bremsstrahlung emission at GHz frequencies, we have developed a model for MBR similar to the model by Conti *et al.* and applied it to the emission of the AMY experimental setup. The upper bound obtained is smaller than the bound measured by AMY, which makes sense because the model assumes incoherence, and the bound given by AMY is calculated in a frequency region where coherence is expected, beside other kinds of radiation.

The MBR model based in the work by Conti *et al.*, when used for the MAYBE experiment, gives a flux value that is ~ 2 times larger than the measured flux. This discrepancy could be due to an unaccurate tracking of the particles at low energies by the ZHS code, which predicts more MBR flux at low energies than the PENELOPE code used by Conti *et al.* Besides, the uncertainty in the antenna gain is not known.

Another useful comparison for the understanding of MBR is the comparative of emission estimations from various experiments and theoretical calculations. These estimations lead us to not being very optimistic about the future of MBR as a viable technique for cosmic ray detection.

7.5 Radiation in ultra-high energy cosmic ray experiments. The ANITA experiment

The ANITA experiment is an experiment located at the South Pole. It consists on an aerostatic balloon upon which a payload with several antennas for the reception of the electric field are located. ANITA was conceived for the detection of the electric field of ice showers induced by neutrinos. This electric field would traverse the ice and reach the atmosphere, where it would be detected by ANITA at an altitude of 36 km. On the other hand, what was detected was 16 events with a polarisation of the electric field compatible with geomagnetic origin, indicating that they were produced by cosmic ray showers in the

atmosphere. 14 out of the 16 events where events for which the electric field had been reflected on the polar ice before reaching the ANITA payload.

We have developed a code, the ZHAireS-Reflex, which is a new ZHAireS version able to calculate the electric field reflected on the ground and detected at high altitude. The code assumes a rectilinear propagation of the rays and calculates the time that the field of a track takes to travel from the emission point to the reception point passing through the reflection point. This time is used later in the ZHS formula to calculate the electric field.

Through the ray tracing algorithm developed in this thesis, we have checked that the straight ray tracing is a good approximation to the trajectory and valid to calculate the electric field up to 85° zenithal angle showers.

We have also discussed the properties of the electric field of a shower after being reflected on the ground, simulated with the ZHAireS-Reflex code. The predictions are very different to those obtained with the standard ZHAireS after extrapolating the antennas to a large altitude, which indicates that correctly taking into account the reflection is important. The Fresnel coefficients on the surface are also relevant, because they tend to suppress the shower emission from low zenithal angles.

We have also checked that the simple model for the electric field of a particle shower reproduces qualitatively the spatial distribution of the reflected electric field.

Thanks to the ZHAireS-Reflex code we have also discovered a quadratic relationship between the flux density of the electric field and the energy of the primary particle, that happens to be valid for several zenithal angles, observation off-axis angles and frequencies. We have also discovered a relationship between the spectrum slope and the observation off-axis angle. This has very relevant experimental applications, such as the determination of the shower energy with a single broadband antenna.

Finally, in this thesis we have reviewed the cosmic ray flux measurement carried out by the ANITA experiment and that was fundamented on the 14 events reflected on the polar ice. This measurement is the first measurement of the kind that was achieved using radio as a stand-alone technique.

Capítulo 8

Resumo e resultados da tese

Os raios cósmicos de enerxías ultra altas son partículas que teñen enerxías de ata 10^{20} eV e que chegan á Terra despois de viaxar polo universo. Estas enerxías son máis de un millón de veces superiores ó que se pode acadar por medio de aceleradores. Os raios cósmicos plantexan certas preguntas que aínda non se puideron resolver, como cal é a súa composición a enerxías ultra altas, cal é a súa orixe (as rexións do universo en que se producen), como se aceleran, como interactúan co medio mentres se desprazan cara a Terra, *etc.*

A existencia de raios cósmicos de enerxías ultra altas que son protóns ou núcleos cargados indica que é moi probable que se produzan neutrinos nas interaccións dos raios cósmicos, limitando a distancia que poden recorrer os raios cósmicos de enerxías máis altas (efecto GZK). Por outra banda, os neutrinos, ó seren partículas que interactúan só mediante a forza débil e cunhas seccións eficaces unhas 10^7 veces menores cás dos hadróns, poden vir desde a outra punta do universo sen desviarse ou interactuar. Isto fainos mensaxeiros cósmicos extraordinarios.

Os métodos de detección de raios cósmicos e neutrinos de enerxías ultra altas involucran a creación de chuveiros de partículas a partir da interacción do raio cósmico cunha partícula dun medio (atmosfera ou xeo, por exemplo). Estes chuveiros mídense con detectores como tanques de auga con fotomultiplicadores, ou telescopios de fluorescencia. A través das cantidades mensurables dun chuveiro pódense derivar propiedades da partícula inicial, como a enerxía, o tipo de partícula, a súa dirección de chegada...

Un dos métodos de detección é a técnica de radio. Esta técnica empezou a desenvolverse nos anos sesenta, acadando uns primeiros resultados esperanzadores, pero a limitación da electrónica da época fixo que se abandonara. Nos últimos anos, e grazas ós avances da electrónica, que permite medir voltaxes con precisión temporal por debaixo do nanosegundo, a técnica de radio está a ver un rexurdimento, con experimentos como ANITA, LOFAR, CODALEMA, ARA ou ARIANNA.

A idea básica da técnica de radio é a seguinte. Cando un raio cósmico ou un neutrino impacta nun medio terrestre, o chuveiro resultante do choque contén partículas cargadas.

Estas partículas cargadas crean un campo eléctrico de radiación ó acelerarse e desacelerarse por colisións co medio, así como por viaxar máis rápido cá velocidade da luz no medio (radiación Cherenkov). Debido á distribución de partículas e ós tamaños do chuveiro, a radiación resultante é coherente a frecuencias de MHz-GHz. Esta pódese detectar con antenas de radio e con módulos electrónicos de adquisición de datos, o que convirte á técnica de radio nunha técnica cunha boa relación eficiacia/custo.

A emisión en radio depende principalmente da interrelación de tres factores. Primeiro, da existencia dunha carga neta no chuveiro. Segundo, do movemento das partículas do chuveiro. E terceiro, das dimensións do chuveiro, que determinan as rexións de frecuencia en que a radiación é coherente. Se a lonxitude de onda de observación é moito máis grande có tamaño do chuveiro, o campo total é proporcional ó exceso de partículas cargadas, N, que contribúen coherentemente, o cal é proporcional á enerxía da partícula primaria E. A potencia do campo eléctrico escala con $N^2 \propto E^2$, o que fai que a técnica de radio sexa máis apta para detectar chuveiros de altas enerxías.

Entender as propiedades do campo eléctrico emitido polos chuveiros, e como reconstruir a partir do mesmo as propiedades da partícula iniciadora do chuveiro, é o problema clave en radio. Existen modelos macroscópicos que tratan o chuveiro a grandes rasgos con correntes macroscópicas. Estes modelos fornecen unhas ferramentas analíticas que aportan intuición sobre a emisión de radiación, pero pola contra non son moi precisos. Os modelos microscópicos baséanse na descripción do chuveiro a traverso das traxectorias de todas as partículas que compoñen un chuveiro. Este modelado faise coa axuda de programas Monte Carlo, e unha vez se coñecen as traxectorias, pódese calcular o campo eléctrico de cada unha de elas e aplicar o principio de superposición para coñecer o campo total. Os modelos microscópicos son máis precisos cós microscópicos, pero requiren un forte uso de cálculos numéricos.

A técnica de radio preséntase apropiada para a procura de neutrinos en medios densos. Os neutrinos poderían interactuar nun gran volume natural e transparente ás frecuencias de radio, co que o chuveiro podería ser detectado dende grandes distancias. A natureza ofrece medios de gran tamaño e transparentes ás frecuencias de radio, como o xeo polar. A Lúa tamén pode usarse para a detección de neutrinos. En medios densos, o principal responsable da radiación electromagnética é o efecto Askaryan, que consiste no arranque de electróns no medio por parte das partículas do chuveiro. Isto crea un exceso de carga negativa, posibilitando a existencia dun campo eléctrico de radiación coherente. Hai tres experimentos que usan esta técnica na Antártida: ANITA (ANtarctic Impulsive Transient Antenna), ARIANNA (Antarctic Ross Ice-Shelf ANtenna Neutrino Array) e ARA

(Askaryan Radio Array). En Groenlandia, está proxectado o experimento GNO (Greenland Neutrino Observatory).

Na atmosfera, podemos detectar o campo eléctrico dos chuveiros iniciados por raios cósmicos. De feito, isto conseguírase xa nos anos 60 do século XX. A pesar de que os medios densos semellan máis axeitados para detectar neutrinos coa técnica de radio, en principio tamén é posible detectar neutrinos na atmosfera. O mecanismo dominante de emisión de radio na atmosfera é o mecanismo xeomagnético, debido á deflexión das partículas por parte do campo magnético terrestre. A deflexión en direccións opostas das cargas positivas e negativas crea unha corrente neta que emite radiación. O efecto Askaryan é subdominante, salvo para certas xeometrías. Sen embargo, a interrelación entre os dous mecanismos propicia uns patróns asimétricos do campo eléctrico no chan dos que se pode inferir información da partícula primaria. Experimentos como LOFAR, (LOw Frequency ARray), AERA (Auger Radio Engineering Array), CODALEMA e Tunka-Rex están a facer medicións de radio usando a atmosfera como volume de detección.

O traballo orixinal desta tese centrouse, precisamente, no estudo da técnica de radio como unha técnica de detección de raios cósmicos e neutrinos de enerxías ultra altas. Revisamos distintas fórmulas para o cálculo do campo eléctrico inducido polos chuveiros de raios cósmicos e neutrinos de enerxías ultra altas. Desenvolvimos un modelo sinxelo para as propiedades espaciais do campo eléctrico coa axuda dun algoritmo de trazado de raios. Estudiamos tamén a radiación de frenado molecular (*molecular bremsstrahlung*, MBR) como un mecanismo alternativo de emisión de campo eléctrico por parte do chuveiro. Por último, discutimos o que sucede cando o campo eléctrico dun chuveiro en aire se reflicte no chan e se detecta a gran altitude e revisamos os resultados do experimento ANITA I.

8.1 Cálculos de emisión de radio

Nos modelos microscópicos, o modelado da cascada faise a partir de segmentos de liña que imitan a traxectoria real que posúen as partículas dun chuveiro. Estes segmentos ou *tracks* serven para construír a corrente eléctrica que se acha presente nas ecuacións de Maxwell. Nesta tese derivamos unha fórmula exacta para o campo eléctrico dun segmento no dominio de frecuencias.

A validez coñecida da fórmula ZHS (Zas-Halzen-Stanev) para o cálculo do campo eléctrico emitido por track ten sido obxecto de debate. Púxose en entredito a súa validez para ángulos preto do ángulo Cherenkov. Demostramos que a fórmula ZHS é unha boa aproximación á fórmula exacta en campo de radiación ($kR \gg 1$), na zona de Fraunhofer da *track*,

e por tanto é axeitada para o cálculo do campo eléctrico en moitas aplicacións prácticas.

Cando o segmento é demasiado grande para a aplicación da fórmula ZHS, pódese subdividir o segmento en segmentos máis pequenos. Se cada un destes verifica as condicións da fórmula ZHS, pódese aplicar a cada subsegmento e engadir todas as contribucións, conseguindo unha boa aproximación ó campo eléctrico. Este procedemento é o que chamamos algoritmo ZHS.

Cando unha partícula viaxa a velocidade superlumínica nun medio material, incluso sen ser acelerada, xenera un campo eléctrico de radiación coñecido como radiación Cherenkov. A fórmula exacta e a fórmula ZHS están en concordancia co campo dunha traxectoria infinita a velocidade constante, que é a fórmula clásica para o campo eléctrico da radiación Cherenkov. Por ende, a fórmula exacta e a fórmula ZHS conteñen a radiación inducida polo movemento superlumínico das partículas.

A fórmula exacta incluiuse no Monte Carlo ZHS para comparar as súas predicións nun chuveiro realista coas da fórmula ZHS. O acordo é moi satisfactorio sempre e cando o observador se atope en campo de radiación.

Outra fórmula alternativa para o cálculo do campo eléctrico dunha *track* é a fórmula dos *endpoints*, onde se interpreta o campo eléctrico como debido exclusivamente a unha aceleración ó principio do segmento e unha deceleración ó final. Esta fórmula, sen embargo, presenta problemas de finitude no ángulo Cherenkov, que é un ángulo moi relevante, pois a radiación emitida nel é máxima. O uso desta fórmula sen mudar o seu comportamento preto do ángulo Cherenkov dá lugar a predicións sen sentido físico.

O método do punto de cadeira (saddle-point approach) é unha aproximación macroscópica ó campo eléctrico dun chuveiro válido non só na zona de Fraunhofer, senón tamén na zona de Fresnel, máis preto do chuveiro que a anterior. A fórmula ZHS e a fórmula exacta, cando se comparan co método de punto de cadeira, dan resultados compatibles.

8.2 Modelo para a emisión de radio en chuveiros en aire

Os programas que calculan o campo eléctrico segundo o modelo microscópico poden tardar bastante tempo en executarse. De feito, para enerxías ultra altas, un non pode simular todo o chuveiro nun tempo razoable, polo que se debe de tomar unha mostra estatística significativa das partículas do chuveiro mediante os algoritmos de *thinning*. Incluso con thinning, os cálculos poden demorar moito tempo.

Por este motivo resulta útil un modelo sinxelo que dea unha primeira aproximación ó campo eléctrico e permita detectar propiedades interesantes que logo podan ser estudiadas a fondo cun Monte Carlo máis preciso. Por esta razón creamos un modelo sinxelo unidimensional para o cálculo do campo eléctrico dun chuveiro. As cantidades físicas relevantes para o cálculo deste campo son só tres: a carga dun punto do chuveiro, a distancia entre este punto e o observador e o tempo de chegada da onda electromagnética ó observador procedente do punto do chuveiro.

Como a atmosfera posúe un índice de refracción que varía coa altura, as ondas que emita o chuveiro vense afectadas pola refracción e cambian a dirección da súa traxectoria. Por este motivo, desenrolamos un código de trazado de raios que permita obter a traxectoria curva dos raios e o tempo que tardan en chegar ó observador.

Este modelo pódese aplicar para obter unha aproximación cualitativa á distribución espacial do campo eléctrico a distintas frecuencias. Unha comparación cos resultados do Monte Carlo ZHAireS revela que a forma da distribución se predi de xeito bastante eficiente cun número mínimo de parámetros.

O modelo pódese empregar tamén para discutir a viabilidade de certos observables do campo eléctrico como indicadores da composición da partícula primaria. Estudiamos a posición do valor máximo do campo eléctrico e o cociente dos campos eléctricos a dúas distancias distintas do punto de impacto do chuveiro no chan. Os resultados semellan indicar que estes métodos pódense empregar en experimentos actuais, pero que a súa precisión na medición da profundidade do máximo do chuveiro só pode chegar a uns 20 g cm^{-2}.

8.3 Antenas para experimentos de partículas

Nesta tese tamén discutimos o teorema de reciprocidade e a súa aplicación para os experimentos de raios cósmicos e de aceleradores que involucren antenas. Nestes experimentos, o campo eléctrico vén de múltiples puntos que poden estar a ángulos moi distintos vistos desde a posición da antena, o cal non é unha situación común entre as aplicacións habituais dunha antena, polo que non existe apenas literatura sobre o tema. Co teorema de reciprocidade derívase unha fórmula para o voltaxe inducido nunha antena por un conxunto de tracks en zona de radiación que é equivalente ó uso da fórmula ZHS en combinación coa lonxitude efectiva (que dá o patrón de recepción) da antena.

8.4 Radiación en experimentos de aceleradores

No campo de radio houbo un debate nos últimos anos sobre a posibilidade de empregar unha técnica análoga a fluorescencia pero con frecuencias de radio. Un tipo de emisión candidata para este obxectivo foi a radiación de frenado molecular ou MBR (*molecular bremsstrahlung*). Segundo as primeiras ideas sobre esta emisión, o campo eléctrico emitido polos electróns de moi baixa enerxía do chuveiro (< 10 eV) sería isótropo e sen polarización definida, como a luz de fluorescencia. Nun experimento en SLAC cun feixe de electróns de 28 GeV que se facía colisionar con brancos de alumina, tentouse medir a cantidade de emisión deste mecanismo poñendo antenas nunha cámara anecoica e concluíron que a súa extensión á detección de chuveiros atmosféricos era viable.

Sen embargo, experimentos posteriores non descubriron una emisión tan pronunciada e parecen indicar que as medidas do experimento de SLAC posuían algún tipo de contaminación por outra clase de campo eléctrico; seguramente debido á filtración do campo eléctrico polarizado na dirección do feixe ó intentar medir a compoñente perpendicular.

O experimento AMY, levado a cabo no INFN en Frascati, tentou repetir os resultados de SLAC cun feixe pulsado de 510 MeV. Os datos de AMY revelan unha cota superior ó MBR medido que se acha unha orde de magnitude por debaixo do medido previamente en SLAC.

O experimento MAYBE, levado a cabo en Argonne, usou un feixe de electróns de 3 MeV de enerxía cinética producido por un acelerador de Van de Graaff, de xeito que eliminaban a radiación Cherenkov ó teren os electróns unha velocidade inferior á da luz no aire. MAYBE atopou un campo eléctrico sen polarizar do que, sen embargo, o seu fluxo se atopaba unha orde de magnitude por debaixo de aquel medido en SLAC.

Conti *et al.* realizaron un experimento cunha pistola de electróns de baixa enerxía, 81 keV de enerxía cinética. Descubriron unha radiación incoherente e sen polarización definida. Facendo a hipótese de que esta emisión é debida á radiación de freado estándar de electróns con enerxía cinética maior ca 1 keV, os autores crearon un modelo de emisión coa axuda do programa PENELOPE, que é compatible coa magnitude e o patrón angular da emisión. Dito patrón angular está focalizado cara o frente do feixe, co cal a isotropía da emisión queda en entredito. Asimesmo, unha extrapolación da magnitude da radiación a chuveiros atmosféricos predi que o fluxo se acharía unha orde de magnitude por debaixo do medido en SLAC.

O código ZHS ten en conta a radiación emitida debida a aceleración e deceleración de partículas. Sen embargo, cando as deceleracións son moi pequenas e continuadas, coma no caso das emisións de bremsstrahlung de frecuencia de $\sim$ GHz, o código ZHS só ten en

conta unha deceleración efectiva que resulta nun campo efectivo, que non é exactamente o campo de bremsstrahlung.

Nesta tese adaptamos o código ZHS para o seu uso nunha cámara anecoica e cun feixe de electróns e positróns como entrada. Coa axuda de GEANT4 simulamos o paso do feixe polos brancos de alumina e pasámolo ó código ZHS como entrada. Coa fórmula ZHS e o patrón de resposta da antena, acadamos a voltaxe que recibe a antena do experimento AMY, á que posteriormente se lle engade o efecto dos cables coaxiais e do amplificador. A fórmula ZHS é capaz de reproducir o comportamento en frecuencia e en tempo do campo eléctrico do experimento AMY, no plano copolarizado. De termos máis datos sobre a calibración da antena, a predición no plano perpendicular sería viable, así como unha mellora dos cálculos no plano copolarizado.

Debido a que o código ZHS non ten en conta a emisión de bremsstrahlung incoherente a frecuencias de GHz, desenvolvimos un modelo para o MBR similar ó de Conti *et al.* e o aplicamos a emisión no experimento AMY. A cota superior que se obtén é menor cá que se mediu en AMY, o cal ten sentido porque o modelo asume incoherencia, e a cota de AMY está calculada nunha rexión de frecuencias onde se espera coherencia, ademáis de outros tipos de radiación.

O modelo de MBR baseado en Conti *et al.*, cando se usa para o experimento MAYBE, dá un valor de fluxo que é ~ 2 veces maior ó medido. Esta discrepancia pode deberse a un modelado das partículas incorrecto a baixa enerxía por parte do código ZHS, que predí máis fluxo de MBR a baixas enerxías có código PENELOPE usado por Conti *et al.* Ademáis, a incertidume da ganancia da antena non é coñecida.

Outra comparación útil para o entendemento do MBR é a comparativa de estimacións para a emisión procedentes de varios experimentos e cálculos teóricos. O conxunto de todas elas nos inclina a non ser moi optimistas sobre o futuro do MBR como unha técnica viable para a detección de raios cósmicos.

8.5 Radiación en experimentos de raios cósmicos de enerxías ultra altas. O experimento ANITA

O experimento ANITA é un experimento localizado no polo sur. Consiste nun globo aerostático no que se achan ancoradas varias antenas para a recepción do campo eléctrico. ANITA foi concebido para detectar o campo eléctrico de chuveiros en xeo inducidos por neutrinos. Este campo eléctrico atravesaría o xeo e pasaría a atmosfera, onde sería

detectado por ANITA a unha altitude de 36 km. Por outra banda, o que se detectou foron 16 eventos cunha polarización do campo eléctrico compatible con orixe xeomagnética, indicando que foran producidos por chuveiros de raios cósmicos na atmosfera. 14 dos 16 eventos eran eventos nos que o campo eléctrico fora reflectido no xeo polar antes de chegar ás antenas de ANITA.

Desenrolamos un código, o ZHAireS-Reflex, que é unha versión nova do ZHAireS coa que se pode calcular o campo eléctrico reflectido no chan e detectado a gran altitude. O código asume unha propagación rectilínea dos raios e calcula o tempo que tarda en percorrer o campo dun track dende o punto de emisión ata o punto de recepción pasando polo punto de reflexión. Este tempo emprégase despois na fórmula ZHS para calcular o campo eléctrico.

A traverso do algoritmo de trazado de raios tamén desenrolado nesta tese, comprobamos que o trazado rectilíneo de raios é unha boa aproximación á súa traxectoria e válido para calcular o campo eléctrico ata chuveiros de 85° de ángulo zenital.

Discutimos tamén as propiedades do campo eléctrico dun chuveiro despois de ser reflectido no chan, simulado co código ZHAireS-Reflex. As predicións son moi distintas de aquelas obtidas co ZHAireS estándar despois de extrapolar ás antenas a gran altitude, o que indica que ter en conta de xeito correcto a reflexión é importante. Os coeficientes de Fresnel para a reflexión na superficie tamén son relevantes, porque tenden a suprimir a emisión dos chuveiros de baixos ángulos zenitais.

Comprobamos tamén que o modelo simple para o campo eléctrico dun chuveiro de partículas reproduce cualitativamente a distribución espacial do campo eléctrico reflectido.

Grazas ó ZHAireS-Reflex tamén descubrimos unha relación cuadrática entre a densidade de fluxo do campo eléctrico e a enerxía da partícula primaria, que resulta ser válida para varios ángulos zenitais do chuveiro, ángulos *off-axis* de observación e frecuencias. Tamén descubrimos unha relación entre a pendiente do espectro e o ángulo *off-axis* de observación. Isto ten aplicacións experimentais moi relevantes, en concreto para a determinación da enerxía dos chuveiros cunha antena de gran ancho de banda de frecuencias.

Por último, nesta tese revisamos tamén a medida do fluxo de raios cósmicos levada a cabo polo experimento de ANITA e que se fundamentou nos 14 eventos reflectidos no xeo polar. Esta medida é a primeira do estilo que se fixo usando radio como unha técnica independiente.

Appendix A

Antenna gains in AMY

The goal is to find the effective length vector $\mathbf{l}_{\rm load}(\nu,\theta,\phi)$, which gives the measured voltage $V_L(\nu)$ at the load of the antenna circuit in response to an incident electric field $\mathbf{E}_{\rm inc}(\nu,\theta,\phi)$:

$$\mathbf{E}_{\rm inc}(\nu,\theta,\phi) = E_\theta(\nu,\theta,\phi)\ \hat{\theta}\ +\ E_\phi(\nu,\theta,\phi)\ \hat{\phi}. \tag{A.1}$$

Here, ν is the frequency, (θ,ϕ) are the spherical coordinates in a given reference frame, and $\hat{\theta}$ and $\hat{\phi}$ are the unit vectors corresponding to the coordinates. $\mathbf{E}_\theta$ and $\mathbf{E}_\phi$ are complex numbers. The vector $\mathbf{l}_{\rm load}$ is defined such that the voltage is obtained from the field as:

$$\boxed{V_L(\nu) = \mathbf{l}_{\rm load}(\nu,\theta,\phi)\cdot\mathbf{E}_{\rm inc}(\nu,\theta,\phi)} \tag{A.2}$$

A.1 Obtaining the effective length from the gain.

This appendix is devoted to explain how to obtain $\mathbf{l}_{\rm load}(\nu,\theta,\phi)$ from the measured antenna gains for each polarisation $G_\theta(\nu,\theta,\phi)$ and $G_\phi(\nu,\theta,\phi)$. The gains are provided by the calibration measurements done for the antenna [1]. The gain G relates the power at the antenna terminals in transmission mode $P_{\rm in}$ with the mean Poynting vector of the electromagnetic wave emitted by the antenna, at a distance r from it:

$$G \equiv \frac{{\rm d}P}{{\rm d}a}\frac{4\pi r^2}{P_{\rm in}}. \tag{A.3}$$

There are two gains, one for each polarisation of the electric field. Let us focus on G_θ. The relationship between the complex component E_θ and the gain is [2]:

$$\frac{{\rm d}P_\theta}{{\rm d}a} = \frac{|E_\theta(\nu,\theta,\phi)|^2}{2Z_n} = \frac{P_{in}}{4\pi r^2}G_\theta(\nu,\theta,\phi) = \frac{1}{4\pi r^2}\frac{1}{2}|I_A|^2 R_A G_\theta(\nu,\theta,\phi), \tag{A.4}$$

where P_{in} (I_A) is the power (current) at the antenna terminals and Z_n is the impedance of the medium (air). The antenna impedance is denoted by Z_A, being R_A its real part. Then the modulus of E_θ is given by:

$$|E_\theta| = \frac{1}{2\sqrt{\pi}r}\sqrt{Z_n R_A}|I_A|\sqrt{G_\theta}, \tag{A.5}$$

where we have dropped the explicit dependence of E_θ and G_θ on ν, θ and ϕ for clarity.

Assuming an outward spherical wave (since we are working in the far-field regime), the phase of the complex component $\mathbf{E}_\theta$ must have an e^{ikr} term. However, there can be another frequency and angle dependent phase $\alpha_\theta(\nu, \theta, \phi)$. The equation for E_θ then reads:

$$E_\theta = \frac{1}{2\sqrt{\pi}r}\sqrt{Z_n R_A}|I_A|\sqrt{G_\theta}\ e^{ikr}\ e^{i\alpha_\theta(\nu,\theta,\phi)}. \tag{A.6}$$

A similar calculation can be done to obtain E_ϕ, the component of the field along $\hat{\phi}$. The total field is then given by:

$$\mathbf{E} = \frac{1}{2\sqrt{\pi}r}\sqrt{Z_n R_A}|I_A|\ e^{ikr}\ \left[\sqrt{G_\theta}\ e^{i\alpha_\theta}\ \hat{\theta} + \sqrt{G_\phi}\ e^{i\alpha_\phi}\ \hat{\phi}\right]. \tag{A.7}$$

Following [3], the electric field can be written using the effective length $\mathbf{l}_{\text{eff}}$ of the antenna, as:

$$\mathbf{E} = ikZ_n\frac{e^{ikr}}{4\pi r}|I_A|\ \mathbf{l}_{\text{eff}}. \tag{A.8}$$

However, in reception mode, with an electric field $\mathbf{E}_{\text{inc}}$ coming at the antenna, the effective length only gives the "open-circuit" voltage V_{oc}, i.e., $V_{\text{oc}} = \mathbf{l}_{\text{eff}} \cdot \mathbf{E}_{\text{inc}}$, while what we need is the voltage at the load V_L. We assume a purely resistive load R_L with 50 Ω,

$$\begin{aligned} V_L &= V_{\text{oc}}\ \frac{R_L}{R_L + Z_A} = \frac{V_{\text{oc}}}{2}\sqrt{\frac{R_L}{R_A}}e^{-i\beta}\left(\frac{4R_L R_A}{|Z_A + R_L|^2}\right)^{\frac{1}{2}} = \frac{V_{\text{oc}}}{2}\sqrt{\frac{R_L}{R_A}}e^{-i\beta}\left(1 - \frac{|Z_A - R_L|^2}{|R_L + Z_A|^2}\right)^{\frac{1}{2}} \\ &= \frac{V_{\text{oc}}}{2}\sqrt{\frac{R_L}{R_A}}e^{-i\beta}(1 - |\Gamma|^2)^{\frac{1}{2}}, \end{aligned} \tag{A.9}$$

where $\Gamma = (Z_A - R_L)/(Z_A + R_L)$ is the antenna reflection coefficient. From the definition of $\mathbf{l}_{\text{load}}$ in Eq. (A.2) and of $\mathbf{l}_{\text{eff}}$ in Eq. (A.8) we get,

$$\mathbf{l}_{\text{load}} = \frac{ie^{-i\beta}}{2}\sqrt{\frac{R_L}{R_A}}(1 - |\Gamma|^2)^{\frac{1}{2}}\ \mathbf{l}_{\text{eff}}, \tag{A.10}$$

where we have multiplied by a factor i because a global phase is irrelevant.

From Eqs. (A.7) and (A.8) we can obtain the effective length:

$$\mathbf{l}_{\text{eff}} = \frac{2}{i}\ \frac{\sqrt{\pi}}{k}\ \sqrt{\frac{R_L}{Z_n}}\left[\sqrt{G_\theta}\ e^{i\alpha_\theta}\ \hat{\theta} + \sqrt{G_\phi}\ e^{i\alpha_\phi}\ \hat{\phi}\right]. \tag{A.11}$$

However, the gain supplied by Satimo [1] is not the standard gain but the *realised* gain. The realised gain [2] is defined as the ratio of radiated power and net delivered power to

the antenna by a generator of 50 Ω, including the part of the power that gets reflected due to mismatch, so that the realised gain is less than (or equal to) the standard gain. Both are related precisely by the reflection coefficient Γ in the following way:

$$G = \frac{G^{\rm cal}}{1-|\Gamma|^2}. \tag{A.12}$$

Writing $k = 2\pi\nu/c_n$ and using Eq. (A.10), we finally arrive at the desired relation between $\mathbf{l}_{\rm load}$ and the measured gains for the two polarisations G_θ and G_ϕ:

$$\boxed{\mathbf{l}_{\rm load}(\nu,\theta,\phi) = \frac{c_n}{2\sqrt{\pi}\nu}\sqrt{\frac{R_L}{Z_n}}\left[\sqrt{G^{\rm cal}_\theta(\nu,\theta,\phi)}\; e^{i\alpha_{\theta,{\rm cal}}(\nu,\theta,\phi)}\;\hat{\theta}_{\rm cal} + \sqrt{G^{\rm cal}_{\phi,{\rm cal}}(\nu,\theta,\phi)}\; e^{i\alpha_{\phi}(\nu,\theta,\phi)}\;\hat{\phi}_{\rm cal}\right]} \tag{A.13}$$

From now on, we will assume that we are working with the calibrated gains and drop the superindexes.

A.2 Polarisation and calibration reference frames for AMY

There are two relevant frames in this discussion. One is the spherical frame $(\theta_{\rm pol}, \phi_{\rm pol})$, called the "polarisation frame" (*pol*), and shown in the bottom panel of Fig. A.1, in which the unit vector $\hat{\theta}_{\rm pol}$ indicates the main polarisation of the antenna. The other one is the "calibration frame" (*cal*) $(\theta_{\rm cal}, \phi_{\rm cal})$, chosen to measure the gains of the horn antennas [1], shown in the top panel of Fig. A.1.

A.2.1 A problem with the calibration in the "calibration frame"

In the calibration frame chosen in [1] the polar axis $\theta_{\rm cal} = 0$ corresponds to the center of the antenna field of view, where the sensitivity is highest. **The problem is that there are no measurements of the direction along which the voltage received at the antenna is maximum.** In other words, we do not know the phases $\alpha_{\theta,{\rm cal}}(\nu,\theta,\phi)$ and $\alpha_{\phi,{\rm cal}}(\nu,\theta,\phi)$ in Eq. (A.13), and we do not know if for instance $\mathbf{l}_{\rm load}$ is proportional (with positive real constants) to $\hat{\theta}_{\rm cal}$ and $\hat{\phi}_{\rm cal}$. The measurement of these two phases would tell us the actual direction of $\mathbf{l}_{\rm load}$. Moreover, the behaviour of the phases in frequency is very relevant for the determination of the frequency spectrum of the received signal.

The problem of the lack of measurements of the phases α_θ and α_ϕ is severe around $\theta_{\rm cal} = 0$, where the unit vectors $\hat{\theta}_{\rm cal}$ and $\hat{\phi}_{\rm cal}$ change rapidly, and even discontinuously at $\theta_{\rm cal} = 0$. For instance, $\hat{\theta}_{\rm cal}$ points in opposite directions for $\phi_{\rm cal} = \pi/2$ and $\phi_{\rm cal} = 3\pi/2$ at $\theta_{\rm cal} \sim 0$ as illustrated in Fig. A.2. However, the effective length $\mathbf{l}_{\rm eff}$ and hence $\mathbf{l}_{\rm load}$ in Eqs. (A.2) and (A.13), must be a continuous function in the $(\theta_{\rm cal}, \phi_{\rm cal})$ space, otherwise the voltage in the antenna would depend on the path followed when moving from one point near $\theta_{\rm cal} = 0$ to another.

A.2.2 How to solve the problem?

One way to circumvent the problem **for the co-pol component** of the field is to realise that, in our simulations without targets for the AMY experimental setup, the track of every particle is approximately contained in the plane determined by the beam axis and the position of the antenna (for the antenna placed as shown in Fig. A.2). The axis $\theta_{\rm cal} = 0$ splits this plane into two semiplanes corresponding to $\phi_{\rm cal} = \pi/2$ and $\phi_{\rm cal} = 3\pi/2$.

As shown in Fig. A.2, the unit vectors in the calibration frame, $\hat{\theta}_{\rm cal}$ and $\hat{\phi}_{\rm cal}$, have opposite signs very near the axis $\theta_{\rm cal} = 0$, depending on which plane ($\phi_{\rm cal} = \pi/2$ or $\phi_{\rm cal} = 3\pi/2$) they are located in. However, we can always choose the effective length parallel to $\hat{\theta}_{\rm pol}$ and always with positive (or negative) component, so that the unit vectors are continuous when crossing the $\theta_{\rm cal} = 0$ axis. Besides, in the plane shown in Fig. A.2, we can ignore the ϕ component of the gain, $G_\phi^{\rm cal}$, and use only $G_\theta^{\rm cal}$, which also makes the phases $\alpha_{\theta,{\rm cal}}$ and $\alpha_{\phi,{\rm cal}}$ irrelevant at a single frequency.

Bibliography

[1] SATIMO. Antenna measurement report, Ref. MR.333.4.12.SATI.A. Calibration of the Dual Ridge Horn antenna DRH20-120401A20 used at the AMY experiment.

[2] R. York. Antenna theory, ece 201c. http://my.ece.ucsb.edu/York/Bobsclass/201C/.

[3] S. J. Orfanidis. Electromagnetic waves and antennas. http://www.ece.rutgers.edu/ orfanidi/ewa/orfanidis-ewa-book.pdf.

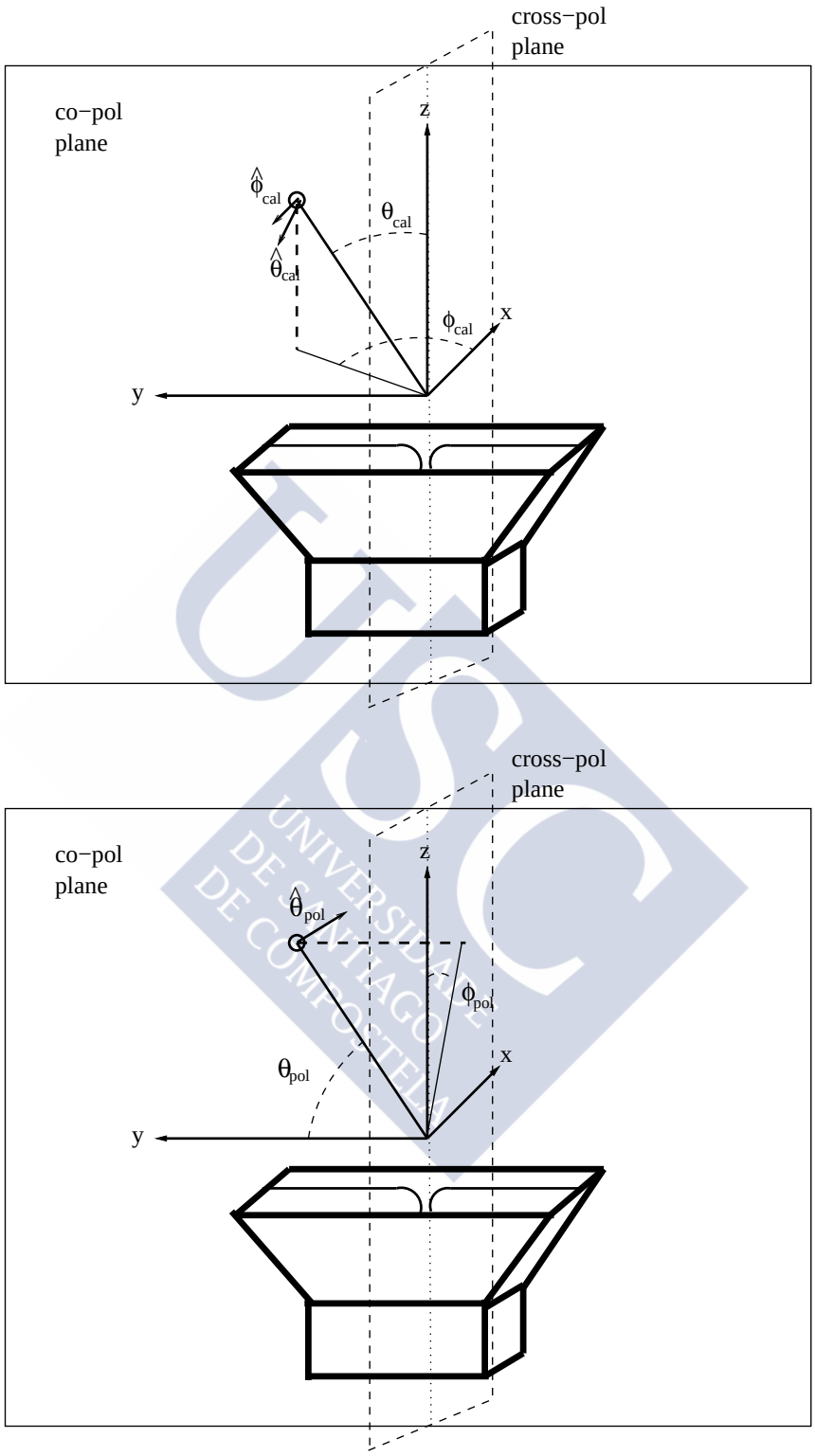

Figure A.1: Calibration frame chosen to measure the antenna gains [1] (top) and polarisation frame (bottom) of the antenna with their respective polar and azimuthal angles.

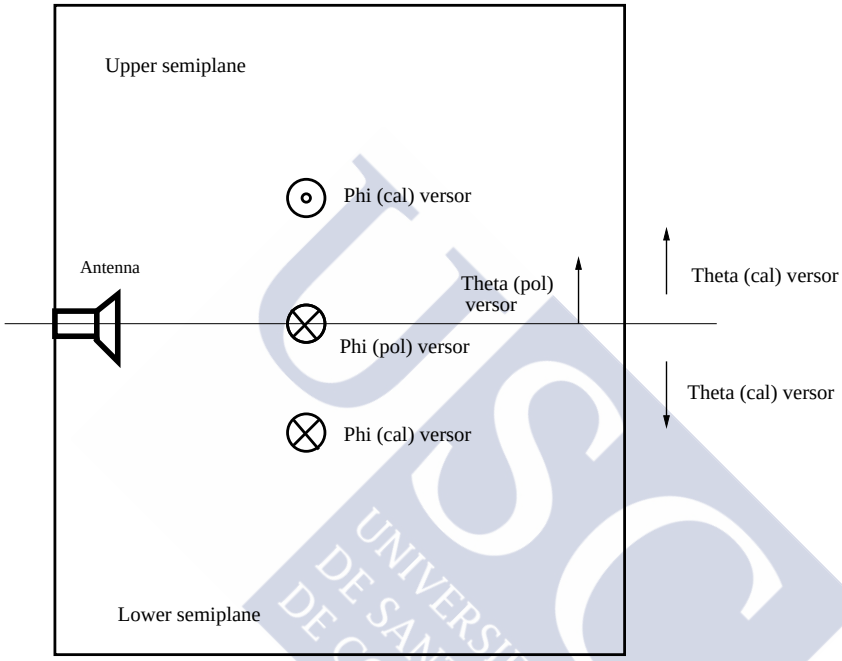

Figure A.2: Plane containing the beam axis and the position of the antenna. The horizontal line indicates the axis $\theta_{\text{cal}} = 0$ of the calibration frame, which divides the plane into two semiplanes corresponding to $\phi_{\text{cal}} = \pi/2$ and $\phi_{\text{cal}} = 3\pi/2$. When crossing that axis, the unit vectors change abruptly as explained before, but we can always choose a certain orientation for the effective length as explained in the text.

USC
UNIVERSIDADE
DE SANTIAGO
DE COMPOSTELA

Appendix B

Calculation of the flux for the MAYBE experiment

In this appendix we relate the experimental definition of the flux F_ν to the electric field. After that, we will show that the measured flux F_ν is precisely the mean Poynting vector per unit frequency.

Let us go back to Eq. (5.32). The antenna receives the field from many directions, but the experimental definition of the flux uses only the maximum effective area, correspoinding to a given direction that we will label as $\theta = \pi/2$. F_ν is in fact given by

$$F_\nu = \frac{\langle P_{\rm sgn}\rangle}{\Delta\nu A_{\rm eff}} = \frac{\langle |V(t)|^2\rangle}{R_L \Delta\nu A_{\rm eff}}, \tag{B.1}$$

where R_L is the resistance of the load circuit, and the load circuit is assumed to be purely resistive ($Z_L = R_L$). After writing explicitely the mean voltage squared $\langle V(t)^2\rangle$, F_ν reads

$$F_\nu = \frac{1}{R_L \Delta\nu A_{\rm eff}} \frac{1}{\Delta t} \int_{t_0}^{t_0+\Delta t} {\rm d}t\ |V(t)|^2. \tag{B.2}$$

If the pulse lasts only Δt we can extend the integration interval to infinity and apply Parseval's identity. Recalling that at the lab we are filtering frequencies in a certain bandwidth $\Delta\nu$, the integration in frequency can be reduced to the bandwidth in consideration.

$$\begin{aligned} F_\nu &= \frac{1}{R_L \Delta\nu A_{\rm eff}} \frac{1}{\Delta t} \int_{-\infty}^{\infty} {\rm d}t\ |V(t)|^2 = \frac{1}{R_L \Delta\nu A_{\rm eff}} \frac{1}{\Delta t} \int_{-\infty}^{\infty} {\rm d}\nu\ |V(\nu)|^2 \\ &= \frac{1}{R_L \Delta\nu A_{\rm eff}} \frac{1}{\Delta t} \int_{\nu_0-\Delta\nu/2}^{\nu_0+\Delta\nu/2} {\rm d}\nu\ 2|V(\nu)|^2 \\ &= \frac{1}{R_L A_{\rm eff}} \frac{1}{\Delta t} 2\langle |V(\nu)|^2\rangle. \end{aligned} \tag{B.3}$$

$\langle |V(\nu)|^2\rangle$ is the mean of the module of the squared voltage. At this point we can use the effective length of an antenna $\mathbf{l}_{\rm eff}$ to obtain the Fourier transform of the voltage $V(\nu)$ from the field $\mathbf{E}(\nu)$. If a plane wave reaches the antenna, the open circuit voltage can be written as

$$V_{\rm oc} = \mathbf{E}(\nu) \cdot \mathbf{l}_{\rm eff}. \tag{B.4}$$

We will assume the main contribution to the field comes from the current lying very near the beam axis. In the plane formed by the beam and the antenna, with the antenna used in MAYBE placed in the copol direction, the effective length is approximately the one for a dipole antenna [1]. The angular pattern of the dipole antenna for energy ($\sin^2\theta$) implies a $\sin\theta$ pattern for the field and the polarization is given by the position of the E-plane ($\hat{\theta}$). The effective length of the dipole antenna can be written as

$$\mathbf{l}_{\text{eff}}(\nu,\theta) = l_{\text{eff}}(\nu,\pi/2)\sin\theta\ \hat{\theta}. \tag{B.5}$$

In the E-plane, the field $E_{\theta,i}$ created by a short particle track using the ZHS formula is polarised along the same direction as the antenna ($\hat{\theta}$). This allows us to write the open circuit voltage as

$$V_{\text{oc}}(\nu) = \sum_i E_{\theta,i}\ \sin\theta_i\ l_{\text{eff}}(\nu,\pi/2), \tag{B.6}$$

where the sum runs over the subtracks in which the total track of the beam ($\sim$1 m) is divided in the ZHS simulation. The voltage at the load is easily calculated from the open circuit voltage using the antenna and load impedances [2],

$$V(\nu) = \frac{Z_L}{Z_L+Z_A}V_{\text{oc}}(\nu) = \frac{Z_L}{Z_L+Z_A}\sum_i E_{\theta,i}\sin\theta_i l_{\text{eff}}(\pi/2). \tag{B.7}$$

Impedance matching ($Z_L = Z_A{}^*$) not only is a desirable experimental condition, but also simplifies calculations,

$$V(\nu) = \frac{Z_L}{2R_L}\sum_i E_{\theta,i}\sin\theta_i\ l_{\text{eff}}(\nu,\pi/2). \tag{B.8}$$

Since $E_\theta\ \sin\theta = E_z$, the sum in the above equation is reduced to the total field in z. Besides, we imposed that $Z_L = R_L$ and hence,

$$V(\nu) = \frac{1}{2}E_z(\nu)\ l_{\text{eff}}(\nu,\pi/2). \tag{B.9}$$

Plugging Eq. (B.9) back in Eq. (B.3) we get

$$F_\nu = \frac{1}{R_L A_{\text{eff}}(\pi/2)}\frac{2}{\Delta t}\frac{1}{4}\langle|E_z|^2|l_{\text{eff}}(\nu,\pi/2)|^2\rangle. \tag{B.10}$$

We assume the bandwidth is small enough for the effective length to be taken constant through all the bandwidth.

The effective length and the effective area must be related. If there is impedance matching and a plane wave is coming at the antenna with an angle $\theta = \pi/2$ with an electric field amplitude E_0 and the same polarization as the antenna, the power obtained using $A_{\rm eff}$ and $l_{\rm eff}$ should be the same. We write both expressions for the power together [2].

$$P_l = \frac{1}{2} R_L |I_L|^2 = \frac{|E_0|^2 |l_{\rm eff}(\pi/2)|^2}{8R_L} = \frac{|E_0|^2}{2Z} A_{\rm eff}(\pi/2) = P_A, \tag{B.11}$$

where Z is the impedance of the medium. The ratio $l_{\rm eff}^2/A_{\rm eff}$ is then equal to

$$\frac{|l_{eff}(\pi/2)|^2}{A_{eff}(\pi/2)} = \frac{4R_L}{Z}, \tag{B.12}$$

which allows us to rearrange Eq. (B.10) properly,

$$F_\nu = \frac{2}{\Delta t} \frac{1}{4R_L} \frac{|l_{\rm eff}(\pi/2)|^2}{A_{\rm eff}(\pi/2)} \langle |E_z|^2 \rangle = \frac{2}{Z\Delta t} \langle |E_z|^2 \rangle. \tag{B.13}$$

Finally, we change the normalization to the one used by the ZHS convention:

$$F_\nu = \frac{1}{2Z\Delta t} \langle |E_{z,\rm ZHS}|^2 \rangle. \tag{B.14}$$

Eq. (B.14) has been derived for the co-polarised case. For the cross-pol flux, we use the x component instead of the z component,

$$F_\nu = \frac{1}{2Z\Delta t} \langle |E_{x,\rm ZHS}|^2 \rangle. \tag{B.15}$$

We will now prove that Eqs. (B.14) and (B.15) for the flux have, as expected, a direct physical connection with the mean Poynting vector. Let us remember that the Poynting vector is the power per unit area and take its mean,

$$\frac{{\rm d}\langle P \rangle}{{\rm d}a} = \frac{1}{\Delta t} \int_{t_0}^{t_0+\Delta t} |\mathbf{E}(t) \times \mathbf{H}(t)| {\rm d}t = \frac{1}{\Delta t} \int_{-\infty}^{\infty} |\mathbf{E}(\nu) \times \mathbf{H}^*(\nu)| {\rm d}\nu. \tag{B.16}$$

If the field arriving at the antenna can be approximated with the ZHS formula, we can introduce the air impedance, almost identical to the vacuum impedance Z_0,

$$\frac{{\rm d}\langle P \rangle}{{\rm d}a} = \frac{1}{\Delta t} \frac{1}{Z_0} \int_{-\infty}^{\infty} {\rm d}\nu |\mathbf{E}(\nu)|^2. \tag{B.17}$$

We must take into account the different normalization due to the Fourier transform convention in the ZHS formula [3, 4], namely $E(\nu) = E_{\rm ZHS}/2$, and we use that $|\mathbf{E}(\nu)| = |\mathbf{E}(-\nu)|$

in order to work with positive frequencies only (otherwise, we are getting only half the existing power).

$$\frac{\mathrm{d}\langle P\rangle}{\mathrm{d}a} = \frac{1}{\Delta t}\frac{1}{Z_0}\int_{-\infty}^{\infty}\mathrm{d}\nu\frac{1}{2^2}|\mathbf{E}_{ZHS}(\nu)|^2 = \frac{1}{\Delta t}\frac{1}{Z_0}\frac{1}{2}\int_{0}^{\infty}\mathrm{d}\nu|\mathbf{E}_{\mathrm{ZHS}}(\nu)|^2. \tag{B.18}$$

The mean power per unit frequency can be obtained performing the derivative with respect to ν under the integral sign,

$$F_\nu = \frac{\mathrm{d}^2\langle P\rangle}{\mathrm{d}a\mathrm{d}\nu} = \frac{1}{2Z_0\Delta t}|\mathbf{E}_{\mathrm{ZHS}}(\nu)|^2. \tag{B.19}$$

The field in Eq. (B.19) must be projected in order to obtain the power of the co-pol or cross-pol components. Eq. (B.19) is the same as Eq. (B.14), the proof that the measured flux is indeed related to the Poynting vector.

Bibliography

[1] C. Williams. First results from the Microwave Air Yield Beam Experiment (MAYBE). In *Proceedings of Intertational Symposium on Future Directions in UHECR Physics (UHECR 2012)*.

[2] S. J. Orfanidis. Electromagnetic waves and antennas. http://www.ece.rutgers.edu/ orfanidi/ewa/orfanidis-ewa-book.pdf.

[3] E. Zas, F. Halzen, and T. Stanev. Electromagnetic pulses from high-energy showers: Implications for neutrino detection. *Physical Review D*, **45**:365, 1992.

[4] D. García-Fernández, J. Alvarez-Muñiz, W. R. Carvalho Jr., A. Romero-Wolf, and E. Zas. Calculations of electric fields for radio detection of ultrahigh energy particles. *Physical Review D*, **87**(023003), 2013.